Sascha Datta

Non-Ionic Binary Surfactant Systems and Microemulsions as Model Systems for Thermal Diffusion Studies

Non-Ionic Binary Surfactant Systems and Microemulsions as Model Systems for Thermal Diffusion Studies

Inaugural-Dissertation

zur Erlangung des Doktorgrades

der Mathematisch-Naturwissenschaftlichen Fakultät

der Universität zu Köln

vorgelegt von

Sascha Datta

aus Leverkusen

Köln

November 2010

| Berichterstatter: | Prof. Dr. Reinhard Strey |
| | PD Dr. Simone Wiegand |

| Tag der mündlichen Prüfung: | 13.01.2011 |

Abstract

Thermal diffusion (or the *Soret* effect) describes the diffusion of matter in the presence of a temperature gradient. Although this process is studied and applied since more than 100 years the underlying molecular mechanism in liquids is still far from being understood. Colloidal dispersions are versatile model systems to study the thermal diffusion behavior of large particles in a solvent. However, the synthesis of colloidal particles with identical morphology is a complex task. On the other hand aqueous surfactant solutions and microemulsions are promising systems to study the *Soret* effect. Compared to colloidal particles the aggregates form spontaneously and do not require any additional stabilisation. Furthermore the radius and the shape of the diffusing aggregates, as well as their interfacial tension can be systematically adjusted via the variation of the composition and temperature. In order to address some important aspects of the thermal diffusion behavior three different types of self-assembled surfactant systems were formulated and systematically studied: (i) At first the role of the ionic dye Basantol$^{®}$ Yellow 215, which causes an unexpected two-mode signal in the classical *Thermal Diffusion Forced Rayleigh Scattering* (TDFRS) experiment [*Ning et al.* Progr Colloid Polym Sci (2006) 133: 111–115], is examined using the system $H_2O - C_{12}E_6$. Systematic phase behavior studies and small angle neutron scattering experiments (SANS) proved that the dye is incorporated into the aggregates like an ionic co-surfactant, influencing not only the thermal diffusion behavior but also the overall properties of the systems. These results strongly suggest that one should refrain from the use of surface-active dyes in TDFRS experiments on self-assembled systems. (ii) To study the dependence of the *Soret* coefficient S_T on the radius of the aggregates and the slope of the interfacial tension, both being controversially discussed in the literature, different microemulsions of the type $H_2O - C_{12}E_5 - n$-alkane were formulated that allow for an isothermal study of these dependencies. Correlating the results of the systematic SANS and interfacial tension measurements with the *Soret* coefficient S_T it was found that within the measurement range S_T depends almost linearly on the droplet radius, the slope of the interfacial tension as well as on the product of both quantities. (iii) In the last part systematic surface tension and TDFRS measurements were performed in binary aqueous *n*-alkyl glucoside (C_iG_j) solutions to study the thermal diffusion behavior around the critical micelle concentration (cmc). The obtained results clearly show that the *Soret* coefficient exhibits an abrupt change at the cmc. To sum up, this work shows that aqueous surfactant systems and microemulsions are eminently suited to elucidate some of the underlying molecular mechanism of the *Soret* effect.

Kurzzusammenfassung

Thermodiffusion (*Soret* Effekt) beschreibt die Diffusion von Materie unter dem Einfluss eines Temperaturgradienten. Obwohl dieser Prozess seit mehr als 100 Jahren studiert und angewendet wird, ist er für Flüssigkeiten auf molekularer Ebene bislang nicht verstanden. Geeignete Modellsysteme für grosse Partikel in Lösung sind kolloidale Dispersionen. Allerdings stellt die chemische Synthese solcher Partikel mit identischer Morphologie eine schwierige Aufgabe dar. Wässrige Tensidsysteme und Mikroemulsionen bieten alternativ vielversprechende Modellsysteme zur Untersuchung des *Soret* Effekts. Im Vergleich zu kolloidalen Partikeln bilden sich die Aggregate in diesen System spontan und benötigen keine weitere Stabilisierung. Darüber hinaus können durch Variation der Temperatur und der Zusammensetzung der Radius, die Form sowie in Mikroemulsionen auch die Grenzflächenspannung systematisch eingestellt werden. Es wurden drei verschiedene Typen von selbstorganisierten Tensidsystemen dargestellt und charakterisiert um jeweils einen bestimmten Aspekt der Thermodiffusion beleuchten: (i) Zuerst wurde der Einfluss des ionischen Farbstoffes Basantol® Gelb 215, welcher in der sog. klassischen *Thermal Diffusion Forced Rayleigh Scattering* (TDFRS) Methode [*Ning et al.* Progr Colloid Polym Sci (2006) 133: 111–115] ein unerwartetes Messsignal verursacht, auf das binäre System $H_2O - C_{12}E_6$ untersucht. Durch systematische Untersuchung des Phasenverhaltens und Messungen der Kleinwinkelneutronenstreuung (SANS) konnte gezeigt werden, dass sich dieser Farbstoff als Cotensid in die Aggregate einlagert und so nicht nur das Thermodiffusionsverhalten, sondern auch die generellen Eigenschaften solcher Systeme beeinflusst. Diese Ergebnisse zeigen deutlich, dass auf die Zugabe von grenzflächenaktiven Farbstoffen in TDFRS Experimenten an mikrostrukturierten Systemen verzichtet werden sollte. (ii) Zur Untersuchung der Radienabhängigkeit, welche in der Literatur kontrovers diskutiert wird, sowie der Abhängigkeit des *Soret* Koeffizienten S_T von der Grenzflächenspannung, wurde durch systematische Variation der Alkankettenlänge in wasserreichen Mikroemulsionen des Typs $H_2O - C_{12}E_5 - n$-Alkan ein Modellsystem zur Verfügung gestellt, das die isotherme Untersuchung der genannten Einflüsse erlaubt. Durch Korrelation der Ergebnisse aus systematischen SANS- sowie Spinning Drop Messungen mit dem *Soret* Koeffizienten S_T wurde gefunden, dass S_T im Messbereich näherungsweise linear vom Tröpfchenradius, der Steigung der Grenzflächenspannung und dem Produkt beider Größen abhängt. (iii) Im letzten Teil dieser Arbeit wurden an binären wässrigen n-Alkyl Glucosid – Lösungen ($H_2O - C_iG_j$) systematische Oberflächenspannungs- und TDFRS Messungen durchgeführt, um das Thermodiffusionsverhalten nahe der kritischen Mizellkonzentration (cmc) zu untersuchen. Die erhaltenen Ergebnisse zeigen eindeutig, dass sich S_T sprunghaft an der cmc ändert. Zusammengenommen zeigt diese Arbeit, dass wässrige Tensidsysteme und Mikroemulsionen aussichtsreiche Modellsysteme zur Aufklärung wichtiger Aspekte des *Soret* Effekts auf molekularer Ebene darstellen.

Danksagung

Herzlich bedanke ich mich bei Herrn Prof. Dr. R. Strey für die freundliche Aufnahme in seinen Arbeitskreis und für die Möglichkeit im Rahmen dieses Projektes meine Doktorarbeit anfertigen zu können. Auch für seine wertvollen Ratschläge, Tipps und Diskussionen bin ich sehr dankbar. Durch seine stete Diskussionsbereitschaft lieferte er mir wertvolle Denkanstöße und Ideen, die maßgeblich zum Gelingen dieser Arbeit beigetragen haben.

Danken möchte ich herzlich Frau PD Dr. Simone Wiegand für ihre Hilfsbereitschaft, Betreuung und Begleitung während meiner Doktorarbeit. Das Zur-Verfügung-Stellen von Ratschlägen, Wissen, Hilfe und Geduld zu jeder Zeit hat mir sehr geholfen.

Herrn PD Dr. Thomas Sottmann gilt mein besonderer Dank. Die Betreuung der Arbeit während des gesamten Zeitraumes sowie der gemeinsame Besuch von Tagungen und die Durchführung von *Mess-Sessions* habe ich als etwas „Nicht-Selbstverständliches" erlebt. Für deine Hilfsbereitschaft und Unterstützung bei allen auftretenden Fragen und Problemen, Lieber Thomas – vielen Dank!

Meinem Doktoranden-Kollegen in Jülich, Bastian Arlt, danke ich für seine große Hilfsbereitschaft und die freundschaftliche Zusammenarbeit, die eine große Bereicherung während meiner Doktorarbeit waren. Auch bei Herrn Dr. Hui Ning bedanke ich mich für die gute Zusammenarbeit und seine Hilfsbereitschaft während der ersten Monate meiner Arbeit.

Bei Herrn Dr. L. Belkoura bedanke ich mich herzlich für seine Erläuterungen und Hilfestellungen beim Durchführen und Auswerten der DLS Messungen und für das Vermessen einer Standard-Vergleichsprobe im Elektronenmikroskop. Herrn Dr. H. Frielinghaus und Dr. P. Busch danke ich für ihre Unterstützung und Hilfsbereitschaft während der SANS Messungen in Garching. Dankbar bin ich auch Herrn Metzner und Herrn Michaelis für ihre jederzeit spontane Hilfsbereitschaft bei technischen Problemen. Herrn W. Röhl danke ich für die Hilfe und Erläuterungen zur Technik und Verwendung verschiedener Apparate sowie für die Ratschläge zur Auswertung der Messungen.

Pierre Dams, Carola Harbauer und Thomas Heinrichs danke ich für ihre Mitarbeit an den hier vorgestellten Projekten im Rahmen ihrer Praktika und Bachelorarbeiten. Besonders Pierre Dams sei hier für seine außerordentlichen Bemühungen bei den Spinning Drop Messungen gedankt.

Weiterhin bedanke ich mich ganz besonders bei meinen Kollegen, Dr. Verena Dahl, Hanna Görke, Pascal und Nadja Wulff, Alexander Müller, Helge Klemmer, Roland Oberhoffer, Setareh Maleknia, Lars Menger, Nils Becker und anderen, die diese Zeit zu einem schönen Erlebnis gemacht haben. Besonders danke ich den hier aufgeführten Personen auch für Ihre spontane Hilfsbereitschaft während der „letzten Züge" des Zusammenschreibens! Meinem Kollegen Dr. Michael Klostermann möchte ich an dieser Stelle für die freundschaftliche Zusammenarbeit und seine Hilfsbereitschaft besonders danken! Dr. Tobias Foster danke ich für seine guten Ratschläge, Korrekturen und Unterstützung! Auch die vielen Gespräche über ernste und weniger ernste (aber immer wichtige) Dinge des Lebens werde ich in Erinnerung behalten.

Der wichtigste Dank gilt meinen Eltern und meinem Bruder, ohne deren Unterstützung diese Arbeit und vieles andere nicht möglich gewesen wären! Ganz besonders herzlich bedanke ich mich bei Anne für alles, was im Einzelnen aufzuzählen den Rahmen an dieser Stelle sprengen würde.

Table of Contents

1 Introduction

About 150 years ago *Carl Ludwig* and *Charles Soret* observed independently the process of thermal diffusion [1, 2] which is therefore also referred to as *Ludwig – Soret* effect. They found that if a temperature gradient is applied to a multicomponent mixture the components separate to a certain extend. Since then this effect was utilized in a wide range of applications. In 1939 for example *Clusius* and *Dickel* succeeded in separating gaseous chlorine into its isotopes using a thermal diffusion column [3, 4]. The same method was subsequently used for the enrichment of uranium in the *Manhattan Project* [5]. In the method of thermal field flow fractionation the thermal diffusion effect is utilized for the separation and analysis of polydisperse macromolecular and colloid systems [6, 7]. In recent years thermal diffusion has also become increasingly relevant for the characterisation of oil reservoirs, i.e. the elucidation of the distribution of crude oil components within the geothermal field [8, 9].

In the context of the phenomenological equations of irreversible thermodynamics (see e.g. [10]) the *Ludwig – Soret* effect is described as the diffusion, that results from the coupling of a heat flux and a mass flux (an introduction is given in section 2.1). Since the response to the temperature gradient is usually different for each component, a concentration gradient builds up which, as a *cross* effect, induces a mass diffusion in the opposite direction to the temperature gradient. In the steady state the ratio of this concentration gradient to the applied temperature gradient is thereby proportional to the ratio of the corresponding transport coefficients. Those are the thermal diffusion coefficient D_T and the mutual diffusion coefficient D. Accordingly, a

quantitative measure for the strength and the direction (i.e. towards the cold or warm region) of the themal diffusion of a certain component in a multicomponent mixture is given by the ratio of both quantities, which is the definition of the *Soret* coeffient

$$S_T \equiv \frac{D_T}{D} \propto \frac{\nabla c}{\nabla T}.$$

(1.1)

Although the process of thermal diffusion is studied and applied since more than 100 years, the underlying molecular mechanism is still far from being understood. While for binary mixtures of non-uniform gases the effect has already been described at the beginning of the last century within the kinetic gas theory, developed by *Enskog* and *Chapman* [11], for liquid systems no such general theoretical description exists. In some cases there is even a lack of qualitative predictions. Thus, it is of major interest to gain a deeper understanding of the underlying molecular mechanism of the thermal diffusion effect in liquids.

In this context, the thermal diffusion effect has in the last years been studied on a broad range of liquid systems. Many experiments have been performed on polar or non-polar mixtures of low molecular weight components (e.g. [12] [13] [14] [15-18]). Thereby, it was found, that in mixtures of polar liquids specific interactions between the molecules dominate the thermal diffusion behavior, while the mass and the size of the molecules are most important for *Lennard-Jones* fluids. Along with the improvement of experimental techniques in recent years [19] [20], investigations were extended to more complex systems, such as polymer solutions [19, 21-23], magnetic fluids [24], colloidal dispersions [25-27] or aqueous solutions containing surfactants [28-31] or bio-macromolecules [32]. Some general influences on the thermal diffusion behavior have thereby been established: The component with larger mass, larger diameter or larger moment of inertia usually moves towards the cold region. Thereby the exact dependence of S_T on the diameter of the diffusing spezies has controversely been discussed in recent time. While *Vigolo et al.* [33] and *Putnam* [34] found a linear size dependence of S_T for ionic microemulsions and spherical polystyrene nano-particles as well as lysozyme solutions, respectively, *Duhr* and *Braun* [35] found a quadratic size dependence for spherical polystyrene particles of µm-size. By studying the thermal diffusion behavior of polymer solutions it was found that the Soret coefficient S_T scales simply with the molecular weight of the polymers [36-38]; However at infinite dilution D_T has been found to become independent of the molecular weight [39].

The interactions-dominated contributions to the thermal diffusion behavior can roughly be devided in particle-solvent and interparticle contributions. Accordingly, in the highly dilute regime, interactions between the diffusing spezies and the solvent will influence the thermal diffusion behavior. Those interactions can for example be the breakdown of the hydrogen bond network of the solution [40] or the formation of an ionic double layer [30]. For systems of higher concentrations, on the other hand it was found that the interparticle interactions (or collective effects) dominate the thermal diffusion behavior [31]. As a general observation the results indicate, that the interfacial tension between the particles (i.e. either colloide, or aggregates) and solvent is of central importance (see [19, 41] for a review).

From the above it becomes clear that for a systematic investigation of the thermal diffusion behavior careful attention must be paid to the experimental design and in particular the choice of the model system [25]. Versatile model systems to study the thermal diffusion behavior of high molecular weight particles in a low molecular solvent are colloidal dispersions. Thereby the particles might be regarded as *big atoms* [42], that interact via *simple, well-defined forces* [25]. However, this approach also rises difficulties: The control of colloidal stability needs to be considered [26, 43]. In addition the chemical microstructure and particle morphology of colloidal particles, which have a major influence on the interfacial particle-solvent interaction is not always reproducible within two individually synthesized batches [44-46].

Promising model systems to study the thermal diffusion behavior systemtically are aqueous surfactant solutions and microemulsions [47-50]. In such systems the surfactant molecules self-assemble e.g. in form of micelles or microemulsion droplets, that can be regarded as the diffusing spezies, in the same way as the particles in colloidal systems. Compared to colloidal particles these thermodynamically stable surfactant systems do not require any additional stabilisation. Furthermore, self-asssembly occurs spontaneously and thus avoids the difficulties associated with the chemical synthesis of colloidal particles. Furthermore, by variation of the composition or temperature, the size and shape of the thermodynamically stable aggregates can systematically be varied, which offers the possibility to study the influence of those properties on the *Soret* coefficient.

The first studies on surfactant systems were mainly focussed on ionic [30, 31, 51, 52] and mixed ionic/non-ionic [53] micelles. These studies demonstrated that at low surfactant concentrations the *Soret* coefficient is strongly influenced by the *Debye − Hückel* length, while at higher

surfactant concentrations electrostatic interparticle interactions are dominant. Non-ionic surfactants in contrast provide model systems that allow studying the influence of parameters such as size, shape and concentration of the diffusing spezies without considering any electrostatic interactions.

There are, however, up to now only very few publications [28, 29] that investigate the thermal diffusion of non-ionic surfactant aggregates. One reason for this lack might be the fact that many commonly used non-ionic surfactants have a lower density than water, which causes overlaying convection effects in several experimental methods, such as thermal diffusion cells that are cooled from below and heated from above [19, 29]. *Wiegand et al.* [54] performed first measurements of the thermal diffusion behavior of the non-ionic surfactant dodecyl hexaethylene glycolether ($C_{12}E_6$) in water using the classical thermal diffusion forced *Rayleigh* scattering (TDFRS) method, that avoids convection problems [29] (refer to section 3.2). Thereby, the motivation was to investigate the thermal diffusion behaviour of the aggregates at intermediate temperature ($T = 25 - 30$ °C) while changing their shape by the variation variation of the surfactant concentration.

However, for these measurements and further investigations on a wider range of non-ionic *n*-alkylpolyglycol ether surfactants (C_iE_j) in water [28] the raw data, being obtained from the TDFRS experiments, deviates significantly from the expected pattern: Instead of the expected one-mode signal a two-mode signal is generally found at lower surfactant concentrations and higher temperatures. *Ning et al.* [28] suspected, that this deviation is connected to the presence of ionic dye molecules in the sample, which need to be added in order to absorb the laser light that creates the temperature gradient. It remained an open question, if the dye affects also the structural and thermodynamic properties of the aqueous surfactant system. It is thus one topic of this work to investigate the influence of the ionic dye on the properties of water – C_iE_j systems.

As it was mentionend above, numerous works in the literature reveal a close connection between the *Soret* effect and the interfacial particle-solvent interaction [25, 30, 35, 53], which in turn is related to the interfacial tension between the particle and the solvent [25]. However, the experimental determination of the interfacial tension between the particle and the solvent is a sophisticated task. Contrarily, in microemulsion systems the interfacial tension is experimentally accessible and can systematically be varied with tuning parameters, such as composition and temperature [50, 55, 56]. Thus, microemulsions provide a unique model system in order to study

the relation between the *Soret* coefficient and the particle/solvent interfacial tension. Furthermore, as it was mentionend before, the size of the aggregates in microemulsion systems can be systematically varied. Accordingly, those systems allow also investigating the controversly discussed relation between the *Soret* coefficient and the size of the diffusing spezies. Nevertheless, investigations of the thermal diffusion in microemulsions are yet rare [33]. In this context, the main topic of this work was the formulation and characterisation of non-ionic microemulsions as model systems that allow relating their structural and thermodynamic properties to the results of thermal diffusion studies, i.e. the *Soret* coefficient.

As a unique feature of self assembled systems a certain concentration exists at which the monomerically dissolved surfatant molecules start to self-aggregate to micellar structures. This concentration is referred to as critical micelle concentration (cmc). It was recently proposed [57] that the *Soret* coefficient as function of the surfactant concentration in binary aqueous surfactant solutions might exhibit an abrupt change at the cmc. In order to clarify this point, as a third topic in this work we want to perform systematic studies on aqueous solutions of surfactants of the type *n*-alkyl glucoside (C_iG_j), that exhibit a fairly high cmc in order to correlate the commonly determined cmc with the trend of the *Soret* coefficient at the respective concentration.

1.1 Motivation and Objectives

This work was performed within the scope of a joint project that was initiated in order to combine the expertise of *T. Sottmann* and *R. Strey* (University of *Cologne)* in the field of surfactant systems and microemulsions with the expertise of *S. Wiegand* (*FZ Jülich*) in the field on thermal diffusion. The major task of this collaboration is the study of the thermal diffusion behavior of the surfactant systems and microemulsions by means of the thermal diffusion forced *Rayleigh* scattering (TDFRS) method. The basis of these studies is a careful characterization of the thermodynamic and structural properties of the self-assembled nanostructured fluids under study. Three particular systems were used in order to elucidate certain aspects of the thermal diffusion behavior:

(i) At first, the pseudo-binary surfactant system water – $C_{12}E_6$ – Basantol® Yellow 215 should be studied in detail in order to investigate the influence of the ionic dye which has to be added to the systems under study in the classical TDFRS experiment. As has been described above, this dye is considered to be responsible for an unexpected two-mode signal in these experiments [28].

Particulary the microstructure of the surfactant system should be studied by means of small angle neutron scattering (SANS) as a function of both, the surfactant concentration and the temperature. In addition, the influence of the dye should be compared with that of the ionic surfactant sodium dodecyl sulphate (SDS).

(ii) The formulation and characterisation of water-rich non-ionic microemulsions is the second objective of this work. The complex phase-behavior and microstructure of microemulsions of the type water – n-alkane – non-ionic surfactant (C_iE_j) has been extensively studied by *Kahlweit* and *Strey* and various other groups at the end of the 1980s (see e.g. [47, 50] for a review). On the basis of this knowledge droplet microemulsions with adjustable size should be formulated at constant temperature. In order to obtain the droplet size and other structural parameters, the microstructure of these systems should be studied with SANS as well. Using these systems, the size dependence of the *Soret* coefficient on the microemulsion droplet size should subsequently be investigated isothermally. Another objective is to study the relation between the interfacial tension between the solvent and the diffusing microemulsion droplets [53] and their thermal diffusion behavior. Therefore the interfacial tension between the coexisting aqueous microemulsion and the oil excess phase should be measured using the *spinning drop* method. The results should then be related to the measurements of the *Soret* coefficient, which are performed by the group in *Jülich*.

(iii) The last but not least objective of this work is focused on the detection of the critical micelle concentration (cmc) in aqueous non-ionic n-alkyl glucoside (C_iG_j) surfactants systems by means of thermal diffusion forced *Rayleigh* scattering measurements. Thus, systematic surface tension measurements should be performed in order to extract the cmc and the effective surfactant head group area, under variation of the temperature, the alkyl chain length and the number of surfactant head groups. Again the results should then be related to the measurements of the *Soret* coefficient, which are performed by the group in *Jülich*.

This thesis is organized as follows: In the next section the fundamentals of the thermal diffusion effect, non-ionic binary surfactant systems and microemulsions are briefly reviewed. Furthermore a brief introduction into neutron scattering is given, that includes the presentation of the scattering models that were applied in this work. Afterwards, the important experimental tool dynamic light scattering and the TDFRS experiment are briefly introduced. Thereby it should be noted that the TDFRS experiments were not performed as part of this work. However, since the

results of these experiments are partly discussed, the method is also presented. The presentation of the results and their discussion are presented seperately for the three aspects that were adressed in this work: (i) First the results of the investigations on the influence of Basantol® Yellow 215 on the binary surfactant system $H_2O - C_{12}E_6$ are presented. (ii) At second follows the investigation of the *Soret* effect at the critical micelle concentration of aqueous solutions of *n*-alkyl glucoside (C_iG_j) surfactants. (iii) In the third part the investigations of non-ionic microemulsions of the type $H_2O - C_{12}E_5 - n$-alkane as model system for thermal diffusion studies are presented. Each of those parts contains a short motivation, which also recalls the objectives for the respective part. This structure should allow to understand each part in its own context. In the end of this thesis a summary is given that resumes the main results of this work and briefly adresses some ideas for further investigations.

2 Fundametals

2.1 The *Soret* effect

In this section the description of the *Soret* effect in terms of the phenomenological equations of fluxes and forces is presented. The detailed description can be found in textbooks of thermodynamics, or physical chemistry, e.g. [58]. At first, the entropy production due to heat transport and the entropy production due to mass transport will be presented. In the next step the coupling of both processes will be described, that leads to the expression of the *Soret* effect [59]. Although there is so far no microscopic understanding of the effect in liquids, some general influences have been identified in the past, that control the thermal diffusion behavior. Subsequently, at the end of this section a brief overview will be given about the main influences that have been identified to control the thermal diffusion effect in liquid systems.

2.1.1.1 *Entropy production due to heat transport*

We consider a closed system consisting of two subsystems at the temperatures T_1 and T_2, respectively. Thereby we assume $T_1 > T_2$. This is schematically illustrated in Figure 2.1-1 (left).
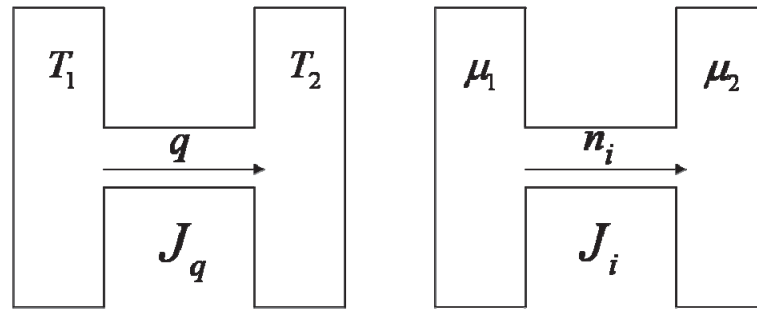
Figure 2.1-1: Schematic illustration for the heat transport (left) and mass transport (right) in a closed binary system.

Since the system does not exchange heat q with its surrounding, the entropy change ΔS, that results from the heat flow J_q inside the system can be expressed as.

$$\Delta S = \Delta S_1 + \Delta S_2 \tag{2.1}$$

If we consider the classic definition of entropy we get

$$\Delta S = q \cdot \left(\frac{1}{T_2} - \frac{1}{T_1} \right). \tag{2.2}$$

We can postulate, that the entropy increases, i.e. $\Delta S > 0$, because of the change inside the closed system, is never negative, and furthermore $T_1 \neq T_2$. For the differential heat transmission dq we then get

$$dS = dq \cdot \left(\frac{1}{T_2} - \frac{1}{T_1} \right). \tag{2.3}$$

If we consider now the entropy production per unit $\dot{\sigma}$ time we get.

$$\dot{\sigma} = \frac{dS}{dt} = \frac{dq}{dt} \left(\frac{1}{T_1} - \frac{1}{T_2} \right) = \frac{dq}{dt} \left[(T_1 - T_2) / T_1 T_2 \right]. \tag{2.4}$$

2.1.1.2 *Entropy production due to mass transport*

Diffusion can also lead to an increase of the entropy. The well known Gibbs equation writes

$$TdS = dU + pdV - \sum_i \mu_i dn_i \, . \tag{2.5}$$

Therein U is the internal energy, p the pressure, V the volume, μ_i the chemical potential of the substance i and n_i the amount of substance i. If the diffusion takes place in a closed system (Figure 2.1-1, right) it is $dU = 0$ and $dV = 0$. Accordingly, relation (2.5) reduces to

$$TdS = -\sum_i \mu_i dn_i \tag{2.6}$$

If the component i diffuses from one place in the system, where its chemical potential has the value $\mu_{i,1}$ to a place, where the value is $\mu_{i,2}$ the resulting change of the entropy is given by

$$dS = -dn_i \left(\mu_{i,2} / T - \mu_{i,1} / T \right) \tag{2.7}$$

Then the resulting entropy production for the diffusion is given by

$$\dot{\sigma} = dS / dt = -\sum_i \left(dn_i / dt \right) \cdot \left(\mu_{i,2} / T - \mu_{i,1} / T \right) . \tag{2.8}$$

2.1.1.3 *The coupling between mass and heat transport*

The entropy production of a system, where more than one process occurs can in general be expressed as a sum of products

$$\dot{\sigma} = \sum_k J_k X_k \, , \tag{2.9}$$

in which the factors X_i and J_i, are so called *corresponding* fluxes and forces. Thus, regarding the entropy production due to heat transport [equation (2.4)], the flux is given by $J_q = \dfrac{dq}{dt}$ and

the corresponding force is $X_q = \left(1/T_1 - 1/T_2\right)$. If we use the gradient instead of the temperature

difference this can be expressed in a more general way by $X_q = \nabla \dfrac{1}{T}$.

In a similar way, for the entropy production due to diffusion, the flux is given by $J_i = dn_i / dt$

and the corresponding force is $X_i = -\left(\mu_{i,2}/T - \mu_{i,1}/T\right)$, or in general $X_i = -\dfrac{\nabla \mu_i}{T}$.

If we use those expressions in (2.9) we get

$$\dot{\sigma} = J_q \nabla \frac{1}{T} - \sum_i J_i \frac{\nabla \mu_i}{T} \qquad (2.10)$$

For small deviations from the equilibrium, furthermore a linear relation exists between the flux J

and the corresponding force X, which is given by

$$J = L \cdot X . \qquad (2.11)$$

This relation is called the phenomenologic equation of fluxes and forces, whereby L is the

phenomenological coefficient, that relates the flux J to the correponding force X. If we further

assume, that a flux J_k is determined by more than one force, i.e. a sum of forces, we obtain

$$J_k = \sum L_{ki} X_i . \qquad (2.12)$$

Thereby, in general a force X_i causes not only a flux of one component 1 but can also induce a

flux of a second component 2, which leads to a so-called *cross effect*. The coupling between heat

flux and mass flux can be regarded as a combination of the *Soret* effect and the *Dufor* effect. In

the former one, a mass flux is in driven by the heat flux, whereas in the latter one a heat flux is

driven by a concentration gradient.

From now on we will regard a binary mixture of components 1 and 2. Using the *Gibbs-Duhem*

relation $n_1 d\mu_1 + n_2 d\mu_2 = 0$, and in analogy $j_1 \nu_1 + j_2 \nu_2 = 0$ [58], where ν_1 and ν_2 are the partial

molar volumes of the components 1 and 2, respectively, equation (2.10) can be written as [59],

$$\dot{\sigma} = J_q \cdot \nabla \frac{1}{T} - J_1 \frac{(\nabla \mu_i)_{p,T}}{T} \left(1 + \frac{v_1 n_1}{v_2 n_2}\right) \tag{2.13}$$

which represents the entropy production due to the heat flux and the diffusion of component 1. With $\nabla \mu_1 = (\partial \mu_1 / \partial n_1) \nabla n_1$ [59] and using the relation $\nabla(1/T) = -(1/T^2)\nabla T$, which is valid for a small temperature difference [58] we obtain for the mass flux of component 1 according to equation (2.12)

$$J_1 = L_{1q} \left(\frac{1}{T^2}\right) \nabla T - L_{11} \frac{\nabla n_1}{T} \left(\frac{\partial \mu_i}{\partial n_1}\right) \left(1 + \frac{v_1 n_1}{v_2 n_2}\right). \tag{2.14}$$

This flux J_1 (2.14) can also be expressed in another form, [59]

$$J_1 = \rho D \nabla c - \rho c (1-c) D_T \nabla T, \tag{2.15}$$

where ρ is the density of the mixture and c is the molar concentration of component 1. D and D_T are the mutual and thermal diffusion coefficient, respectively. In the steady, state, i.e. where the detectable flux vanishes ($J_1 = 0$) [equation (2.15)] can be rearranged to

$$S_T \equiv \frac{D_T}{D} = -\frac{1}{c_1(1-c_1)} \frac{\nabla c}{\nabla T}, \tag{2.16}$$

which is the definition of the *Soret* coefficient S_T of component 1 in the binary system under study. The sign of S_T determines the direction of the thermal diffusive motion: Per definition, a positive S_T of component 1 corresponds to the movement of component 1 towards the colder region in the system.

2.1.1.4 *Main contributions to Thermal Diffusion in Liquid Systems.*

While for mixtures of gases the *Soret* effect was already theoretically described by *Chapman* and *Enskog* from the theory of non-uniform gases [11], no such theoretical description for liquid systems exists. However, some general contributions have been identified, which control the thermal diffusion effect. These are schematically illustrated in Figure 2.1-2 and will briefly be presented in the following:
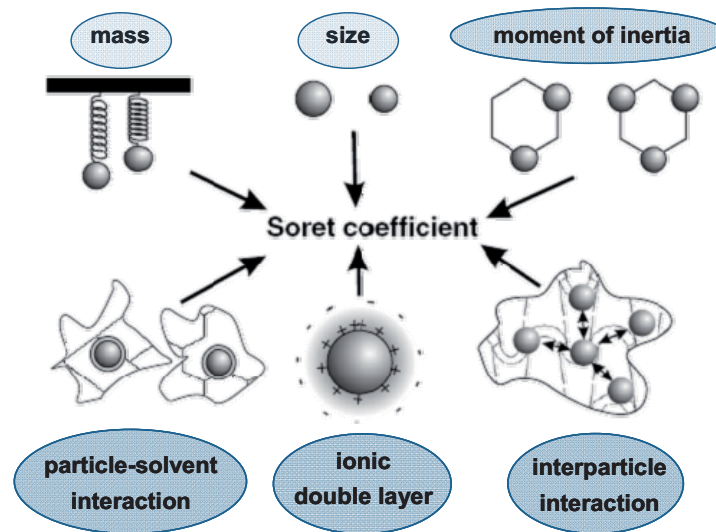
Figure 2.1-2: Schematic illustration oft he main contributions to the *Soret* coefficient in liquids (according to [2]).

The physical parameters, like mass, diameter or moment of inertial can fairly easily be accessed. Some general rules have been established: In general the component (i.e. particle, molecule or aggregate) with larger mass, larger diameter or larger moment of inertia moves towards the cold region. Regarding the mass, from the thermal diffusion behavior of polymer solutions simple scaling laws as function of molecular weight and density have been derived [36-38], however at infinite dilution S_T has been found to become independent of the molecular weight [39]. The exact dependence of D_T on the diameter has controversely been discussed in recent time: While *Vigolo et al.* [33] and *Putnam* [34] found a linear size dependence of S_T for ionic microemulsions and polystyrene spheres as well as for lysozyme solutions, respectively, *Duhr* and *Braun* [35] found a quadratic size dependence for the polystyrene spheres. Chemical contributions, i.e. interaction with the solvet, ionic double layer and interparticle interactions can roughly be devided in single particle and interparticle contributions. In the highly dilute regime interactions between the particles (or molecules or aggregates) and the solvent will influence the thermal diffusion behavior. Those interactions can for example be the breakdown of the hydrogen bond network of the solution [40] or the formation of an ionic double layer [30]. As a general observation, measurements indicate that the interfacial tension between the particle (either colloide, or aggregates) and solvent is of central importance (see [19, 41] for a review). For systems of higher concentrations, on the other hand it was found that the interparticle interactions (or collective effects) dominate the thermal diffusion behavior [31]. From this brief overview, it becomes obvious that a general theory that covers all those influences is far from existing.

A more detailed introduction, that reviews also several theoretical approaches and simulation results is beyond the scope of this work, but can be found e.g. in reference [19].

2.2 The Amphiphilic Film and Interfacial Curvature

Surfactants are amphiphilic molecules, which consist of a hydrophilic (polar) head-group and a hydrophobic (nonpolar) tail. Due to their amphiphilic molecular structure, in aqueous solutions those molecules try to avoid direct contact between water and their hydrophobic tail (for a review see e.g. [48, 49, 60, 61]). As a consequence the surfactant molecules tend to aggregate and various self-organized microstructures are formed, which can be discontinuous (e.g. micelles, cylinders) or continuous (e.g. cylinder networks, planar lamellae or bicontinous). Regardless of their shape the surfactant aggregates can also be regarded as an amphiphilic film. Thereby, the properties of the amphiphilic film has can be used in order to describe the structural evolution in such surfactant systems. As will be shown later, this concept of the amphiphilic film can also be applied to ternary microemulsions.

It has been realized, that the main parameter determining the self-organized microstructure of surfactant systems is the local curvature of the amphiphilic film. The local shape of the two-dimensional film is exactly be determined by two principal curvatures c_1 and c_2, which are defined by their curvature radii:

$$c_1 = \frac{1}{r_1} \; ; c_2 = \frac{1}{r_2} \tag{2.17}$$

Figure 2.2-1a shows exemplarily shows the principle curvature c_i and the corresponding curvature radii r_i of a homogeneous sphere of radius R. It can easily be deduced, that for a perfect sphere both radii r_1 and r_2 have the same value and equal sign, so that $r_1 = r_2 = R$. By convention, the sign is defined as positive when the film is curved away from the aqueous phase and negative if it tends to enclose water. If r_1 and r_2 have opposite signs the film has a saddle-shaped geometry [62] (Figure 2.2-1b). This is the case for structures with connected topology, such as the "sponge-like" bicontinuous L_3-phase [63], which is shown in the upper part of Figure 2.2-1b).
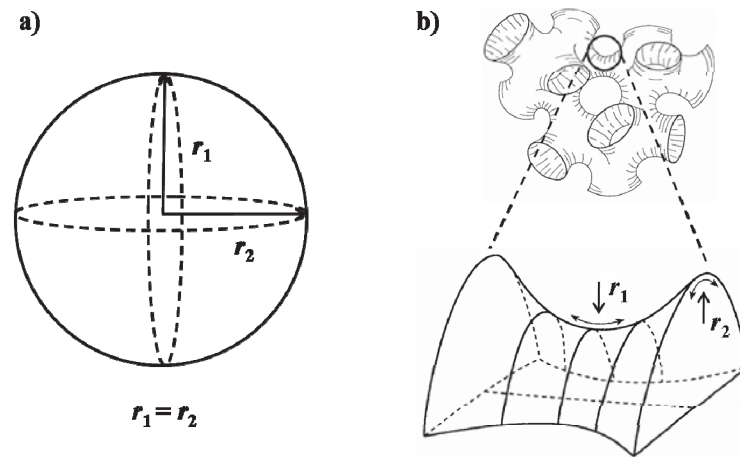
Figure 2.2-1: Schematic drawing for the definition of the curvature radii r_1 and r_2 which allow the description of each point on the two-dimensional amphiphilic film. a) Perfect sphere: Both radii are equal. b) Saddle-shaped segment (lower part according to [62], upper part taken from [63]): This picture describes sponge-like structures such as the L_3-Phase. (Figure adapted from [64].)

The mean curvature of the amphiphilic film is defined as:

$$H = \frac{1}{2}(c_1 + c_2) \tag{2.18}$$

and the *Gauss*ian curvature is defined as the product of both curvatures:

$$K = c_1 \cdot c_2 . \tag{2.19}$$

Thus, for spherical aggregates, such as micelles or oil-in-water microemulsion droplets both quantities, H and K, are positive. In the case of a saddle-shaped film the mean curvature vanishes, $H \approx 0$ and K will become negative, $K < 0$.

The preferred microstructure at certain conditions can be related to the bending energy of the amphiphilic film (e.g.[65-67]). The widely known theory of *Helfrich* [68] is based on the mechanical properties of the two-dimensional amphiphilic film, whereby the total curvature elastic energy of the membrane is expressed as:

$$E_b = \int \left[\frac{\kappa}{2}(c_1 + c_2 - c_0)^2 + \overline{\kappa} c_1 c_2 \right] dS \tag{2.20}$$

where the integral is taken over the whole surface. The quantity c_0 is the so-called *spontaneous curvature*. κ and $\bar{\kappa}$ are the bending rigidity and the *saddle-splay* modulus, respectively. Minimizing E_b with respect to c_1 and c_2 for a given c_0 yields the optimal structure of the amphiphilic film in a certain condition.

As mentioned above the occurrence of different microstructures can be directly related to the curvature of the amphiphilic film, which in turn is determined by the shape of the surfactant molecules it is build from. For non-ionic surfactant molecules it is well known that the shape of these molecules depends on both the temperature dependent hydration of the surfactant head-group (e.g. [69, 70]) and the chain conformation of the surfactant tail [71]. Thereby, the shape of the surfactant molecules can be quantified by the so-called *molecular packing parameter* Π which was introduced within the widely known theory of *Israelachvili et al.*[72, 73]:

$$\Pi = \frac{v_s}{a_s l_s}.$$ (2.21)

Here, v_s is the volume of one surfactant molecule, l_s the length and a_s the equilibrium area per molecule at the aggregate surface. Thus, Π essentially contains information about the relation between the cross-section of the surfactant head-group and the tail. A schematic overview of the relation between the packing parameter Π and the resulting shape of the surfactant aggregates [72] is given in Table 2-1.

Table 2-1: Values of the packing parameter Π for different aggregate structures [72] with schematic representation of the geometry of surfactant of the surfactant molecules (illustration adapted from [74]).

Packing Parameter Π	Schematic Representation of Surfactant Molecule	Aggregate Structure
$0 < \Pi < \dfrac{1}{3}$		Spherical Micelle
$\dfrac{1}{3} < \Pi < \dfrac{1}{2}$		Cylinder
$\dfrac{1}{2} < \Pi < 1$		Flexible Bilayer Vesicle
$\Pi = 1$		Planar Bilayer
$\Pi > 1$		Inverse
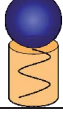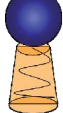
For non-ionic surfactants the molecular shape and hence the packing parameter Π can be significantly adjusted by a variation of the temperature. Thus, at low temperatures the surfactant head groups will be strongly hydrated by water as a result of strong hydrogen bonds and hence the head group volume is supposed to exceed that of the hydrophobic chain, i.e. Π will be small. Consequently, the amphiphilic film is formed by surfactant molecules with a conical shape and spherical aggregates with a positive mean curvature will be formed. With increasing temperature the surfactant head groups are partially dehydrated while simultaneously the number of possible chain conformations increases. Accordingly the tail to head volume ratio of the surfactant molecules, i.e. the packing parameter Π, will increases which leads to a gradual decrease of the mean curvature of the amphiphilic film.

For non-ionic surfactant systems this trend could indeed be verified form extensive structural investigations.

Using various techniques, such as freeze fracture electron microscopy (FFEM) (e.g. [75-78]), small angle neutron and X-ray scattering (e.g. [79-82]) and self-diffusion NMR (e.g. [75, 76, 83]) *Strey* could deduce a general trend for the evolution of the interfacial curvature *H* with the temperature. This trend is schematically shown in Figure 2.2-2. [84]: Starting at the left end of

the temperature the principle curvatures c_1 and c_2 coincide ($c_1 = c_2$). Thus both radii become equal, $r_1 = r_2$ which is true for a spherical structure. In this case H will become positive, $H = c_1 = c_2$, [refer to equation (2.18)] and the film will be curved away from the water domain. With increasing the temperature ($T < T_1$) both principle curvatures will still remain positive, as is the value for H, but the droplets will deform into an elongated or elliptic structure ($0 < c_2 < c_1$). When $T = T_l$, the principle curvature c_2 vanishes and the aggregates exhibit a cylindrical structure. When the mean temperature T_m is reached both principle curvatures cancel each other out ($c_1 = -c_2$). At that point the mean curvature H vanishes and a sponge-like bicontinuous microstructure is found. For further increased temperatures, ($H < 0$), the inverted trend is seen: At T_u inverted cylindrical structures are found, where the film is curved around the water. At even higher temperatures where both principle curvatures are negative the structures will become more spherical up to the point $c_1 = c_2 < 0$, where inverted spherical droplets exist.
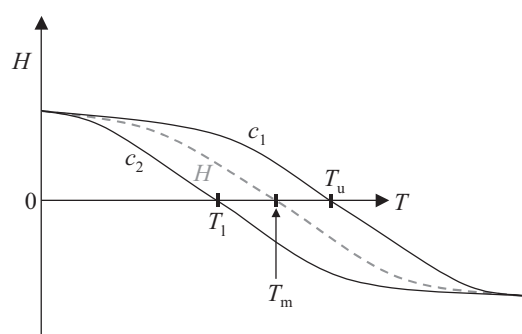
Figure 2.2-2: Schematic representation of the principle curvatures c_1 and c_2 as well as the mean curvature H as function of temperature in a non-ionic microemulsion at the optimum state according to [84]. See text for details.

Although originally derived for microemulsions containing non-ionic surfactants, this temperature dependence of the mean curvature H can also be applied to binary water - non-ionic surfactant systems. In the following sections an overview about the microstructure found in those systems and non-ionic microemulsions will be given.

2.3 The Binary System Water – Non-Ionic Surfactant

In this section a short overview about the general aspects of the phase behavior and microstructure of binary surfactant systems is presented. Since this work focuses mainly on the system water – $C_{12}E_6$, this introduction is given using the example of aqueous non-ionic

surfactant systems of the type water – *n*-alkyl polyoxyethylene ether (C$_i$E$_j$). Furthermore, the influence of additives, such as ionic cosurfactants and salt is briefly explained.

Early studies of the phase behavior and thermodynamic properties of surfactant systems of the type water – non-ionic surfactant C$_i$E$_j$ were performed by *Corkill et al.* 1961 [85] and by *Clunie et al.* 1967 [86]. A systematic overview about the phase behavior of a wide range of C$_i$E$_j$ – surfactants under variation of the size of the hydrophilic head-group and the hydrophobic alkyl-chain is given by *Mitchell* and co-workers [87]. *Strey* furthermore presented a systematic study of the influence of additives on such surfactant system [88].

At constant pressure a binary system is described by two independent variables, the temperature *T* and a composition variable, in this case the overall mass fraction of surfactant (C)

$$\gamma = \frac{m_C}{m_C + m_A},$$
(2.22)

where m_i are the masses of water (A) and surfactant (C). Alternatively the volume fraction

$$\phi_C = \frac{V_C}{V_C + V_A}$$
(2.23)

can be used with the respective volumes V_C and V_A.

Figure 2.2-1 shows a schematic phase diagram of the non-ionic surfactant system water – C$_i$E$_j$.
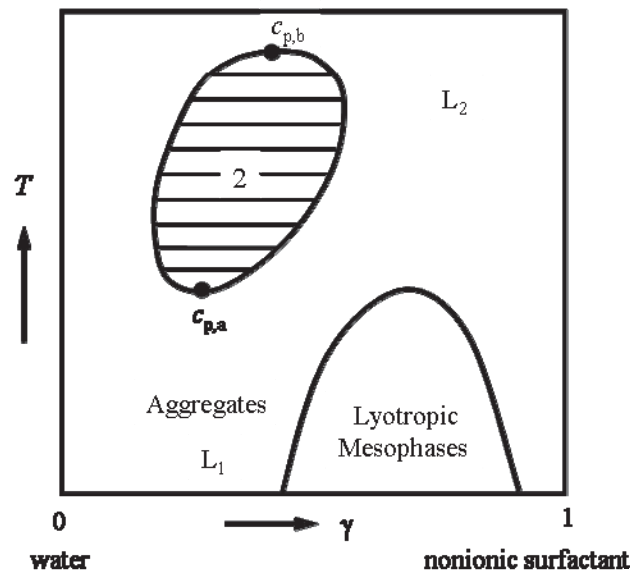
Figure 2.3-1: Schematic phase diagram a water – non-ionic surfactant system (taken from [88]).

Adding surfactant to pure water, the surfactant molecules will first dissolve monomerically. Passing a certain concentration the molecules will form aggregates of about 100 molecules, which are called micelles. Therefore the respective concentration is called critical micellation concentration (*cmc*). The microstructure within the isotropic micellar phase (L_1) has extensively been studied in the past, e.g. [89-92]. At low temperatures and surfactant concentrations the micelles exhibit in general a spherical shape. As has been discussed in section 2.2 the curvature of the amphiphilic film decreases with increasing temperature. Thus, at higher temperatures the aggregates adopt a more elongated or cylindrical shape and eventually form a network of interconnected cylinders [91-93]. However, the transition from spherical to cylindrical micelles not only depends on the temperature but also on the surfactant fraction. This effect is discussed by *Zilman et al.* [93] in terms of the energy contribution of the semi spherical cylinder end-caps, which increase at increasing surfactant concentration. The binary system water – non-ionic surfactant (A – C) in general exhibits two miscibility gaps: A lower miscibility gap, whose upper critical point is usually located below $T = 0$ °C (not shown in Figure 2.3-1) and an upper closed miscibility gap. However the upper critical point of this miscibility gap $c_{p,b}$ is usually located at temperatures $T > 100$ °C and is therefore experimentally difficult to determine [94]. On the other hand, the lower critical point $c_{p,a}$ lies usually below 100°C. For surfactants of the type C_iE_j $c_{p,a}$ is usually located at surfactant mass fraction between 1-6 wt% [95]. At higher surfactant concentrations lyotropic mesophases occur, such as the hexagonal (H_1), cubic-bicontinuous (V_1) or lamellar phase (L_α) [87]. At the right-hand side of the phase diagram a surfactant-rich solution of inverse micelles (L_2) is found at increased temperatures.

The extension of the lyotropic mesophases strongly depends on the structure of the surfactant. In the case of long-chain strongly structured surfactants the lamellar phase (L_α) extends into the dilute region of the phase diagram where it intersects with the upper miscibility gap [87, 88, 96]. Figure 2.3-2 shows the schematic phase diagram of such a strongly structured surfactant of the type C_iE_j in water [97]. Next to the diluted lamellar phase at small surfactant mass fractions the isotropic L_3 - Phase exist. Furthermore several two-phase regions occur and, according to the *Gibbs'* phase-rule, triple lines exist in between adjacent two-phase regions.
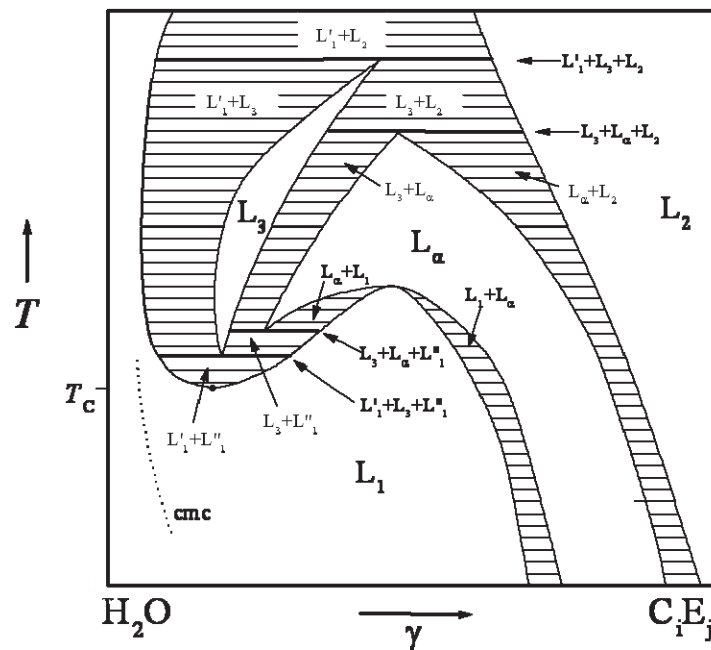
Figure 2.3-2: Schematic phase diagram of a strongly structured surfactant of the type C_iE_j in water according to [97] (taken from [74]).

It was found that the extension of the L_α - Phase towards the dilute region depends at given length of the alkyl-chain i on the head-group size j, or vice versa [87, 98]. For example $C_{12}E_4$ and $C_{12}E_5$ form highly diluted lamellar phases in water and the phase diagram schematically resembles that one shown in Figure 2.3-2. In contrast, the system water – $C_{12}E_6$ shows no dilute lamellar phase and the upper miscibility gap is not connected with the region of lyotropic mesophases. A more detailed description of the system water – $C_{12}E_6$ will be given in section 4.

2.3.1 Pseudobinary Systems: Ionic Cosurfactant and Salt

If a component is added to the binary (A – C) system, this additive can be attributed to the component, in which it preferably dissolves. Regarding that component and the additive as one *pseudocomponent* allows treating the system as a so called *pseudobinary* system. The influence of various additives, such as alcohols, salts and non-ionic and ionic cosurfactants on binary

aqueous non-ionic surfactant systems has extensively been studied [88, 99-106]. For this work both the influence of an ionic cosurfactants and salts is important and will therefore briefly be explained in the following. Thereby, the amount of a cosurfactant in a *pseudobinary* water – surfactant/cosurfactant mixture can be specified by the weight fraction

$$\delta = \frac{m_{cosurfactant}}{m_{cosurfactant} + m_{surfactant}}.$$
(2.24)

The amount of salts added to the mixture can be quantified by the weight fraction

$$\psi = \frac{m_{salt}}{m_{Salt} + m_{water}}.$$
(2.25)

In the following different components will be separated by a hyphen, whereas components and additives within a *pseudocomponent* are separated by a slash.

As was explained in section 2.2 the phase behavior and the microstructure in a surfactant system are related to the curvature of the amphiphilic film. Adding an ionic cosurfactant to a non-ionic binary surfactant system will mainly influence the properties of the amphiphilic film by electrostatic interactions. This effect was extensively studied, e.g. [105-108]. In the pure non-ionic surfactant system the head-groups become steadily dehydrated with increasing temperature. As a result the curvature of the amphiphilic film is reduced. Thereby the screening of the hydrophobic moiety of the surfactant is also reduced and eventually, at the cloud point at given surfactant concentration, the homogeneous mixture decomposes into a surfactant-rich and a water-rich phase. If some of the non-ionic surfactant molecules in the amphiphilic film are replaced by ionic cosurfactant molecules the electrostatic repulsion between the head-groups of the latter ones increases the curvature. Therefore the electrostatic forces counterbalance the effect of the dehydration of the head-groups with increasing temperature and higher temperatures that finally lead to phase separation [101, 103, 107-109]. Accordingly, the phase behavior is shifted to higher temperatures. The strength of this effect is dependent on the fraction of the ionic cosurfactant in the surfactant mixture ψ (2.25). In this context, an ionic cosurfactant represents a hydrotropic salt, which increases the mutual solubility of water and surfactant. On the other hand, the addition of a lyotropic salt, such as NaCl decreases the solubility of the surfactant in water because the ions *consume* hydration water at the cost of the hydration of the surfactant

head-groups. Therefore the phase behavior is shifted towards lower temperatures upon addition of a lyotropic salt [88, 106]

2.4 Non-Ionic Microemulsions

Adding oil (B) to a non-ionic binary aqueous surfactant system (A – C) results in a ternary A – B – C mixture. At certain temperatures and compositions those systems form a microemulsion. Microemulsions are thermodynamically stable, macroscopically isotropic mixtures of at least three components, (A) being polar (e.g. water), (B) non-polar (e.g. alkane) and the amphiphile (C). A and B are in general mutually immiscible. The amphiphile (C) is miscible with each of both components over a certain temperature and concentration range. In a ternary mixture of the three components A, B and C the amphiphile will preferentially be adsorbed at the interface between the polar (A) and non-polar (B) component. Thereby the interfacial tension between (A) and (B) is effectively reduced. As a consequence, this allows the dispersion of the immiscible components A and B in each other. Depending on the temperature and composition, the ternary system A – B – C shows rich phase behaviour, which is strongly related to the phase behaviour of the respective binary systems. Furthermore in microemulsions a large variety of microstructures is found. As for the binary system A – C (refer to section 2.3) the phase behaviour and the temperature-dependent structural evolution in microemulsion systems are closely related to the nature of the amphiphilic film. The evolution of the interfacial tension between the oil-rich and water-rich excess phases coexisting with the microemulsion phase is another important property of those systems. An overview about non-ionic microemulsions can e.g. found in [47, 50, 56, 84]. The aim of this section is to give an introduction to the relations and concepts used to investigate and understand the properties of the non-ionic microemulsions studied in this work.

2.4.1 Phase Behavior

Studying microemulsion systems requires the knowledge of the phase behavior. It has turned out that all ternary mixtures of the type water (A) – oil (B) – non-ionic surfactant (C) follow the same general pattern [50, 110, 111]. This is governed by the interplay between the three binary systems water– oil (A – B), water– non-ionic surfactant (A – C) and oil– non-ionic surfactant (B – C). Therefore it is a feasible approach to regard the phase behavior of those binary side systems first. Since the effect of pressure p is weak [112] and p is usually kept approximately constant (working at ambient pressure) the phase behavior can be described by the concentration

variables and the temperature. Thus in the following the phase diagrams of the three binary systems are briefly introduced at first. Subsequently the phase behavior of the ternary system water (A) – oil (B) – non-ionic surfactant (C) is represented in a phase prism with the *Gibbs* phase triangle A – B – C as the base and the temperature as ordinate [47]. The three sides of this phase prism are thereby represented by the three binary *side systems* mentioned above.

2.4.1.1   Binary Side Systems

The phase diagrams of the three binary *side systems* water– oil (A – B), water– non-ionic surfactant (A – C) and oil – non-ionic surfactant (B – C) are schematically shown in Figure 2.4-1. The binary system water – oil (A – B) system shows a miscibility gap which extends almost over the whole temperature and concentration region. The system oil – non-ionic surfactant (B – C) shows a lower miscibility gap with an upper critical point cp_α. The corresponding critical temperature T_α is usually below zero degrees *Celsius* (at ambient pressure) and therefore not in the experimental range. The binary system water – non-ionic surfactant (A – C) which was already introduced in section 2.3 is the most complex. It shows two miscibility gaps, a lower one and an upper closed one. The upper critical point of the lower miscibility gap is usually far below the melting point of the mixture and therefore plays no role in the phase behavior at experimentally accessible conditions. In the one-phase region at ambient temperature above the critical micellization concentration (*cmc*) the surfactant molecules form aggregates. At higher concentration also liquid crystalline phases and a solid surfactant-rich phase are found [87, 91].
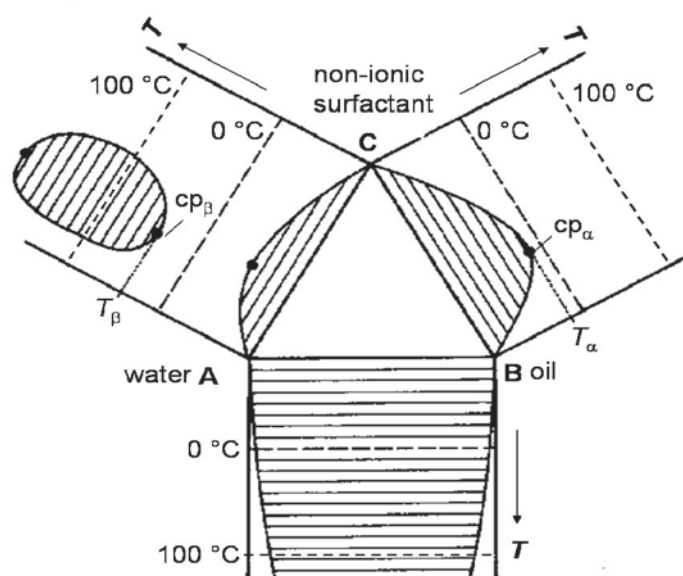
Figure 2.4-1: Schematic representation of the three binary systems water (A) – oil (B), water (A) – non-ionic surfactant (C) and oil (B) – non-ionic surfactant (C), which mark the sides of an unfolded phase prism with the A-B-C – plane as base and the temperature as ordinate (taken from [47]).

The upper miscibility gap, which occurs at higher temperatures is closed and thus shows a lower and upper critical point. The upper critical point is usually located above 100 °C, while the lower critical point cp_β is located within the experimental window. The occurrence of the upper miscibility gap is related to the dehydration of the surfactant head-group, which results from the destabilisation of the hydrogen bonds with increasing temperature (refer to section 2.3).

The phase behavior of a ternary A – B – C mixture is determined by the interplay between the upper miscibility gap of the A-C mixture and the lower miscibility gap of the B – C mixture. It can further be deduced, that at low temperatures the surfactant will preferably be dissolved in water, while at higher temperatures it will rather be dissolved in the oil.

2.4.1.2   *The Phase Prism*

In Figure 2.4-2 a schematic drawing of the phase prism of the ternary system water – oil– non-ionic surfactant (A – B – C) is shown [84]. The general phase behavior is strongly connected to the solubility of the surfactant (C) in water (A) and oil (B) at different temperatures, as described for the individual binary systems above. With increasing temperature the solubility of the surfactant (C) in water (A) decreases, while at the same time its solubility in oil (B) increases. Thus, as a general feature a ternary mixture A – B – C of approximately equal amounts of water and oil will separate into a water-rich microemulsion coexisting with an oil excess phase at lower temperatures. An oil-rich microemulsion in coexistence with a water excess phase will form at higher temperatures. The former state is denoted $\underline{2}$ (*Winsor* I) and the latter one is denoted $\overline{2}$ (*Winsor* II). In the temperature range between those two states a three-phase state exists, where the microemulsion phase (middle phase) is in equilibrium with a water-rich and an oil-rich excess phase (denoted as 3 or *Winsor* III).
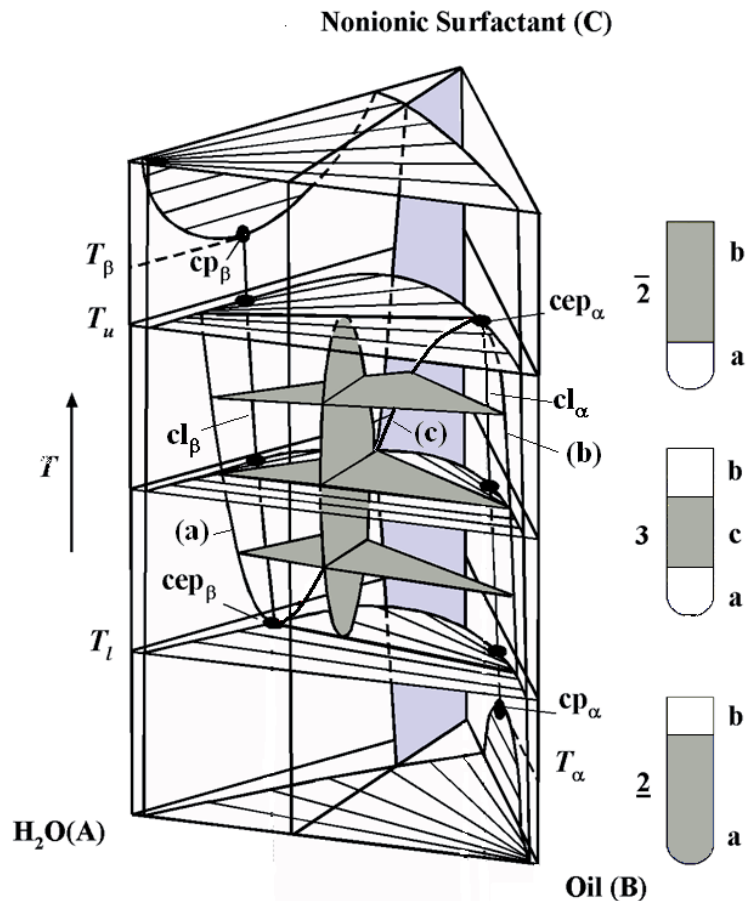
Figure 2.4-2: Schematic drawing of the phase prism illustrating the temperature-dependent phase behavior of the ternary system water (A) – oil (B) – non-ionic surfactant (C). At the right hand side schematic sample tubes are shown denoting the two- and three-phase states existing at different temperatures (a: water-rich, b:oil-rich, c: middle phase). (Figure taken from [84]).

These three states are schematically illustrated by the test tubes at the right hand side of Figure 2.4-2. This general temperature – dependent behavior is also referred to as *phase inversion* [50]. Thereby the three-phase body lies, with respect to the temperature in the range $T_u > T > T_l$. This will be described more systematically in the following:

Starting from the lower critical point of the upper miscibility gap cp_β in the binary system water – surfactant (A – C) at the critical temperature T_β the critical line cl_β proceeds into the phase prism until it ends at the critical end point cep_β at $T = T_l$. The critical end point cep_β lies on the lower critical tie line, which marks the lowest temperature of the existence of the three phase body. At this temperature the microemulsion phase (c) and the water-rich phase (a) become indistinguishable and thus at temperatures $T < T_l$ the system exists in the two phase state $\underline{2}$. The opposite behavior is found when starting at the oil-rich side of the phase prism at the upper critical point cp_α of the lower miscibility gap located at T_α in the B – C plane. From this point the

critical line cl_α proceeds into the phase prism up to the critical end point cep_α. The corresponding temperature T_u marks the upper margin of the existence of the three phase body. In analogy to the case at T_l, at this temperature another critical tie line is found, where the middle phase (c) becomes equal to the oil rich-phase (b). Consequently at temperatures $T > T_u$ the system exists in the form of an oil-rich microemulsion (b) in equilibrium with a water excess phase (a), as illustrated by the upper sample tube at the right-hand side of Figure 2.4-2.

Within the three-phase body the composition of the three coexisting phases (a), (b) and (c) at given temperature between T_u and T_l are determined by the vertices of the corresponding three-phase triangles, which are connected by the lines (a), (b) and (c), respectively. From the shape of the line (c) in Figure 2.4-2 it can be seen that the composition of the middle phase (top of the three-phase triangle c) changes from water-rich to oil-rich with increasing temperature.

2.4.2 Sections through the Phase Prism

In order to determine the phase bahavior of microemulsions it has proven useful to study sections through the phase prism [47, 55]. Since the determination of the whole phase prism is a time-consuming task, those sections should provide the characteristic variables required to sufficiently describe the particular system under study.

2.4.2.1 $T(\gamma)$ – Section

One of those sections is the so-called $T(\gamma)$ – section (or *Fish* – section) [47, 55, 113], which is schematically shown in Figure 2.4-3.
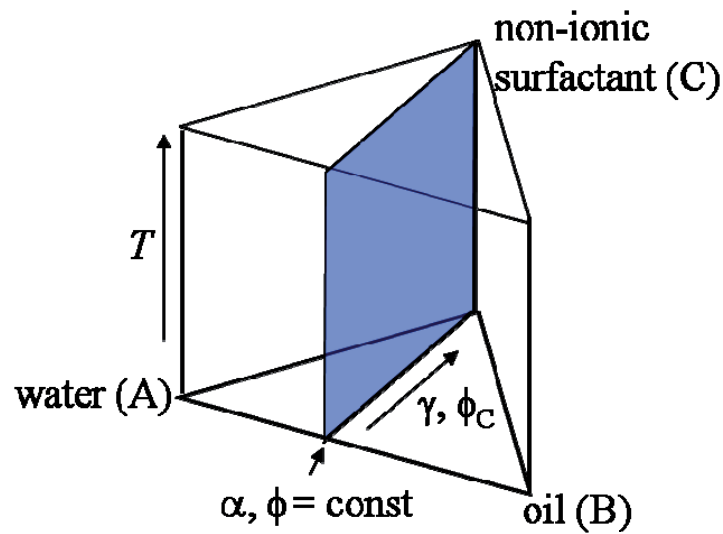
Figure 2.4-3: Schematic representation of the $T(\gamma)$ – section through the phase prism. The shaded plane represents the section, which is obtained by variation of temperature and surfactant mass fraction γ, while keeping the mass fraction of oil in the water – oil (A – B) component α constant. (Alternatively the volume fractions ϕ and ϕ_C can be used. See text for details.)

The $T(\gamma)$ – section (shaded plane in Figure 2.4-3) can be obtained by determination of the phase boundaries as function of the temperature (*isoplethal method*) with systematic variation of the surfactant mass fraction

$$\gamma = \frac{m_{Surfactant}}{m_{Surfactant} + m_{Oil} + m_{Water}} \qquad (2.26)$$

while the mass fraction of oil in the mixture of water and oil

$$\alpha = \frac{m_{Oil}}{m_{Oil} + m_{Water}} \qquad (2.27)$$

is kept constant. Instead of working with mass fractions, the analogous volume fractions

$$\phi = \frac{V_{Oil}}{V_{Oil} + V_{Water}} \qquad (2.28)$$

and

$$\phi_C = \frac{V_{Surfactant}}{V_{Surfactant} + V_{Oil} + V_{Water}} \qquad (2.29)$$

can be used. The general pattern of the phase behavior found in a $T(\gamma)$ – section is shown in Figure 2.4-4. Starting with a binary mixture of water and oil ($\gamma = 0$) at equal amounts of water and oil ($\phi = 0.50$) of course two phases will exist over the whole temperature range. Adding a non-ionic surfactant, first the solvents and the macroscopic interface will be saturated with surfactant monomers. The surfactant mass fraction γ_0 determines the point at which the solvents and the macroscopic interface are completely saturated and a third, microemulsion phase (c) first occurs at the mean temperature $\tilde{T}$. If at $\tilde{T}$ γ is further increased the volume of the microemulsion phase (c) will steadily increase, since the surfactant solubilizes more oil and water. The point $\tilde{X}$ defines the lowest surfactant mass fraction $\tilde{\gamma}$ where the oil and water can completely be solubilized in the microemulsion phase.
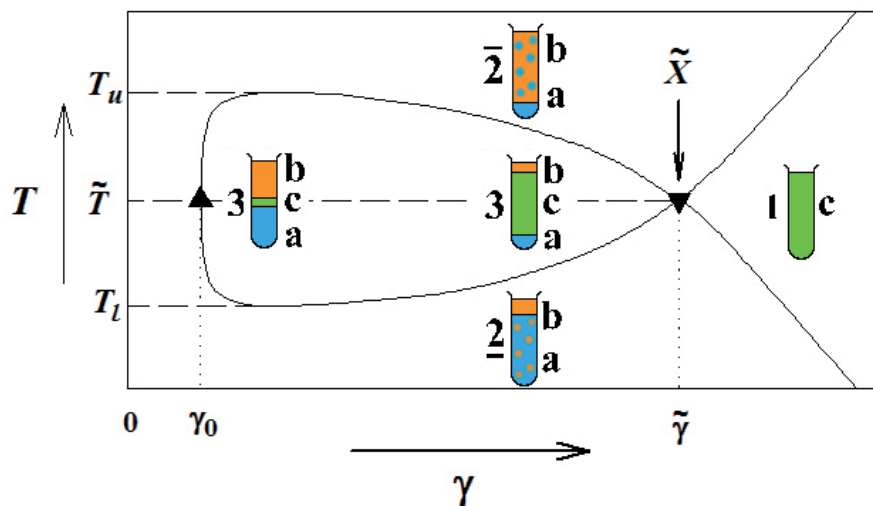
Figure 2.4-4: Schematic representation of the general phase behavior pattern found in a $T(\gamma)$ – section) through the phase prism at $\alpha \approx 0.50$. γ_0 is the smallest mass fraction of surfactant at which the three-phase region is found, i.e. at which oil and water are saturated with surfactant. The three-phase region exists in the range $\gamma_0 < \gamma < \tilde{\gamma}$. Thereby $\tilde{\gamma}$ represents the minimum surfactant mass fraction at which a one-phase microemulsion can be formulated (and is therefore and important value in order to estimate the efficiency of the surfactant. (Figure adapted from [64].)

At lower temperatures the surfactant will preferably dissolve in the water and hence a water-rich microemulsion exists in equilibrium with an oil excess phase ($\underline{2}$). At higher temperatures the surfactant will preferably dissolve in the oil and thus an oil-rich microemulsion exists in equilibrium with a water excess phase ($\overline{2}$). At temperatures in between the three-phase state (3) is found within the range of the three-phase body ($\gamma_0 < \gamma < \tilde{\gamma}$) and a one-phase microemulsion at higher surfactant mass fractions ($\gamma > \tilde{\gamma}$). The temperatures T_l and T_u define the lowest and highest temperature, respectively, to which the three-phase body extends.

Thus, investigating a $T(\gamma)$ – section through the phase prism allows to obtain the parameters γ_0, $\tilde{\gamma}$, $\tilde{T}$, T_1 and T_u. Especially $\tilde{\gamma}$ and $\tilde{T}$ are important parameters, since $\tilde{\gamma}$ defines the minimum surfactant mass fraction needed to solubilize water and oil in a single-phase microemulsion and $\tilde{T}$ is a measure for the phase inversion temperature. Both of the parameters can easily be obtained by determination of the phase boundaries that enclose the one-phase region of the $T(\gamma)$ – section and extrapolating them to the $\tilde{X}$– point.

2.4.2.2   *T(wB) – Section*

In this work mainly oil-in-water (o/w) microemulsions were investigated. The phase behavior of water-rich microemulsions can most conveniently be studied by performing sections through the phase prism at a constant mass fraction of surfactant in the mixture of water and surfactant

$$\gamma_a = \frac{m_{Surfactant}}{m_{Surfactant} + m_{Water}} \qquad (2.30)$$

(or oil and surfactant γ_b, respectively) [55, 113]. The phase behavior can then be determined as a function of the temperature and the overall oil weight fraction

$$w_B = \frac{m_B}{m_B + m_A + m_C}. \qquad (2.31)$$

Figure 2.4-5 schematically shows such a $T(w_B)$ – section through the phase prism at the water-rich side.
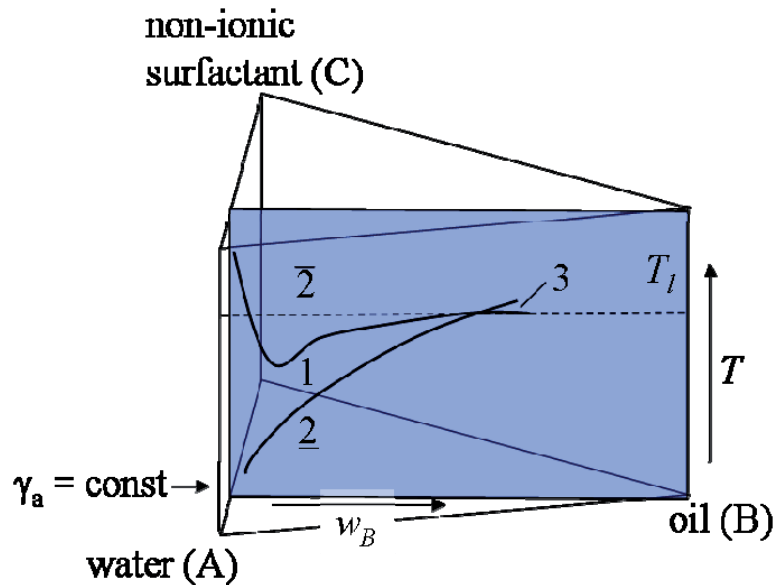
Figure 2.4-5: Schematic drawing of a $T(w_B)$ – section through the phase prism at the water-rich corner. Such a section is obtained by keeping the mass fraction of surfactant with respect to the water-plus-surfactant component γ_a constant and measuring the phase behavior under variation of the absolute mass fraction of oil in the ternary system w_B. (See text for details.)

In analogy to systems containing equal amounts of water and oil at small oil concentrations, (refer to Figure 2.4-4) the sequence of the occurring phases with increasing temperature is $\underline{2} \rightarrow 1 \rightarrow \overline{2}$. The upper phase boundary originates from the upper miscibility gap of the binary system water – non-ionic surfactant (A – C) (refer to Figure 2.4-1). Therefore the $1 \rightarrow \overline{2}$ phase boundary is also referred to as *near critical boundary* (*ncb*) [50, 55]. With increasing mass fraction of oil w_B the *ncb* in Figure 2.4-5 passes through a temperature minimum and ascends again. However, those minima in the near critical boundaries, are only found in so-called *strongly structured* systems, e.g. systems formulated with long chain surfactants, such as $C_{12}E_5$ [50, 55]. For weak surfactants, e.g. C_4E_1, at the water-rich side, a monotonic decrease of the *ncb* towards T_l is found.

At the same time the $\underline{2} \rightarrow 1$ phase boundary ascends monotonically with increasing value of w_B. It marks the amount of oil which can be solubilized in a single phase microemulsion at given temperature. Therefore the $\underline{2} \rightarrow 1$ phase boundary is referred to as *emulsification failure boundary (efb)*. The ability of the microemulsion to take up oil increases steadily with increasing temperature. Both phase boundaries intersect at the lower critical endpoint temperature T_l. Therefore $T(w_B)$– sections provide an experimental method to determine T_l (and T_u if the section

is performed at the oil-rich side, i.e. a $T(w_A)$-section. Since the microemulsion droplets at the *efb* are maximally swollen, their shape is expected to be spherical. Thus, $T(w_B)$ – sections have proven suitable in order to study water- or oil-rich droplet microemulsions [114, 115].

2.4.3 Structural Evolution in Non-Ionic Microemulsions

The relation between the temperature-dependence of the curvature of the amphiphilic film and the structural evolution in non-ionic surfactant systems was briefly presented in section 2.2. On the basis of the introduction given there, an overview of the microstructure found in a non-ionic microemulsion in connection with the phase behavior will be presented in this section.

The phase diagram in Figure 2.4-6 represents a vertical section through the phase prism, which is obtained by determination of the phase transition temperatures as function of the oil to oil-plus-water ratio α at a constant surfactant mass fraction $\gamma > \widetilde{\gamma}$ (*Shinoda*-Cut [75, 116, 117]).
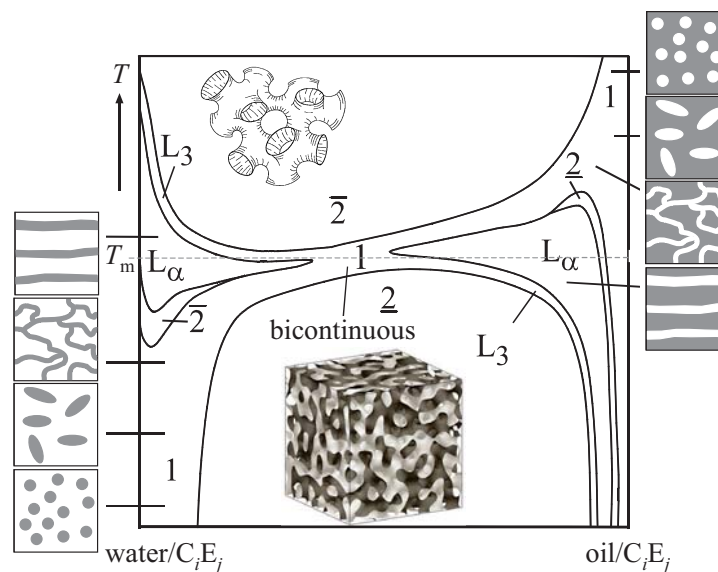
Figure 2.4-6: Schematic section through the phase prism ranging from the water-rich side to the oil-rich side for a non-ionic microemulsion. The phase transition temperature is obtained as function variation of the oil to water-plus-oil ratio α and constant surfactant mass fraction $\gamma > \widetilde{\gamma}$ (*Shinoda* cut) [75, 116, 117]. A one-phase channel proceeds from small temperatures at the water-rich side to higher temperatures at the oil-rich side. The microstructure found within the phase diagram reflects the temperature-dependence of the amphiphilic film (refer to section 2.2): At the water-rich side at low temperatures spherical oil-swollen micelles are found, which become more elongated with increasing temperature (drawings at the left hand side of the figure) up to the L_3-Phase having a negative value of H. At the oil-rich side the opposite trend is found: Water-swollen droplets are found at high temperatures, which get elongated with decreasing temperature (drawings at the right hand side of the figure). Around T_m structures with zero mean curvature (e.g. L_α and bicontinuous) are found. (Figure taken from [64].)

Starting at the water-rich side at low temperatures oil-in-water (o/w) droplets are found. The mean curvature of the amphiphilic film H is positive. Increasing the temperature, H decreases and approaches zero (refer to Figure 2.2-2). Remaining at the same composition this leads to more elongated structures, i.e. the structures will proceed from a spherical to a more elliptical shape. Further increasing the temperature leads to a cylindrical structure [118] and eventually the formation of an interconnected cylindrical network [83, 119-121].

At temperatures around T_m the mean curvature vanishes, leading to a swollen lamellar phase in water-rich microemulsions. At slightly higher temperatures the formation of passages between the bilayers leads to the formation of the isotropic L_3-Phase [122]. Increasing the oil to oil-plus-water ratio (α) results in a decrease of the $L_3 - L_\alpha$ phase transition temperature. This effect is related to the penetration of oil into the hydrophobic domains of the amphiphilic film, which bends the film towards the water-rich domains. If the oil fraction is increased to approximately the same amount as water, $\alpha \approx 0.5$ a bicontinuous structure, having a zero mean curvature exists.

On the oil-rich side the inverse progression of the phase behavior with temperature will be observed, i.e. starting from spherical water-in-oil droplets at higher temperatures to cylindrical and lamellar phases with decreasing temperature.

2.4.4 Oil-in-Water Microemulsions

In this work investigations of the *Soret* effect in microemulsion systems where mainly performed with non-ionic water-rich microemulsions. Therefore in the following section a more detailed introduction to this type of microemulsions will be given. In Figure 2.4-7 a schematic phase diagram $T(w_B)$-section through the phase prism at the water rich side is shown including the different kinds of microstructures (refer to Figure 2.4-2 and Figure 2.4-5). This type of phase diagram was already briefly presented in the previous section (Figure 2.4-5) and will be described here in deeper detail.
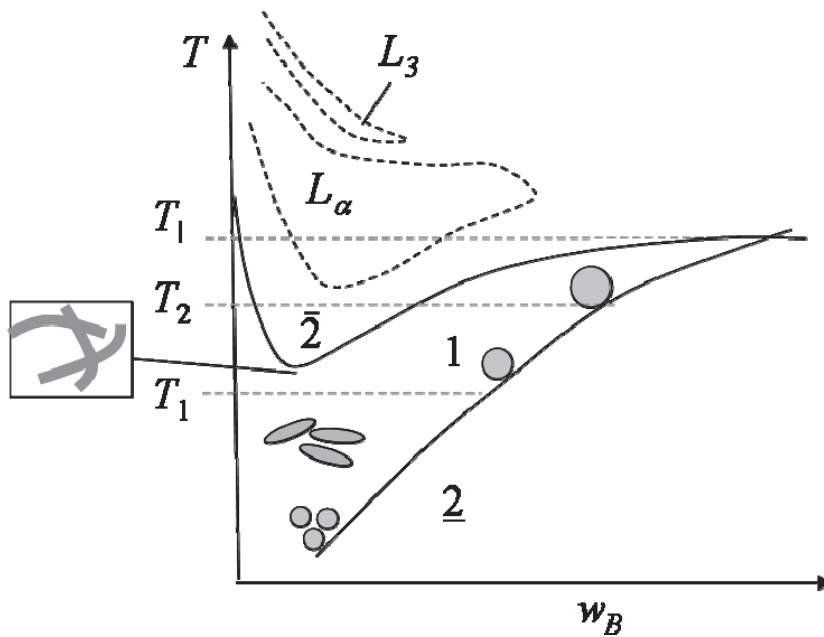
Figure 2.4-7: Schematic phase diagram, representing a $T(w_B)$-section through the phase prism of a strongly structured non-ionic microemulsion. Close to the emulsification failure boundary the aggregates exhibit a spherical droplet structure turning into an elongated and eventually cylindrical shape with increasing temperature (schematic grey drawings). Around the minimum of the near critical boundary (*ncb*) a network of interconnected cylinders is found, which decomposes into a surfactant-rich and a water-rich network at the $1 \rightarrow \overline{2}$ phase transition. At further increased temperatures above the *efb* a lamellar phase (L_α) as well as a L_3-Phase is found [47, 80].

The emulsification failure ($1 \rightarrow \underline{2}$) boundary (*efb*) marks for a given temperature the maximum amount of oil, which can be solubilized in a water-rich one-phase microemulsion. With increasing temperature the capability of the surfactant to solubilize the oil increases. It is known, that the oil-in-water droplets, existing at the *efb* have an almost perfect spherical shape [84, 123]. Therefore the radius of the droplets can be varied by proceeding along the *efb* from small oil mass fractions w_B at low temperatures towards values of w_B and temperatures (grey spheres in Figure 2.4-7). Thereby the one-phase region is limited by the point, where the *efb* intersects with the near critical ($1 \rightarrow \overline{2}$) boundary (*ncb*) near T_l.

The progression of the microstructure with the temperature was already discussed in the previous section. Increasing the temperature from the starting point at the emulsification failure boundary at a small value of w_B (indicated by three small grey spheres in Figure 2.4-7) leads to a decrease of the mean curvature. Since the total value of the interfacial area is fixed by the composition this allows to solubilize a higher amount of oil, which leads to an elongination of the aggregates. Further increasing the temperature will lead to cylindrical structures and eventually to the

formation of a network of interconnected rods around the minimum of the *ncb* [119, 120, 124]. At slightly higher temperatures, when passing the *ncb*, this network decomposes into a surfactant-rich and a dilute network (this phase separation will further be discussed below). This phase separation of different network phases leads to the formation of an additional two phase region which appears in from of a closed loop on the water-rich side of the phase prism. Those two-phase regions occur at temperatures just below T_1 at the water-rich side and just above T_u at the oil-rich side, respectively and were subject to extensive studies in the past (e.g. [55, 88, 113, 125]). From theoretical considerations it was found, that those two-phase regions play an important role in order to explain the origin of the three-phase body [92, 126, 127]. The minimum in the near critical phase boundary which can be found for water-rich microemulsions formulated with strong surfactants (see above) is only one feature of these additional two phase regions.

At still higher temperatures the mean curvature approaches zero and a lamellar phase (L_α) is formed. As the curvature becomes negative with further increasing T, the L_3-phase is found [80, 88, 97], which emerges through passage formation between adjacent bilayers [128].

Figure 2.4-8 shows two parts of isothermal *Gibbs* phase triangles, representing the water-rich corner of a non-ionic microemulsion system at two different temperatures, T_1 (a) and T_2 (b).
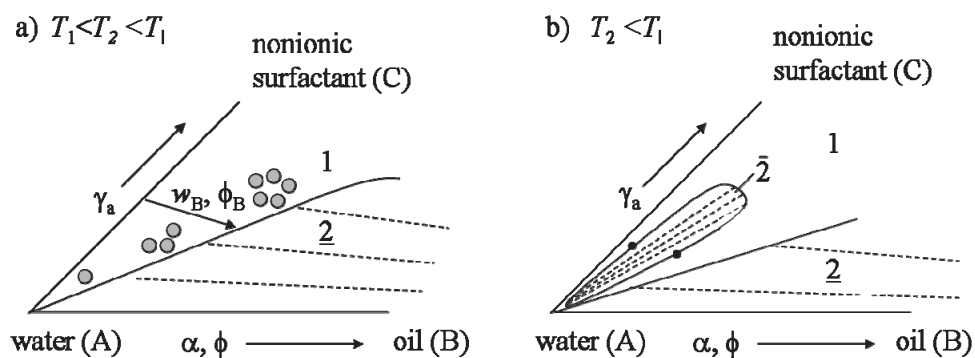
Figure 2.4-8: Schematic isothermal cuts (water-rich side) through the phase prism at two different temperatures T_1 and T_2 according to the dashed lines in Figure 2.4-7. a) At the temperature T_1, which lies below the minimum of the *efb* in Figure 2.4-7. The $1 \rightarrow \underline{2}$ phase boundary is a straight line in this region of the isothermal phase diagram. The slope of the straight binodal line is determined by the size of the droplets, which exhibit an almost perfect spherical structure close to the phase boundary. With increasing γ_a the particle number density increases, while the droplet radius remains constant. Figure 2.4-8 b shows the schematic isothermal cut which is obtained at T_2 in Figure 2.4-7, lying above the minimum of the *efb*. The closed miscibility gap ($\overline{2}$), which has the form of a lobe, causes the minimum in the *efb* in the $T(\gamma)$–section. This lobe occurs only in strongly structured microemulsions, i.e. formulated with long-chain surfactants [55].

Such triangles can be constructed from the phase boundaries in vertical $T(w_B)$-sections like that one schematically shown in Figure 2.4-7. The temperatures T_1 (a) and T_2 (b) in Figure 2.4-8 resemble the isotherms in the $T(w_B)$-sections (dashed grey straight lines in Figure 2.4-7). Both temperatures lie below the lower critical end-point temperature T_l.

Figure 2.4-8 a) corresponds to the temperature T_1 lying below the minimum of the near critical boundary (refer to Figure 2.4-7).

Starting from a point at the A-C side of the triangle, i.e. a water – surfactant solution with a fixed surfactant weight fraction γ_a, the oil mass fraction w_B can be increased until a phase separation occurs at the $(1 \rightarrow \underline{2})$ phase boundary. This path is indicated by the arrow in Figure 2.4-8a. Thus, the $(1 \rightarrow \underline{2})$ phase boundary in the isothermal phase diagram represents the isothermal emulsification failure boundary. As mentioned above, at the *efb* the shape of the droplets is almost perfectly spherical. The tie lines in the two-phase region ($\underline{2}$) point towards the oil corner, because an oil excess phase separates at the *efb*. The binodal, which separates the one-phase from the two-phase region, is a straight line in this part of the *Gibbs* triangle. It originates at the water-corner (strictly spoken from the cmc, which however is negligible small for non-ionic surfactants with sufficiently long alkyl-chain in water [55, 80]). The size of the droplets, existing along the straight binodal line, is determined by its slope [55, 113]. Thus by variation of the total area of the surfactant film, which is achieved by adjusting the mass fraction of surfactant in the mixture of surfactant and water γ_a, the number density of the droplets is varied (indicated by the grey spheres in Figure 2.4-8a.

The water-rich corner of the isothermal *Gibbs* triangle shown in Figure 2.4-8b corresponds to the temperature T_2 in Figure 2.4-7, being higher than T_1 but still below T_l. Starting again from a point at the A-C side of the triangle at fixed γ_a and increasing the oil fraction w_B, the observed phase sequence will be $1 \rightarrow \overline{2} \rightarrow 1 \rightarrow \underline{2}$. Therefore, phase inversion is obtained at constant temperature. Within the lope a surfactant-rich cylinder network phase coexists with a water-rich one [92, 126, 127]. Thus, the tie lines point in almost perpendicular directions to those within the central miscibility gap ($\underline{2}$), which point towards the oil corner. The closed lobe exhibits two critical points, one at its water-rich side and one at its oil-rich side. If the temperature is raised towards T_l the critical point on the oil-rich side of the lobe approaches the central miscibility gap and touch it at T_l, at the beginning of the three phase region [55].

It has been shown that the binodal line in the isothermal phase diagrams in Figure 2.4-8 is a straight line for low values of the volume fraction of the dispersed phase $\phi_{disp} = \phi_B + \phi_C$, which is the sum of the absolute volume fraction of oil ϕ_B and surfactant ϕ_C, respectively. A spherical droplet structure is assumed for the aggregates existing close to this phase boundary [55, 113]. For a constant temperature the droplet radius is fixed by the spontaneous curvature, being $r = R = 1/c_0$. Neglecting the thickness of the interfacial layer the volume fraction of the dispersed phase may be approximated by ϕ_B. This can then be expressed as

$$\phi_B = n_p (4\pi/3)R^3 ,\tag{2.32}$$

and the interfacial area per unit volume is given by

$$A_v = n_p 4\pi R^2 ,\tag{2.33}$$

where n_p is the number density of the droplets. Elimination of n_p yields

$$\frac{3\phi_B}{A_v} = R = 1/c_0 = \text{const} .\tag{2.34}$$

The interfacial area per unit volume can also be expressed using the volume fraction of the internal interface $\phi_{c,i}$ and the volume and head-group area of a surfactant molecule v_S and a_S, respectively by

$$A_v = \frac{\phi_{c,i}}{v_S} a_S .\tag{2.35}$$

$\phi_{c,i}$ is given by $\phi_{c,i} = \phi_c - \phi_{mon,b}$, with ϕ_c being the total volume fraction of surfactant. $\phi_{mon,b}$ is the volume fraction of the surfactant, which is monomerically dissolved in the oil (neglecting the monomeric solubility of the surfactant in water). Thus (2.34) can be rewritten

$$R = \frac{3\phi_B}{\phi_{c,i}} \frac{v_S}{a_S} .\tag{2.36}$$

Since $\phi_{c,i}$ increases linearly with increasing surfactant mass fraction in the water – surfactant mixture γ_a, and ϕ_B increases linearly with w_B, relation (2.36) implies a straight binodal line in the isothermal phase diagram. The experimental result, showing that this is indeed the fact for small volume fractions of the dispersed phase [55], manifests the assumption of a spherical microstructure close to the emulsification failure boundary.

When the thickness of the surfactant shell and the polydispersity of the droplets are taken into account, the expression (2.36) becomes [129, 130]

$$R = 3\frac{v_S}{a_S}\frac{\phi_B + 0.5\phi_{c,i}}{\phi_{c,i}}\frac{1+p^2}{1+3p^2}\,,\qquad (2.37)$$

with $p = \sigma / R_0$ being the dimensionless polydispersity index, which is obtained from the standard deviation σ of the *Gauss*ian distribution of the radius around its mean value r_0.

2.5 Neutron Scattering

Light- , X-ray- and neutron scattering are widely applied techniques to investigate structural properties of different materials, e.g. crystals, polymers, colloidal solutions or other inhomogeneous media if there is a "contrast" which can be assigned to the structure. Since the structural length scales in micellar systems and microemulsions are in the nanometer range, X-ray- and neutron scattering must be applied. X-rays are scattered by the electrons in the investigated media, while neutrons are scattered by the nuclei of the atoms. Thus, the contrast originates from differences in the electron density in the case of X-rays, while in the case of neutrons it originates from differences in the so-called scattering length density of the nuclei. This quantity is considerably different for protons and deuterons. Therefore neutron scattering allows adjusting the contrast by exchanging protonated substances by deuterated ones or using deuterated solvents. Therefore this technique was chosen to study the microstructure of the binary systems and microemulsions in this work. In this section a brief overview about the theoretical principles and experimental method of neutron scattering is given in the scope which is necessary to understand the SANS results presented in this thesis. For a deeper insight into the theory and experimental possibilities the reader is referred to profound treatises given e.g. by *Lindner* and *Zemb* [131] or *Glatter* and *Kratky* [132].

2.5.1 The SANS Experiment

The SANS measurements were carried out using the instruments *KWS 1* (microemulsions) and *KWS 2* (binary systems) at the *Jülich Centre for Neutron Science (JCNS)*, hosted at the *Reasearch Neutorn Soucre Heinz Maier-Leibnitz (FRM II)* in Garching, Germany. A general schematic drawing of the *KWS* instruments is shown in Figure 2.5-1. Since the principle features of the setups are similar for both instruments here a general description is given. The experimental details for the measurements of the binary systems and microemulsions are given in subsection 4.2 and subsection 6.2, respectively. The neutrons are set free during the nuclear fission reaction of ^{235}U in the fuel element, which is located inside a moderator bath containing D_2O. In the moderator tank the originally *fast* neutrons loose energy due to collision with the D_2O molecules, i.e. get moderated to the average thermal energy of the D_2O (300K). Special beamguides are used to deliver these *thermal neutrons* to the experiment. The velocity selector allows only neutrons of certain velocities to pass. Using the *de Broglie* relation [133] which connects the velocity *v* of a neutron with its wavelength λ over

$$\lambda = \frac{h}{mv},$$
(2.38)

with *h* being the *Plank Constant* and *m* the rest-mass of the neutron this allows to select neutrons of a certain wavelength by adjusting rotation speed of the velocity selector.
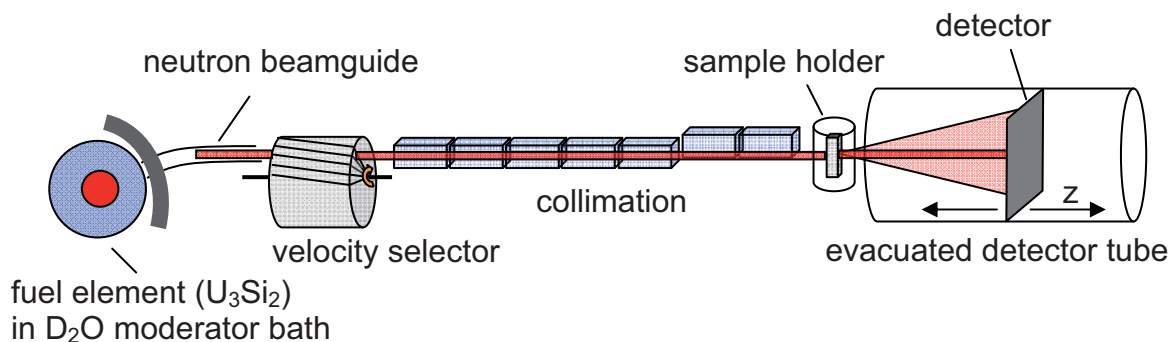
Figure 2.5-1: Schematic drawing of the small angle neutron scattering instrument *KWS 1* and *2*. Detailed information about the neutron source and beamguidance and the *KWS* instruments can be found at the *FRM 2* [134] and *JCNS* webpages [135], respectively. For experimental details refer to the text and subsections 4.2 (*KWS 2*) and 6.2 (*KWS 1*).

Before the neutron beam hits the sample its divergence and diameter is adjusted by a collimator. The neutrons that pass through the sample, which is positioned in a thermostated cell holder, can be either scattered or transmitted without change of travelling direction. While the transmitted neutrons are collected by a beam stop the scattered neutrons are detected by a two dimensional

60×60 cm^2 scintillation detector (^{6}Li-glass). To cover different scattering angles, the detector can be moved along the z - axis in the evacuated detector tube to adjust the sample-to-detector distance.

2.5.2 Raw Data Treatment

The scattering experiment yields the scattering intensity distribution within the area of the detector. The edges of the detector area as well as possibly occurring unexpected noise can be *masked* and therefore excluded from further processing. Radially averaging yields the experimentally detected scattering intensity of the sample I_{Sa}. In order to obtain the absolute intensity a calibration using a standard whose absolute (incoherent) scattering intensity $d\Sigma / d\Omega$ is known, is necessary. Next to the measurement of the experimental scattering intensity of the calibration standard I_{St} is measured. The experimentally obtained scattering intensities I_{Sa} and I_{St} are corrected by the intensity of the environmental background I_{Bg}, and the scattering intensities of the empty cells of the sample and the calibration standard I_{Ec} and $I_{Ec,St}$, respectively. The intensity of the environmental background is obtained by blocking the beam with a neutron absorbing cadmium sheet. Furthermore the transmissions of the sample and the calibration standard T_{Sa} and T_{St} are measured on an extra detector which is placed very close to the forward direction of the beam. According to this procedure the absolute intensity of the sample $I(q)$ is given by

$$I(q) = \frac{I_{Sa} - I_{Bg} - \dfrac{T_{Sa}}{T_{Ec}}(I_{Ec} - I_{Bg})}{I_{St} - I_{Bg} - \dfrac{T_{St}}{T_{Ec,St}}(I_{Ec,St} - I_{Bg})} \cdot \frac{T_{St}}{T_{Sa}} \cdot \frac{d_{St}}{d_{Sa}} \cdot \frac{d\Sigma}{d\Omega}(St) . \qquad (2.39)$$

For the measurements in this work plexiglas of 1.5 mm path length was used as absolute calibration standard. Collimation and aperture settings were chosen in order to optimize the neutron flux without limiting the resolution or exceeding detector capacity. The raw data was radially averaged and normalized according to the procedure described above using the program *QtiKWS* [136] provided by the *JCNS*. The data which were collected at $\lambda = 11.9$ and 12.0 Å, were adjusted to those collected at $\lambda = 4.8$ Å, without absolute calibration. From the obtained absolute intensities the incoherent background I_{incoh} was subtracted for further evaluation of the scattering curves.

2.5.3 Scattering Theory

The incident beam passes through the sample with the wave vector $\vec{k}_i$, with the absolute value $\left|\vec{k}_i\right| = 2\pi/\lambda$. Some of the radiation is interacting with the sample and is scattered about an angle θ. Assuming *quasielastic* scattering, i.e. without a wave length change of the neutrons during the scattering process, the absolute value of the wave vector of the scattered beam $\vec{k}_s$ is also $2\pi/\lambda$ (see Figure 2.5-2).
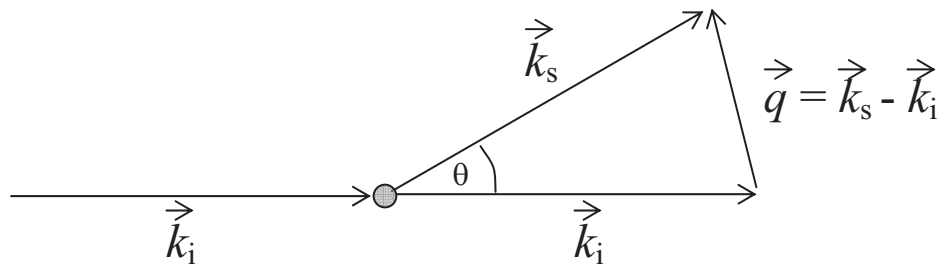
Figure 2.5-2: Schematic drawing for the definition of the scattering vector $\vec{q}$.

In this case the scattering vector $\vec{q}$ is defined by the change of the direction of the wave vector

$$\vec{q} \equiv \left|\vec{k}_s\right| - \left|\vec{k}_i\right|. \tag{2.40}$$

Thus, the absolute value of $\vec{q}$ is given by

$$q \equiv \left|\vec{q}\right| = \frac{4\pi}{\lambda}\sin\frac{\theta}{2}. \tag{2.41}$$

In the scattering experiment the scattering intensity $I(q)$ is measured as function of the scattering vector $\vec{q}$. For a monodisperse collection of spherically symmetric particles in solution the scattering intensity *I(q)* as function of the scattering vector *q* can be written as (*decoupling approximation*) [137, 138]

$$I(q) = n_p \Delta\rho^2 V^2 P(q) S(q) + b_{incoh}. \tag{2.42}$$

Therein $P(q)$ is the form factor, which is the square of the scattering amplitude of the scattering particles

$$P(q) = \left[A(q) \right]^2 \tag{2.43}$$

$S(q)$ is the structure factor describing the interaction of particles. $\Delta\rho$ is the scattering length density difference between the particles of volume V and the solvent, n is the number particle density and b_{incoh} is the incoherent background scattering.

Equation (2.42) implicitly assumes spherically symmetric monodisperse particles. Polydispersity can be taken into account by convoluting the form factor with a *Gauss*ian size distribution $W(R, R_0, \sigma)$. The scattering intensity is then given by:

$$I(q) = n\Delta\rho^2 S(q) \int_0^\infty V^2 P(q, R) W(R, R_0, \sigma) dR + b_{incoh}. \tag{2.44}$$

However, with respect to the interaction of the aggregates, polydispersity is not taken into account by this approximation. Therefore $S(q)$ in (2.44) represents and effective averaged structure factor.

2.5.4 Scattering Models

2.5.4.1 *Spherical Micelles*

To describe spherical micelles the form factor of a homogeneous sphere [139, 140] has been extended by assuming a diffuse interface between the micelles and the solvent to account for thermal disorder and penetration of solvent molecules into the interface by *Strey et al.* [81, 141] They showed that surfactant layers can be described well by a *Gauss*ian scattering length density profile instead of a step profile. Therefore the form factor for a homogeneous sphere was convoluted with a *Gauss*ian distribution function. A similar approach was used by *Stieger et al.* [142] to describe thermo responsive microgel particles having a *fuzzy* internal structure. The expression for the scattering intensity after including polydispersity writes

$$I(q) = \frac{36\pi}{3} \phi_{disp} R_0^3 \frac{(\Delta\rho)^2}{(qR_0)^6} e^{-q^2 t^2} \times$$

$$\left[\frac{1}{2}(1 - \cos 2qR_0 e^{-2\sigma^2 q^2}) \right.$$

$$-q(R_0 \sin 2qR_0 + 2q\sigma^2 \cos 2qR_0)e^{-2\sigma^2 q^2} \tag{2.45}$$

$$+\frac{1}{2}q^2(-4qR_0\sigma^2 \sin 2qR_0 e^{-2\sigma^2 q^2} + R_0^2 + \sigma^2$$

$$\left. +R_0^2 \cos 2qR_0 e^{-2\sigma^2 q^2} + \sigma^2 \cos 2qR_0 (1 - 4\sigma^2 q^2)e^{-2\sigma^2 q^2} \right].$$

From fitting the resulting form factor to the experimental scattering data the mean radius R_0, the thickness parameter of the diffuse interface t and the standard deviation of the size distribution of the radius of the micelles σ are obtained as free parameters.

2.5.4.2   *Gaussian Shell with Diffuse Interface and Core Scattering*

The model for the scattering intensity of a *Gauss*ian shell with diffuse interface and core scattering was derived by *Foster et al.* [143] in order to include the contribution of coherent scattering of the microemulsion droplet core into the scattering model of a polydisperse shell with diffuse interface [144]. The scattering amplitude of the core is the well known (normalized) amplitude for a homogeneous sphere [140]

$$A_{core}(q) = \frac{4\pi}{q^3 V_{core}} \{\sin(qR) - qR\cos(qR)\}. \tag{2.46}$$

Therein V_{core} is simply the volume of a sphere with radius R. The expression for the scattering amplitude of the surfactant film was given by *Gradzielsky et al.* [144]

$$A_{film}(q) = \frac{4\pi l_s}{q V_{film}} \exp\left\{-\frac{q^2 t^2}{2}\right\} \{qt^2 \cos(qR) + R\sin(qR)\}, \tag{2.47}$$

with V_{film} being the volume of the surfactant film

$$V_{fim} = 2\pi(4Rt^2 + l_s(t^2 + R^2)). \tag{2.48}$$

The parameter t is a measure for the thickness of the amphiphilic film and l_s is the length of a surfactant molecule, which can be approximated by the ratio of the volume v_s and the head-group area a_s of the surfactant molecule $l_s \approx v_s / a_s$ [143]. The resulting scattering amplitude for the core-shell model is then

$$A_{cs}(q) = \Delta\rho_{core} V_{core} A_{core}(q) + \Delta\rho_{film} V_{film} A_{film}, \tag{2.49}$$

with $\Delta\rho_{core} = \rho_{bulk} - \rho_{core}$ and $\Delta\rho_{film} = \rho_{bulk} - \rho_{film}$. With the expression of the form factor (2.43), this yields

$$\begin{aligned}
[A_{cs}(q)]^2 &= \Delta\rho_{core}^2 V_{core}^2 A_{core}^2(q) \\
&+ \Delta\rho_{film}^2 V_{film}^2 A_{film}^2(q) \\
&+ 2\Delta\rho_{core}\Delta\rho_{film} V_{core} V_{film} A_{core}(q) A_{film}(q).
\end{aligned} \tag{2.50}$$

Including the polydispersity according to equation (2.44), the scattering intensity of the non-interacting droplets ($S(q) = 1$) is expressed by

$$I(q) = I_{film}(q) + I_{core}(q) + I_{cross}(q). \tag{2.51}$$

Therein the contribution of the film scattering is the result, that was given in ref. [144]

$$I_{film}(q) = \phi_{c,i} \frac{4\pi v_s}{a_s q^2 (R_0^2 + \sigma^2)} \Delta\rho_{film}^2 \exp(q^2 t^2)\{f_1 + f_2 + f_3 + f_4\}. \tag{2.52}$$

with

$$\begin{aligned}
f_1 &= \tfrac{1}{2} q^2 t^4 \left\{ 1 + \cos(2qR_0)\exp\left(-2q^2\sigma^2\right) \right\} \\
f_2 &= q t^2 \left\{ R_0 \sin(2qR_0) + 2q\sigma^2 \cos(2qR_0) \right\} \exp\left(-2q^2\sigma^2\right) \\
f_3 &= \tfrac{1}{2} R_0^2 \left\{ 1 - \cos(2qR_0)\exp\left(-2q^2\sigma^2\right) \right\} \\
f_4 &= \tfrac{\sigma^2}{2} \left\{ 1 + 4qR_0\sin(2qR_0)\exp\left(-2q^2\sigma^2\right) + \cos(2qR_0)\left\{ 4q^2\sigma^2 - 1 \right\}\exp\left(-2q^2\sigma^2\right) \right\}
\end{aligned} \tag{2.53}$$

The contribution of the core scattering is [143]

$$I_{core}(q) = \phi_{c,i} \frac{4\pi a_s}{\nu_s q^6 (R_0^2 + \sigma^2)} \Delta\rho_{core}^2 \{g_1 + g_2 + g_3\} \qquad (2.54)$$

with

$$g_1 = \tfrac{1}{2}\left\{1 - \cos(2qR_0)\exp\left(-2q^2\sigma^2\right)\right\}$$

$$g_2 = -q\left\{R_0\sin(2qR_0) + 2q\sigma^2\cos(2qR_0)\right\}\exp\left(-2q^2\sigma^2\right)$$

$$g_3 = \tfrac{1}{2}q^2\left\{-4q\sigma^2 R_0\sin(2qR_0)\exp\left(-2q^2\sigma^2\right) + R_0^2 + \sigma^2 \right. \qquad (2.55)$$

$$+ R_0^2\cos(2qR_0)\exp\left(-2q^2\sigma^2\right)$$

$$\left. + \sigma^2\cos(2qR_0)\{1 - 4q^2\sigma^2\}\exp\left(-2q^2\sigma^2\right)\right\}$$

and the contribution of the cross-term writes

$$I_{cross}(q) = \phi_{c,i} \frac{8\pi}{q^4 (R_0^2 + \sigma^2)} \exp\left(\frac{q^2 t^2}{2}\right) \Delta\rho_{film}\Delta\rho_{core} \{h_1 + h_2 + h_3\}, \qquad (2.56)$$

with

$$h_1 = \tfrac{R_0}{2}\left\{1 - \cos(2qR_0)\exp\left(-2q^2\sigma^2\right)\right\}$$

$$h_2 = q\sin(2qR_0)\exp\left(-2q^2\sigma^2\right)\left\{\sigma^2 + \sigma^2\left\{2q^2\sigma^2 - \frac{1}{2}\right\} - \frac{R_0^2}{2}\right\}$$

$$h_3 = q^2\left\{t^2\sin(2qR_0)\exp\left(-2q^2\sigma^2\right)\left\{\frac{1}{2q} + q\sigma^2\right\} - \frac{R_0 t^2}{2}\right. \qquad (2.57)$$

$$\left. - R_0\cos(2qR_0)\left\{\frac{t^2}{2} + 2\sigma^2\right\}\exp\left(-2q^2\sigma^2\right)\right\}.$$

The free parameters of this model are the mean radius R_0, the thickness of the amphiphilic film t and the standard deviation of the polydispersity distribution σ.

2.5.4.3 *Elongated Aggregates – Bulk Contrast*

To model the scattering curves of elongated aggregates we applied a model for cylindrical aggregates with polydisperse cross section.

$$I(q) = n\Delta\rho^2 S(q)L^2 P_{rod}(q)\int_0^\infty A^2 P_{cross}(q,R)W(R,R_{0,cyl},\sigma_{cyl})dR + b_{incoh} \qquad (2.58)$$

If the length L is much larger than the cross section radius $R_{0,cyl}$, the axial factor can regarded to be independent from the cross section factor [139]. The axial contribution $P_{rod}(q)$ is given by the well known orientational averaged form factor for long rods [145]

$$P_{rod}(q) = \frac{2Si(qL)}{qL} - 4\frac{\sin^2(qL/2)}{q^2L^2}$$ (2.59)

and

$$P_{cross}(q) = \left(\frac{J_1(qR)}{qR}\right)^2$$ (2.60)

is the cross section contribution for a spherical cross section of area $A = 2\pi R^2$ [139]. Here Si is the sin-integral function.

It should be mentioned that, although a size distribution of the cylinder length is physically likely, polydispersity is just taken into account for the cross section part of the form factor by using equation (2.58) in order to simplify the model and thereon accelerate the calculation. Thus the free parameters for this model are the length L, the mean radius of the cylinder cross section $R_{0,cyl}$ and the standard deviation of the cross section σ_{cyl}. The integral in equation (2.58) was calculated numerically with integration limits from 0 to $20\sigma_{cyl}$, ensuring that the integral over the *Gauss*ian within those limits is ≥ 0.99.}

2.5.4.4   *Critical Scattering*

For measurements close to the upper miscibility gap critical scattering is known to come into play [146, 147]. This contribution to the scattering intensity can be described by the well known modified *Ornstein-Zernike* structure factor [147, 148]:

$$S(q) = 1 + \frac{I_0}{1 + q^2\xi^2}$$ (2.61)

Herein I_0 is equal to $nk_BT\chi_T$ where n is the number particle density, k_B is the *Boltzmann* constant, T is the absolute temperature and χ_T is the osmotic isothermal compressibility. ξ is the correlation length of the critical fluctuations. The critical parameters ξ and χ_T grow while approaching the critical temperature.

2.5.4.5 *Hard Sphere Interactions*

To model the repulsive interactions that occur due to higher surfactant fractions we used the well known *Percus-Yevick* model for hard sphere solutions. The expression for the structure factor is given in [149].

$$S(x) = \left(1 + 24\phi_{disp}\frac{G(x)}{x}\right)^{-1} \tag{2.62}$$

with $x = qd_{HS}$, while d_{HS} is the effective hard core diameter of the spheres. The factor $G(x)$ writes

$$G(x) = F + Y + Z, \tag{2.63}$$

with

$$F = \frac{\alpha}{x^2}(\sin x - x\cos x)$$

$$Y = \frac{\beta}{x^3}(2x\sin x + (2 - x^2)\cos x - 2) \tag{2.64}$$

$$Z = \frac{\gamma}{x^5}\left\{-x^4\cos x + 4\left[(3x^2 - 6)\cos x + (x^3 - 6x)\sin x + 6\right]\right\},$$

and

$$\alpha = (1 + 2\phi_{disp})^2 / (1 - \phi_{disp})^4$$

$$\beta = -6\phi_{disp}\left(1 + \phi_{disp}/2\right)^2 / \left(1 - \phi_{disp}\right)^4 \tag{2.65}$$

$$\gamma = \tfrac{1}{2}\phi_{disp}(1 + 2\phi_{disp})^2 / (1 - \phi_{disp})^4$$

With $\phi_{disp} = \phi_C + \phi_C$ in the ternary microemulsions and assuming $\phi_{disp} \approx \phi_{c,sample}$ for the aqueous binary surfactant systems studies in this work, the effective hard sphere diameter d_{HS} remains as free parameter.

2.5.4.6 *Sticky hard sphere interactions*

In this work the modified structure factor of *Baxter*'s equation for hard spheres with surface adhesion (*sticky hard spheres*)[150] as given by *Menon et al.* [151] was used. The expression for the structure factor writes

$$S(x) = A^{-2}(x) + B^{-2}(x), \tag{2.66}$$

where $x = aq$ with $a = \delta + \Delta$. δ represents the inner *hard core* diameter of the particle and Δ is the thickness of the attractive well of the potential of depth u_0. Using this structure factor together with the core-shell form factor model (2.51) Δ was set equal to t and a was set to $a = 2(R_0+t)$ in order to reduce the number of free parameters. With the relative thickness of the attractive well $\varepsilon = \Delta/a$ the so called *stickyness parameter* τ of the potential is defined by

$$\tau = (12\varepsilon)^{-1}\exp(u_0 / kT). \tag{2.67}$$

The terms *A(x)* and *B(x)* are given by

$$A(x) = 1 + 12\eta\left\{\alpha\left[\frac{\sin x - x\cos x}{x^3}\right] + \beta\left[\frac{1-\cos x}{x^2}\right] - \frac{\lambda}{12}\frac{\sin x}{x}\right\}$$

$$\tag{2.68}$$

$$B(x) = 12\eta\left\{\alpha\left[\frac{1}{2x} - \frac{\sin x}{x^2} + \frac{1-\cos x}{x^3}\right] + \beta\left[\frac{1}{x} - \frac{\sin x}{x^2}\right] - \frac{\lambda}{12}\left[\frac{1-\cos x}{x}\right]\right\}$$

with

$$\alpha = \frac{(1+2\eta-\mu)}{(1-\mu)^2}, \beta = \frac{(-3\mu+\mu)}{2(1-\mu)^2} \text{ and } \mu = \lambda\eta(1-\mu). \tag{2.69}$$

The effective volume fraction of the spheres η is defined as

$$\eta = \phi_{disp}\frac{a^3}{\delta^3} \tag{2.70}$$

and λ is the smaller solution of quadratic equation

$$\lambda^2 - 12\left(\frac{\tau}{\eta} + \frac{\eta}{1-\eta}\right)\lambda + \frac{12+6\eta}{\eta(1-\eta)^2} = 0 \tag{2.71}$$

Accordingly the free parameters obtained from modelling using this model are the effective volume fraction η, and the depth of the attractive potential well u_0.

2.5.4.7   Charged particle interactions

Electrostatic interparticle interactions are taken into account using the structure factor for charged macroions based on a screened repulsive potential [152, 153]:

$$U(r) = \pi \varepsilon \varepsilon_0 {d_{eff}}^2 \psi_0 z^2 \, exp\left(- \frac{\kappa(r - d_{eff})}{r} \right) \tag{2.72}$$

Here r is the interionic center-to-center distance of the macroions of diameter d_{eff}. $\psi_0(z)$ is the surface potential being a function of the effective number of charges z. The *Debye-Hückel* inverse screening length κ is determined by the concentration of salt in terms of single charged ions in the surrounding solution. The parameters describing the electrostatic interactions between the aggregates are the effective charge of the micelles z, the effective micelle radius $R_{eff} = \frac{1}{2} d_{eff}$ and the salt concentration c_{salt}. The RMSA structure factor was calculated with the program *GIFT neogenes* provided by *Glatter et al.* [154].

3 Experimental and Methods

3.1 Dynamic Light Scattering (DLS)

In the method of dynamic light scattering (DLS) (or quasi-elastic light scattering) the scattering process is – as it is in small angle neutron scattering – also assumed to be elastic. This means the wavelength λ of the scattered light is the same as for the incident light. If the scattered light is detected on a detector at constant scattering angle θ (or scattering vector q, see equation(2.41)) a time dependent fluctuation of the scattering intensity $I(q,t)$ can be observed. In dynamic light scattering we assume the intensity fluctuations arising from positive or negative interference of the light scattered from different scattering centres in the sample, which change their position randomly over time (e.g. *Brown*ian motion of the particles). Thus, the intensity fluctuation measured on a detector at certain scattering angle θ can be used to obtain information about dynamic processes in the sample. For a more detailed treatise see e.g. ref. [155].

Usually in DLS this information is extracted from the intensity fluctuation $I(q,t)$ by constructing the time correlation function (TCF), which is defined as [155]:

$$\langle I(q,0)I(q,\tau)\rangle \equiv \lim_{T\to\infty}\frac{1}{T}\int_{0}^{T}I(q,t)I(q,t+\tau)dt \tag{3.1}$$

Equation (3.1) relates the intensity of the signal at a time t with the intensity at a later time $t + \tau$, where τ denotes the length of the time step in between. If τ has a very small value, the difference of the signal at $I(q,t)$ and $I(q,t + \tau)$ will be small, which means the signals are *correlated*. At the limit $\tau \to 0$ the intensities will be equal and thus the correlation function will become the mean value of the intensity square $\langle I(q,t)^2 \rangle$. For very long values of τ, the intensities are *uncorrelated* and the time correlation function becomes the square of the mean intensity $\langle I(q,t) \rangle^2$. By dividing equation (3.1) through the square of the mean intensity one obtains the normalised time – intensity correlation function

$$g^{(2)}(q,\tau) \equiv \frac{\langle I(q,0)I(q,\tau) \rangle}{\langle I(q,t) \rangle^2}. \tag{3.2}$$

However, for the analysis of the data of the scattering experiment usually the time-field correlation function

$$g^{(1)}(q,\tau) \equiv \frac{\langle E(q,0)E^*(q,\tau) \rangle}{\langle I(q,t) \rangle^2} \tag{3.3}$$

is used, which is related to $g^{(2)}$ by the *Siegert* relation (for details see ref. [155]):

$$g^{(2)}(q,\tau) = 1 + \beta [g^{(1)}(q,\tau)]^2. \tag{3.4}$$

The factor β in equation (3.4) is a device parameter, which would become unity in the case of perfect experimental geometry (usual values in reality $\beta \approx 0.8$ [155]).

Assuming a dilute solution of monodisperse spheres in *Brown*ian motion the time-field correlation function takes the form of a single exponential decay function

$$g^{(1)}(q,\tau) = e^{-\Gamma\tau}, \tag{3.5}$$

where the inverse relaxation time Γ is related to the *free* particles diffusion coefficient D by

$$\Gamma = q^2 D. \tag{3.6}$$

Using the *Stokes-Einstein* relation

$$D = \frac{k_B T}{6\pi\eta R_H} \tag{3.7}$$

with the *Boltzmann* constant k_B, the temperature T and the dynamic viscosity η allows to calculate the hydrodynamic radius R_H.

Relation (3.5) is valid only in case of monodisperse particles, which exhibit only translational diffusion. However in praxis the systems under study are polydisperse and maybe not ideal spheres. Therefore $g^{(1)}(q,\tau)$ is a sum of exponentials, each corresponding to one relaxation mode weighted by the scattering intensity of the particle, given by

$$g^{(1)}(q,\tau) = \int A(\Gamma)\exp(-\Gamma\tau)d\Gamma , \tag{3.8}$$

with $A(\Gamma)$ is the distribution function of the inverse relaxation times Γ.

The DLS experiments in this work were performed on a commercially available device (ALV, Langen, Germany. Type: ALV/SP-86#059 Laser Goniometer), working at $\lambda = 633$ nm. The sample is prepared in a cylindrical sample tube, which is located in a thermostated toluene bath with $\Delta T \pm 0.05$ K te mperature stability. A high precision thermometer with a PT100 temperature sensor (Greisinger GMH 3710, $\Delta T \pm 0.05$ K) is used to measure the temperature in very close vicinity of the sample tube. The scattering intensity $I(q,t)$ is detected with a photomultiplier at angles $30° < \theta < 150°$ and the photon count rates at each angle are automatically read in a computer. Further processing is performed using the program package BATCON [156], which contains as essential feature the program package CONTIN [157, 158] (and references therein) in order to extract the time-field correlation function $g^{(1)}(q,\tau)$ as well as the distribution function $A(\Gamma)$.

3.2 Thermal Diffusion Forced *Rayleigh* Scattering (TDFRS)

Setup and Measurement Principle

All thermal diffusion measurements that are presented in this work were performed by using the thermal diffusion forced *Rayleigh* scattering TDFRS experiment. Therefore this experiment will briefly be introduced in the following section. A detailed description can be found e.g. in references [21, 159]. Figure 3.2-1 shows a schematic drawing of the setup. The experiment operates as follows: A laser beam, operating at $\lambda = 980$ nm is split into two beams of equal

intensity (writing beams) and brought to interference in the sample cell under a certain angle. Thereby the beams create an interference grating in the sample with a grating vector $q = \frac{4\pi}{\lambda} \sin(\frac{\theta}{2})$. Due to the absorption of the laser light by the sample, this optical intensity grating is converted into a temperature grating. This in turn leads to a mass diffusion due to the thermal diffusion effect. Both effects, the build up of the thermal grating and subsequently the mass diffusion lead to a modulation of the refrative index along the interference grating in the sample that is schematically scetched at the right hand side of Figure 3.2-1.
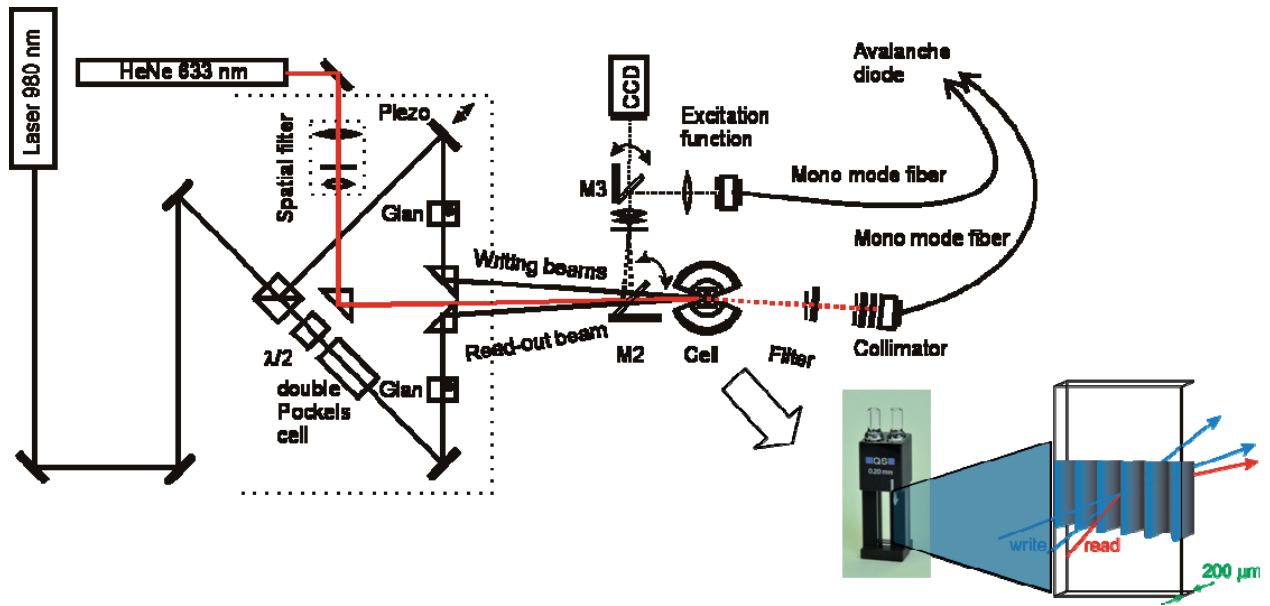
Figure 3.2-1: Schematic drawing of the IR-TDFRS setup according to [159]. See text for details.

The refractive index grating is probed by the diffraction of a second laser (read out beam), that operates at a different wavelength (HeNe $\lambda = 633$ nm) than the writing beam. The heterodyne signal intensity of the diffracted beam ζ_{het} is measured by an *Avalanche* diode as a function of time. The signal is normalized to the thermal plateau. For binary solutions this normalized heterodyne signal can be described by the following equation [21]

$$\zeta_{het}(t) = 1 - \left(\frac{\partial n}{\partial T}\right)_{w,p}^{-1} \left(\frac{\partial n}{\partial w}\right)_{p,T} \times S_T w(1-w)\left(1 - e^{-q^2 Dt}\right) \qquad (3.9)$$

which relates the time dependent measurement signal to the *Soret* coefficient S_T and the diffusion coefficient D. w is the mass fraction of one of the components and the factors $\left(\frac{\partial n}{\partial T}\right)_{w,p}$ and

$\left(\frac{\partial n}{\partial w}\right)_{p,T}$ are the so called contrast factors, that need to be determined by additional experimental methods [159]. The thermal diffusion coefficient D_T is obtained from the definition of the *Soret* coefficient $S_T \equiv \dfrac{D_T}{D}$.

Samples

The solution under study is filled in a quartz cell of 0.2 mm path length (right hand side of Figure 3.2-1), which is positioned in a brass or copper sample holder inside the isolated sample cell. A circulating water bath with ± 0.02 K temperature stability is applied to control the temperature of the sample holder in the sample cell. Inside the sample cell the temperature is measured by a stationary installed PT100 temperature sensor. In the classical setup [28], the writing laser operates at a wavelength of $\lambda = 488$ nm and is absorbed by a dye, which needs to be added into the sample. In the setup, that is shown in Figure 3.2-1 an infrared laser ($\lambda = 988$ nm) is used, which is absorbed by the water molecules [160]. Unless otherwise stated, the latter setup, which is called infrared (IR)-TDFRS is used for all TDFRS measurements, that are referred to in this work.

4 Binary System H_2O – $C_{12}E_6$

4.1 Motivation and Objectives

Thermal diffusion of non-ionic and ionic surfactants in water has been subject to several studies in recent years: *Piazza et al.* [31, 53] studied the thermal diffusion behavior of sodium dodecyl sulphate (SDS) in water as well as of mixtures of SDS and β-dodecyl-maltoside (DM) in water. Focussing on the investigation of the influence of electrostatic interactions on the thermal diffusion behavior, they found a quadratic dependence of the *Soret* coefficient on the *Debye – Hückel* length [31]. *Ning et al.* [28] studied the thermal diffusion behavior of non-ionic *n*-alkyl-poly oxyethylene surfactants (C_iE_j) in water using the classical thermal diffusion forced *Rayleigh* scattering (TDFRS) method. Due to the small spacing between the high temperature and low temperature regions in the sample in the order of several micrometers (refer to section 3.2) the equilibration times in the experiments are reasonably fast (in the order of seconds). Thus, this method is especially appropriate for high molecular weight components, such as polymers or aggregates with slow dynamics [19, 21]. In order to create the temperature grating in the classical TDFRS setup a small amount of a dye must be added into the sample to absorb the laser light of the interfered writing beams and convert it into thermal energy. Thereby, it is an important constraint that the properties of the dye should not be affected by the properties of the solution such as ionic strength or pH in aqueous systems [29]. On the other hand, the nature of the dye should not affect the properties of the solution under study, which can be a delicate issue especially for nanostructured fluid systems.

For this pupose, *Ning et al.* [29] used the trivalent organic cobalt complex Basantol® Yellow 215 (in the following also referred to as BY215) [161] performing measurements on decyl octaethylene glycolether ($C_{10}E_8$) in water. In order to exclude any influence of the dye on the thermal diffusion behavior of the aqueous $C_{10}E_8$ solutions, additional measurements were performed using the uncharged organic dye alizarin which is only soluble in the presence of surfactant. Comparing the results of those experiments no significant difference was found between the *Soret* coefficients, either containing the trivalent cobalt complex BY215 or the pure organic molecule alizarin as absorbing dye. Also a good agreement between the diffusion coefficients *D* obtained from TDFRS measurements and separately measured with DLS was found in the system $H_2O – C_{10}E_8$. Thus, for this system no influence of Basantol® Yellow 215 on the thermal diffusion behavior was found.

In contrast, further investigations on a wider range of non-ionic surfactants of the type C_iE_j (C_6E_4, C_8E_4, $C_{12}E_5$, $C_{12}E_6$, $C_{10}E_8$ and $C_{16}E_8$) in water demonstrated that only two surfactants in this group, namely C_6E_4 and $C_{10}E_8$ show the expected TDFRS signal [28]. For all the other surfactants unxepected TDFRS signals were detected. In order to illustrate the problem Figure 4.1-1 exemplarily shows the TDFRS signal intensity as a function of the time (refer to 3.2) in a logarithmic scale, obtained with the classical setup for the system $H_2O – C_{12}E_6$ containing the dye Basantol® Yellow 215 (BY215) at three different temperatures [160]. For all three temperatures the signal intensity increases quickly first and reaches a plateau after approximately 0.2 ms. This process stems from the build up of the tempearture gradient. The corresponding intensity is normalized to a value of 1. Starting from this plateau, the much slower thermal diffusion process is observed. This part of the curve is called concentration part. At $T = 20$ °C (blue squares) the signal shows only one mode, i.e. the concentration part of the signal runs into a plateau after $t \approx 1$ s. Contrarily at $T = 30$ and 40 °C (red triangles and circles, respectively) the

concentration parts of the signals do not run into a plateau, but decreases again after passing a maximum between $t = 0.1$ and 1 s. Thus, this second mode has a negative amplitude, i.e. the concentration grating gets weakened. As can be seen, the amplitude of the second mode is larger at higher temperatures.
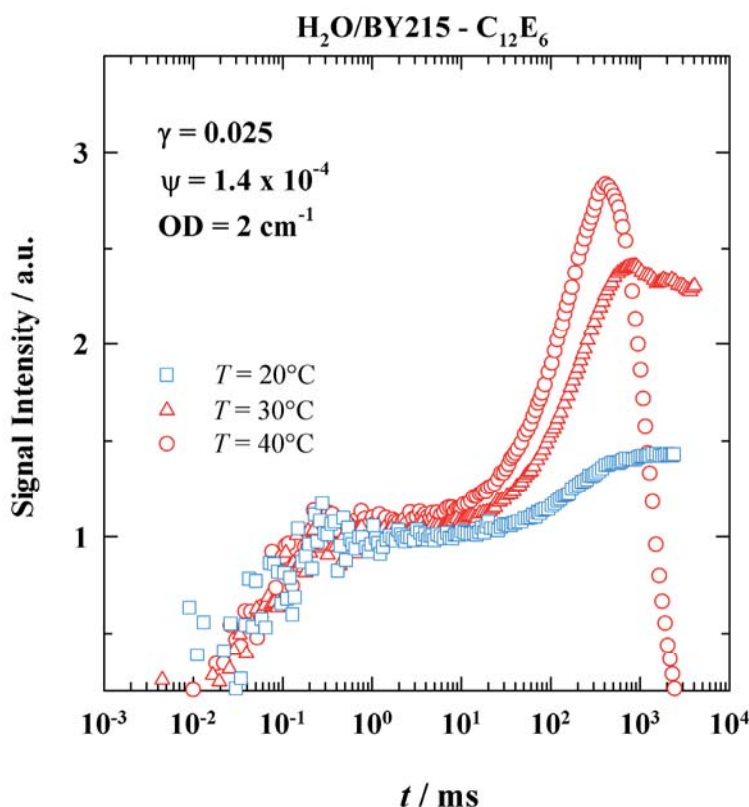
Figure 4.1-1: Signals of the system H_2O – $C_{12}E_6$ ($\gamma = 0.025$) containing the dye Basantol® Yellow 215 obtained with the classical TDFRS setup. The samples were prepared using a stock solution of H_2O/BY215 [160] with a mass fraction of BY215 of $\psi = 1.4 \times 10^{-4}$ corresponding to $c_{BY} = 1.5 \cdot 10^{-4}$ mol/L in order to adjust an optical density of OD = 2 cm^{-1}. The first ascending part of the signal (up to t ≈ 0.7 ms) stems from the build-up of the temperature grating. This process is much quicker than the thermal diffusion, therefore the signal reaches an intensity plateau after $t ≈ 1$ ms (thermal plateau). The concentration part of the signal results from the thermal diffusion process. It starts from that first plateau. Note that the signals are normalized to the intensity of the thermal plateau of 1 [160]. See text for details.

Such a two-mode signal is generally found at lower surfactant concentrations and higher temperatures. For $C_{12}E_5$ in water a two-mode signal was even obtained for all measured temperatures and surfactant concentrations. Furthermore *Ning et al.* [28] observed that the second mode can be suppressed by the addition of salt. This observation was a first hint that the second mode in the concentration part of the TDFRS signal might be caused by the charged dye molecules of BY215 in the system.

Ning et al. [28] found that at low surfactant weight fractions $\gamma < 0.02$ the two-mode signal occurs over the whole investigated temperature range. Increasing γ, the expected one-mode signal is observed at low temperatures, while the two-mode signal still occurs at higher temperatures. Studying the thermal diffusion behavior of samples with $\gamma > 0.20$ only one-mode signals are found for all studied temperatures.

In a subsequent work [160] we investigated the thermal diffusion behavior of $C_{12}E_6$ and $C_{12}E_5$ in water using two types of TDFRS setups, namely the classical TDFRS and the so called infrared-TDFRS (IR-TDFRS), which was recently developed in the group of *Wiegand* [159] (refer also to section 3.2). In the latter setup an infrared laser as writing beam is utilized, operating at a wavelength of $\lambda = 980$ nm, which corresponds to a weak absorption band of water. Thus, this setup allows avoiding the addition of a dye for aqueous solutions. In those measurements, no second mode was observed in the concentration signal of $C_{12}E_6$ and $C_{12}E_5$ in water, even if BY215 was additionally added into the samples. According to those results, it can be concluded that the occurrence of the second mode in the classical TDFRS measurement signal requires three constraints: The first (i) is the presence of the ionic dye BY215 in the sample. Secondly (ii) the writing laser must be absorbed by the dye molecules. As a further constraint (iii) the sample must either have a sufficiently high temperature, or low surfactant concentration.

Particularly the third (iii) finding implies for the pseudo-binary surfactant systems H_2O/BY215 - C_iE_j the existence of a correlation between the influence of the ionic dye on the microstructure and the phase behavior on the one hand, and the occurrence of the second mode in the classical TDFRS measurements on the other hand.

In this context it was the objective of this work to clarify the influence of the ionic dye Basantol[®] Yellow 215 on the microstructure of the non-ionic surfactant system $H_2O - C_{12}E_6$. At first the influence of BY215 on the phase behavior should carefully be studied. Thereby the concentration of the dye should be chosen to match the conditions in the TDFRS measurements. Systematic small angle neutron scattering (SANS) measurements should be performed over a certain $C_{12}E_6$ weight fraction and temperature range in order to systematically investigate the influence of the dye on the microstructure of the $C_{12}E_6$ aggregates in water. In addition, both, the phase behavior and microstructure of the system $H_2O - C_{12}E_6$ should be investigated upon addition of SDS in order to compare the influence of this well known ionic surfactant with the effect of BY215. On the basis of those investigations it was the aim to derive a first qualitative correlation of the influence of the ionic dye and the occurece of the second mode in the classical TDFRS signal. Those results are expected to contribute to the understanding of the underlying molecular diffusion process and the understanding of thermal diffusion in nanostructured fluids in general.

4.2 Samples and Experimental

Samples

The phase behavior of the pseudobinary system $H_2O – BY215 – C_{12}E_6$ was studied in two different ways: On the one hand Basantol® Yellow 215 was considered as a cosurfactant, while on the other hand in order to match the TDFRS experimental conditions of a constant optical density $(OD = 2 \pm 0.2 \text{ cm}^{-1}, \lambda = 488 \text{ nm})$ [29] it was added at a fixed concentration in the aqueous phase.

Considering BY215 (or SDS) as cosurfactant, i.e. with constant mass fraction of cosurfactant in the surfactant mixture δ [equation (2.24)], the samples were prepared by adding water to separately prepared $C_{12}E_6$/BY215 (or $C_{12}E_6$/SDS) surfactant mixtures. Considering BY215 as a hydrophilic pseudo-component the samples were prepared by using a water/BY215 solution (either D_2O or H_2O) with fixed concentration of BY215, $c_{BY} = 1.5 \cdot 10^{-4} \text{ mol/L}$. This concentration was chosen in order to adjust the optical density of the samples to $OD = 2 \pm 0.2 \text{ cm}^{-1}$ at a wavelength of $\lambda = 488 \text{ nm}$ [29] as mentioned above. For the corresponding samples containing SDS the same concentration $c_{SDS} = 1.5 \cdot 10^{-4} \text{ mol/L}$ was chosen in order to obtain the same molar ratios $n_{BY215}/n_{C12E6} = n_{SDS}/n_{C12E6}$.

Preparing the SANS samples, H_2O was replaced by D_2O. In order to adjust the same molecular compositions of samples containing H_2O and D_2O, the $C_{12}E_6$ fraction in the SANS measurements is specified by the volume fraction of surfactant, ϕ_C. Samples were prepared by weight, using the densities of the components $\rho^0_{H2O} = 0.998 \text{ g/cm}^3$, $\rho^0_{D2O} = 1.105 \text{ g/cm}^3$ and $\rho^0_{C12E6} = 0.980 \text{ g/cm}^3$. The densities of the D_2O/BY215 and H_2O/BY215 solutions were set to the values of the pure components D_2O and H_2O, respectively, which is a reasonable approximation with regard to the small concentration of BY215. The temperature dependence of the volume fractions is neglected. The compositions and temperatures of the SANS samples examined in this study are compiled in Table 8-2.

Phase Behavior

In order to study the phase behavior the mixture was studied in sample tubes equipped with a magnetic stirring bar and sealed with a PE stopper. Cloud points were determined by visual inspection under variation of the temperature at constant surfactant concentration. Therefore samples were placed in a temperature controlled water bath with a temperature stability of $\Delta T \pm 0.01$ K. The samples were stirred and then allowed to equilibrate before the

number and type of phases was determined via visual inspection of both, the transmitted and scattered light. The temperature was first varied in larger increments below and above the cloud point. By stepwise decreasing the size of the temperature increments down to $\Delta T = 0.1$ K the cloud points were determined with an accuracy of $\Delta T \pm 0.05$ K. After recording the cloud point the sample was diluted and the preocedure was repeated. To exclude systematic errors additional samples were prepared at interjacent concentrations.

SANS measurements

The SANS measurements were conducted within two visits (Feb. and May 2008) using the *KWS*2 intrument in the *Jülich Center for Neutron Science* (*JCNS)*, that is hosted at the *Forschungsneutronenquelle Heinz Maier-Leibnitz* (FRM II) in Garching, Germany.

The samples were filled at room temperature in Hellma Quartz cells with an optical path length of 1 mm and equilibrated to the desired temperature in the cell holder before each measurement. Thereby the temperature was controlled with an accuracy of $\pm$ 0.1 *K*. The data were collected at wavelengths of $\lambda = 4.8$ and 11.9 Å, ($\lambda = 4.8$ and 12.0 Å Feb. 2008), with a wavelength distribution of the velocity selector of $\Delta\lambda/\lambda = 0.2$ (full width at half maximum) [135]. Measurements were performed at sample-to-detector distances of 2 and 8 m, thereby covering a range of the scattering wave vector $q = (4\pi/\lambda)sin(\theta/2)$ from 0.0036 to 0.33 Å, was covered, where θ is the scattering angle. The collimation and aperture settings were chosen in order to optimize the neutron flux without exceeding the detector capacity. Transmissions of the samples ranged from 0.84 to 0.91 for the measurements at $\lambda = 4.7$ Å and from 0.61 to 0.71 at $\lambda = 11.9$ Å, respectively. The raw data was radially averaged and normalized according to standard procedures using the program *QtiKWS* [136] provided by the *JCNS*. Plexiglas of 1.5 mm path length was used as absolute calibration standard. The absolute intensities obtained of the data sets that were collected in February and May, respectively, differed by a factor of up to 1.28. Since uncertainties did occur in the absolute calibration of the data collected in February, those data were adjusted to overlap with the data collected in May. The data being collected at $\lambda = 11.9$ and 12.0 Å, were adjusted to those collected at $\lambda = 4.8$ Å, without absolute calibration. From the obtained absolute intensities the incoherent background I_{incoh} was subtracted for further evaluation of the scattering curves.

4.3 Results

4.3.1 Phase Behavior

The phase diagram of the pure binary non-ionic surfactant system $H_2O - C_{12}E_6$ is shown in Figure 4.3-1. The system shows an isotropic one-phase region (1) at lower temperatures and $C_{12}E_6$ mass fractions, and a two-phase region (2) at higher temperatures [87, 91]. The lower phase boundary of the upper miscibility gap (circles) is shown with the critical point (full circle) being found at $\gamma = 0.021 \pm 0.01$ and $T = 51.53 \pm 0.02\,°C$, which differs only slightly from literature values [91, 95].
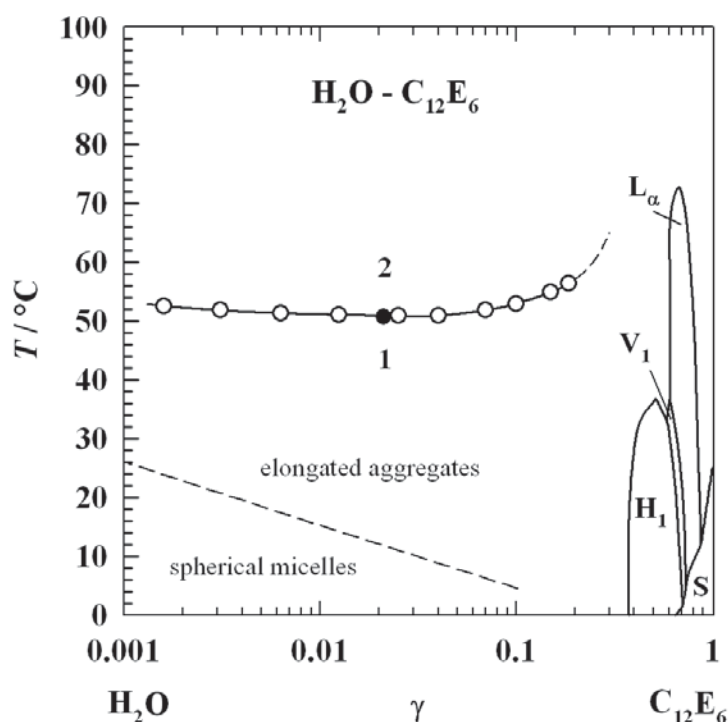
Figure 4.3-1: Phase diagram of the system $H_2O - C_{12}E_6$. The transition line between spherical micelles and elongated aggregates (dashed line) was redrawn from reference [91]. The liquid crystalline phases (H_1), (V_1), (L_α) and the solid phase (S) are shown as guide to the eyes according to *Mitchell et al.* [87].

It is known [91, 127, 162] that, above the critical micelle concentration (cmc), at low temperatures and low surfactant fractions the $C_{12}E_6$ molecules self asssemble to spherical micelles, whereas at higher temperatures and higher surfactant fractions the aggregates exhibit a more elongated or cylindrical shape. The dashed line represents the transition form spherical micelles to elongated aggregates. This transition line was determined by *Strey* and *Pakusch* [91]

from quasielastic light scattering and *T*-jump experiments, and also manifests itself in an abrupt change of the viscosity of the solution [88]. If the surfactant weight fraction is further increased over $\gamma > 0.35$, hexagonal (H$_1$), normal bicontinuous cubic (V$_1$) and lamellar (L$_\alpha$) liquid crystalline structures are found [87]. At further increased masss fraction of C$_{12}$E$_6$, $\gamma > 0.70$ a solid phase (S) is found [87].

In order to study the influence of the ionic dye Basantol® Yellow 215 on the lower phase boundary of the upper miscibility gap, at first C$_{12}$E$_6$ was partly replaced by BY215, adjusting a constant ratio of dye to C$_{12}$E$_6$ molecules. In other words the dye was considered to act as a cosurfactant. The result is shown in Figure 4.3-2.
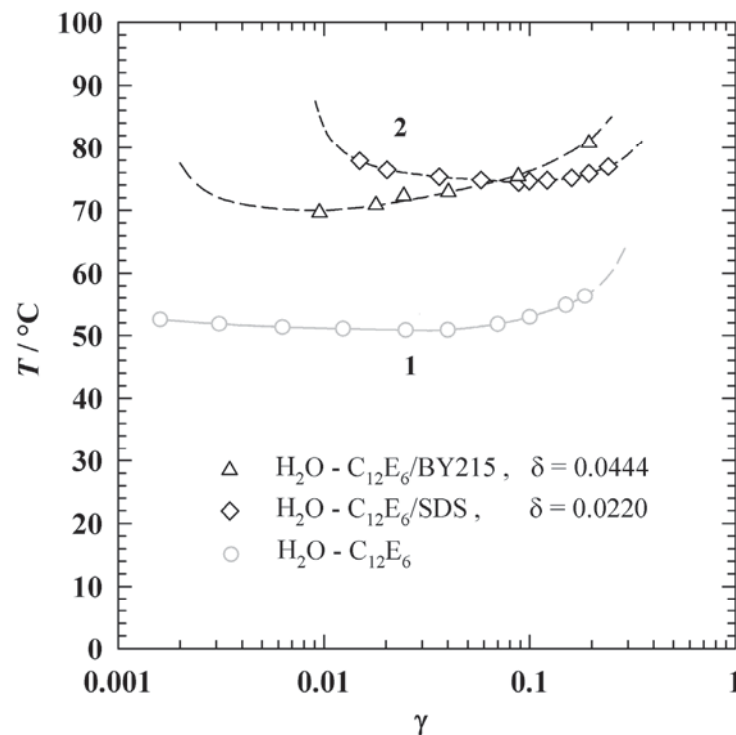
Figure 4.3-2: Lower phase boundary of the upper miscibility gap of the systems H$_2$O – C$_{12}$E$_6$/BY215 (triangles) and H$_2$O – C$_{12}$E$_6$/SDS (diamonds). For BY215 the mass fraction of cosurfactant in the C$_{12}$E$_6$/BY215 mixture was $\delta = 0.0444$ and for SDS the corresponding value was $\delta = 0.0220$. Those values correspond to molar ratios between the cosurfactant and C$_{12}$E$_6$ of $n_{BY215}/n_{C12E6} = 0.0215$ and $n_{SDS}/n_{C12E6} = 0.0344$, respectively. The grey circles represent the phase boundary of the pure binary system H$_2$O – C$_{12}$E$_6$.

As can be observed, adding Basantol® Yellow 215 with a mass fraction of $\delta = 0.0444$ in the mixture of BY215 and C$_{12}$E$_6$ (corresponding to a molar ratio $n_{BY215}/n_{C12E6} = 0.0215$) leads to a shift of the phase boundary of approximately $\Delta T \approx (+)25\ °C$ to a higher temperature (triangles in Figure 4.3-2). Thereby the phase boundary shifts in an almost parallel way compared to the

phase boundary of the pure binary sytem H_2O – $C_{12}E_6$ (grey circles). This behavior, i.e. the shift of the phase boundary to higher temperatures, or in other words the increasing mutual solubility of surfactant and water, is well known from the addition of an ionic cosurfactant, such as sodium dodecyl sulphate (SDS) [107, 108]. This effect is caused by the electrostatic repulsion between the head groups of the cosurfactant molecules that lead to (i) a repulsion of the aggregates and (ii) an increase of the curvature of the amphiphilic film. Both effects counterbalance the formation of a second surfactant-rich phase (refer to section 2.3.1 and references cited there).

In the following the effect of the ionic dye Basantol[®] Yellow 215 is compared with that of SDS, determining the lower phase boundary of the upper miscibility gap of the system H_2O – $C_{12}E_6$/SDS. A value of $\delta = 0.0220$ was chosen from preliminary test measurements in order to obtain a shift of the phase boundary in the same order of magnitude as for BY215. The result is shown as diamonds in Figure 4.3-2: As can be seen, the addition of SDS shifts the lower phase boundary of the upper miscibility gap to a temperature, that corresponds almost quantitatively to that of H_2O – $C_{12}E_6$/BY215 at $\delta = 0.0444$. The corresponding molar ratios in the surfactant mixtures are $n_{SDS}/n_{C12E6} = 0.0344$ and $n_{BY215}/n_{C12E6} = 0.0215$, respectively. Accordingly, the molar ratio of SDS to $C_{12}E_6$ in the surfactant mixture (n_{SDS}/n_{C12E6}) is by a factor 1.6 larger, compared to that of Basantol® Yellow 215 (n_{BY215}/n_{C12E6}) leading to almost the same temperature shift of the phase boundary. This effect might be explained by the fact that Basantol[®] Yellow 215 carries three charges and therefore induces a stronger electrostatic repulsion than SDS.

Upon closer examination of Figure 4.3-2, it can be seen that the shape of the phase boundary of the system H_2O – $C_{12}E_6$/BY215 is different from that of H_2O – $C_{12}E_6$/SDS. While the phase boundary of the latter system (diamonds) exhibits a minimum around $\gamma \approx 0.1$, the phase boundary of the system containing the ionic dye (triangles) gradually decreases in temperature with decreasing surfactant weight fraction γ. Thereby, for surfactant mass fractions $\gamma > 0.10$ the phase boundary of H_2O – $C_{12}E_6$/BY215 lies at slightly higher temperatures than that of H_2O – $C_{12}E_6$/SDS. The observation, that the phase boundary H_2O – $C_{12}E_6$/BY215 descends in temperature with decreasing surfactant weight fraction γ points to a higher monomeric solubility of Basantol[®] Yellow in water compared to SDS. This might be understood as follows: Since this experiment is performed at a fixed molecular ratio of BY215 in the mixture of $C_{12}E_6$ and BY215 ($n_{BY215}/n_{C12E6} = 0.0215$), more dye molecules would be monomerically dissolved in water with increasing water fraction. Hence, with decreasing γ, the fraction of dye molecules, that are

incorporated into the aggregates, affecting their curvature and solubility due to electrostatic repulsion is also reduced. This would lead to a decreasing cloud point temperature with decreasing surfactant mass fraction γ, which corresponds to the shape of the phase boundary in Figure 4.3-2.

In contrast to the fixed ratio of Basantol$^{®}$ Yellow 215, in the mixture of $C_{12}E_6$ and dye, that was applied in the experiments described above, in the TDFRS experiment the dye concentration c_{BY} is kept constant with respect to the H_2O/BY215 mixture at $c_{BY} = 1.5 \cdot 10^{-4}$ mol/L , corresponding to a mass fraction of BY215 of $\psi = 1.4 \cdot 10^{-4}$ in the mixture H_2O/BY215, in order to adjust the optical density to $OD = 2 \, cm^{-1}$ [29, 160]. This means, that the dye is considered rather as an hydrophilic additive than a co-surfactant. The phase behavior of the pseudobinary system H_2O/BY215 – $C_{12}E_6$ is shown in figure 4.3-3 (triangles).
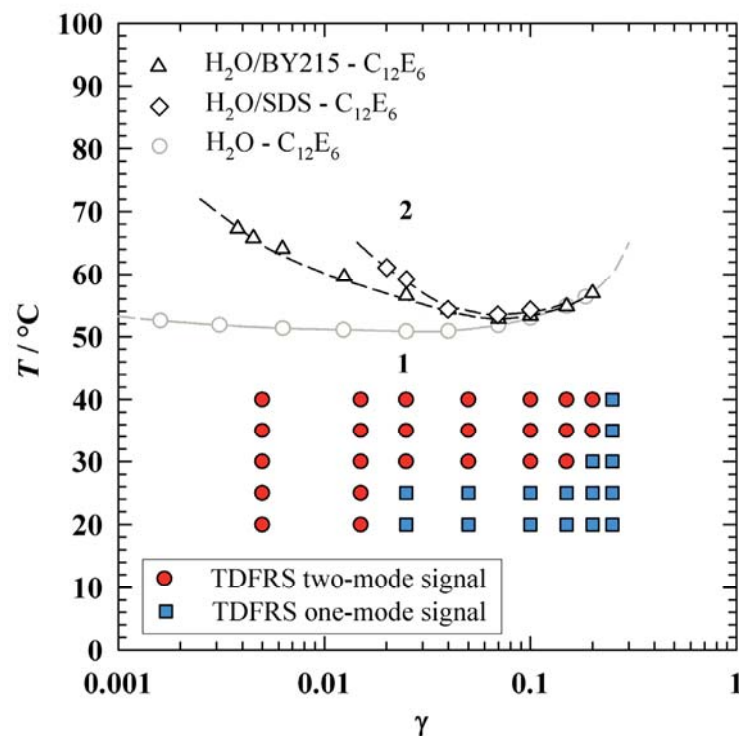
Figure 4.3-3: If in the binary system H_2O – $C_{12}E_6$ water is replaced by an aqueous solution of Basantol$^{®}$ Yellow 215, ($c_{BY} = 1.5 \cdot 10^{-4}$ mol/L) as in the TDFRS experiment (triangles) the phase boundary shifts to increasingly higher temperatures with decreasing γ. This effect is even more significant, if BY215 is replaced by SDS (diamonds) at the same concentration $c_{SDS} = 1.5 \cdot 10^{-4}$ mol/L . The grey circles represent the pure binary system H_2O – $C_{12}E_6$.

Comparing the phase behavior of the binary (grey circles) and the pseudo-binary system containing the dye (triangles), it becomes obvious that the cloud point temperature of the latter is

increasingly shifted to higher temperatures with decreasing surfactant weight fraction γ. This finding is a strong evidence, that the dye molecules are incorporated preferentially in the aggregates, i.e. acting as a cosurfactant. Thereby the shift of phase boundary to higher temperatures with decreasing γ can be understood as follows: As a result of the fixed concentration of BY215 with respect to the aqueous component H_2O/BY215 in this experiment, the molar ratio of BY215 to $C_{12}E_6$ molecules, n_{BY215}/n_{C12E6} increases with decreasing γ. This would in turn lead to an increased number of charges per aggregate with decreasing γ, which could explain the observed shape of the phase boundary.

Using SDS instead of Basantol® Yellow 215, i.e. studying the phase behavior of the system H_2O/SDS – $C_{12}E_6$ (diamonds in Figure 4.3-3) leads to qualitatively the same behavior. However, although the SDS concentration $c_{SDS} = 1.5 \cdot 10^{-4}$ mol/L in the aqueous component H_2O/SDS (corrresponding to a mass fraction $\psi = 4.3 \times 10^{-5}$) was set to the same value as for the experiment containing the dye, the shift of the phase boundary towards higher temperatures with decreasing $C_{12}E_6$ fraction is more pronounced in the case of SDS.

The less pronounced increase of the phase boundary in the system H_2O/BY215 – $C_{12}E_6$ points to a smaller electrostatic repulsion, with decreasing $C_{12}E_6$ fraction. This confirms the assumption of a higher monomeric solubility of the ionic dye in water compared to that of SDS. The reason for the higher monomeric solubility in water might certainly be a difference in structure between Basantol® Yellow 215 and SDS. The dye is a charged complex and presumably does not exhibit a similarly strong amphiphilic character as SDS. Thus, BY215 might be less effectively incorporated into the aggregates. It might also be assumed that the monomerically dissolved dye molecules are dissociated to a larger extend. This would lead to an additional screening of the electrostatic repulsion of the aggregates, which would also weaken the influence of the dye as an ionic cosurfactant.

To sum up, from the phase behavior studies it was found, that, although different in intensity, the ionic dye Basantol Yellow® 215 influences the phase behavior of the non-ionic surfactant system H_2O – $C_{12}E_6$, qualitatively in the same way as the ionic surfactant SDS. This observation strongly suggests that the ionic dye is incorporated into the aggregates as an ionic cosurfactant. If the experimental conditions match the TDFRS experimental conditions, i.e. fixed concentration of the dye with respect to the aqueous component, we find a pronounced influence on the phase behavior just by decreasing the weight fraction of $C_{12}E_6$. The fact that the second mode in the

concentration signal of the TDFRS measurements occurs particularly at small weight fractions of $C_{12}E_6$, suggests that this second mode might be related to the strong shift of the phase boundary to higher temperatures and therewith to the incorporation of the ionic dye into the aggregates.

In order to investigate the manifestation of this correlation in the microstructure of the aggregates we performed systematic small angle neutron scattering (SANS) measurements at different temperatures and $C_{12}E_6$ fractions in the system water – $C_{12}E_6$ – Basantol Yellow® 215. As for the phase behavior measurements, the influence of SDS on the microstructure was also studied for comparison.

4.3.2 SANS Measurements

Samples were prepared for the systems $D_2O – C_{12}E_6$, $D_2O/BY215 – C_{12}E_6$ and $D_2O/SDS – C_{12}E_6$ at small (ϕ_C = 0.0025, 0.0051 and 0.0075) and larger (ϕ_C = 0.102) volume fraction of $C_{12}E_6$, ϕ_C in order minimize critical scattering. Note that H_2O is replaced by D_2O in order to generate a sufficient scattering contrast. To adjust the same molecular compositions of samples containing H_2O and D_2O, the $C_{12}E_6$ fraction in the SANS measurements is specified by the volume fraction of surfactant, ϕ_C. The dye was added as an additive to D_2O (see phase diagram in Figure 4.3-3), adjusting the concentration of BY215 to $c_{BY} = 1.5{\cdot}10^{-4}$ mol/L in order to match the conditions of the TDFRS experiments [28, 29]. For the system $D_2O – C_{12}E_6/SDS$ the concentration of SDS was set to the same value, i.e. $c_{SDS} = 1.5{\cdot}10^{-4}$ mol/L .

In the following at first the influence of Basantol® Yellow 215 and SDS will qualitatively be discussed for the samples with the lowest volume fraction of $C_{12}E_6$, i.e. ϕ_C = 0.0025. Figure 4.3-4, shows the recorded scattering intensity $I(q)$ as function of the scattering vector q for the three systems $D_2O – C_{12}E_6$ (circles), $D_2O/BY215 – C_{12}E_6$ (triangles) and $D_2O/SDS – C_{12}E_6$ (diamonds) at ϕ_C = 0.0025 and four different temperatures in the range from T = 21.3 °C to T = 65.5 °C. Note that for the pure binary system $D_2O – C_{12}E_6$ the sample is in the two phase state at T = 65.5 °C (refer to Figure 4.3-1). Consequently SANS measurements were not performed for this system at that temperature. From Figure 4.3-4 it becomes obvious that the curves of the different systems and temperatures show the most significant deviation in their forward scattering intensity, i.e. at small q-values. In the intermediate q-region, from $0.01 \le q \le$ 0.07 Å^{-1} the curves show a decrease as function of q, that becomes, as a common feature for all systems, steeper with increasing temperature. From q-values larger than approximately

$q \approx 0.08$ Å^{-1} the scattering curves of all systems and temperatures decrease steeply with increasing q towards the incoherent background, that is reached at approximately $q \geq 0.15$ Å^{-1}. The differences of the scattering curves of the different systems and the influence of the temperature will now be discussed:
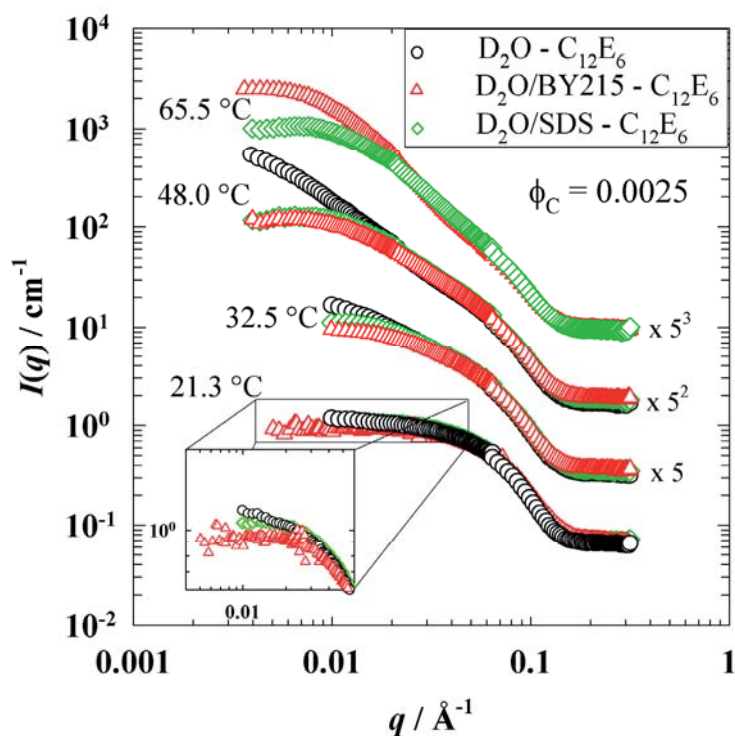
Figure 4.3-4: SANS curves of the three systems $D_2O - C_{12}E_6$ (circles), $D_2O/BY215 - C_{12}E_6$ (triangles) and $D_2O/SDS - C_{12}E_6$ (diamonds) at $\phi_C = 0.0025$ and four different temperatures in the range from $T = 21.3$ °C to $T = 65.5$ °C. Replacing D_2O by $D_2O/BY215$ or D_2O/SDS results in a decrease of the forward scattering intensity I_0. With increasing temperature this difference gets more pronounced. At $T = 65.5$ °C additionally a significant difference between the BY215-, and SDS-samples can be seen. Note that H_2O, was replaced by D_2O and the volume faction of $C_{12}E_6$ ϕ is used instead of γ in order to retain the same molar fraction of $C_{12}E_6$, as in the phase behavior experiments. The concentration of BY215 and SDS, respectively, in the aqueous component was set to $c = 1.5 \cdot 10^{-4}$ mol/L in agreement with phase behavior measurements and the condition in the TDFRS measurements. The inset shows the scattering intensities at $T = 21.3$ °C in the q-range from 0.004 - 0.05 Å^{-1}.

For the pure binary system $D_2O - C_{12}E_6$ (circles in Figure 4.3-4) in the q-range between approximately $0.01 \leq q \leq 0.07$ Å^{-1} already at $T = 21.3$ °C a slight increase of the scattering intensity $I(q)$ with decreasing q is observed, that reflects the onset of the elongation of the aggregates [90]. This is in good agreement with the results of *Strey et al.* [91] who determined the transition line between spherical micelles and larger aggregates via quasielastic light scattering and T-jump experiments (refer to Figure 4.3-1). Increasing the temperature to $T = 32.5$ °C, a more significant increase of the scattering intensity at low q-values is observed that indicates the existence of cylindrical aggregates. This micellar growth from spherical to

cylindrical aggregates, which occurs upon increasing the temperature has extensively been studied in the past and is related to the dehydration of the surfactant head-groups with increasing temperature [90, 91, 139, 163, 164]. At $T = 48.0$ °C an even stronger increase of the forward scattering intensity is found, which can be ascribed to critical scattering [90, 146]. As has been shown by *Foster et al.* [165] the formation of cylindrical networks leads also to an increase of the forward scattering intensity. However, according to reference [93] the formation of cylindrical networks in the system $D_2O – C_{12}E_6$ is not expected below a volume fraction of $C_{12}E_6$ ϕ_C of $\phi_C \approx 0.01$. Thus, for our measurement at $\phi_C = 0.0025$ this effect could rather be excluded.

Now the scattering pattern of the two charged systems $D_2O/BY215 – C_{12}E_6$ and $D_2O/SDS – C_{12}E_6$ should be discussed. At intermediate q-values for both, $D_2O/BY215 – C_{12}E_6$ and $D_2O/SDS – C_{12}E_6$, respectively the evolution of the scattering intensity as function of the temperature, qualitatively resembles that of the system $D_2O – C_{12}E_6$: An increase of the scattering intensity in the intermeditae q-region with decreasing scattering vector q is found upon increasing the temperature. This indicates that the aggregates in those systems exhibit also a transition from spherical to cylindrical aggregates. However, at small q-values, i.e. approximately below $q < 0.02$ Å^{-1}, the scattering curves of the charged systems $D_2O/BY215 – C_{12}E_6$, and $D_2O/SDS – C_{12}E_6$ show a different pattern than that the pure non-ionic binary system $D_2O – C_{12}E_6$. This will be discussed now for the different temperatures:

Although at first sight at $T = 21.3$ °C this difference is not very pronounced, it is visible in the inset in Figure 4.3-4 that at small q-values the scattering intensity of $D_2O/BY215 – C_{12}E_6$ is slightly lower than that of $D_2O – C_{12}E_6$. Increasing the temperature, from $T = 21.3$ to 32.5 °C a deviation of the scattering curves of $D_2O/BY215 – C_{12}E_6$ and $D_2O/SDS – C_{12}E_6$ from the trend of the binary system to lower scattering intensities at $q < 0.02$ Å^{-1} is clearly visible. Hence, the difference between the charged systems and $D_2O – C_{12}E_6$ becomes more pronounced.

At $T = 48.0$ °C a larger q-range was covered in the scattering experiments in order to study those deviations in more detail. While at this temperature for $D_2O – C_{12}E_6$ a significant increase of the forward scattering intensity is observed, the curves of the two charged systems significantly decrease with decreasing q. The absence of critical scattering for $D_2O/BY215 – C_{12}E_6$ and $D_2O/SDS – C_{12}E_6$ can be understood as follows: It already has been observed from the phase behavior studies (refer to Figure 4.3-3), that compared to $D_2O – C_{12}E_6$ the cloud point temperatures of the charged systems are shifted to significantly higher temperatures with

decreasing $C_{12}E_6$ fraction. This shift was ascribed to the existence of electrostatic repulsion between the aggregates, due to the incorporation of the charged dye-, or SDS molecules. As it is well known in the literature from studies on ionic aggregates, e.g. mixed micelles of $C_{12}E_6$ and SDS [100, 101, 103, 166] electrostatic interactions also induce a long range order in the microstructure of the system, which in turn is reflected by a decrease of the scattering intensity at low q-values. Accordingly, since the systems shown in Figure 4.3-4 are dilute ($\phi_C = 0.0025$), which means that excluded volume effects can be ruled out, this scattering pattern at $T = 48.0\ °C$ supports the assumption that the ionic dye Basantol® Yellow 215 is incorporated into the aggregates in the similar way as SDS.

While up to $T = 48.0\ °C$ the systems $D_2O/BY215 - C_{12}E_6$ (red circles) and $D_2O/SDS - C_{12}E_6$ (green diamonds) exhibit almost perfectly the same scattering pattern, at $T = 65.5\ °C$ significant deviations between the two curves can be obsereved in the small q-region, i.e. below approximately $q < 0.011\ Å$. Thereby the system containing BY215 shows an almost constant forward scattering intensity, which is significantly higher, than that of the system containing SDS, which in turn shows a distinct bend towards a decreasing forward scaterring intensity with decreasing q. This observation could possibly be explained by the different distance to the cloud point curve of both systems: From the trend of the cloud point curve of the system $D_2O/BY215 - C_{12}E_6$ (triangles in Figure 4.3-3) it can be deduced that the measurement point at $T = 65.5\ °C$ for this system, lies in the vicinity of the upper miscibility gap. In contrast, for $D_2O/SDS - C_{12}E_6$ (squares in Figure 4.3-3) the trend of the cloud point curve suggests, that the miscibility gap might even be outside the experimental window at $\phi_C = 0.0025$. Indeed, for this system already at $\phi_C = 0.005$ a cloud point could not be observed up to a temperature of $T \approx 85\ °C$. Therefore it can be assumed that a more pronounced effect of critical scattering occurs only for the former system. Assuming furthermore that for both systems electrostatic repulsion, leading to a decrease of the forward scattering intensity, exist, for $D_2O/BY215 - C_{12}E_6$ this would be counterbalanced by the critical scattering effect. Hence, this would explain the absence of a bend towards a lower forward scattering intensity for this sytem.

In the next step the scattering curves will be analyzed quantitatively using appropriate scattering models in order to examine the influence of the ionic dye Basantol® Yellow 215 on the binary surfactant system water – $C_{12}E_6$. Therefore we first analyze the scattering pattern of the pure binary system $D_2O - C_{12}E_6$, that has been studied in the literature before (e.g. [90]). In Figure 4.3-5 the scattering intensities $I(q)$ are shown as function of the scattering vector q on a

logarithmic scale for D$_2$O – C$_{12}$E$_6$ at ϕ_C = 0.0025 at T = 21.3 (a), 32.5 (b) and 48.0 (c) °C. Note that the incoherent background scattering I_{incoh} is substracted from the experimentally obtained scattering intensities.
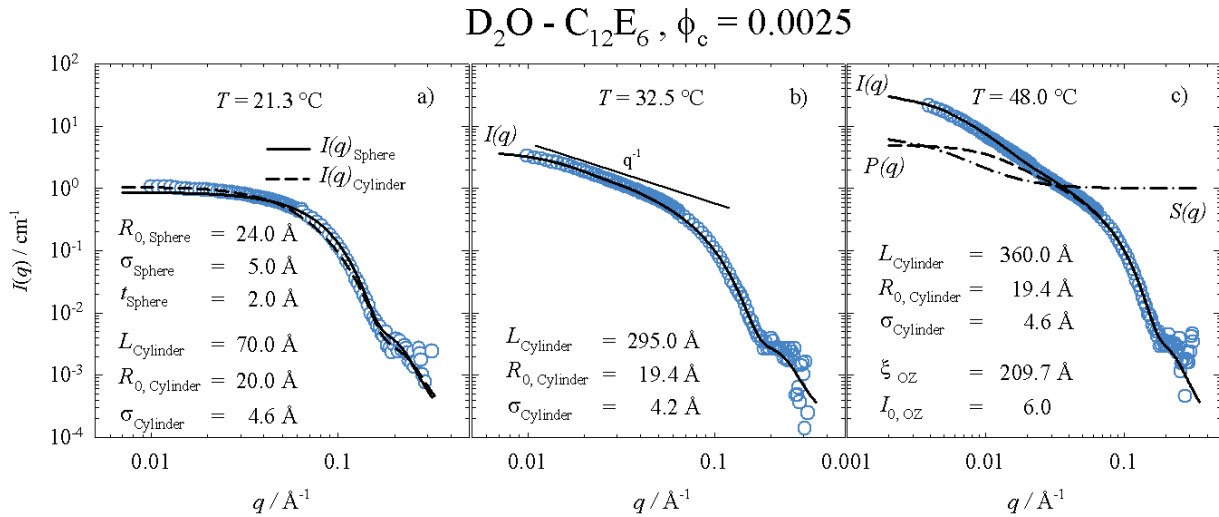
Figure 4.3-5: SANS curves (circles) of the system D$_2$O – C$_{12}$E$_6$ at three different temperatures T = 21.3 (a), 32.5 (b) and 48.0 (c) °C, at ϕ_C = 0.0025. Note that the incoherent scattering intensity I_{incoh} is substracted from the experimentally obtained scattering intensities. The lines represent fits of appropriate models to the experimentally obtained scattering intensity. See text for details.

As discussed already qualitatively before, the scattering curve at T = 21.3 °C (Figure 4.3-5a) mimics the scattering from polydisperse spherical micelles at the onset of the transition to elongated aggregates. Accordingly, the slight increase of the scattering intensity at low values of q is a strong indication for the growth of the aggregates. With increasing q-values above approximately $q > 0.09$ Å^{-1} the scattering intensity $I(q)$ steeply decays as function of q and approaches a "shoulder" around $q \approx 0.2$ Å^{-1}. This shoulder can be assigned to the minimum and a following maximum of the form factor, which are smeared out due to the polydispersity of the aggregates and the wavelength distribution of the incident beam. The steep decay of the scattering curve before the minimum suggest the existence of almost spherical micelles, while the position of the minimum and the following maximm are related to their mean radius.

Accordingly, the scattering intensity was described by the scattering intensity of a form factor of a polydisperse sphere with diffuse interface [equation (2.45)] (full line in Figure 4.3-5) and as an alternative approach by a form factor of a cylinder with polydisperse cross section [equation (2.58)] (dashed line). Thereby long range interaction could be neglected due to the low surfactant concentration [$S(q) \approx 1$]. As can be seen the form factor of a polydisperse sphere with diffuse

interface describes the scattering curve almost quantitatively at intermediate and large q-values, i.e. $q \geq 0.03$ Å^{-1}, while quantitative deviations are found at smaller q-values. On the contrary the form factor of a cylinder describes the scattering curve quantitatively at low values of q, while it cannot describe the experimental scattering intensity around $0.05 < q < 0.14$ Å^{-1}.

The ambiguity of both models is consistent with the sphere-to-rod transition of the aggregates described above [93]. Alternatively a model of ellipsoids could be applied [100]. However, it will not be possible to differentiate between a polydisperse mixture of elongated and spherical micelles or ellipsoidal aggregates by small angle neutron scattering.

Our measurements presented in Figure 4.3-5a were performed at lower a surfactant concentration ($\phi_C = 0.0025$) compared to the works, that are presented in the literature (e.g. [90, 100, 167]), but it is known, that the change in micellar size at lower concentrations and temperatures is small [168, 169]. Thus, the mean radius $R_0 = 24.0$ Å, with a diffuse interface of thickness $t = 2.0$ Å, obtained from our fit at $T = 21.3$ °C (see Figure 4.3-5a) is in good agreement with values presented in the literature [90, 100, 167], that range from $R = 20$ to 30 Å. We found a polydispersity of $\sigma = 5.0$ Å. It must however be mentioned that the smearing of the minimum in the scattering curve stems as well from the wavelength distribution $\Delta\lambda/\lambda$. Thus, the polydispersity of the aggregates is overestimated to some extend by this value.

At $T = 32.5$ °C (Figure 4.3-5b) a q^{-1}-like decrease of the scattering intensity in the intermediate q – range can be observed, which is a clear indication for cylindrical aggregates, [90]. Hence, the scattering curve is quantitatively described by the cylinder form factor model. The mean radius $R_0 = 19.4$ Å, is slightly smaller, compared to the almost spherical aggregates at $T = 21.3$ °C. Such a decrease in radius with transition from spherical to rod-like aggregates has been reported before for the binary systems $H_2O – C_{12}E_5$ [80, 170] and $H_2O – C_8E_5$, respectively [90]. The effect can be explained with the smaller head group size of the surfactant as a result of a decreasing hydration with increasing temperature [69, 70].

At $T = 48.0$ °C (Figure 4.3-5c) the scattering curve of the binary system $H_2O – C_{12}E_6$ shows a significant increase in the forward scattering intensity, which points to critical scattering, although the concentration of this sample, $\phi_C = 0.0025$ is approximately two orders of magnitude lower than the critical concentration ($\phi_C \approx 0.021$). *Wilcoxon* and co-workers [171] investigated the effect of *critical* scattering *off the critical isochore* and found that the effect of density fluctuations, resulting in an increased forward scattering intensity, is also observed at

concentrations other than the critical. From their investigation by means of quasielastic light scattering and *T*-jump experiments *Strey et al.* [91] already found critical fluctuations in this region of the phase diagram of $H_2O - C_{12}E_6$, that were also confirmed by the theoretical calculation of the spinodal line of the phase separation in this system by *Zilman et al.* [93]. Furthermore, as was pointed out before, the formation of cylindrical networks can be neglected at $\phi_C = 0.0025$. Therefore it is reasonable to describe the increase of the scattering intensity by the product of the modified *Onstein-Zernike* structure factor [equation (2.61)] and the cylinder form factor. As can be seen, this model describes the experimental scattering curve quantitatively. We obtained an amplitude parameter of the critical scattering of $I_0 = n_p k_B T \chi_T = 6.0$ and a correlation length $\xi_{OZ} = 209.7\,\text{Å}$. The parameters used in the cylindrical form factor are $L = 360\,\text{Å}$, $R_{0,\text{cyl}} = 19.4\,\text{Å}$ and $\sigma_{\text{cyl}} = 4.62\,\text{Å}$. It can be seen, that the aggregates are further increased in their length, compared to 32.5 °C, but exhibit the same cross section radius R_0.

In the next step the effect of the charged dye Basantol® Yellow 215 and SDS on the SANS scattering pattern is examined. As was already pointed out in the discussion of the phase behavior, the molar ratio of BY215 to $C_{12}E_6$ (n_{BY215}/n_{C12E6}) increases with decreasing $C_{12}E_6$ fraction ϕ_C as the concentration of BY215 in D_2O is kept constant. Assuming in fact, that BY215 acts partially as a cosurfactant, its influence on the microstructure should be seen most significantly at small values of ϕ_C. In Figure 4.3-6 the scattering curves of the system $D_2O/BY215 - C_{12}E_6$ at $T = 21.3$ (a) and 48.0 (b) °C are shown together with the scattering curve of the system $D_2O/SDS - C_{12}E_6$ at $T = 48.0$ °C (c) for $\phi_C = 0.0025$. As was pointed out in the qualitative discussion before, for the charged systems at higher temperatures ($T = 65.5$ °C, refer to Figure 4.3-4), the influence of both critical scattering and electrostatic repulsion of the aggregates is assumed to dominate the scattering pattern at low *q*-values. Since these effects counterbalance each other, the physical meaning of a model description of the scattering curves that has to account, electrostatic interaction and critical scattering, would rather be ambiguous. Thus, we did not apply a model description to the scattering curves of the charged system for $T = 65.5$ °C.
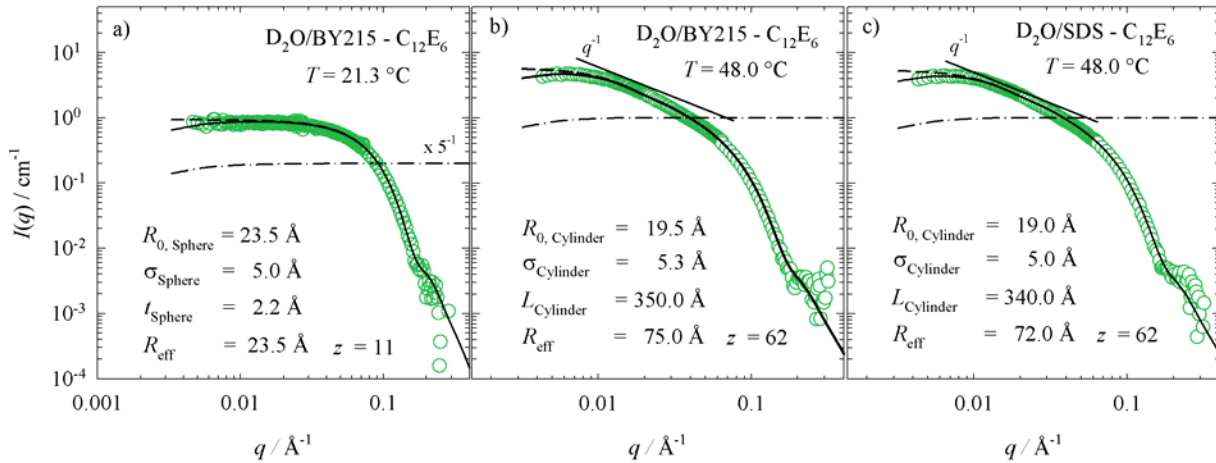
Figure 4.3-6: SANS curves of the charged systems $D_2O/BY215 – C_{12}E_6$ at $T = 21.3$ (a) 48.0 °C (b), and $D_2O/SDS – C_{12}E_6$, at $T = 48.0$ °C (c) at $\phi_C = 0.0025$. The molar ratios of the charged additive to $C_{12}E_6$ for $\phi_C = 0.0025$ are $n_{BY215}/n_{C12E6} = n_{SDS}/n_{C12E6} = 0.027$. The experimental scattering intensities (circles) are shown after subtraction of the incoherent background. The lines represent fits to appropriate models as described in the text. The parameter for the salt-concentration was adjusted for all samples to $c_{salt} = 10^{-9}$ mol/l. Dashed line in a: Form factor of a sphere. Dashed line in b and c: Form factor of a Cylinder. Dash-dotted lines in a,b and c: Structure factor of charged particles. Full lines in a, b and c: Product of form factor and structure factor.

At first the scattering curve of the system $D_2O/BY215 – C_{12}E_6$ at $T = 21.3$ °C shown in Figure 4.3-6a is discussed. As can be seen, the scattering curve shows a very slight decrease of the forward scattering intensity, while the scattering curve of the binary system (Figure 4.3-5a) showed even a small increase at the same conditions. This slight decrease in the forward scattering intensity of the $D_2O/BY215 – C_{12}E_6$ sample points towards the existence of repulsive electrostatic interactions between the micelles. Accordingly, the experimental scattering intensity $I(q)$ (circles) in Figure 4.3-6a was described using the product (full line) of the RMSA structure factor [152, 153] (dash-dotted line in Figure 4.3-6a), that is based on a screened *Coulomb* interaction potential [equation (2.72)] between the aggregates, and the form factor $P(q)$ for polydisperse spheres with diffuse interface (dashed line). Although the interaction effect is small, the experimentally obtained scattering intensity is exactly described by the combination of those models. The model parameters are shown in Figure 4.3-6a. The parameters of the form factor are very similar to those used to describe the scattering curve of the system $D_2O – C_{12}E_6$ at the same $C_{12}E_6$ fraction ϕ_C and temperature (refer to Figure 4.3-5a). This result suggests that the dye BY215 has, at those conditions, no significant influence on the shape and size of the micelles. The free parameters of the structure factor model are the effective radius R_{eff}, the effective charge of the aggregates z and the concentration of salt c_{salt} in the surrounding medium in terms of single-charge ions. We set the effective radius equal to the radius of the spherical micelles, $R_{eff} = R_0 = 23.5$ Å in order to reduce the number of free parameters. The values obtained for the

remaining parameters are $z = 11$ and $c_{salt} = 10^{-9}$ mol/L. Since Basantol® Yellow 215, is a trivalent complex [29] an average number of dye molecules per aggregate of n_{BY} / aggregate ≈ 3.7 can be estimated from the obtained value of z. The concentration of salt $c_{salt} = 10^{-9}$ mol/L, which determines the reciprocal *Debye* screening length κ in the potential [equation (2.72)], would equal a concentration of BY215 of $c_{BY} = 1.7\text{x}10^{-9}$ mol/L. This would imply that the fraction of freely dissolved BY215 in the surrounding medium with respect to the total amount of BY215 is $c_{BY,free} / c_{BY} \approx 1.1\text{x}10^{-5}$. Here, it should be mentioned that this calculation should be regarded as a rather rough estimation because, as was shown by *Fritz et al.* [172], different sets of model parameters can lead to the same structure factor curve. Furthermore we have no additional information about the monomeric solubility of the dye and its degree of dissociation. Nevertheless, this ratio confirms the picture of the dye being incorporated to a high extend into the aggregates instead of being freely dissolved in the solution.

The scattering intensity of the system $D_2O/BY215 – C_{12}E_6$ at $\phi_C = 0.0025$ and $T = 48.0$ °C is shown in Figure 4.3-6b. The decrease of the scattering intensity at small q-values is more significant compared to the sample at 21.3 °C, shown in Figure 4.3-6a. In the q-range between 0.01 and 0.04 Å^{-1} $I(q)$ decreases almost proportional to q^{-1}, which clearly indicates the presence of cylindrical aggregates. The scattering curve can quantitatively be described by the product (full line) of the form factor model (dashed line) of a cylinder with polydisperse cross section and the structure factor for charged aggregates (dash-dotted line). However, it has to be mentioned, that the structure factor explicitly assumes spherical particle. In case of nonspherical particles an equivalent spherical radius must be determined. There are several studies in the literature, that apply this structure factor to describe the scattering of elongated aggregates such as prolate spheroids and cylinders [137, 173, 174]. Following *Galantini* and co-workers [174], who base on the equivalence between the second virial coefficients of cylindrical and spherical particles [175], an effective radius for a cylinder with cross section d and length L can be expressed as

$$R_{eff} = \frac{1}{4}\left\{3d^2L\left[\frac{L}{d} + \frac{1}{2}(3+\pi) + \frac{\pi d}{4L}\right]\right\}^{1/3}. \tag{4.1}$$

In the scattering pattern Figure 4.3-6b the length L of the cylindrical micelles manifests itself in the onset of the q^{-1}-like decrease of the scattering intensity at small q-values. However, the

determination of L is ambiguous, since in the same q-region the scattering intensity is suppressed due to the electrostatic interactions between the aggregates. Thus, the scattering of longer cylinders would be counterbalanced by a stronger electrostatic interaction and vice versa, which makes the unambiguous determination of the length L and the interaction parameters R_{eff}, z and c_{salt} impossible.

The analysis of the scattering curve using the discussed form- and structure factor yielded a mean radius for the cylinder cross section $R_{0,cyl} = 19.5$ Å with a polydispersity $\sigma_{cyl} = 5.3$ Å, a cylinder length $L = 350$ Å and an effective radius $R_{eff} = 75$ Å. Using equation (4.1), an equivalent radius of $R_{eff} = 67$ Å is obtained. The obtained value for the radius and the length of the aggregates, respectively, differs only slightly from the value obtained for the pure binary system $D_2O – C_{12}E_6$ at $T = 48.0$, $L = 360$ Å (refer to Figure 4.3-5c). This supports the picture that the small fraction of Basantol® Yellow 215, that is incorporated into the aggregates induces indeed electrostatic repulsion between the aggregates, but has only a small influence on their size and shape.

For the number of charges per aggregate we obtained $z = 62$ while we simply set the value for the salt concentration in accordance with the measurement at $T = 21.3$ °C to $c_{salt} = 10^{-9}$ mol/L. The increased number of charges at $T = 48.0$ °C, compared to $T = 21.3$ °C ($z = 11$, Figure 4.3-6a) can be explained with the increased length of the aggregates. This means that on average more molecules are incorporated into a single aggregate. Although the cross section radius of the cylinder is somewhat smaller than that of the sphere, it seems to be still large enough to host the Basantol® Yellow 215 molecules. It might thereby be possible, that the smaller cross section radius of the cylindrical aggregates leads to a preferred incorporation of dye molecules in the end-caps of the cylinders.

Figure 4.3-6c shows the scattering curve of the system $D_2O/SDS – C_{12}E_6$ (circles) at $\phi_C = 0.0025$ and $T = 48.0$ °C. As can be seen, the scattering intensity $I(q)$ of this system can also quantitatively be described as a product (full line) of the structure factor for charged particles [152, 153] (dash-dotted line) and the form factor $P(q)$ for cylindrical micelles (dashed line). Comparing the parameters obtained from the analysis of the SDS scattering curves with those containing BY215, it can be seen that the length L, the mean radius R_0 as well as the effective radius R_{eff} and the polydispersity σ of the cylindrical aggregates containing SDS are in general a few percent (3 %, 1 %, 4 % and 5 %, respectively) smaller than those of the system containing

the ionic dye. In the case of the number of charges per aggregate, z exactly the same value $z = 62$ is found for both systems. Thus, taking into account the uncertainties due to the absolute calibration and sample composition, the parameters obtained for both charged systems at $T = 48.0\,°C$ and $\phi_C = 0.0025$ are in good agreement. This result is remarkable, since SDS is a single-charged ionic surfactant, whereas BY215 carries three charges. It strongly indicates that Basantol® Yellow 215 is not fully dissociated. Furthermore, the charges might be delocalized within the dye molecule, whose exact structure we do not know. In this case it might be possible that this *smearing* leads to an additional screening of the electrostatic repulsion. On the contrary, in the monovalent SDS molecule the negative charge is located in the head group of the surfactant and therefore directly exposed to the micellar interface. Both described effects might explain the rather similar strength of interaction between the micelles containing BY215 compared to those containing SDS.

So far, it was shown that Basantol® Yellow 215 has a significant influence on the scattering intensity of the system water – $C_{12}E_6$ at $\phi_C = 0.0025$. Now the influence of the dye at larger $C_{12}E_6$ volume frations will be examined. Please keep in mind, that the concentration of BY215 in water ($c_{BY} = 1.5 \times 10^{-4}$ mol/L) remains constant. Accordingly, the molar ratio of dye to $C_{12}E_6$, n_{BY215}/n_{C12E6} decreases with increasing volume fraction ϕ_C of $C_{12}E_6$. Thus we expect that, in accordance with the result from the phase behavior studies, the effect of the dye on the scattering curves will be less pronounced at higher values of ϕ_C.

Figure 4.3-7 shows the SANS curves of the three systems $D_2O – C_{12}E_6$ (blue circles), $D_2O – C_{12}E_6/BY215$ (red triangles) and $D_2O – C_{12}E_6/SDS$ (green diamonds) at $\phi_C = 0.0051$ and different temperatures. The constant concentration of BY215 (or SDS, respectively) in water c_{BY} (or c_{SDS}) $= 1.5 \times 10^{-4}$ mol/L leads to a molar ratio of n_{BY215}/n_{C12E6} (or n_{SDS}/n_{C12E6}) $= 0.014$.
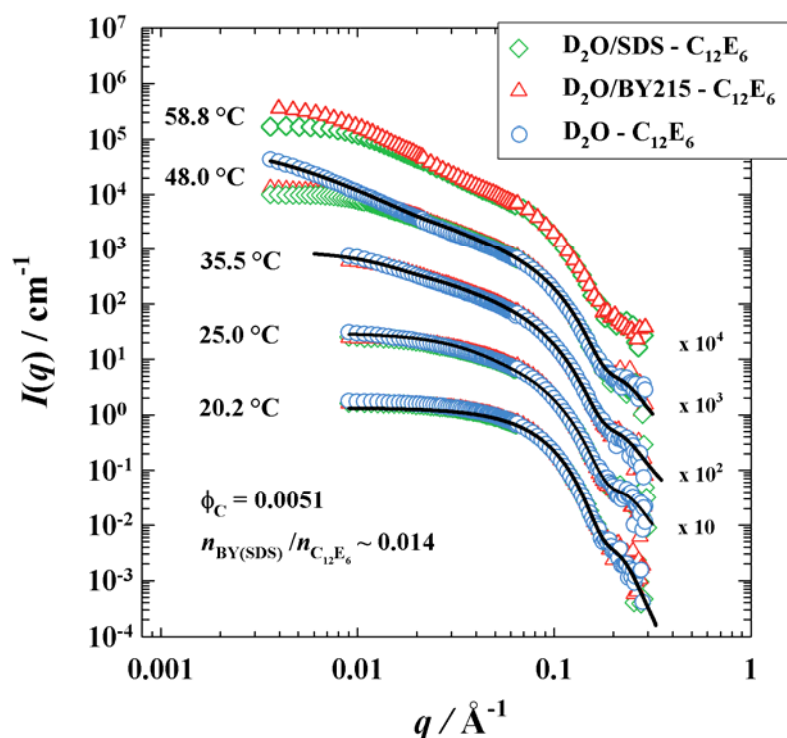
Figure 4.3-7: SANS curves of the three systems $D_2O – C_{12}E_6$ (circles), $D_2O – C_{12}E_6$/BY215 (triangles) and $D_2O –$ $C_{12}E_6$/SDS (diamonds) at $\phi_C = 0.0051$ and different temperatures. The lines represent fits of appropriate scattering models to the experimental scattering intensity. See text for details. The values of the free parameters are given in Table 8-2.

As can be seen, at $\phi_C = 0.0051$ up to $T = 35.5\ °C$ no significant difference between the scattering intensities of the pure binary and the charged systems is found in the measured q-range. (Note that no measurements were performed at small q-values for these temperatures.) This is a significant difference to the scattering of the respective samples at $\phi_C = 0.0025$ (refer to Figure 4.3-4) around $0.01 < q < 0.02\ Å^{-1}$ who showed a significantly decreased scattering intensity in this q-region already at $T = 32.5\ °C$. This confirms our assumption, that, as a result of the decreasing molar ratio of dye to $C_{12}E_6$, n_{BY215}/n_{C12E6} with increasing volume fraction ϕ_C of $C_{12}E_6$, the influence of the dye on the scattering pattern becomes smaller.

At $T = 48.0\ °C$ the scattering intensity of the pure binary system shows a significant increase, that was also found for the sample at $\phi_C = 0.0025$ (refer to Figure 4.3-5) and was ascribed to critical scattering. The two charged systems in contrast show now a significantly smaller forward scattering, which is qualitatively the same result as for $\phi_C = 0.0025$ at $T = 48.0\ °C$ (refer to Figure 4.3-4). Increasing the temperature to $T = 58.8\ °C$ a significant difference is observed between the scattering intensities of both charged systems at low q-values, which was also found

at $\phi_C = 0.0025$ and increased temperature ($T = 65.5\,°C$). Thus, it is found that the temperature-dependent evolution of the scattering pattern for the three systems is qualitatively similar to the trend, that was observed for the samples at $\phi_C = 0.0025$ in Figure 4.3-4, however it can furthermore be observed, that the deviation of the scattering in the low q-region between the two charged systems and the pure binary system is larger for $\phi_C = 0.0025$. As was pointed out above, this result confirms our assumption of a decreasing influence of the charged dye with increasing volume fraction ϕ_C of $C_{12}E_6$.

The lines in Figure 4.3-7 represent the modelled scattering intensities obtained from different scattering models, as will be described in the following: At $T = 20.2\,°C$, the form factor of polydisperse spheres with diffuse interface was applied. It can be seen that, again in qualitative agreement with the sample at $\phi_C = 0.0025$, slight deviation occur at low q-values. The obtained values for the mean radius and the polydispersity are $R_0 = 22.9\,\text{Å}$ and $\sigma = 4.5\,\text{Å}$, respectively. Those values deviate not more the maximal 4.6 % from the values at $\phi_C = 0.0025$ and 21.3 °C [$R_0 = 24.0\,\text{Å}$ and $\sigma = 5.0\,\text{Å}$ (refer to Figure 4.3-5a)], which indicates, that the size of the micelles, at least at low temperatures and surfactant fractions ϕ_C is rather independent on ϕ_C. The scattering curve at $T = 25.0\,°C$ was described by the scattering of a cylinder form factor. Thereby it can be observed that the fit in the intermediate q-range is fairly poor. This indicates that the aggregates, although being already significantly elongated, do not yet show reveal the scattering of cylinders with $L \gg R_0$ being assumed in the scattering model we used (refer to section 2.5.4.3). Increasing the temperature up to $T = 35.5\,°C$ the scattering curve is quantitatively described by this model. Accordingly, the length of the aggregates increases with increasing temperature from $L = 130\,\text{Å}$ at $T = 25.0\,°C$ to $L = 364\,\text{Å}$ at $T = 35.5\,°C$, respectively. The cross section radius R_0 remains rather constant, being $R_0 = 19.0\,\text{Å}$ and $19.6\,\text{Å}$ for 25.0 °C and 35.5 °C, respectively, which is in very good agreement with the values at $\phi_C = 0.0025$ ($19.4\,\text{Å} \leq R_0 \leq 20.0\,\text{Å}$). This indicates that at increased temperatures the cross section of the cylindrical aggregates is not significantly dependent on ϕ_C, which is the same result, that was found for the radius of the spheres at lower temperatures. At $T = 48\,°C$, the product of the cylinder form factor, and the structure factor for critical scattering describes the experimental scatetring intensity almost perfect, with the parameters $L = 365\,\text{Å}$, $R_0 = 19.2\,\text{Å}$, $\xi_{OZ} = 265\,\text{Å}$ and $I_0 = 7.4$. Comparing the length L to the value at 35.5 °C ($L = 364\,\text{Å}$) indicates that the length of the cylinders does not increase significantly any more from $T = 32.5\,°C$ to 48.0 °C. This observation is however ambiguous, since the superposition of scattering intensity due to critical scattering at low q-values on the scattering of the cylinders in the same q-region prohibits the

exact determination of L. The value of the cross section radius is again in the same range as for the lower temperatures. For the charged system, we did not apply a model description at higher temperatures ($T = 48.0$ and 58.8 °C, respectively), since the modeling of the critical scattering effects and electrostatic repulsion in the low q-region is too ambiguous, as was pointed out in the qualitative discussion of the samples at $\phi_C = 0.0025$ (Figure 4.3-6).

Figure 4.3-8 shows the scattering curves of the two systems $D_2O – C_{12}E_6$ (blue circles) and $D_2O – C_{12}E_6$/BY215 (red triangles) at $\phi_C = 0.0076$ and different temperatures. (Note, that the system $D_2O – C_{12}E_6$/SDS has not been investigated at this concentration.) From the constant concentration of BY215 in water ($c_{BY} = 1.5 \times 10^{-4}$ mol/L) results a molar ratio of $n_{BY215}/n_{C12E6} \approx 0.0091$ for this sample.
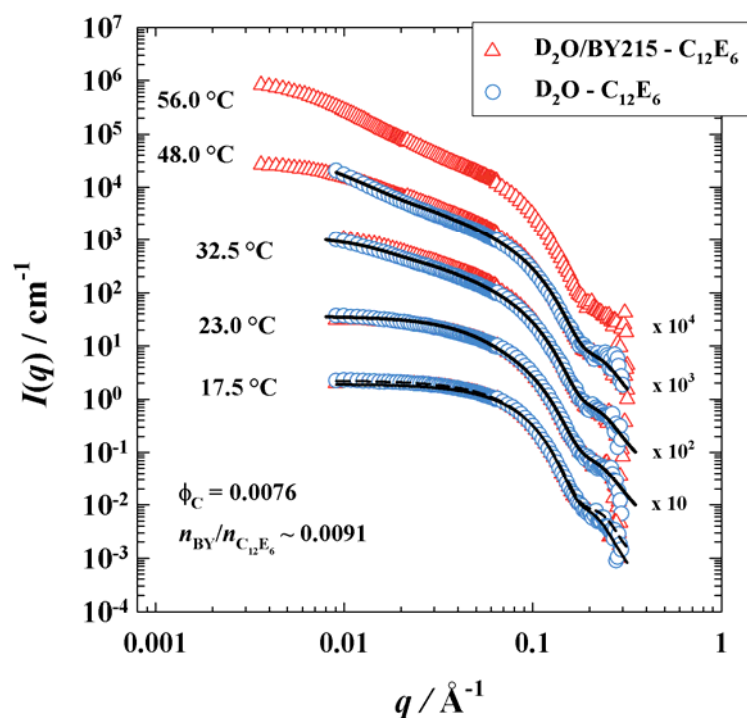
Figure 4.3-8: SANS curves of the two systems $D_2O – C_{12}E_6$ (circles), $D_2O – C_{12}E_6$/BY215 (triangles) at $\phi_C = 0.0076$ and different temperatures. The lines represent fits of appropriate scattering models to the experimental scattering intensity. See text for details. The values of the free parameters are given in Table 8-2.

It can be observed, that up to $T = 32.5$ °C almost the same scattering pattern in the intermediate q-range is observed for $D_2O – C_{12}E_6$ and $D_2O – C_{12}E_6$/BY215, which is in agreement with the further reduced ratio of dye molecules to $C_{12}E_6$. At $T = 48.0$ °C in the scattering curve of the system $D_2O – C_{12}E_6$ the onset of critical scattering at $q \approx 0.01$ Å^{-1} can be seen, in similarity with

the observations at $\phi_C = 0.0025$ and $\phi_C = 0.0051$, respectively. As the surfactant fraction is roughly by factor 3 closer to the critical composition ($\phi_C \approx 0.021$) than for $\phi_C = 0.0025$ the effect of critical scattering should be more pronounced for the sample at $\phi_C = 0.0076$. A further analysis of this point is however not possible since we did not record the scattering data at small q-values for the binary system at $T = 48$ °C and $\phi_C = 0.0076$. Nevertheless, the scattering curve of the system $D_2O/BY215 – C_{12}E_6$ does in contrast not exhibit a significant increase of the forward scattering intensity, which indicates, that the influence of the dye is still observed at $T = 48.0$ °C and $\phi_C = 0.0076$, i.e. a ratio of dye molecules to $C_{12}E_6$ of $n_{BY215}/n_{C12E6} \approx 0.0091$. However, comparing the scattering curves of the system $D_2O/BY215 – C_{12}E_6$ at further increased temperatures, i.e. at $T = 48.0$ and 56.0 °C respectively, with the forward scattering intensity of this system at $\phi_C = 0.0051$ and $T \geq 48.0$ °C (Figure 4.3-7), it can be observed, that the influence of the charged dye, seen at low q-values, is smaller. This will be discussed in more detail later.

The full line at $T = 17.5$ °C, represents the scattering of a form factor of polydisperse spheres with diffuse interface. Using this model yielded values for the mean radius R_0 and the polydispersity σ of $R_0 = 23.2$ Å, and $\sigma = 4.8$ Å, respectively, which is again in the same range as the values at $\phi_C = 0.0025$ and $\phi_C = 0.0051$, respectively, at low temperatures. However, for $\phi_C = 0.0076$ a slight increase of the scattering intensity is found at low q-values, indicating a slight elongation of the aggregates already at $T = 17.5$ °C. Exemplarily for this curve we applied the well known form factor model for polydisperse prolate ellipsoids to describe the scattering curve (dashed line in Figure 4.3-8). (The details of the model can be found in references [138]. It can be seen, that this model describes the scattering intensity at low q-values slightly better, than the sphere model. The parameters are the minor radius $R_0 = 24.5$ °C, the axis ratio $\nu = 1.7$ and the polydispersity $\sigma = 2.9$ Å. The value of the minor radius differs only 5 % from the mean radius that was obtained from the sphere model ($R_0 = 23.2$ Å), which cofirmes, that the aggregates are indeed only slightly elongated, and exhibit not yet a real cylindrical structure at this temperature.

For $T = 23.0$ °C, and 32.5 °C, respectively, the full lines in Figure 4.3-8 represent the scattering intensity of the form factor for cylindrical aggregates. It can be observed, that the fit of this model at $T = 23.0$ °C is rather poor, which has already been observed for the curve at $\phi_C = 0.0051$ and $T = 25.0$ °C shown in Figure 4.3-7. At $T = 32.5$ °C the scattering curves are described quantitativley by the form factor of cylindrical aggregates, while at further increased temperature, i.e. $T = 48.0$ °C a combination of the cylinder form factor and the structure factor

for critical scattering is applied. The values of the model parameters for the curves at $\phi_C = 0.0051$ and $T = 23.0$, 32.5 and 48.0 °C, respectively, are in good agreement with the values at smaller $C_{12}E_6$ volume fractions and are compiled in Table 8-2.

The scattering curve of the system $D_2O/BY215 – C_{12}E_6$ at $\phi_C = 0.0076$ and $T = 48.0$ °C shows a small increase a low q-values. This is remarkable, since for $\phi_C = 0.0025$ and 0.0051, respectively a small decrease of the forward scattering intensity was found. This supports again the assumption, that the influence of the dye gets smaller with increasing $C_{12}E_6$ fration. Accordingly, the increase of the curve for this sample at $T = 56.0$ °C at low q-values is even more significant.

Raising the $C_{12}E_6$ fraction to $\phi_C = 0.102$, i.e. further lowering the ratio $n_{BY215}/n_{C12E6} \approx 6.8 \times 10^{-4}$, it is visible from Figure 4.3-9 that at this $C_{12}E_6$ fraction no influence of the ionic dye is observed. Obviously this molar ratio of BY215 to $C_{12}E_6$ is too small to lead to an observable influence on the scattering intensity. From the phase behavior studies (Figure 4.3-3) it could be observed that also the phase boundaries of the systems $D_2O – C_{12}E_6$ and $D_2O/BY215 – C_{12}E_6$ coincide at this $C_{12}E_6$ fraction, $\gamma \approx 0.1$. However, at this $C_{12}E_6$ fraction the second mode in the TDFRS measurements was still observed [29] as it is indicated by the red circles in Figure 4.3-3. Obviously, the thermal diffusion behavior, that shows a second mode in the TDFRS measurement is, at least at this small ratio of BY215 to $C_{12}E_6$, more sensitive to the influence of the dye compared to its influence on the scattering pattern of the SANS measurements.
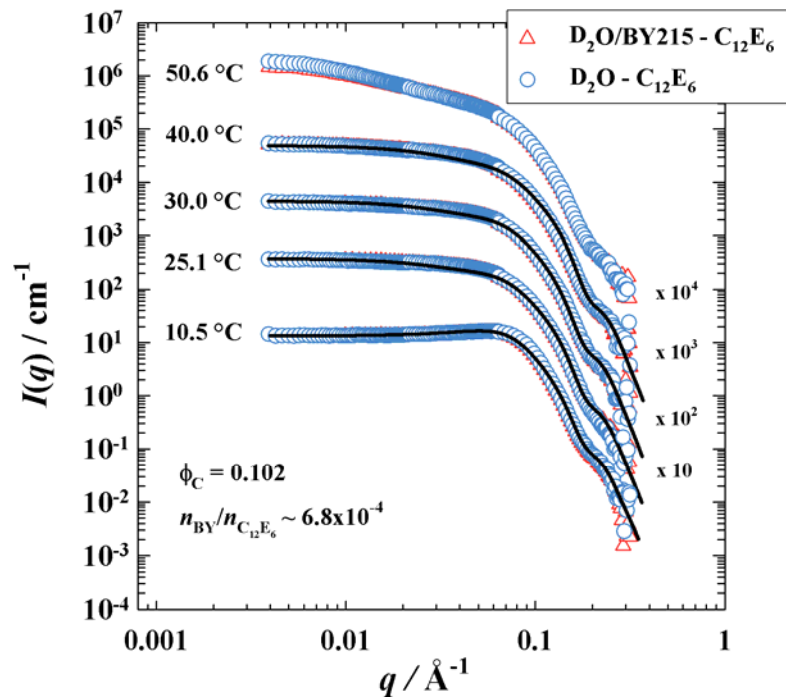
Figure 4.3-9: SANS curves of the two systems $D_2O - C_{12}E_6$ (circles), $D_2O - C_{12}E_6$/BY215 (triangles) at $\phi_C = 0.102$ and different temperatures. The lines represent fits of appropriate scattering models to the experimental scattering intensity. See text for details. The values of the free parameters are given in Table 8-2.

It is furthermore visible, that in contrast to the scattering curves at lower concentrations up to $T = 40.0\,°C$ no increase of the scattering intensity with decreasing q-values is found. This indicates the absence of any cylindrical aggregates at $\phi_C = 0.102$. Thus, the sphere-model was applied as form factor to model the scattering intensities at this increased $C_{12}E_6$ fraction. Additionally, due to the increased surfactant concentration interactions between the aggregates are expected. To account for those interactions, at first, we applied the structure factor for monodisperse hard spheres [equation (2.62)] [149]. At $T = 10.5\,°C$ this model in combination with the model for polydisperse spheres with diffuse interface could almost perfectly reproduce the experimental scattering intensity (full line). However, at increased temperatures this model failed, because it yielded a significantly lower forward scattering intensities (not shown) than the experimentally obtained curves. Thus, it was assumed, that a better description of the scattering intensity could be obtained by using a model that accounts also for attractive interactions between the aggregates. The structure factor for hard spheres with surface adhesion [sticky hard spheres (section 2.5.4.6)], describes the micelles consisting of a hard core and an attractive square well potential [150, 151]. This model has been used in several works to describe scattering curves of non-ionic micelles [99, 176, 177] as well as microemulsion droplets [143,

178]. Alternatively the attractive interaction can be included by describing the effective structure factor as the sum of the hard sphere (HS) and the *Ornstein-Zernike* (OZ) structure factor [179]:

$$S(q) = S_{HS} + \frac{I_0}{1 + q^2 \xi^2} \, . \tag{4.2}$$

Thereby, S_{HS} in equation (4.2) represents the hard sphere structure factor according to equation (2.62). The best fit (full lines) to the scattering curves at $\phi_C = 0.102$ and $T = 25.1, 30.0$ and $40.0\,°C$, respectively was obtained by the product of the latter model as structure factor and form factor of a polydisperse sphere. Setting $\xi = R_0 + t$, being obtained from the form factor model leaves the effective hard sphere diameter d_{HS} and I_0 as structure factor parameters. The latter quantity can thereby be regarded as a measure for the strength of the attractive interaction. As can be seen in Figure 4.3-9 this approach yields a fairly good description of the scattering curves at $\phi_C = 0.102$ up to $T = 40.0\,°C$. Thereby the mean radius of the spherical micelles at $\phi_C = 0.102$, is almost constant at $R_0 = 22 \pm 0.5\,\text{Å}$ over the whole temperature range (all values are given in Table 8-2). From those observations, it can be deduced that obviously no significant elongation of the micelles with increasing temperature is observed at this concentration. The *interaction parameter* I_0 in the structure factor model increases from $I_0 = 1.2$ at $T = 25.1\,°C$, over $I_0 = 1.4$ at $30.0\,°C$ to $I_0 = 2.1$ at $40.0\,°C$, respectively. This shows that the interaction is pure repulsive at $T = 10.5\,°C$ but consists also of an attractive contribution already at a temperature $T = 25.1\,°C$ which is relatively far from the cloud point temperature at this $C_{12}E_6$ fraction ($\Delta T \approx 29\,K$; refer to Figure 4.3-3). The effective hard sphere diameter d_{HS} slightly increases from $d_{HS} = 78.0\,\text{Å}$ at $10.4\,°C$ to $84.0\,\text{Å}$ at $25.1\,°C$ but is not further increased up to $40.0\,°C$, confirming the observation that the spherical micelles do not significantly change their shape and size with increasing temperature. According to those results the transition from globular micelles to larger aggregates in the phase diagram of $H_2O - C_{12}E_6$ in reference ([91] refer to Figure 4.3-1) might be interpreted as a transition from spherical to cylindrical micelles at low $C_{12}E_6$ fractions and as a transition from non-interacting to interacting aggregates at larger $C_{12}E_6$ fractions.

Increasing the temperature for the samples at $\phi_C = 0.102$ to $T = 50.6\,°C$, an increase of the scattering intensity with decreasing scattering vector q is observed. However, it was not possible, to describe this scattering curve with the models that were previously applied. From the calculations of *Zilman et al.* [93] in this region of the phase diagram of the system $H_2O - C_{12}E_6$

the existence of cylindrical netwerks can be assumed (refer to Figure 2 in this reference), which also exhibit itselfs in an increase of the scattering intensity with decreasing q in the intermediate q-region. Accordingly the describtion of the scattering curve at $\phi_C = 0.102$ and $T = 50.6$ °c might be achieved by using the form factor for self-assembled networks, that was derived by *Foster et al.* [165]. This issue was however not the objection of this work but might be a good starting point for further investigation in order to test this model on a binary surfactant system.

In the next step the evolution of the scattering intensity of the system $D_2O/BY215 – C_{12}E_6$ as function of the $C_{12}E_6$ volume fraction ϕ_C should qualitatively be examined at a fixed temperature. Therefore in Figure 4.3-10 the scattering curves of the system $D_2O/BY215 – C_{12}E_6$ $\phi = 0.0025$ (circles), 0.0051 (rectangles) and 0.0076 (diamonds), respectively, are shown at $T = 48.0$ °C.
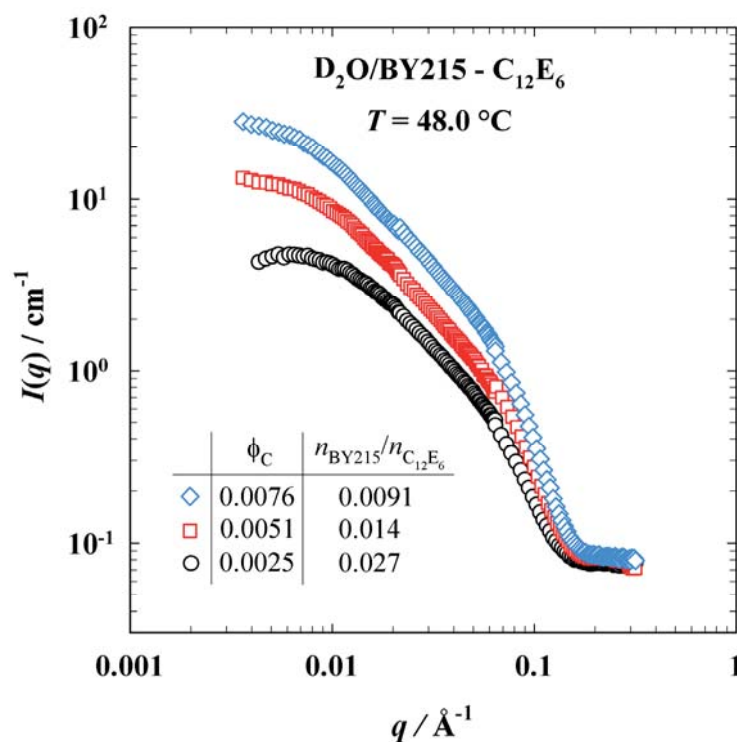
Figure 4.3-10: SANS curves of the system $D_2O/BY215 – C_{12}E_6$ at $T = 48.0$ °C, with $\phi_C = 0.0025$ (circles), $\phi_C = 0.0051$ (rectangles) and $\phi_C = 0.0076$ (diamonds). The corresponding values of the molar ratio of BY215 to $C_{12}E_6$, n_{BY215}/n_{C12E6} are given in the inset. The scattering intensities $I(q)$ are shown before subtraction of the incoherent background scattering. It can be seen that $I(q)$ becomes significantly smaller with decreasing volume fraction of $C_{12}E_6$ and thus increasing ratio n_{BY215}/n_{C12E6}.

As can be seen, from $\phi_C = 0.0025$ over 0.0051 to 0.0076 the increase of the scattering intensity at intermediate q-values becomes more pronounced with increasing surfactant volume fraction.

This increase might be caused by two effects: At first the effect of critical scattering would result in an increased forward scattering intensity, which was previously discussed for the system $D_2O - C_{12}E_6$ (refer to Figure 4.3-5c). In the system $D_2O/BY215 - C_{12}E_6$ the ratio n_{BY215}/n_{C12E6} varies with the $C_{12}E_6$ volume fraction ϕ_C, which leads to a strongly asymmetric shape of the lower phase boundary of the miscibility gap as could be seen in Figure 4.3-3. From the minimum in the phase boundary (triangles in Figure 4.3-3) the critical composition can be estimated being in the region of $\gamma \approx 0.07$. Therefore the difference in temperature ΔT between the measurement point at $T = 48.0\,°C$ and the phase boundary significantly decreases with increasing $C_{12}E_6$ fraction from $\phi_C = 0.0025$ over 0.0051 to 0.0076. This would explain the increase of the scattering intensity at smaller q-values from $\phi_C = 0.0025$ (circles) over 0.0051 (squares) to 0.0076 (diamonds) seen in Figure 4.3-10. The second effect is the decrease of the number of charges z per aggregate, resulting from the decrease of the ratio n_{BY215}/n_{C12E6} with increasing $C_{12}E_6$ fraction ϕ_C. This would also explain the evolution of the *bend* of the scattering intensity at small q-values towards a smaller scattering that becomes less pronounced at higher ϕ_C.

4.4 Discussion and Conclusion

The phase behavior (Figure 4.3-2 and Figure 4.3-3) and SANS measurements (Figure 4.3-4 and Figure 4.3-6) performed in this work provide clear evidence that the ionic dye Basantol[®] Yellow 215 is incorporated into the surfactant aggregates. In the SANS measurements the influence of the ionic dye exhibits itself in a decreased intensity in the low q-region of the scattering curves due to electrostatic interaction between the aggregates. Thus a striking similarity of the scattering pattern of the SDS- and BY215- containing aqueous surfactant solutions was found. The scattering intensities at intermediate and large q-values can be described by the form factor of spherical micelles with a diffuse interface (2.45) at lower temperatures and the form factor of cylindrical aggregates (2.58) at higher temperatures. Thereby, apart from the interaction among the aggregates we could not observe a significant influence of Basantol[®] Yellow 215 or SDS on the shape or size of the micelles. Regardless of the system i.e. $H_2O - C_{12}E_6$, $H_2O/BY215 - C_{12}E_6$ or $H_2O/SDS - C_{12}E_6$, respectively, for spherical micelles the values of the mean radius R_0 were determined to be in the range $21.5\,Å \leq R_0 \leq 24.0\,Å$. For the cylindrical aggregates we found slightly smaller radii of the cross

section, being in the range $18.9\,\text{Å} \leq R_0 \leq 20.0\,\text{Å}$. The lengths of the cylinders varied with the temperature from $L = 130\,\text{Å}$ at $T \approx 25.0\,°\text{C}$ to $L \approx 365\,\text{Å}$ at $48.0\,°\text{C}$.

These results clearly indicate, that by the TDFRS measurements, which were performed with the classical setup by *Ning et al.* [160] (Figure 4.3-3) not the thermal diffusion of non-ionic micelles, but mixed micelles of $C_{12}E_6$ and Basantol® Yellow 215. was studied. Thereby, at 0.25 vol% $C_{12}E_6$ ($\phi_C = 0.0025$) the influence of the ionic dye is more pronounced and decreases in strength with increasing value of ϕ_C, in strong correlation with the ratio of dye molecules to $C_{12}E_6$, n_{BY215}/n_{C12E6}, which also decreases with increasing ϕ_C. Furthermore, it was found, that the influence of the dye on the scattering curves of $D_2O/BY215 – C_{12}E_6$ becomes more pronounced if the temperature is increased (refer to Figure 4.3-4 and Figure 4.3-6).

Thus, the second mode in the concentration part of the TDFRS signal that occurs at low values of the $C_{12}E_6$ fraction ϕ_C or higher temperatures can clearly be related to the influence of the dye on the phase behavior and microstructure, that increases with the number of dye molecules per aggregate. The number of aggregates n_{agg} is thereby given by

$$n_{agg} = \frac{V_C}{V_{agg}} = \frac{\phi_C V_{tot}}{V_{agg}}, \quad (4.3)$$

where V_{agg} is the volume of the aggregate at given temperature and volume fraction ϕ_C of $C_{12}E_6$, which can be calculated from the dimensions of the aggregates and V_{tot} is the total volume of the sample. Since we found, that the dye is mainly incorporated into the micelles, it might then also be reasonable to calculate the number of BY215 molecules per aggregate

$$N_{BY,agg} = \frac{n_{BY}}{n_{agg}} = \frac{V_{agg} c_{BY} N_A V_{tot}}{\phi_C V_{tot}} = \frac{V_{agg} c_{BY} N_A}{\phi_C}, \quad (4.4)$$

wherein N_A is the *Avogadro* number.

The value of $N_{BY,agg}$ increases with decreasing volume fraction ϕ_C of $C_{12}E_6$, under the assumption that (at least for low temperatures) at the same time the micelles exhibit a considerably constant volume V_{agg}. Please note, that we thereby assume the change of the concentration of the dye c_{BY}, being neglectable. Regarding the variation of the temperature, V_{agg} will increase with increasing

T, because we found, that the length of the cylindrical aggregates in general increases with *T*, while their cross section radius R_o remains almost constant. Therefore, according to (4.4) at constant volume fration ϕ_C of $C_{12}E_6$ the number of aggregates n_{agg} (4.3) would decrease as function of *T* and thus the number of dye molecules in one aggregate $N_{BY,agg}$ would increase.

As a test for this relation we calculate $N_{BY,agg}$ using equation (4.4) exemplarily for the system $H_2O/BY215 - C_{12}E_6$ at $\phi_C = 0.0025$ at $T = 21.3$ and 48.0 °C. Calculating V_{agg} with the structural parameters obtained from fitting the form factor models to the scattering curves of this sample (refer to Figure 4.3-6a and b, respectively), we obtain $N_{BY,agg} = 2$ for the spheres at 21.3 °C and $N_{BY,agg} = 15$ for the cylinders at 48.0 °C. From the number of charges per aggregate *z*, being obtained from the fit of the structure factor to the scattering curves of this sample, a number of dye molecules per aggregate n_{BY}/aggregate ≈ 3.7 at 21.3 °C and n_{BY}/aggregate ≈ 21 at 48.0 °C, respectively, has been estimated (refer to the discussion of Figure 4.3-6a and b). Thus, for both temperatures the values of $N_{BY,agg}$ and n_{BY}/aggregate are in the same order of magnitude, while the former is based on the dimension of the aggregates and the concentration of the dye whereas the latter is based on the structure factor of the scattering curves. Regarding the uncentaincies that were previously discussed in the context of the structure factor model and the uncertainty of the exact dye concentration this is a reasonable agreement between both approaches.

In Figure 4.4-1 the variation of $N_{BY,agg}$ as function of ϕ_C and *T* within the phase diagram of the pseudo-binary surfactant system $H_2O/BY215 - C_{12}E_6$ is schematically illustrated: At low temperatures and low $C_{12}E_6$ volume fractions ϕ_C, spherical micelles with incorporated dye molecules exist, while at higher values of ϕ_C the aggregates are rather *uncharged*. With increasing temperature, the aggregates become elongated and also more dye molecules are incorporated into one aggregate.
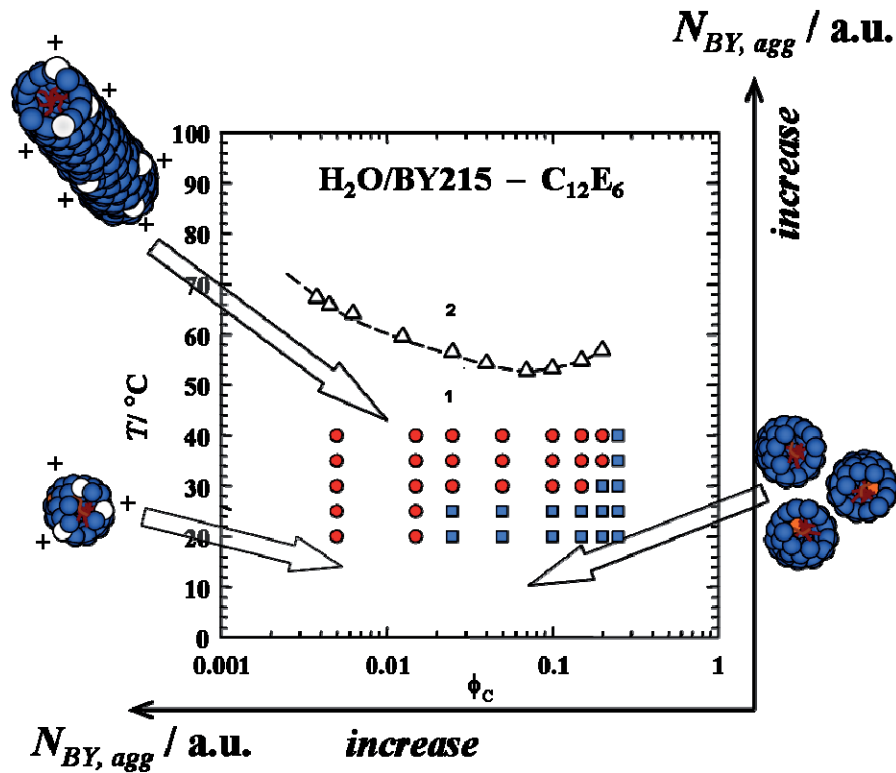
Figure 4.4-1: Illustration of the occurrence of the second mode (red circles) in the TDFRS signal within the phase diagram of the pseudo-binary system H_2O/BY215 – $C_{12}E_6$ as a result of a large number of dye molecules in one aggregate $N_{BY,agg}$ at high temperatures or low volume fraction ϕ_C of $C_{12}E_6$. The triangles represent the phase boundary of the system. The blue squares represent the TDFRS measurements, where the expected one-mode signal was found [28]. See text for details.

As can be seen, the occurence of the second mode in the classical TDFRS experiment (red circles) occurs at low values of ϕ_C for all measured temperatures, while at increased values of ϕ_C it occurs only upon increasing the temperature. At the highest investigated value of ϕ_C only one-mode signals did occur [28]. Thus, assuming, that the second mode occurs, when a certain *threshold* value of $N_{BY,agg}$ is exceeded our model describes the occurrence of the second mode within the $C_{12}E_6$ fraction and temperature range in the system H_2O/BY215 – $C_{12}E_6$ due to a large number of dye molecules in one aggregate $N_{BY,agg}$ fairly good.

As a conclusion, our investigation shows that especially in the case of complex fluids, the properties of the system might strongly be influenced by the addition of a light adsorbing dye in thermal diffusion experiments. Therefore, it is a good advice to avoid the addition of such an additive in optical experiments e.g. the TDFRS, thermal lens [43] or z-scan [180] whenever possible. This was also recently pointed out by *Rusconi et al.* [43], who therefore used an infrared laser in their thermal lens setup, that is absorbed by the water molecules and thus avoids the addition of a dye for aqueous solutions. For the TDFRS method for aqueous solutions this

problem has also recently been overcome by *Wiegand et al.* [159] developing a setup that utilizes an infrared laser (IR-TDFRS). Accordingly, all TDFRS measurements in aqueous surfactant systems and microemulsions, that are referred to in the following chapters of this work were performed with this IR-TDFRS setup.

5 Binary System H_2O – C_iG_j: *Soret* Effect at the Critical Micelle Concentration

5.1 Motivation and Objectives

This part of the work focuses on the thermal diffusion behavior non-ionic *n*-alkyl-(poly)glucoside surfactants, C_iG_j in water around the critical micelle concentration (cmc). Using the so called thermal lens method an abrupt change of the measurement signal around the cmc was observed by *Santos et al.* [57] studying the thermal diffusion behavior of potassium laurate in water. Unfortunately in their work, an evaluation of S_T was not possible due to the presence of a dye which complicated the analysis. Therefore, it remained unclear to which extend the cmc is also visible in the Soret coefficient. Motivated by those observations, our objective was to perform systematic studies on alkyl-glucoside surfactants (in the literature also referred to as sugar derived surfactants), since they exhibit a fairly high cmc. In particular the goal was to examine the *Soret* coefficient of the surfactants *n*-octyl β–D-glucopyranoside (C_8G_1), *n*-heptyl β-D-glucopyranoside (C_7G_1) and *n*-octyl β-glucomaltoside (C_8G_2) in water around their critical micelle concentrations (cmc) at different temperatures. Therefore, at first systematic surface tension measurements should be performed in order to determine the cmc for different temperatures using a well established common method. The thereby obtained cmc values, as well as the head group area of the surfactants under study should be compared with literature. On the basis of this data, the occurrence of the cmc in the *Soret* coefficient should be studied by means

of the thermal diffusion forced Rayleigh scattering. At first, S_T should be studied as function of the molar surfactant concentration c around the cmc at various temperatures. Thereby, according to the observation of *Santos et al.* [57] it should be validated, if the formation of micelles is exhibited in S_T as function of c. In a second approach, S_T should be studied as function of the temperature for a given surfactant concentration that equals the cmc in the temperature range under study. It should be evaluated, if the formation of the micelles at a certain temperature is visible from the trend of the *Soret* coefficient as function of temperature.

5.2 Experimental

The cmc was determined by surface tension measurements as function of the surfactant concentration c, using the widely known *Du Noüy* ring method [181]. We used a Krüss digital Tensiometer K10T. This tensiometer requires a correction of the experimentally obtained surface tension $\gamma^{s,\exp}$ in order to account for the mass and the dimension of the ring [182]. This correction is given by

$$\gamma^s = 1.07\gamma^{s,\exp}F, . \tag{5.1}$$

where γ^s is the true surface tension and F is the correction factor of the tensiometer, which is also a function of $\gamma^{s,\exp}$. For the device we used [182] F is given by

$$F = 0.725 + \sqrt{0.4036 \cdot 10^{-3} \frac{\gamma^{s,\exp}}{\rho^0_1 - \rho^0_2}\left(\frac{s}{\mathrm{cm}^3}\right) + 0.0128} . \tag{5.2}$$

With the macroscopic densities $\rho^0_1 - \rho^0_2$, representing the density of air and solution, respectively. In a good approximation, the difference of densities $\rho^0_1 - \rho^0_2$ is assumed to be the density of the solution. The sample temperature is controlled by a circulating water bath (Lauda RC 6) with an accuracy of $\pm$ 0.1 K.

For the concentration series, the surfactant solution of the highest concentration was prepared in a 50 ml graduated flask. From this solution 30 ml were transferred in the sample container of the tensiometer and the surface tension of the solution was measured at each required temperature. Thereby at each temperature the measurement was repeated, until a constant value of γ^s was obtained over three measurements within 90 minutes. The remaining surfactant solution in the flask was diluted to the next concentration, by simply refilling the flask up to the graduation

mark with pure water. Before measuring the next concentration, the sample container of the tensiometer was throroughly rinsed with pure water and rinsed with a small amount of the following measurement solution. The surface tension measurements of the more and more diluted solutions were repeated until a sufficiently low concentration below the cmc was reached. In order to avoid systematic errors in this procedure, seperately prepared solutions at various concentrations were measured additionally.

5.3 Results

In this section the results of the cmc measurements of the aqueous solutions of n-octyl β–D-glucopyranoside (C_8G_1), n-heptyl β-D-glucopyranoside (C_7G_1) and n-octyl β-glucomaltoside (C_8G_2) will be presented. The cmc was measured for each binary system at different temperatures with the objective to correlate those findings with the results of the thermal diffusion behavior measurements at the cmc, which were performed in *Jülich*, using the IR-TDFRS setup.

First the determination of the cmc by surface tension measurements will be exemplarily described for the system $H_2O – C_8G_1$. Thus, Figure 5.3-1 shows the surface tension γ^s of this system as function of the molar surfactant concentration c on a linear (a) and logarithmic (b) scale. Note that the surfactant concentration in this section is given as the molar concentration c, since the theoretical discussion in literature is usually presented using molar concentrations. Originating from the surface tension of pure water, (γ^s_0), γ^s decreases first steeply with c and exhibits a gradually smaller slope with further increasing surfactant (Figure 5.3-1a). At a certain concentration the surface tension curve exhibits a sharp bend and remains approximately constant at further increasing the surfactant concentration c. This bend occurs because the solution is saturated with monomerically dissolved surfactant molecules at this concentration. Further added surfactant molecules will self-aggregate to micellar structures. Hence the corresponding surfactant concentration is the critical micelle concentration (cmc). It can be seen in Figure 5.3-1a, that the surface tension γ^s is almost independent of c at concentrations larger than the cmc, which shows that the concentration of the micelles has only a small effect on the surface tension of the solution. From the semi-logarithmic plot of γ^s as function of c (Figure 5.3-1b) it is visible, that in the region of highest dilution (in Figure 5.3-1b below $c \approx 7 \times 10^{-4}$ mol/l), γ^s first decreases not in an exponential fashion with increasing c followed by an exponential decay over almost two orders of magnitude in the concentration range below the

cmc. This trend of γ^s as function of c is described quantitatively by the empirical *Langmuir-Szyszkowski* equation [183]

$$\gamma^s(c) = \gamma_0^s - a\ln(bc+1). \tag{5.3}$$

With the parameters a and b, accordingly, the cmc can be determined by two ways: (i) either graphically from the intersection between the fit of the data below the cmc to the *Langmuir-Szyszkowski* equation, or (ii) analytically by solving this equation for the mean value of γ^s at $c \geq$ cmc, using the previously obtained parameters *a* and *b* according to [equation(5.3)]. Comparing the cmc values obtained from both methods, we found deviations of less than 1 %. Hence, in the following, we will refer to the values that were determined analytically only.
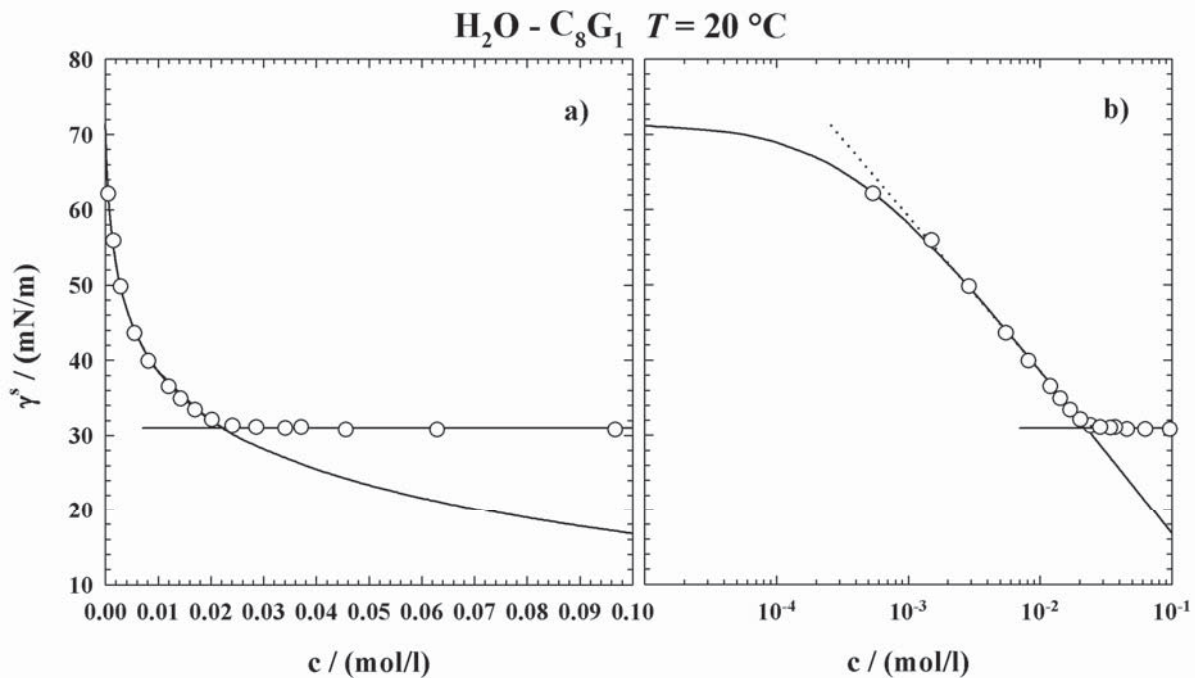
Figure 5.3-1: Surface tension γ^s as function of the surfactant concentration for the system $H_2O - C_8G_1$ at $T = 20$ °C. a): Linear concentration axis. b): Logarithmic concentration axis. The deviation from a logarithmic dependence (dotted line) of γ^s as function of c is observed for small values of c. The solid line below the cmc represents a fit to equation (5.3) with $\gamma_0^s = 71.2$ mN/m, which corresponds to the surface tension of pure water. The solid horizontal line represents the approximately constant value of σ at $c \geq$ cmc.

The logarithmic decay at concentrations below the cmc is furthermore described for sufficiently dilute solutions (i.e. assuming the solution is ideal and the activity coefficient of the surfactant approaches unity) at constant pressure and temperature by the *Gibbs* adsorption isotherme [10]

$$\left(\frac{\partial \gamma^s}{\partial \ln(c)}\right)_{p,T} = -\Gamma RT \ . \tag{5.4}$$

Γ is called the surface excess concentration (see e.g. [184]) and is defined by the molar number of surfactant molecules n_s per unit area A

$$\Gamma = \frac{n_s}{A} \ . \tag{5.5}$$

Using the *Avogardo* number A, Γ can be related to the head group area per surfactant molecule a_s by

$$a_s = \frac{1}{A\Gamma} \ . \tag{5.6}$$

Thus, plotting γ^s as function of $\ln(c)$ in the range where γ^s as function of c shows a logarithmic trend (straight dotted line in Figure 5.3-1b) enables to obtain the head group area of the surfactant molecules $a_{s.}$

For our measurements of C_7G_1 and C_8G_1, respectively, in water, the surface tension as function of the surfactant concentration resembled perfectly the pattern, described above (Figure 5.3-1a and b) for all measured temperatures (the curves are shown in the appendix, section 8.3, Figure 8.3-1 and Figure 8.3-2). However, as pictured in Figure 5.3-2a and b for the system $H_2O – C_8G_2$, the surface tension γ^s as function of c shows strong deviations from the expected trend: From both, the linear and the semi-logarithmic plot, it is visible that a sharp bend that is expected to follow the logarithmic decay at c = cmc is not observed. In contrast, at some concentrations, γ^s as function of c bends rather gradually and exhibits a distinct minimum first, before an almost constant value of γ^s is reached at further increased concentrations. Furthermore, as can be observed in Figure 5.3-2b, the values of γ^s at low concentrations are not quantitatively described by the *Langmuir-Szyszkowski* equation (5.3).
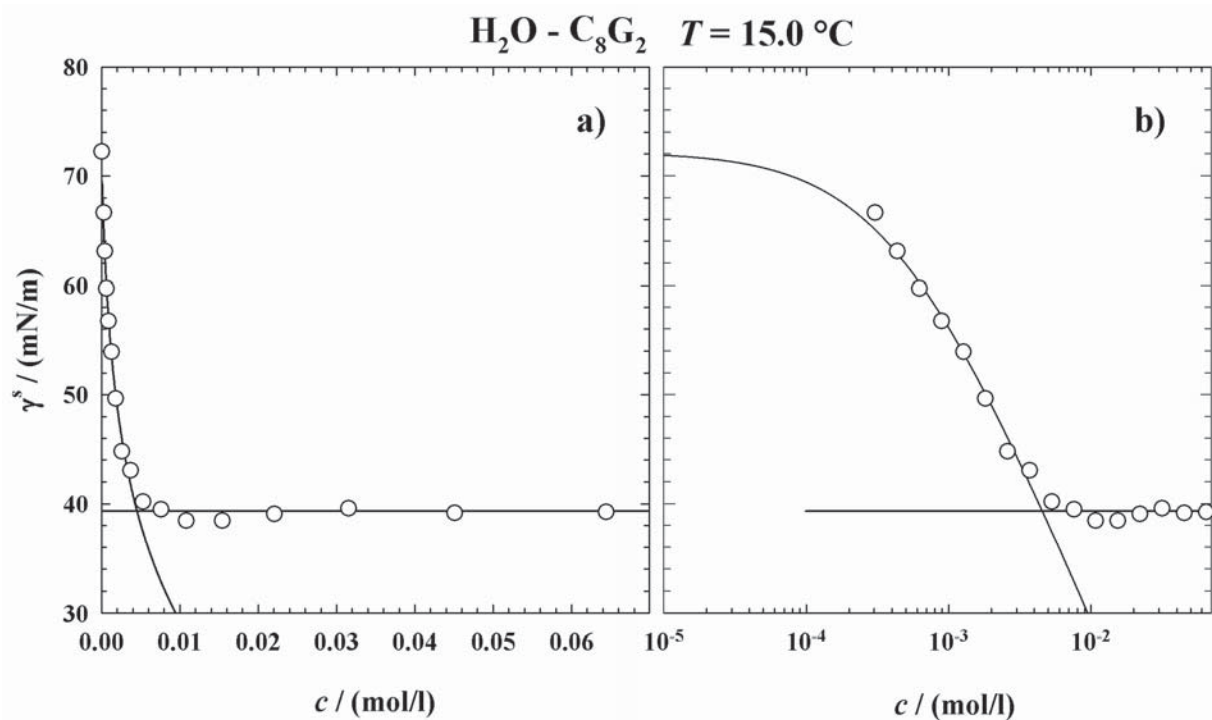
Figure 5.3-2: Surface tension γ^s as function of c for C_8G_2 in water at $T = 15$ °C. a): linear concentration axis. b): logarithmic concentration axis. A similar pattern for the curves was found for all investigated temperatures (refer to Figure 8.3-3, in the appendix 8.3). Note that the concentration scales differently from Figure 5.3-1. See text for details.

From the pattern of γ^s as function of c for C_8G_2 in water it can be deduced that (i) a mistake in the experimental handling did occur or (ii) the material contains impurities. Regarding the first point, it might be possible, that the equilibration times for the solutions were to short. However we repeated the measurement for a given temperature until γ^s was constant over three measurements with at least one hour of time difference. In order to further clarify this issue it is scheduled to repeat the measurements on $H_2O - C_8G_2$ using the material from another supplier.

Nevertheless, in the next step we want to evaluate the cmc values and to compare them with literature values. The values of the cmc and the fitting parameters a and b [see equation(5.3)] are listed in Table 8-3.

5.3.1.1   CMC Values

Figure 5.3-3 shows the determined cmc as function of the temperature for the three surfactants C_7G_1 (circles), C_8G_1 (squares), and C_8G_2 (triangle), respectively, dissolved in water.
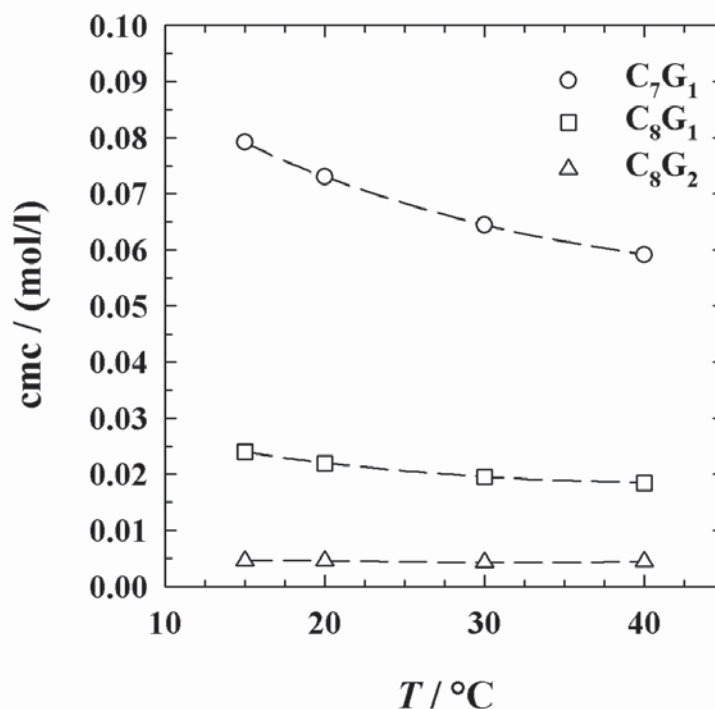
Figure 5.3-3: Critical micelle concentration (cmc) for C_7G_1 (circles), C_8G_1 (squares), and C_8G_2 (triangle), respectively, in water as function of temperature. See text for details.

The cmc of C_7G_1 (circles) decreases from 0.0792 mol/l at $T = 15\ °C$ to 0.0591 mol/l at 40 °C. For C_8G_1 (squares) the cmc lies at considerably smaller values, ranging from 0.024 mol/l at $T = 15\ °C$ to 0.0185 mol/l at 40 °C. This difference is a consequence of the longer alkyl chain of C_8G_1 compared to C_7G_1. According to reference [48] the cmc falls typically by a factor $2 – 3$ per additional CH_2 group in the alkyl chain implied by an decrese in hydrophilicity (oder so ähnlich). In the temperature range of our measurements, the difference between the cmc of C_7G_1 and of C_8G_1 in water corresponds to a factor of 3.3 (15 °C) to 3.2 (40 °C). Thus, the deviations of the cmc of C_7G_1 and C_8G_1 in water show a fairly good agreement with the literature. Regarding the absolute values of the cmc we find also a very good agreement with the literature data: For C_8G_1 in water values at $T = 25\ °C$ in the range from 0.020 – 0.023 mol/l are frequently observed [185-187]. For C_7G_1 a value of 0.072 mol/l is given in reference [187].

The determined cmc values of C_8G_2 are found in the range 0.0043 – 0.0046 mol/l. However, it is expected [188, 189] that for alkyl glucosides and alkyl maltosides the degree of head group polymerization has very little influence of the cmc. For example, comparing C_8G_1 and C_8G_2 in water at 25°C, *Boyd et al.* [188] found cmc values at 0.0182 mol/l and 0.0191 mol/l, respectively. Their findings coincide with the extrapolated cmc of 0.022 mol/l for C_8G_1 at respective tmeperature (open squares in Figure 5.3-3). However the determined cmc of C_8G_2 deviates by a

factor of 4.4 – 4.8 from both, the values of C_8G_1 from this work (0.020 – 0.023 mol/l) and the value for C_8G_2 given by *Boyd et al.* [188]. This confirms our assumption, that the values for C_8G_2 in water are not reliable, which was already illustrated in Figure 5.3-2.

Regarding the trend of the cmc as function of *T*, for C_7G_1 (circles) and C_8G_1 (squares) a significant decrease of the cmc with increasing temperature is visible from Figure 5.3-3. This trend is expected for non-ionic surfactants due to an increase of the hydrophobicity of the surfactant molecules, induced from the weakening of the hydrogen bonds with increasing temperature. Typically, at further increasing temperatures, the cmc of non-ionic surfactants passes through a minimum and increases again [91, 190, 191]. For C_8G_1 the trend of the cmc indicates that we can expect a minimum around $T \approx 42\,°C$ [192], which was also observed by *Aoudia* and *Zana* [190].

For non-ionic surfactants, the decrease of the cmc as function of *T* can be generally described by a logarithmic decay of the type [48, 193]

$$cmc \approx \exp(|x| / kT) \tag{5.7}$$

in the lower temperature range at negative slope. Thereby the quantity *x* relates to the difference of the chemical potential of a surfactant molecule when being transferred from the solution into the aggregate [48]. According to relation (5.7), a plot of ln(*cmc*) as function of $1/T$ yields a linear dependency. In Figure 5.3-4 those plots of ln(cmc) as function of $1/T$ are shown for the surfactants under study C_7G_1 (circles), C_8G_1 (squares) and C_8G_2 (triangles) in water, respectively.
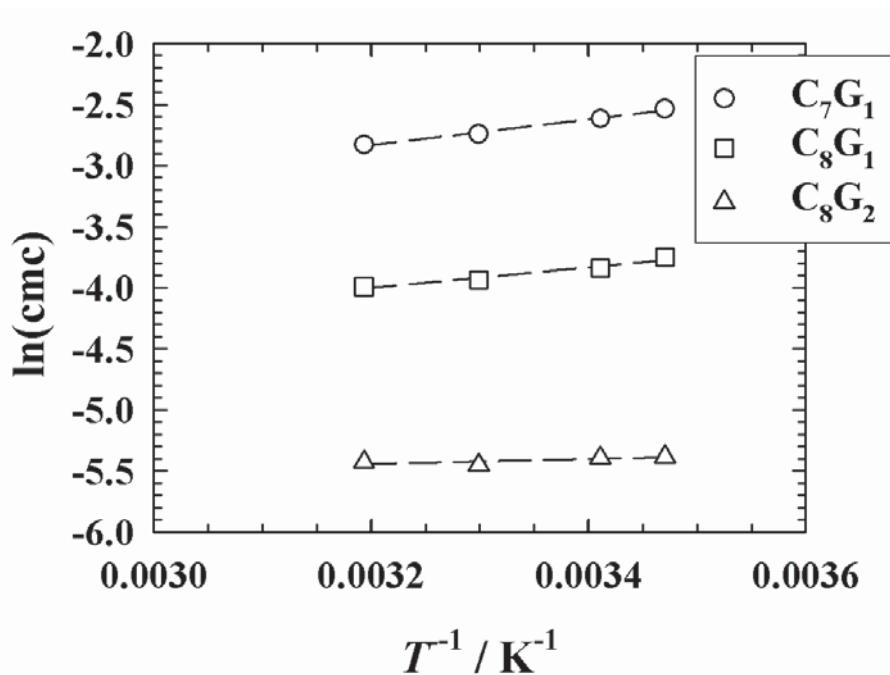
Figure 5.3-4: Logarithm of the cmc as function of $1/T$ according to relation (5.7) for the C_7G_1 (circles), C_8G_1 (squares) and C_8G_2 (triangles) in water, respectively.

For C_7G_1 (circles), an almost perfect linear trend can be observed, while for C_8G_1 (squares) slight deviations are visible. Those deviations might be explained by the vicinity of the minimum in the *cmc* vs. *T* curve for this system, that was mentioned above [190, 192]. The slope of the linear increase (dashed lines) for C_7G_1 in water is slightly larger ($|x|/k = 1053$), than for C_8G_1 ($|x|/k = 844$). According to this interpretation, a larger slope of ln(*cmc*) as function of $1/T$ would be expected for the surfactant with the larger alkyl chain. This discrepancy might be explained from the fact, that relation (5.7) does not take into account the occurrence of a minimum in the cmc vs. *T* curve, which was also pointed out be *Kim et al.* [193]. For C_8G_2 a slope of ln(*cmc*) as function of $1/T$ of ($|x|/k = 203$) was found. However, since the cmc values of our measurements of the latter system seems not to be reliable (cf. Figure 5.3-2) a further interpretation of the temperature dependence of the cmc for C_8G_2 is not provided at this point.

5.3.1.2 Surfactant Head Group Area

As described above, the head group area of the surfactant molecules, a_s, can be derived from the slope of the logarithmic decline of γ^s as function of c [equations (5.4)-(5.6)]. Accordingly, in Figure 5.3-5 the head group areas a_s of the surfactants C_7G_1 (circles), C_8G_1 (squares) and C_8G_2 (triangles) in water, respectively, are shown as function of the temperature. The values of a_s (Table 8-3) were calculated from the surface excess concentration Γ, which in turn was

determined from the slope of the logarithmic decay of σ as function of c in the region $c < $ cmc (refer to figure Figure 5.3-1b).
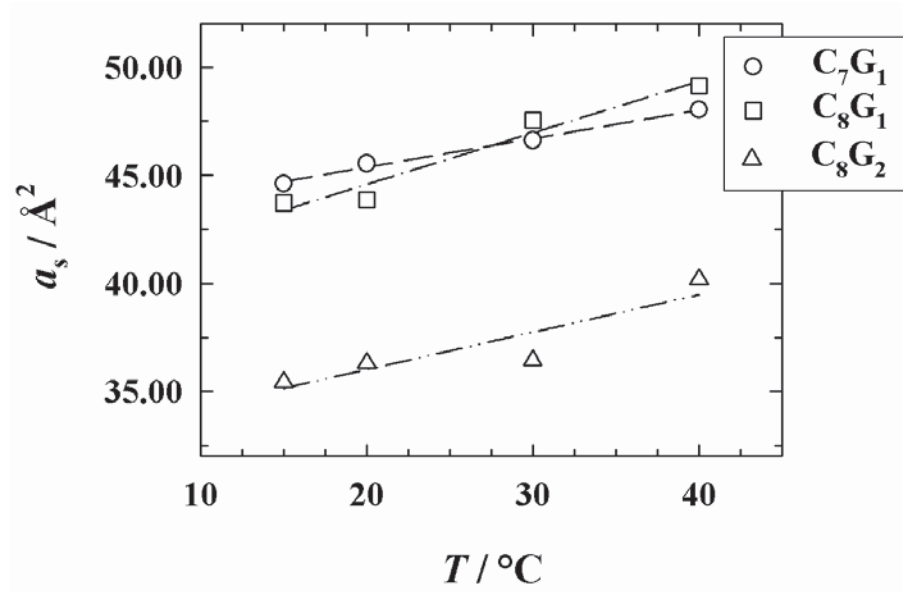
Figure 5.3-5: Temperature dependence of the head group area of the surfactants C_7G_1 (circles), C_8G_1 (squares) and C_8G_2 (triangles) in water, respectively. See tesxt for details. The lines represent linear fits for C_7G_1 (dashes), C_8G_1 (dash-dots) and C_8G_2 (dash-dot-dots).

For all three surfactants under study the head group area a_s shows an increase as function of the temperature. This might be explained by an increasing effective area within the amphiphilic film that is occupied by a surfactant molecule due to an increased thermal motion of the molecules at increased temperatures. Obviously, this effect then overbalances the loss of hydration water that is known to occur with increasing temperature. It can be seen from Figure 5.3-5 that for C_8G_1 (dash-dotted line) the increase of a_s with increasing T is slightly stronger than for C_7G_1. This could point to an influence of the longer alkyl chain of the former one, compared to C_7G_1 (dashed line and open squares). The absolute values of C_7G_1 and C_8G_1 are in the same range: For C_7G_1 the head group area increases from 44.6 Å^2 at 15 °C to 48.0 Å^2 at 40 °C. The head group area of C_8G_1 increases at the same time from $a_s = 43.7$ to 49.1 Å^2. The mean values are $a_s = 46.2$ Å^2 for C_7G_1, and 46.1 Å^2 for the C_8G_1, respectively. For C_8G_1 in water, at $T = 25$ °C *Boyd et al.* [188] found a value of $a_s = 42$ Å^2. *Matsumura et al.* [185] reported for C_8G_1 a value of $a_s = 48$ Å^2 at ambient temperature. Hence the values of our measurement for C_8G_1 are in very good agreement with this literature. Since the structure of the head group is the same for C_7G_1, it can be deduced, that the values we found for this surfactant are also reliable. Despite the much larger maltoside head group *Boyd et al.* [188] found for C_8G_2 within the range of the experimental error

the same value of the effective head group area as for C_8G_1. This was explained by the fact that the strongly hydrated head groups behave like *bulk water* [188] and therefore exhibits a similar effective head group area in the amphiphilic film. However, we find a significantly lower head group area for C_8G_2 (triangles in Figure 5.3-5). This indicates again, that our measurements are not reliable and need to be repeated.

To sum up: From our measurements of the surface tension as function of the surfactant concentration of C_7G_1 and C_8G_1 in water, respectively, we found a good agreement with literature values for the cmc, giving the trend of the cmc as function of the temperature, as well as the surfactant head group area. For C_8G_2 in water the measurements did not show the expected trend and the obtained values deviate significantly from literature. The surface tension vs. surfactant concentration of the latter system indicates either a systematic error in the experimental handling or the presence of impurities in the surfactant. Accordingly the investigation of the *Soret* coefficient around the cmc, by means of TDFRS measurements was performed on C_7G_1 and C_8G_1, only. Measurements of the surface tension and TDFRS measurement on a newly purchased batch of C_8G_2 will be performed soon.

5.4 Discussion and Conclusion

Now we want to relate the cmc values of C_7G_1 and C_8G_1, respectively, in water to the measurements of the *Soret* coefficient, which were performed by means of the TDFRS method. Thereby all measurements of S_T, that are referred to in the following, are performed using the infrared (IR) TDFRS method [159], in order to avoid the addition of any light absorbing dye.

First it should be examined, how the critical micelle concentration is reflected in the *Soret* coefficient as function of the surfactant concentration c. Figure 5.4-1a shows the *Soret* coefficient for C_8G_1 in water [192] as function of c for the temperatures, at which the cmc values were previously determined by surface tension measurements, $T = 15$ °C (squares), 20 °C (circles), 30 °C (diamonds) and 40 °C (triangles). We observe for high diluted solutions at $c \approx 0.024$ mol/l, that S_T seems to be independent of concentration and temperature (compare the oval in Figure 5.4-1a). Above $c \approx 0.024$ mol/l the curves of the different temperatures deviate:

For $T = 15$ °C and 20 °C the curves show a systematic decay, whereby S_T changes its sign from positive to negative. Such a sign change of S_T as function of the solution composition has

previously been observed by *Ning* and *Wiegand* [40] for mixtures of acetone/water and dimethylsulfoxide/water, respectively. There, the sign change was related to the breakdown of the hydrogen bond network of the solution. For $T = 30$ (squares) and 40 (triangles) °C S_T first increases with increasing surfactant concentration before it decreases again. A more detailed analysis [192] of this pattern is beyond the scope of this work. Nevertheless, for all temperatures, the change from a rather constant value of S_T as function of c to a systematic deviation of the curves occurs in the same range where the cmc is found, from 0.024 mol/l to 0.0185 mol/l (refer to Figure 5.3-3). Accordingly, this suggests, that the formation of the micelles, and thus the cmc, is reflected in this behavior. Figure 5.4-1b shows exemplarily the data for $T = 40$ °C (triangles) and 20 (circles) °C, respectively in closer detail. It is obvious, that for both temperatures the slope of the curves (full lines are guides to the eyes) show a distinct change at a concentration that corresponds to the respective value of the cmc (dotted lines), as it has been determined by surface tension measurements.
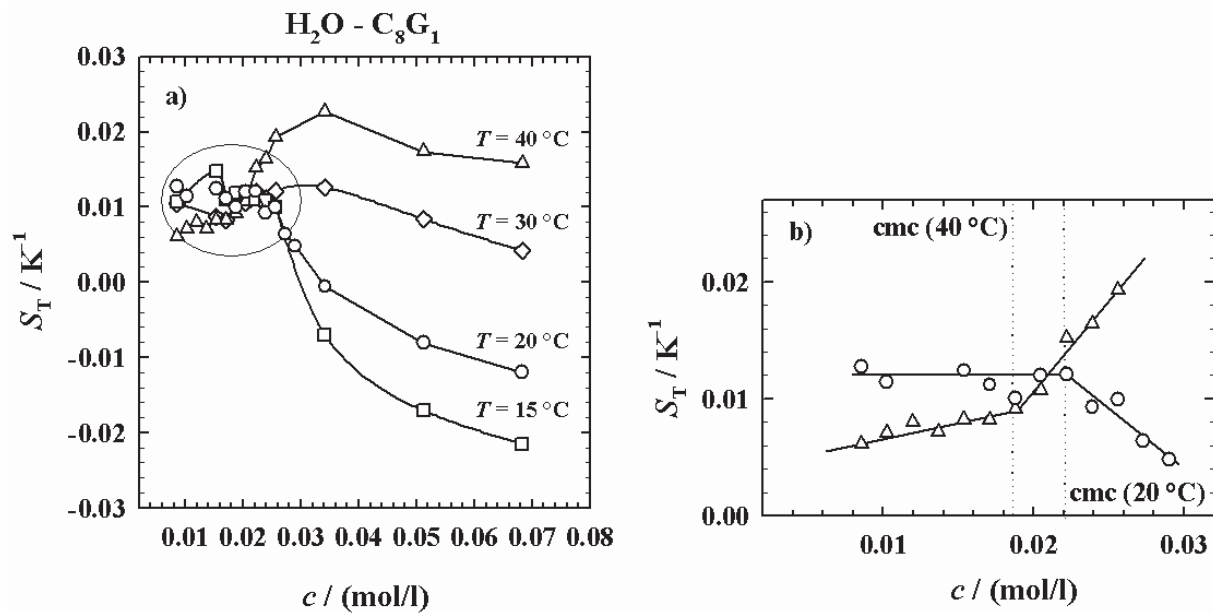
Figure 5.4-1: *Soret* coefficient S_T as function of the surfactant concentration c in the system $H_2O – C_8G_1$. a): $T = 40$ (triangles), 30 (diamonds), 20 (circles) and 15 (squares) °C. b): Detailed plot for $T = 40$ (triangles) and 20 (circles) °C. The full lines are guide to the eyes. The dotted lines mark the cmc at given temperature. Figure according to [192].

Thereby at 20 °C the slope is almost zero below the cmc and becomes negative, while at 40 °C a positive slope is found below the cmc, which then becomes even more pronounced. We suggest that the sudden bend of the S_T vs. c occurs due to the formation of micelles, which exhibit a significantly different diffusion behavior, than the single surfactant molecules. Thus for C_8G_1 in

water, the cmc is clearly reflected in the dependence of S_T on the surfactant concentration at given temperature. For C_7G_1 in water a qualitatively similar behavior was found: As indicated in Figure 5.4-2 by an oval, the Soret coefficient remains independent from concentration and temperature up to a certain surfactant concentration c.
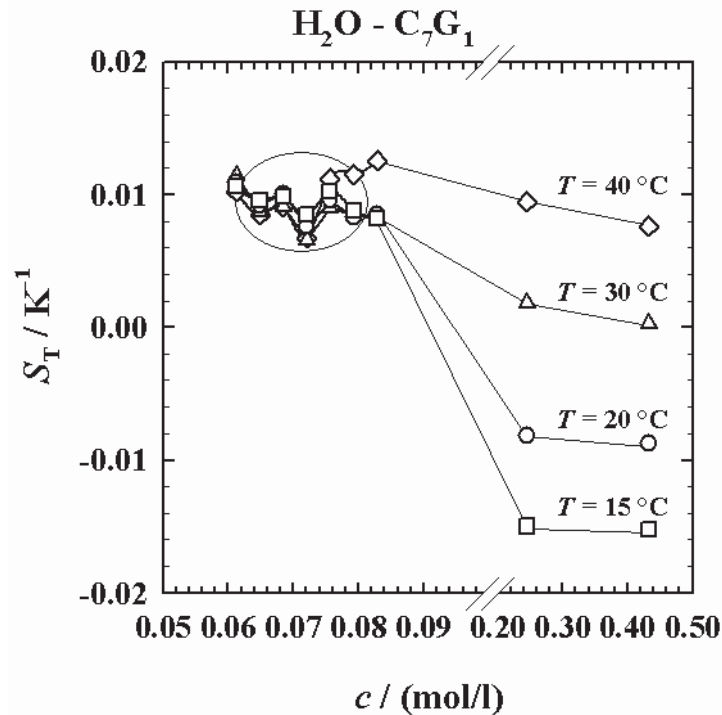
Figure 5.4-2: *Soret* coefficient S_T as function of the surfactant concentration c in the system $H_2O – C_7G_1$ at $T = 40$ (diamonds), 30 (triangles), 20 (circles) and 15 (squares) °C [194].

The occurrence of a temperature dependence of the Soret coefficient with increasing surfactant concentration was already observed and described for the C_8G_1–system (Figure 5.4-1a). Although at first sight, this pattern appears to be similar to C_8G_1 in water. The data points of C_7G_1 in the range around the cmc (oval in Figure 5.4-2) did not yet allow extracting a certain value for the cmc in the same way, as was shown for C_8G_1 in Figure 5.4-1b. Further measurements will be object of future work.

Another possibility to correlate the cmc to the measurements of the *Soret* coefficient might be plotting S_T as function of T for at constant surfactant concentration c, that matches the cmc at a certain temperature in the temperature range under study. Thereby we assume, that the slope of such a curve shows a distinct change at the temperature of micelle formation. In analogy to the cmc this temperature is referred to as critical micelle temperature (cmt) in the following. In Figure 5.4-3a S_T is plotted as function of T for the system $H_2O – C_7G_1$ at three different surfactant concentrations $c = 0.075$ (circles), 0.079 (triangles) and 0.083 mol/l (squares),

respectively. The chosen concentrations are in the range, of the cmc for this system around $T = 20\,°C$, as was previously determined by the surface tension measurements (refer to Figure 5.3-3). For a clearer presentation an offset of $+\,0.01$ and $+\,0.02\,K^{-1}$ was added to the curves relating to $c = 0.079$ and $0.083\,ml/l$, respectively.
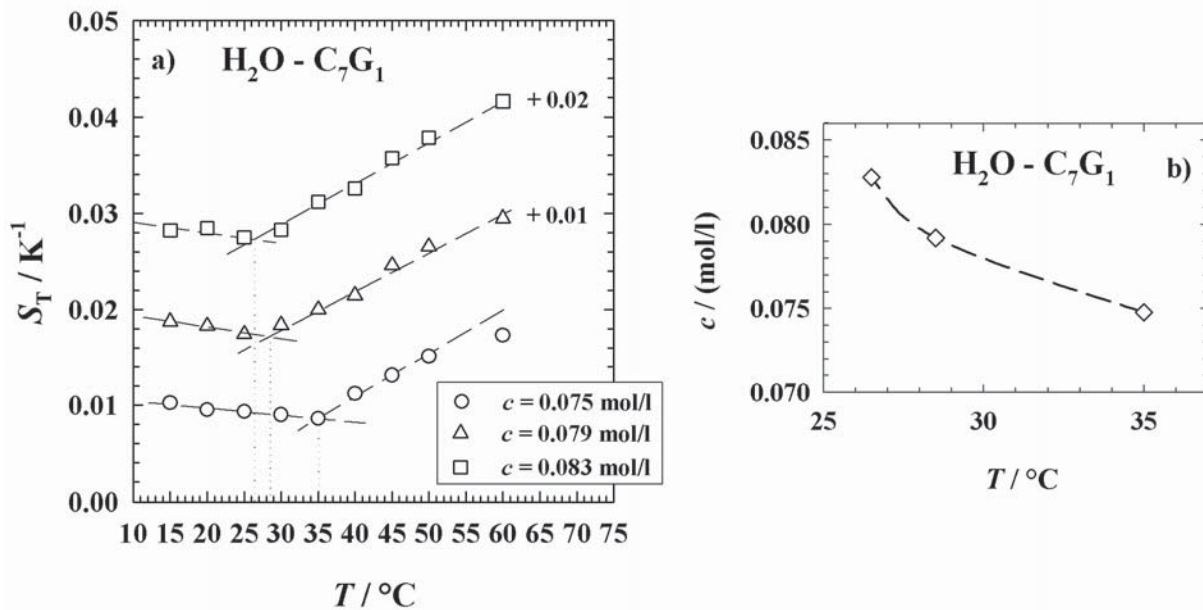
Figure 5.4-3: a): *Soret* coefficient S_T as function of T for C_7G_1 in water at three different surfactant concentrations $c = 0.075$ (circles), 0.079 (triangles) and 0.083 mol/l (squares), respectively. Note that for a clearer presentation an offset of $+\,0.01$ and $+\,0.02\,K^{-1}$ was added to the curves of $c = 0.079$ and 0.083 ml/l, respectively [194]. b): The concentration plotted as function of the temperature that is assigned to the change of the slope of S_T as function of T for a given c [intersection of the dotted lines in a)].

It can be observed in Figure 5.4-3a, that for all three concentrations S_T first decreases linearly as function of T. At a certain temperature, indeed a sudden change of the slope towards a pronounced, almost linear increase of S_T can be seen (dashed lines as guide to the eyes). We assume that this temperature corresponds to the cmt for a respective concentration. The corresponding temperatures (dotted lines in Figure 5.4-3a) are $T = 26.5\,°C$ ($c = 0.083$ mol/l), $28.5\,°C$ ($c = 0.079$ mol/l) and $35.0\,°C$ (0.075 mol/l). Plotting the respective sample concentrations as function of those temperatures in Figure 5.4-3b, yields qualitatively the same pattern, as was found for the cmc, being determined from surface tension measurements, as function of T in Figure 5.3-3. However, comparing the sample concentrations from Figure 5.4-3b at which a certain temperature (cmt) was assigned to the formation of micelles, with the cmc values of C_7G_1 in water in the same temperature range (26.5 – 35 °C) (refer to Figure 5.3-3), it is

obvious that the cmc as function of T is not exactly matched by the change of the slope in the S_T vs. T pattern: The cmc values at related temperatures are by a factor of about 1.2 smaller than the respective sample concentrations in Figure 5.4-3b.

For the system $H_2O – C_8G_1$ the *Soret* coefficient S_T as function of T is shown in Figure 5.4-4, for three concentrations $c = 0.22$ (squares), 0.21 (triangles) and 0.19 mol/l (circles), respectively, that correspond to the cmc in the range between $T = 20$ and 40 °C (refer to Figure 5.3-3). Thereby the dotted lines in Figure 5.4-4 mark the corresponding temperatures (here referred to as cmt) determined from the plot of the cmc as function of T in Figure 5.3-3.
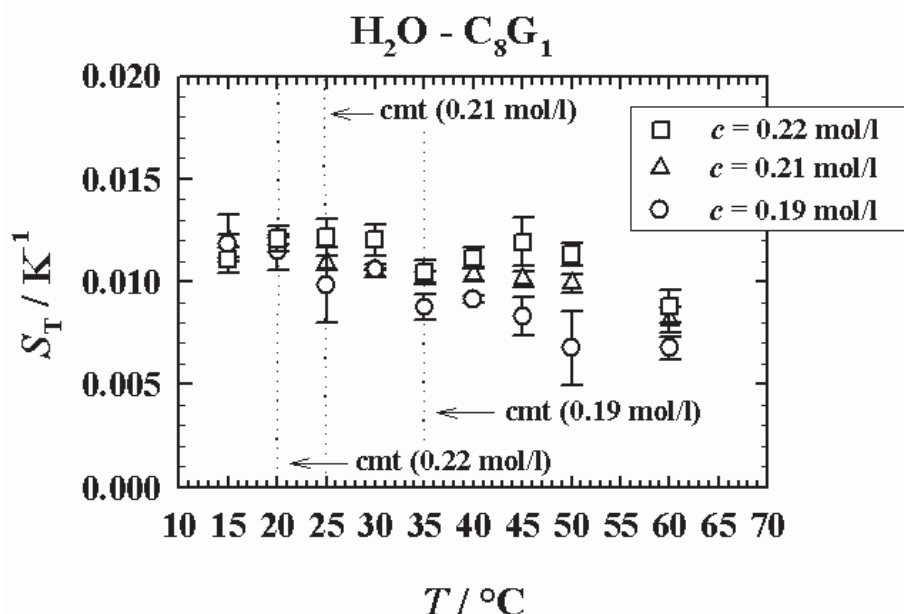
Figure 5.4-4: *Soret* coefficient S_T as function of T for C_8G_1 in water at three different sample concentrations $c = 0.19$ (circles), 0.21 (triangles) and 0.22 mol/l (squares), respectively. The dotted lines mark the temperatures (referred to as cmt) at which the sample concentration should equal the cmc according to Figure 5.3-3. See text for details.

Within the experimental error Figure 5.4-4 does not give any evidence for a distinct change of the slope of S_T as function of T. Thus for C_8G_1 in water, plotting S_T as function of T does not allow the detection of a critical micellation temperature as it was found for C_7G_1 in water. It might be possible, that the experimental error for the measurements with C_8G_1 (Figure 5.4-4) is too large for a determination of such a change of the slope for this system. The clarification of this issue is object of presently ongoing work.

From the results presented above it can be concluded that the formation of the micelles at the cmc is visible in the *Soret* coefficient as function of the surfactant concentration, as it was indicated by the observations of *Santos et al.* [57]. Furthermore, our measurements indicate, that the formation of micelles can also be observed from the trend of S_T as function of T at a given

concentration. However, we were not able to deduce a systematic pattern from these observations, that would allow a precise determination of the cmc in a systematic way.

6 Ternary System H_2O – $C_{12}E_5$ – *n*-alkane: Microemulsion Droplets

6.1 Motivation and Objectives

The dependence of the *Soret* coefficient on the particle radius is a topic which receives a lot of attention in the field of thermal diffusion. Numerous studies have been conducted which deal with this topic. They cover theoretical concepts, simulations and experiments. *Galliero* and *Volz* [195] studied the thermo diffusion in nanofluids by molecular dynamics simulations. They found that for nanoparticles with diameters in the range from 0.8 to 4 nm the *Soret* coefficient S_T depends linearly on the diameter. This linear size dependence of S_T was confirmed by experimental findings of *Vigolo et al.* [33] for ionic microemulsions and experiments by *Putnam* [34] who studied carboxyl functionalized polystyrene spheres and lysozyme. On the contrary *Duhr* and *Braun* [35] measured a quadratic size dependence of S_T based on earlier experimental results also using carboxyl functionalized polystyrene spheres. However, it needs to be mentioned that the largest investigated diameters in the two newer publications [33, 34] are clearly below 100 nm, while the earlier work by *Duhr* and *Braun* includes also particles with diameter of 1 μm.

From this very brief overview it becomes obvious that the size dependence of the *Soret* coefficient is controversially discussed in the literature. Thereby the choice of an appropriate model system to extract the size dependence of S_T is one of the major tasks.

Using charged colloidal dispersions one has to account for various additional parameters, such as screening length, particle charge and degree of ionization or surface potential. Furthermore it is not easy to reproduce those properties of the particles within two separately synthesized batches [33, 44, 45]. In order to overcome those problems, *Vigolo et al.* [33] chose for their investigation a thermodynamically stable water-in-oil (w/o) microemulsion system containing sodium di-2-ethylhexylsulfosuccinate (AOT)-water-isooctane. They assume swollen spherical micelles [196, 197] with a hydrodynamic radius ranging from approximately 2-15 nm. However, their work lacks of a close inspection of the microstructure of the aggregates. So far no systematic study has been performed investigating the thermal diffusion of non-ionic microemulsion systems. Those systems allow a systematic variation of the droplet radius, independently from the influence of ionic charge and screening length. Furthermore in microemulsion systems the interfacial tension between the microemulsion droplets and the solvent is experimentally accessible and can be varied in a systematic way by tuning the composition and temperature [50, 55, 56]. This feature is in particular interesting, because it allows to validate a theoretical approach, that was proposed by *Parola* and *Piazza* [41] and relates the *Soret* coefficient to both, the radius of the diffusing particle and the slope of the temperature dependent interfacial tension.

In this context the objective of this part of the present thesis was to provide a non-ionic droplet microemulsion which enables a systematic investigation of the *Soret* coefficient as function of the droplet size and the interfacial tension. Having formulated the microemulsion the microstructure as well as the interfacial tension should systematically be studied. An important constraint for the investigation of the thermal diffusion behavior was the formulation of non-ionic microemulsion systems that allows for a variation of the droplet size and interfacial tension at isothermal conditions. Thereby, the influence of the temperature can be ruled out.

As the basis for any further characterization, the phase behavior of ternary microemulsion systems of the type H_2O – *n*-alkane – $C_{12}E_5$ must carefully be studied. The phase diagrams should be measured in terms of $T(w_B)$ – sections through the phase prism in order to determine the emulsification failure boundary where a spherical droplet structure is presumed. Subsequently, on the basis of the phase behavior studies, a systematic investigation of the microstructure should be conducted by means of small angle neutron scattering (SANS) and dynamic light scattering (DLS) experiments. From the SANS studies the microstructure of the aggregates such as size, shape and polydispersity as well as the type and intensity of interparticle

interaction should be extracted. The scattering data should therefore be analyzed using appropriate models for the scattering intensity distribution.

Having determined the structural parameters, samples should be prepared for the investigation of the thermal diffusion behavior. These measurements are performed by the cooperation partners in *Jülich* using the thermal diffusion forced *Rayleigh* scattering (TDFRS) setup. In addition to the *Soret* coefficient S_T, the analysis of the TDFRS data yields the mutual diffusion coefficient D. In order to compare and validate those data, it was the objective of this work to determine the diffusion coefficient D of the microemulsion droplets independently by means of dynamic light scattering (DLS).

In a further step, the variation of the *Soret* coefficient with the number density of the microemulsion droplets should be studied while keeping the droplet radius constant. Therefore, the influence of the number particle density n on the diffusion coefficient D should be investigated by means of DLS.

As the second objective, the correlation between the interfacial tension of the droplets and the *Soret* coefficient S_T should be investigated. In particular the goal was to validate the relation proposed by *Parola* and *Piazza* [41], which relates S_T with both, the particle radius and the derivative of the interfacial tension with respect to the temperature. The variation of the interfacial tension with the temperature has extensively been studied by *Sottmann* and *Strey* for non-ionic microemulsions [56]. In this work the interfacial tension of the systems under investigation should be measured in the relevant temperature regime.

On the basis of this data, the derivative of the interfacial tension with respect to the temperature should be calculated in order to study the correlation between this quantity and the *Soret* coefficient according to *Parola* and *Piazza* [41].

6.2 Samples and Experimental

Phase behavior measurements

In order to prepare water-rich microemulsions, water and surfactant were weighted into the sample tube first, adjusting the required surfactant mass fraction γ_a of the water/surfactant mixture. Then the alkane was added adjusting the desired oil mass fraction w_B. The general

procedure used to determine the phase boundaries was similar to that described in section 4.2. However, because the phase boundaries (especially the emulsification failure boundary (*efb*)) are kinetically hindered, especially at small values of w_B and γ_a, changes in the procedure were made: For the detection of the *ncb* the sample was quenched into the two-phase state at first by quenching in a separate water bath at a temperature at least ~ 5 K above the expected phase transition temperature. Afterwards the sample was transferred in another water bath equilibrated to the temperature under study and stirred for 2 min with constant stirring rate. Then the stirring was stopped and the phase state of the sample was determined via visual inspection of both, the transmitted and scattered light. This procedure was repeated for each temperature studied. In order to determine the *efb* the water-rich microemulsion samples were frozen in an ice/water/salt mixture and allowed to melt again. This procedure was repeated three times, in order to obtain a sufficient phase separation. Then the sample was transferred in the equilibrated water bath of the temperature under study and was stirred for 8 min at constant stirring rates, before the phase state of the microemulsion was determined.

SANS Measurements

The SANS measurements on droplet microemulsions were performed in *shell contrast*. Therefore the scattering length densities of the water and the droplet core (*n*-alkane) were adjusted to the same value. The scattering length density of a pure component ρ_i can be calculated from

$$\rho_i = N_A \frac{\rho^0}{M} \sum_k b_k \, , \qquad (6.1)$$

using the molecular weight M of the component, its density ρ^0 and the scattering lengths b_k of each atom k in the molecule (see e.g. Table 2, p. 151 in ref. [131]). The scattering length density ρ of a homogeneous multicomponent mixture can be obtained from the volume fraction weighted scattering length densities of each component ρ_i by

$$\rho = \sum_i \rho_i \phi_i \, . \qquad (6.2)$$

The purity of D_2O used for the SANS samples, with respect to contamination with H_2O, was checked by near-infrared absorption measurements [198]. The extinction of the D_2O used was

measured against a reference D_2O sample with 99.996 % purity at $\lambda = 1361$ nm (Perkin-Elmer Lambda19). The molar fraction of H_2O in D_2O could then be read from the calibration curve given in Ref. [198]. With the molar masses and densities of H_2O and D_2O (refer to Table 8-1) the volume fraction of D_2O was determined to $\phi_{D2O} = 0.988$. Using equation (6.2) this yields a scattering length density of $\rho = 6.3054 \times 10^{-10}$ cm^{-2}. The scattering length densities of the *n*-alkanes were then matched to the scattering length density of D_2O (contaminated with H_2O) by using a mixture of protonated and deuterated *n*-alkanes. The values for the scattering length densities and the macroscopic densities of the pure components are given in Table 8-1. Table 6-1 contains the values of the macroscopic densities, that were calculated from the densities of the protonated and deuterated alkanes as well as the scattering length densities of the alkane mixtures.

Table 6-1: Volume fraction of protonated oil ϕ_h and the macroscopic density ρ^0 of the mixtures of protonated and deuterated alkanes used to prepare the SANS samples of droplet microemulsions. Mixtures were prepared to match the scattering length density of the D_2O (contaminated with H_2O, $\rho^0 = 6.3054 \times 10^{10}$ cm^{-2}).

Alkane mixture	ϕ_h	ρ^0
		[g · cm^{-3}]
n-Octane (h18/d18)	0.0206	0.8117
n-Octane (h18/d18) / *n*-Decane (h22/d22), $\beta_{Octane} = 0.750$	0.0259	0.8181
n-Octane (h18/d18) / *n*-Decane (h22/d22), $\beta_{Octane} = 0.502$	0.0313	0.8243
n-Decane (h22/d22)	0.0425	0.8372
n-Dodecane (h26/d26)	0.0599	0.8572
n-Tetradecane (h30/d30)	0.0739	0.8731

DLS Measurements

An introduction into the DLS technique and the respective setup has been given in section 3.1. The samples were prepared by weight using sample tubes of 8 mm inner diameter that were closed with a ground glass stopper. A thermostated water bath close to the DLS-setup was used to pre-equilibrate the samples in the one-phase state. They were quickly transferred into the toluene bath of the DLS setup, in order to avoid phase separation. Thereby special care was taken that the water was wiped off the sample tubes in order to avoid the transfer of dust into the toluene bath. The measurements were performed at $\lambda = 632$ nm and the scattered light was detected varying the scattering angle between $\theta = 30$ and $150°$ in steps of $20°$. Three measurements were performed at each angle in order to minimize statistical errors. The time-

intensity autocorrelation function was evaluated, using the program CONTIN [157] as has been described in section 3.1.

Spinning Drop Tensiometrie

The interfacial tension σ_{ab} between the water-rich microemulsions in this work was determined with the so called *Spinning Drop* method, developed by *Vonnegut* [199] in 1942. A detailed description of the method can e.g. be found in [130]. The principle of this method is briefly explained as follows: A small drop of the oil phase is brought into a horizontally rotating glass capillary that is filled with the denser water-rich microemulsion phase. As a result of the centrifugal force and the interfacial tension, the oil droplet, which exhibits the smaller macroscopic density, will adopt the shape of a cylindrical droplet parallel to the horizontal rotation axis. For sufficiently elongated droplets, i.e. in the case $l \gg r$, the droplet can be regarded as a cylinder with a radius r and length l with spherical end caps. With this assumption the interfacial tension σ_{ab} is given by [199]

$$\sigma_{ab} = \frac{1}{4}(\rho^0_1 - \rho^0_2)\omega^2 r^3. \tag{6.3}$$

Thereby ω is the angular velocity, $\omega = 2\pi n/60$, with n being the rotation number [min^{-1}] and $(\rho^0_1 - \rho^0_2)$ is the difference of the macroscopic densities of both phases.

For each water-rich microemulsion under study approximately 10 g of a stock solution of water – $C_{12}E_5$ with a mass fraction of $C_{12}E_5$, $\gamma_a = 0.030$ was prepared. This stock solution was brought into a modified separating funnel [130] and then the *n*-alkane, was added to adjust a mass fraction of oil of $w_B \approx 0.30$. The mixture was thoroughly shaken and allowed to equilibrate in a temperature controlled water bath ($\pm$ 0.05 K) at the desired temperature for one week, in order to obtain a complete phase separation. Afterwards, the funnel was removed from the water bath and the lower, water-rich microemulsion phase was quickly released into a sample tube from the valve at the bottom of the funnel. As the respective oil excess phases for the systems still remained slightly turbid after one week, we used separately prepared *n*-alkane solutions, that contained 2 wt% of $C_{12}E_5$ (monomeric solubility of $C_{12}E_5$ in *n*-alkane) instead.

The measurements were performed using a modified [130] SITE 04 Spinning Drop Tensiometer (Krüss, Hamburg, Germany), which allows the measurement of interfacial tensions down to $\sigma_{ab} = 10^{-5}$ mNm^{-1}. The setup consists of a thermostated, horizontally rotating glass capillary that

is sealed at each end by a septum and can be rotated up to $1 \cdot 10^4$ revolutions per minute. The temperature is controlled by a thermostated circulating oil bath (Lauda RE 307) to an accuracy of ± 0.1 K. Two syringes are mounted at the sides of the capillary in order to fill in the phases and remove the waste solution.

First, the pre-equilibrated water-rich microemulsion phase was brought in the capillary at the desired temperature and a rotation velocity of approximately 1000 min^{-1}. Then the rotation was interrupted and the similarly pre-equilibrated oil phase was injected using a *Hamilton* micro syringe. Thereby the injected volume varied between 0.2 and 3 µl in order to obtain single cylindrical droplets. For the determination of the radius the oil droplet inside the water-rich microemulsion phase was moved to the position of the optical window of the microscope by adjusting the tilt angle of the capillary. The diameter $2r$ of the cylindrical oil droplet was determined as function of the rotation velocity by using graduation marks inside the ocular of the microscope. Thereby, the calibration of the scale was achieved by comparing the number of graduation marks that were previously obtained from observing a linear steel wire of known diameter in the capillary. The values of the interfacial tension result from the average of at least 20 measurements under variation of the rotation speed of the capillary. For the determination of the densities of both phases at the respective temperature a digital densitometer DMA60 (Anton Paar KG, Graz, Austria) was used. Thereby the temperature was controlled to an accuracy of ± 0.02 K by a circulating water bath (Lauda RM 6, Lauda-Königshofen, Germany).

6.3 Results

6.3.1 Phase Behavior

The effect of the droplet size on the thermal diffusion behavior was studied by means of the non-ionic microemulsion system $H_2O - C_{12}E_5 - n$-alkane. In order to study the effect of the droplet radius at isothermal conditions, the oil component of the microemulsion was systematically varied, using the pure alkanes *n*-octane, *n*-decane, *n*-dodecane and *n*-tetradecane corresponding to a number of carbon atoms in the alkane chain $k = 8$, 10, 12 and 14, respectively. In addition two mixtures of *n*-octane and *n*-decane with mass fractions of *n*-octane $\beta = 0.75$ ($\langle k \rangle = 8.5$) and 0.50 ($\langle k \rangle = 9$), respectively were used. The phase behaviour of the water-rich microemulsions was studied performing $T(w_b)$-sections through the phase prism at a

constant fraction of the surfactant in the water/surfactant mixture of $\gamma_a = 0.03$. The $T(w_B)$ –
sections are shown in Figure 6.3-1a-e.
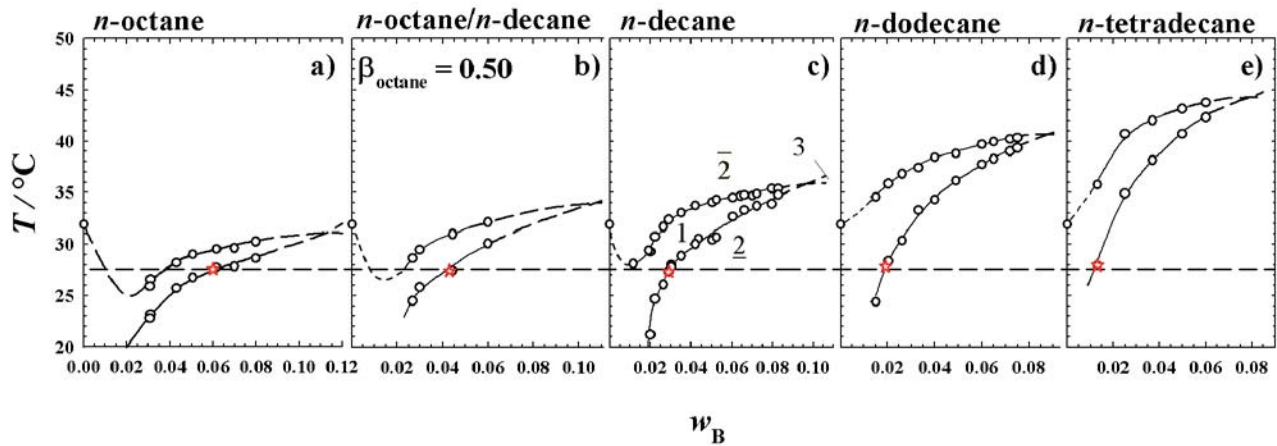
Figure 6.3-1: $T(w_B)$-sections through the phase prism of the systems H_2O – $C_{12}E_5$ – n-alkane at $\gamma_a = 0.030$ for
different n-alkanes: a) n-octane, b) n-octane/n-decane ($\beta = 0.50$), c) n-decane, d) n-dodecane, e) n-tetradecane. The
isotherm $T = (27.6 \pm 0.3)$ °C at which TDFRS-measurements were performed is shown as a dashed line. The
stars denote the intersection of the *efb* with this isotherm for each system. Note that the system
n-octane/n-decane ($\beta = 0.750$) is not shown for reasons of clarity.

As can be seen in all cases a sequence of phases was found, that is typical for water-rich
microemulsions formulated with non-ionic surfactants. Thus, for low temperatures a two-phase
coexistence $\underline{2}$ of an oil-in-water (o/w)-microemulsion and an oil-excess phase is found. At
intermediate temperatures a thermodynamically stable, single phase microemulsion exists. The
$\underline{2}$-1 phase transition temperature, *i.e.* the *emulsification failure boundary* (*efb*), ascends
monotonically with increasing oil weight fraction w_B. At high temperatures a variety of different
two and three phase states can be found – here simply denoted as $\overline{2}$. The upper phase boundary
1-$\overline{2}$, i.e. the *near critical boundary*, originates from the point ($\gamma_a = 0.030$, $T = 31.85$ °C), that lies
on the cloud point curve of the binary side system (refer to Figure 2.4-1) water – $C_{12}E_5$. For the
microemulsion containing pure n-octane (k = 8), n-octane/n-decane ($\beta = 0.50$, i.e. k = 9) and
pure n-decane (k = 10) the *ncb* descends steeply with increasing w_B and runs through a
pronounced minimum upon further addition of oil. Thereby, this minimum stems from the
additional two-phase region, occurring in the form of a closed lobe below T_l at the water-rich
side (and above T_u at the oil-rich side) [55, 113] (refer to Figure 2.4-8). Within this closed lobe a
dilute and concentrated cylinder network phase coexist. Note that these lobes are found in
strongly structured microemulsions only [50, 55]. For the microemulsions containing longer

alkanes, with k = 12 and k = 14, however, no minimum can be observed in the upper phase boundary within the experimental w_B-steps.

For the *n*-octane microemulsions, the *ncb* intersects the *efb* at an oil weight fraction of $w_B = 0.11$. Here, the one phase region closes and a three phase region can be observed for higher w_B-values. As described in section 2.4.4 the temperature $T \approx 32\ °C$ of this intersection point corresponds to the temperature of the lower critical end point T_l. Starting from the *n*-octane microemulsion the intersection point between the *ncb* and the *efb* steadily shifts to lower w_B-values as the oil chain length increases indicating that the solubilization of longer *n*-alkanes becomes increasingly inefficient. This is a well known trend which was already observed for balanced microemulsions of the type water – *n*-alkane – C_iE_j. Thus, for the tetradecane microemulsion the one phase region already closes at $w_B \approx 0.07$.

Simultaneously with increasing oil chain length the intersection point between the *ncb* and *efb* shifts to higher temperatures form $T_1 = 32\ °C$ at k = 8 to $T_1 = 44\ °C$ at k = 14. This finding can be explained by a decreasing solubility of $C_{12}E_5$ in the alkane (or vice versa) with increasing k, which leads to a shift of miscibility gap in the binary system $C_{12}E_5 – n$-alkane to higher temperatures, and is in turn reflected in the location of the phase boundaries in the $T(w_B) –$ sections of the ternary systems [47, 113].

The dashed straight line in Figure 6.3-1 represents an isotherme "through" the $T(w_B)$ - sections at $T = 27.6\ °C$. The red stars mark the intersection of this isotherme with the *emulsification failure boundary* for each system (k = 8, 9, 10, 12 and 14). It should be noted here that narrow one-phase regions could cause problems in the TDFRS measurement for the following reason: For the TDFRS measurement a clean and dry surface of the glass cuvette is indispensable [200]. Therefore the sample, that is pre – equilibrated in a water bath, should quickly be dried and carefully cleaned before inserting it into cell holder of the TDFRS setup. If the one-phase temperature range is to narrow, this procedure can lead to phase separation.

As an additional system we studied a mixture of *n*-octane/*n*-decane, with a mass fraction of *n*-octane, $\beta = 0.75$ (according to k = 8.5). For this system the phase transition temperatures as function of w_B were determined only around $w_B = 0.0505$, in order to find the intersection of *efb* with the isotherme $T = 27.6$. In Table 6-2 the composition i.e. mass fractions of oil w_B, the corresponding volume fractions of oil ϕ_B as well as the mass fractions of the dispersed phase

$\phi_{disp} = \phi_B + \phi_C$ at the intersection points of the *efb* with the isotherme $T = 27.6$ °C for the system H$_2$O – C$_{12}$E$_5$ – *n*-alkane under variation k are compiled. The maximum mass fraction of oil that can be solubilized in a one-phase droplet microemulsion at $T = 27.6$ °C increases by a factor of 4.6 from $w_B = 0.013$ (k = 8) to 0.060 (k = 14). Including the constant (mass) fraction γ_a of surfactant in the H$_2$O/C$_{12}$E$_5$ mixture of $\gamma_a = 0.030$, this leads to an increase of the droplet volume fraction ϕ_{disp} by a factor of 2.3 from $\phi_{disp} = 0.048$ to 0.112.

Table 6-2: Composition of the microemulsions of the type H$_2$O – C$_{12}$E$_5$ – *n*-alkane, $\gamma_a = 0.030$, at the intersection between the *efb* and the isotherm $T = (27.6 \pm 0.3)$ °C according to the red stars in the $T(w_B)$-sections shown in Figure 6.3-1a-e. The corresponding point $T_{efb} = 27.6$ °C is also given for the system H$_2$O – C$_{12}$E$_5$ – *n*-octane/*n*-decane ($\beta = 0.75$), $\gamma_a = 0.030$, for which the $T(w_B)$-section is not shown in Figure 6.3-1. k: (effective) chain length of the *n*-alkane, w_B: mass fraction of oil, ϕ_B = volume fraction of oil, ϕ_{disp} = droplet volume fraction.

n-alkane	k	w_B	ϕ_B	ϕ_{disp}
octane	8	0.0600	0.0831	0.1115
octane/decane ($\beta = 0.75$)	8.5	0.0505	0.0696	0.0983
octane/decane ($\beta = 0.50$)	9	0.0430	0.0589	0.0880
decane	10	0.0290	0.0392	0.0690
dodecane	11	0.0191	0.0252	0.0554
tetradecane	12	0.0131	0.0171	0.0475

Figure 6.3-2 shows the variation of the droplet volume fraction ϕ_{disp} as function of the chain length k of the *n*-alkane. At first, ϕ_{disp} drops strongly with increasing k, but shows a less steep decay from k = 10 over 12 to 14, respectively. This can be understood by considering the shape of the emulsification failure boundaries of the respective systems, shown in Figure 6.3-1a-e. From there it is obvious that the slope of the *efb* becomes larger with decreasing mass fraction of oil in the system w_B for all the systems. Accordingly, for a small value of w_B, i.e. for the larger values of k, a shift of the *efb* to higher temperatures leads to a smaller variation of w_B than it does for the systems with decreasing k. From this picture it can be understood, that in turn for longer *n*-alkanes the variation of k has a smaller effect on w_B than it has for the systems with shorter *n*-alkanes, which corresponds to nonlinear trend of the droplet volume fraction of ϕ_{disp} as function of k, in Figure 6.3-2.
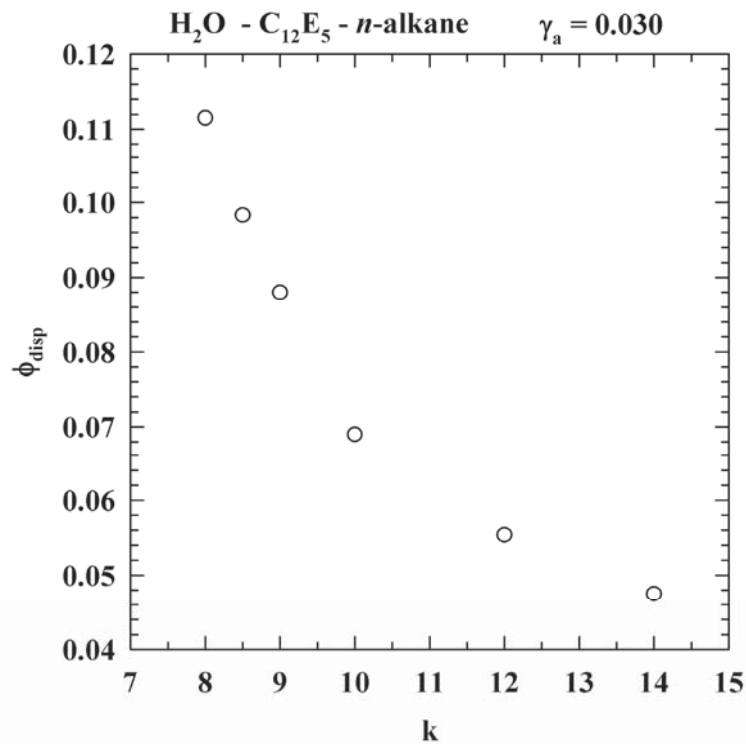
Figure 6.3-2: Droplet volume fraction ϕ_{disp} at the intersection of the *efb* with the isotherm $T = 27.6\,°C$ as function of the (effective) alkyl chain length k of the *n*-alkanes in the system $H_2O – C_{12}E_5 – n$-alkane, at constant mass fraction of surfactant in the mixture of water-plus-surfactant, $\gamma_a = 0.030$. (Refer also to Figure 6.3-1.)

Having determined the phase behavior of microemulsions of the type $H_2O – C_{12}E_5 – n$-alkane, in order to realize thermal diffusion experiments at isothermal conditions, in the next step the microstructure of this system should be studied in order to enable a systematic correlation with the thermal diffusion behavior.

From the TDFRS measurements the *Soret* coefficient S_T the mutual diffusion coefficient D, and hence the thermal diffusion coefficient D_T are obtained as transport variables of the system (refer to section 3.2). The mutual diffusion coefficient D is thereby related to the hydrodynamic radius R_H of the microemulsion droplets via the *Stokes-Einstein* relation (3.7). The validity of the transport properties, obtained from TDFRS, was verified in the scope of a benchmark test in comparison with other experimental methods by several groups [201, 202]: Evaluating three different binary organic mixtures, it was shown that the values of the mutual diffusion coefficient D obtained from TDFRS measurements do not deviate more than 7 % from the average values of all experimental methods applied in this test [201]. Despite this good agreement, and due to the fact that nonionic microemulsions were not examined before with the TDFRS method, we first wanted to determine the diffusion coefficients D of the microemulsion droplets under study with an additional experimental method. Therefore in the next step we performed dynamic light

scattering (DLS) measurements. From the measured values of D the hydrodynamic radii should be calculated and compared with the respective values obtained from the TDFRS measurements.

6.3.2 Dynamic Light Scattering (DLS) Measurements

6.3.2.1 Structural Evolution

The first goal of the DLS measurements is to examine the variation of the diffusion coefficient D and thus the hydrodynamic radius R_H of the self assembled aggregates. The structural evolution should exemplarily be studied for the system $H_2O – C_{12}E_5 – n$-decane at a surfactant to water-plus-surfactant ratio $\gamma_a = 0.030$ and a mass fraction of n-decane $w_B = 0.0290$, corresponding to the composition at the efb at $T = 27.6\ °C$, that was determined from the phase behavior measurements. Figure 6.3-3 shows the $T(w_B)$ - section at the water-rich side of this system, which was also shown in Figure 6.3-1c. The efb for the DLS sample was determined to $T_{efb} = 27.00$ (red star), which slightly differs from T_{efb} that was determined in the phase behavior studies. DLS measurements were performed under variation of T (dashed line in Figure 6.3-3) in order extract the distribution functions $A(\Gamma)$ of the inverse relaxation time Γ from the CONTIN analysis of the correlation function $g^2(\tau)$ for each temperature.
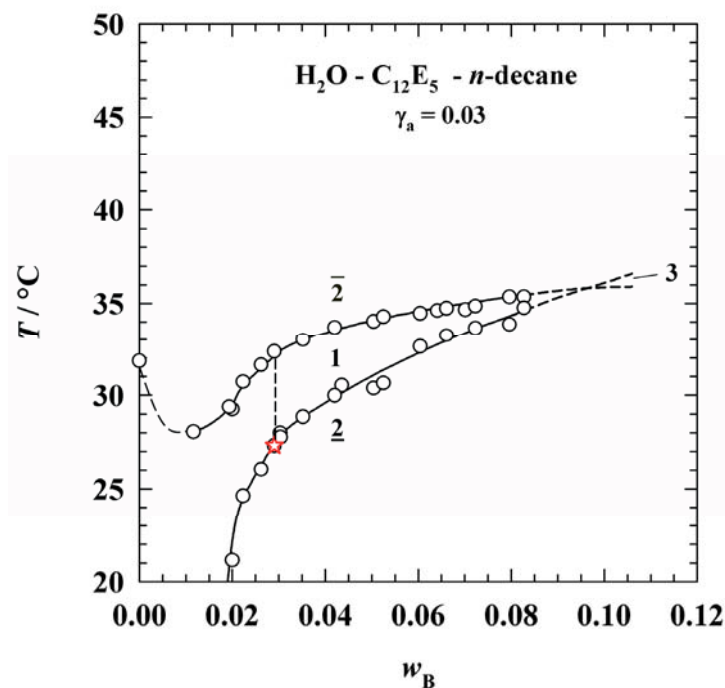
Figure 6.3-3: $T(w_B)$-section of the system $H_2O – C_{12}E_5 – n$-decane at $\gamma_a = 0.030$. The red point marks the efb of the DLS sample at $w_B = 0.029$ and $T = 27.00\ °C$. DLS measurements were performed at this composition under variation of the temperature, as indicated by the dashed line. See text for details.

Accordingly in Figure 6.3-4 the distribution function $A(\Gamma)$, weighted by the relaxation time Γ is shown as function of Γ for different temperatures from $T_{efb} = 27.00$ (a) to 32 °C(e) and different scattering angles $\theta = 30$ (squares), 90 (circles), and 150 ° (triangles), respectively. It is visible, that the maximum of $A(\Gamma)\mathrm{x}\Gamma$ shifts to higher relaxation rates Γ with higher scattering angles, according to the relation $\Gamma = q^2 D$. Starting from the *efb* at $T = 27.00$ °C (Figure 6.3-4a) and increasing the temperature up to $T = 28.00$ °C (b and c) the shape and position of the peaks both remain almost unchanged (the dashed line is shown as guide to the eyes). Increasing the temperature from 28.00 °C to 29.67 °C (Figure 6.3-4d-e), the maximum of the peaks for all three scattering angles, respectively, shifts to smaller inverse relaxation times. This indicates a slower diffusion, which in turn points to the formation of elongated structures [203, 204].
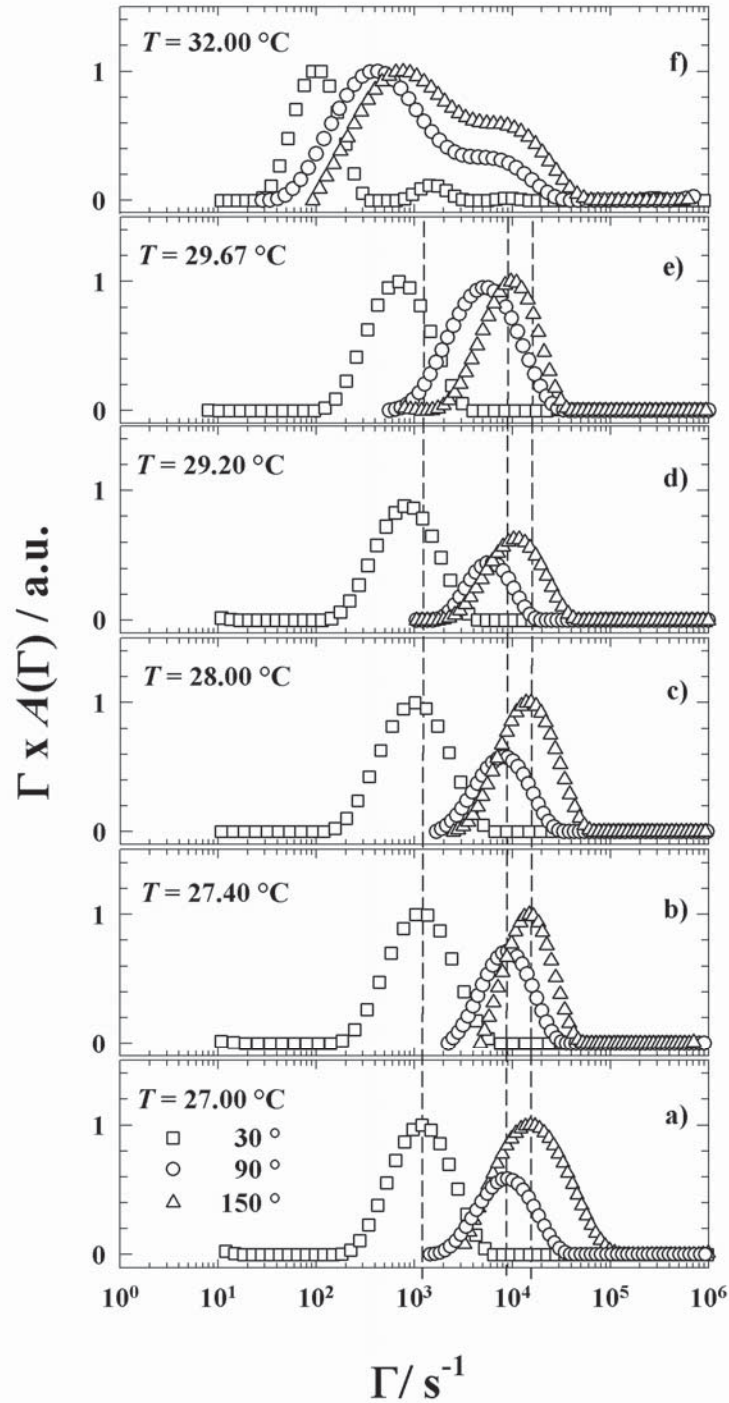
Figure 6.3-4: Distribution function $A(\Gamma)$ of the inverse relaxation time, weighted by Γ as function of Γ of the system $H_2O - C_{12}E_5 - n$-decane, $\gamma_a = 0.030$. $w_B = 0.029$. The distribution functions were extracted from the CONTIN analysis of the DLS measurements at different temperatures and different scattering angles $\theta = 30\ °$ (squares), 90 ° (circles) and 150 ° (triangles).

Increasing the temperature further to $T = 32.00\ °C$ (f), which is close to the near critical $1-\overline{2}$ phase transition (c.f. Figure 6.3-3), the shape of the distribution functions change significantly: For all three angles $\theta = 30$ (squares), 90 (circles) and 150 (triangles) °, the main

maximum is significantly shifted towards smaller inverse relaxation times Γ. In addition, for $\theta = 90$ and $150\,°$, the weighted distribution functions $A(\Gamma)x\Gamma$ are strongly broadened and show a shoulder around $9000\ \mathrm{s}^{-1}$ ($\theta = 90\,°$, circles) and $15000\ \mathrm{s}^{-1}$ ($\theta = 150\,°$, triangles), which must stem from the dynamics of another, faster diffusion process. The shape of the distribution function $A(\Gamma)x\Gamma$ at $\theta = 30\,°$ differs from that at $90\,°$ and $150\,°$: While the main peak is also shifted significantly towards smaller relaxation times Γ the width of this peak is not significantly changed. In addition at $30\,°$ also a second peak can be seen at $\Gamma \approx 1500\ \mathrm{s}^{-1}$ and even a very small, third peak around $\Gamma \approx 10000\ \mathrm{s}^{-1}$. However these faster modes of the correlation function at $30\,°$ show a much smaller intensity than the first peak at $\Gamma \approx 100\ \mathrm{s}^{-1}$. A detailed analysis of the processes that are reflected by the different modes is beyond the scope of this work. Nevertheless, the evolution of the distribution function of the inverse relaxation times $A(\Gamma)x\Gamma$ are in qualitative agreement with the pattern found for elongated structures in non-ionic and ionic microemulsions by *Hellweg et al.*[203, 204].

In order to calculate the equivalent hydrodynamic radius of the structures, using the *Stokes-Einstein* relation (3.7), the mean value of the diffusion coefficient D according to the most intensive peak is extracted from the CONTIN analysis of the correlation functions. This approach yields the hydrodynamic radius R_H only in the case of spherical particles. For elongated aggregates the radius R_H of an equivalently diffusing sphere is obtained. Accordingly, in Figure 6.3-5 the values of the hydrodynamic radius R_H as a function of the temperature are shown, that were obtained for the sample $H_2O – C_{12}E_5 – n$-decane, $\gamma_a = 0.030$, $w_B = 0.0290$. In agreement with the qualitative analysis of the distribution functions of the inverse relaxation time, discussed above (Figure 6.3-4) the structural evolution of the aggregates from spherical droplets to elongated structures exhibits itself in an increase of the (equivalent) hydrodynamic radius R_H. In the range from $T_{efb} = 27.00\,°\mathrm{C}$ to $T = 29.67\,°\mathrm{C}$ the hydrodynamic radius increases from $R_H = 10.5$ nm to $R_H = 18.93$ nm, which corresponds to an increase by factor of approximately 1.8. In contrast, from $T = 29.67\,°\mathrm{C}$ to $T = 32.00\,°\mathrm{C}$ the value of R_H increases to 233.9 nm, corresponding to an increase by a factor of approximately 12.4. This significant growth, which occurs within the "upper" half of the one-phase region with respect to the temperature (refer to Figure 6.3-3), might be caused not only by the elongation of the aggregates, but also by an superposition of scattering due the formation of cylindrical network structures and critical fluctuations. As can be seen in Figure 6.3-5 between $T = 27.00\,°\mathrm{C}$ and $T = 29.67\,°\mathrm{C}$ (i.e. the "lower half" of the one-phase region) the variation of the hydrodynamic radius R_H can almost perfectly be described by a quadratic equation (full line). Without consideration of any physical

meaning of the corresponding parameters, we use this dependency to determine the hydrodynamic radius of the aggregates of the system $H_2O - C_{12}E_5 - n$-alkane in our study at the emulsification failure boundary.
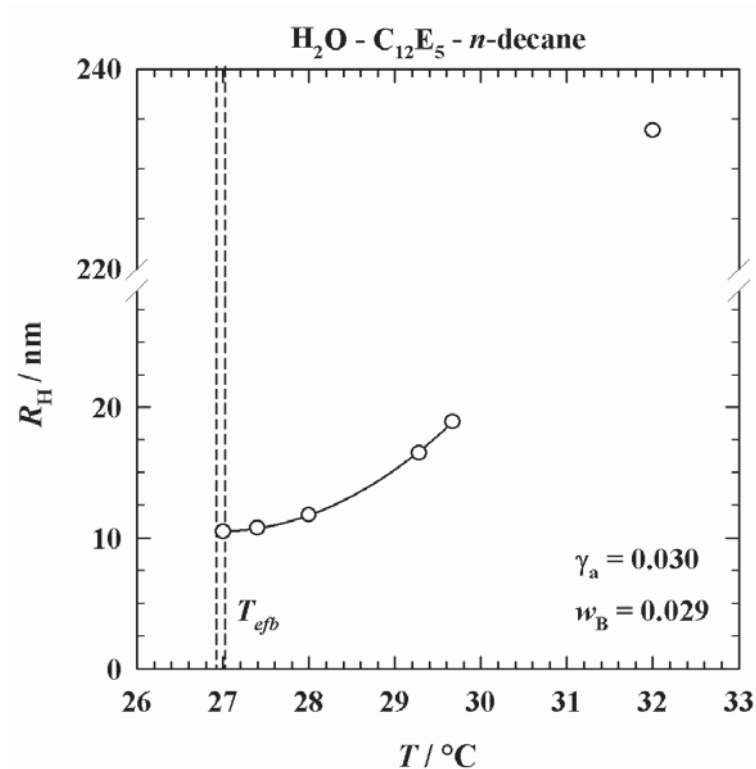
Figure 6.3-5: Effective hydrodynamic radius R_H obtained from DLS measurements of the system $H_2O - C_{12}E_5 -$ *n*-decane at $\gamma_a = 0.030$ and $w_B = 0.0290$ as a function of the temperature.

6.3.2.2   *Hydrodynamic Radius at the Emulsification Failure Boundary*

Temperature dependent DLS measurements were performed on different microemulsions varying the *n*-alkane chain length k according to the composition previously determined by the phase behavior measurements (refer to Figure 6.3-1:; refer to Table 6-3 for the exact composition and phase transition temperatures of the samples). The hydrodynamic radii of the samples as function of the temperature are shown in Figure 6.3-6a-e. For each sample, the temperature of the emulsification failure boundary T_{efb} (± 0.05 K) is represented by the dashed lines.
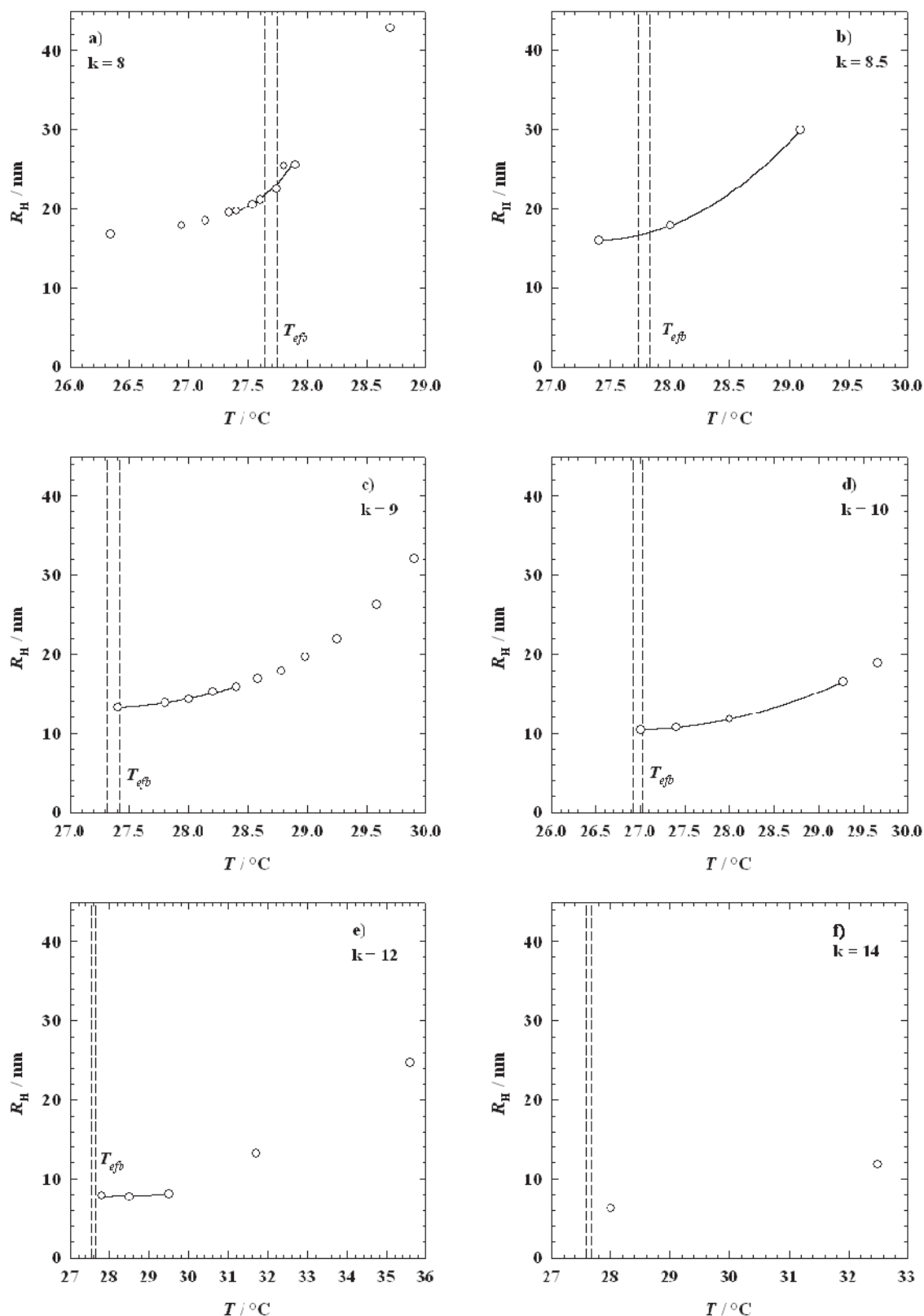
Figure 6.3-6: Effective hydrodynamic radius R_H as a function of T obtained from DLS measurements for the systems H_2O - $C_{12}E_5$ - n-alkane at $\gamma_a = 0.030$; different n-alkanes of chain length k were used. a): n-octane, k = 8. b): n-octane/n-decane, $\beta = 0.75$, k = 8.5. c): n-octane/n-decane, $\beta = 0.50$, k = 9. d): n-decane, k = 10. e): n-dodecane, k = 12. e): n-tetradecane, k = 14. The weight fraction of the n-alkane in the samples corresponds to the intersection of the *efb* and the isotherm $T = (27.6 \pm 0.3)$ °C according to the red stars in the $T(w_B)$-sections shown in Figure 6.3-1a-e. The composition samples and the values of the phase transition temperature at the *efb* (T_{efb}, dashed lines in the figures) can be found in Table 6-3.

For the systems k = 8, and k = 8.5, (Figure 6.3-6a and b, respectively), DLS measurements were performed also below the *efb*. This was done in order to study the variation of the hydrodynamic radius as a function of temperatures below the *efb*. It can clearly be seen from Figure 6.3-6a and b that for those two systems the hydrodynamic radius still slightly decreases with decreasing T below the *efb*. The most likely reason for this observation is the vicinity of the *efb* to the lower critical end point temperature T_l at which cylindrical structures are known to exist. Being only a few degrees below T_l the existence of prolates and oblates is presumable. Another explanation could be, that the phase transition temperature at the *efb* was slightly overestimated by the measurement in terms of optical inspection. This point will further be discussed later.

It can be observed from Figure 6.3-6a-d that for the systems containing *n*-alkanes of chain length k = 8, 8.5, 9 and 10, respectively, the decrease of the hydrodynamic radius R_H with decreasing temperature follows a quadratic pattern in the vicinity of the *efb* (full lines). It can furthermore be seen, that the influence of the temperature on the hydrodynamic radius, i.e. the slope of the full lines, decreases from *n*-octane (k = 8, Figure 6.3-6a) to *n*-dodecane (k = 12, Figure 6.3-6e). Again this behavior can be understood from the distance of the *efb* at $T = 27.6 \pm 0.3$ °C, to the lower critical end-point temperature T_l, which becomes considerably smaller with decreasing *n*-alkane chain length k. Accordingly, the variation of the length scale with temperature, that shows a maximum at T_m, is more pronounced in the systems containing *n*-alkanes with smaller chain length k. Furthermore, critical scattering effects and the formation of cylindrical network structures, both leading to a smaller effective diffusion coefficient in the DLS, are more likely to occur in the vicinity of the *ncb*, i.e. for the systems with a narrow one-phase region. In contrast, in the system H_2O – $C_{12}E_5$ – *n*-dodecane (k = 12), (Figure 6.3-6e), that exhibits a large distance between T_l and the *efb*, R_H stays almost constant in the vicinity of the *efb*.

In order to determine the hydrodynamic radius R_H at the temperature of the *efb* as accurately as possible, the full lines in Figure 6.3-6a-e were extrapolated to the temperature of the *efb*, T_{efb}, for each sample.

Table 6-3 summarizes the composition of the DLS samples together with the temperature of the *efb* for each sample and the corresponding hydrodynamic radius R_H being determined according to the procedure described above. Furthermore, the values of R_H that were in analogy determined from the TDFRS measurements [205] are compiled.

Table 6-3: Sample compositions, phase transition temperature at the *efb* $T_{1\text{-}2}$ (T_{efb}) and hydrodynamic radius R_H for the DLS and TDFRS measurements of the microemulsions of the type H_2O - $C_{12}E_5$ - *n*-alkane at $\gamma_a = 0.030$, using different *n*-alkanes of chain length k. k = 8: *n*-octane. k = 8.5: *n*-octane/*n*-decane, $\beta = 0.75$. k = 9: *n*-octane/*n*-decane, $\beta = 0.50$. k = 10: *n*-decane. k = 12: *n*-dodecane. k = 14: *n*-tetradecane.

k	w_B	ϕ_B	ϕ_C	$\phi_{c,i}$	ϕ_{disp}	$T_{1\text{-}2}$ (T_{efb}) [°C]	$R_{H,DLS,\,efb}$ [nm]	$R_{H,TDFRS,\,efb}$ [205] [nm]
8	0.0600	0.0831	0.0284	0.0270	0.1115	27.69	22.92	25.19
8.5	0.0505	0.0696	0.0288	0.0278	0.0983	27.78	16.80	18.21
9	0.0430	0.0589	0.0292	0.0281	0.0880	27.36	13.28	12.99
10	0.0290	0.0392	0.0298	0.0291	0.0690	26.97	10.50	10.02
12	0.0191	0.0252	0.0302	0.0298	0.0554	27.58	7.78	7.30
14	0.0130	0.0171	0.0305	0.0301	0.0475	27.63	6.26	6.45

6.3.2.3 *Temperature Correction TDFRS Setup*

The hydrodynamic radii, which we determined for each sample at the *efb* by DLS measurements, will now be compared to the hydrodynamic radii, which were extracted from the TDFRS measurements. Thereby the corresponding values of the diffusion coefficients D were obtained using the same approach as described above, i.e. by measuring and extrapolating the determined values of D according to quadratic or linear fits to the temperature of the *efb*, T_{efb}. All TDFRS measurements were performed by *Bastian Arlt* in *Jülich*, using the infrared (IR)-TDFRS setup, which allows the study of aqueous systems without the addition of any light absorbing dye. However, we found significant deviations between the diffusion coefficients D determined with the TDFRS technique and the DLS measurements. Figure 6.3-7 shows the discrepancy of the diffusion coefficients D obtained by DLS (circles) and TDFRS (diamonds) for the system H_2O – $C_{12}E_5$ – *n*-octane/*n*-decane, $\beta = 0.5$ (k = 9). As can be seen, the TDFRS technique reveals an apparently slower diffusion. This difference becomes furthermore more pronounced at higher temperatures. These increasing deviations of D at higher temperatures might stem from a different weighting of larger particles in the different methods. Another reason might be a different contribution to the observed diffusion coefficients due to the change of the aggregate shape with increasing temperature.

Apart from that, in the vicinity of the *efb* (dashed vertical lines in the figure), where the microemulsion droplets exhibit a spherical structure, the diffusion coefficients obtained from TDFRS and DLS were expected to agree almost quantitatively [201, 202]. In contrast, the value

of D obtained with TDFRS (diamonds) at the *efb* is significantly smaller than the respective value obtained by DLS (circles).
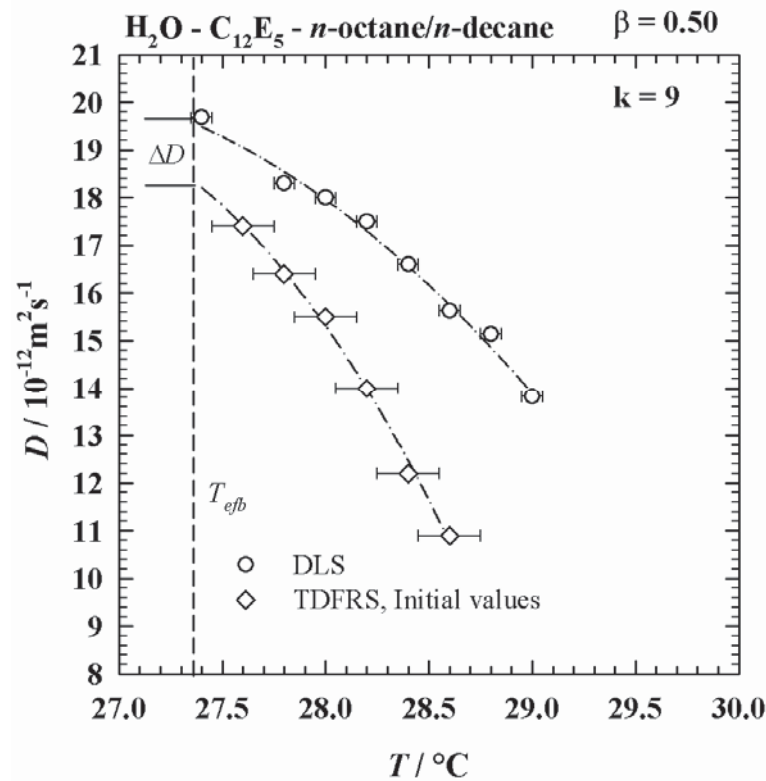
Figure 6.3-7: Diffusion coefficient D as function of the temperature for the system H_2O - $C_{12}E_5$ - *n*-octane/*n*-decane, $\beta = 0.50$ (k = 9), $\gamma_a = 0.030$, $w_B = 0.0430$, obtained by DLS (circles) and TDFRS (diamonds) measurements. The diamonds represent the values of the initial TDFRS measurements. The phase transition temperature $T_{efb} = 27.36 \pm 0.05$ °C for this sample is marked by the straight dashed lines. The experimental error of the TDFRS measurement temperature is $\Delta T = \pm$ 0.15 K, which is larger than for the DLS setup $\Delta T = \pm 0.05$ K, due to the stronger temperature fluctuation in the brass sample holder utilized in the TDFRS setup.

Upon closer inspection of Figure 6.3-7 it was suspected, that the observed deviation between the diffusion coefficients D obtained by DLS and TDFRS, results rather from a discrepancy in the determination of the exact temperature of the samples between both of the setups. In the case of the DLS, this aspect could be clarified in a relatively facile way, because the setup allows placing the Pt100 temperature sensor of the high precision thermometer (Greisinger GMH 3710) inside the toluene bath close to the sample. Therefore we regard the measurement temperatures within the experimental error (±0.05 K) to be reliable. However in the case of the TDFRS setup (refer to section 3.2) the temperature sensor is stationary integrated in the brass sample holder unit in short distance from the sample. Thus, it was taken into consideration, that the measured temperature does not represent the true local temperature of the sample. This assumption should

be verified by utilizing the fact that the count rate of the read out laser in the TDFRS setup shows in general a sudden increase as function of the temperature, when a phase separation occurs. For this test we chose the $1 - \overline{2}$ phase transition of the balanced microemulsion system H_2O – n-octane – $C_{10}E_4$, $\alpha \approx 0.50$ [206, 207] because this phase transition can readily be observed and the corresponding phase boundary lies in the same region as the isotherme under study in our work. The $T(\gamma)$ - section of this system is shown at the left hand side of Figure 6.3-8. The dashed lines in the phase diagram, intersecting at the $\overline{\overline{X}}$ - Point of microemulsion system, were redrawn according to reference [206]. At surfactant mass fractions larger than approximately $\gamma \approx 0.16$, a lamellar phase occurs, which is in good agreement with the phase diagram presented in the work of *Kahlweit et al.* [207]. For the "tracking" of the phase transition with the TDFRS signal we chose a sample with a surfactant mass fraction of $\gamma = 0.154$. The $1 - \overline{2}$ phase transition temperature at $\gamma = 0.154$ was carefully determined to $T_{1-\overline{2}} = 27.85 \pm 0.05$ °C by optical inspection. At the right hand side of Figure 6.3-8 the count rate of the read-out signal of the TDFRS is shown as function of the temperature for this sample. It can be seen that the mean value of the count rate shows a strong increase from approximately 450 MHz at $T = 27.5$ °C to approximately 4000 MHz at $T = 27.6$ °C. This effect results from the scattering, appearing due to the phase separation at the $1 - \overline{2}$ transition (illustrated by the schematic sample tubes in Figure 6.3-8). Accordingly, the corresponding temperature measured in the sample holder of the TDFRS setup was determined to $T_{1-\overline{2}} = 27.55 \pm 0.05$ °C, which corresponds to a temperature difference of $\Delta T = +0.3$ K. We understand this difference as a local effect, which might be induced by the heating of the sample with the laser that is obviously not detected by the temperature sensor in the sample holder. Thus, for all following TDFRS measurements, the data is corrected by this difference.
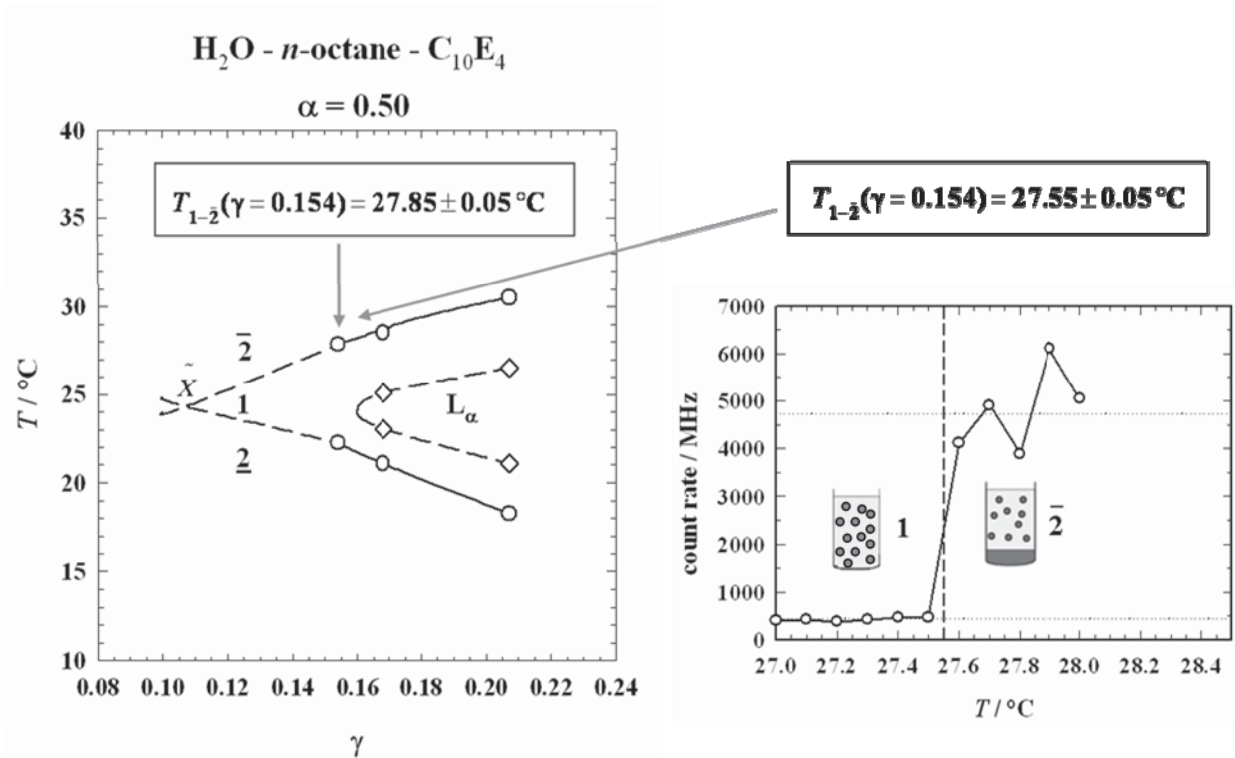
Figure 6.3-8: left: $T(\gamma)$-section of the microemulsion system H_2O – n-octane – $C_{10}E_4$ at $\alpha = 0.50$ [206, 207]. See text for details. Right: Count rate of the read out laser of the TDFRS experiment (circles, full line) as function of T for the microemulsion sample H_2O – n-octane – $C_{10}E_4$, $\alpha = 0.50$, $\gamma = 0.154$. The $1-\bar{2}$ phase transition is seen from a sudden increase of the count rate. The one- and two-phase state, respectively, are illustrated by the schematic sample tubes in the figure.

The diffusion coefficients D obtained by TDFRS as function of these corrected temperatures (black diamonds) are shown together with the initially obtained values (grey diamonds), in Figure 6.3-9. From the proceeding of the diffusion coefficients obtained from TDFRS as a function of the corrected temperature (black dashed line as guide to the eyes), it can be deduced, that the difference to values of D obtained by DLS (circles) in the vicinity of the *efb* is approximately $\Delta D \approx 0.7 \times 10^{-12}$ $m^2 s^{-1}$. This corresponds to a difference of approximately 4 %, which is in the range of the deviations between the TDFRS method and other methods obtained from the benchmark test by various groups [201, 202].
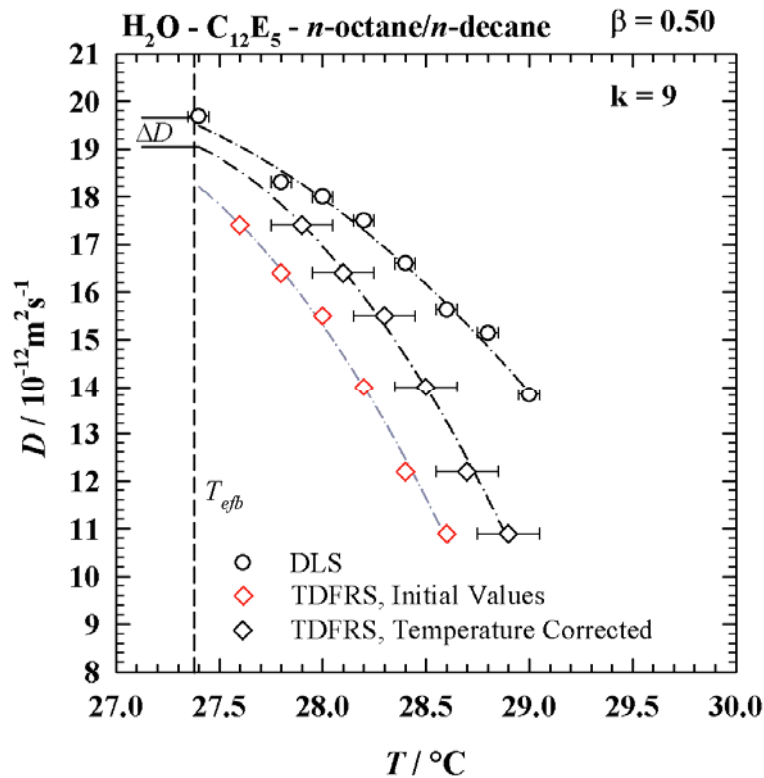
Figure 6.3-9: Diffusion coefficient *D* as a function of the temperature of H$_2$O - C$_{12}$E$_5$ - *n*-octane/*n*-decane, β = 0.50 (k = 9), γ$_a$ = 0.030, w_B = 0.0430, obtained by DLS (circles) and TDFRS (diamonds) measurements. The grey diamonds represent the values of the initial TDFRS measurements, before, and the black diamonds, respectively after including the temperature correction. The phase transition temperature T_{efb} = 27.36 ± 0.05 °C for this sample is marked by the straight dashed lines. The experimental error of the TDFRS measurement temperature is Δ*T* = ± 0.15 K, which is higher than for the DLS setup Δ*T* = ± 0.05 K, due to the stronger temperature fluctuation in the brass sample holder utilized in the TDFRS setup.

6.3.2.4   Comparison of TDFRS and DLS

In the next step we want to examine the hydrodynamic radius R_H of the microemulsion system H$_2$O – C$_{12}$E$_5$ – *n*-alkane as function of the alkane chain length k and the droplet volume fraction ϕ_C at isothermal conditions. Thereby the values of R_H obtained by TDFRS and DLS measurements should be compared. The compositions and 1 – 2 phase transition temperatures (T_{efb}) of the samples were given in Table 6-3. According to the observations described above, the temperatures of the TDFRS measurements were corrected by Δ*T* = +0.3 K.

Accordingly, Figure 6.3-10 shows the hydrodynamic radius R_H obtained from DLS (circles) and TDFRS (diamonds) measurements, respectively as function of the alkane chain length k (left) and as function of the volume fraction of the dispersed phase ϕ_{disp} (right).
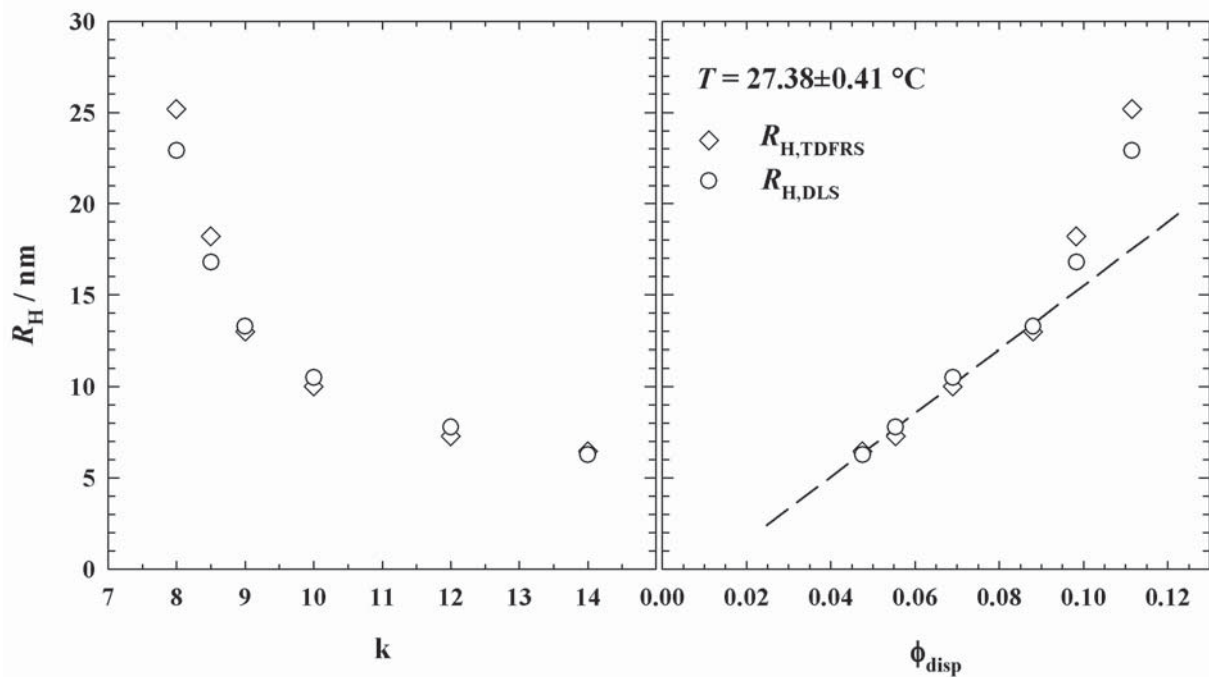
Figure 6.3-10: left: Hydrodynamic radius of the microemulsion droplets of the system $H_2O - C_{12}E_5 - n$-alkane under variation of the alkane chain length k at $T = T_{efb}$ for each sample (refer to Table 6-3) obtained from DLS (circles) and TDFRS (diamonds) measurements. Left: R_H as function of the alkyl chain length k. Right: R_H as function of the droplet volume fraction ϕ_{disp}.

From the left hand side of Figure 6.3-10 a nonlinear decline of the hydrodynamic radius R_H with increasing alkane chain length k is visible. Thereby, for both methods, R_H declines at first steeply with increasing k, however the slope of the decline becomes smaller with larger k. Note that, qualitatively the same trend was also observed for the evolution of the volume fraction of the dispersed phase ϕ_{disp} under variation of k, that was shown in Figure 6.3-2. According to [equation(2.37)], the droplet radius should show an almost linear dependence on ϕ_{disp}. At the right hand side of Figure 6.3-10 the hydrodynamic radius obtained by DLS (circles) and (TDFRS) measurements, respectively is shown as function of ϕ_{disp}. The aforementioned linear dependence of the hydrodynamic radius R_H on ϕ_{disp} is indicated by the dashed line. Up to $\phi_{disp} = 0.088$, which corresponds to the system $H_2O - C_{12}E_5 - n$-octane/n-decane ($\beta = 0.5$, k = 9) the values of the hydrodynamic radius R_H agree with this pattern. However for the systems of higher volume fractions of the dispersed phase, i.e containing n-octane/n-decane ($\beta = 0.75$, k = 8.5, $\phi_{disp} = 0.098$) and n-octane (k = 8, $\phi_{disp} = 0.112$), respectively, a significant deviation towards higher values of R_H is found. It might be possible that those deviations stem from a slight anisotropy of the aggregates, leading to an apparently larger hydrodynamic radius. It might furthermore be possible, that the detection of the *efb* by visual inspection yields a slightly overestimated phase transition temperature. This point will be discussed later.

Comparing the values of R_H obtained from DLS and TDFRS measurements, for the systems containing the alkanes *n*-octane/*n*-decane, $\beta = 0.50$ (k = 9), *n*-decane (k = 10), *n*-dodecane (k = 12) and *n*-tetradecane (k = 14) only slight deviations ($\Delta R_H \leq 6.6\%$) between both methods are found. In the context of the literature [201, 202], this can be considered as good agreement between the TDFRS and DLS. More significant deviations are again found for the two systems containing *n*-octane (k = 8) and *n*-octane/*n*-decane, $\beta = 0.75$ (k = 8.5), which are the systems with the two highest volume fractions of the dispersed phase ϕ_{disp}: for *n*-octane (k = 8), the values of R_H differ by approximately 9.0% while for the *n*-octane/*n*-decane – system, ($\beta = 0.75$ (k = 8.5), a slightly smaller difference of about 7.7% is observed. For those deviations different reasons could come into question: (i) It was already discussed, that the temperature dependent structural change of the aggregates around the *efb* becomes stronger with increasing value of k as a consequence of the location of the measurement point in the phase diagram, i.e. in closer vicinity of T_l (refer to Figure 6.3-1). Thus, the systems k = 8 and 8.5, respectively, might be more sensitive to small deviations of the measurement temperature resulting in structural changes of the aggregates. This might lead to a difference of the hydrodynamic radius R_H. (ii) It is known from the literature [155, 203], that at increased volume fractions of the dispersed phase ϕ_{disp} contributions due to particle-particle interaction occur, which affect the measured diffusion coefficient D. Since in the DLS, the diffusion coefficient is derived from the intensity fluctuation of the scattered light, while in the TDFRS the time dependant build up of the steady state is analyzed, it might be possible that the interactions effect the obtained diffusion coefficients to a different extend. Furtheremore, for the calculation of R_H only the most intensive peak is extracted from the CONTIN analysis of the correlation functions (refer to section 6.3.2.1). It might be a reasonable assumption, that slower modes are underrated by this procedure, which would lead to a smaler effective value of R_H. Nevertheless, these results suggest studying the influence of the volume fraction of the dispersed phase on the diffusion coefficient in a systematic way.

6.3.2.5   *Variation of the Droplet Number Particle Density*

Accordingly, the influence of the droplet volume fraction ϕ_{disp} on the diffusion of the microemulsion droplets at the *efb* should be studied under variation of the number particle density of the droplets n_p at constant droplet radius R. This can be achieved in an isothermal way by tuning the mass fraction of surfactant in the mixture of water and surfactant γ_a, i.e. proceeding along the straight binodal line, which represents the isothermal *efb* at the water-rich side of the *Gibbs* phase triangle (refer to Figure 2.4-8). The number particle density n_p of the droplets can be

calculated by dividing the total interfacial area, given by $\phi_{c,i}\, a_s/v_s$, by the interfacial area of one droplet $4\pi(R_0^2 + \sigma^2)$ [143, 144]:

$$n_p = \phi_{c,i}\, \frac{a_s}{v_s\, 4\pi(R_0^2 + \sigma^2)} . \qquad (6.4)$$

Since at the isothermal *efb* the radius can assumed to be constant, equation (6.4) implies that n_p is proportional to the volume fraction of the surfactant at the internal interface $\phi_{c,i}$.

This study was performed using the system $H_2O - C_{12}E_5 - n$-decane. We chose four water-plus-surfactant mass fractions, i.e. $\gamma_a = 0.0166$, 0.030, 0.0420 and 0.0540 (dividing the initial value $\gamma_a = 0.030$ by a factor 1.8 and multiplying by 1.4 and 1.8, respectively).

Figure 6.3-11 shows the $T(w_B)$ – sections of the microemulsion system $H_2O - C_{12}E_5 - n$-decane under variation of γ_a. The shape of the phase boundaries show the typical behavior of a strongly structured water-rich nonionic microemulsion, that was already discussed in the context of the variation of the n-alkane (refer to Figure 6.3-1). It can in addition be observed, that the extension of the one-phase region (1) increases upon increasing the surfactant mass fraction γ_a in the water/surfactant mixture. Accordingly, the amount of oil, which can be solubilized in a one-phase microemulsion, increases with increasing amount of surfactant in the system, i.e. from $\gamma_a = 0.0166$ Figure 6.3-11(a) over $\gamma_a = 0.0300$ (b) and $\gamma_a = 0.0421$ (c) to $\gamma_a = 0.0540$ (d). As a result, at constant temperature, the maximum mass fraction of oil w_B, being solubilized in the microemulsion (*emulsification failure*) increases almost proportional to γ_a.
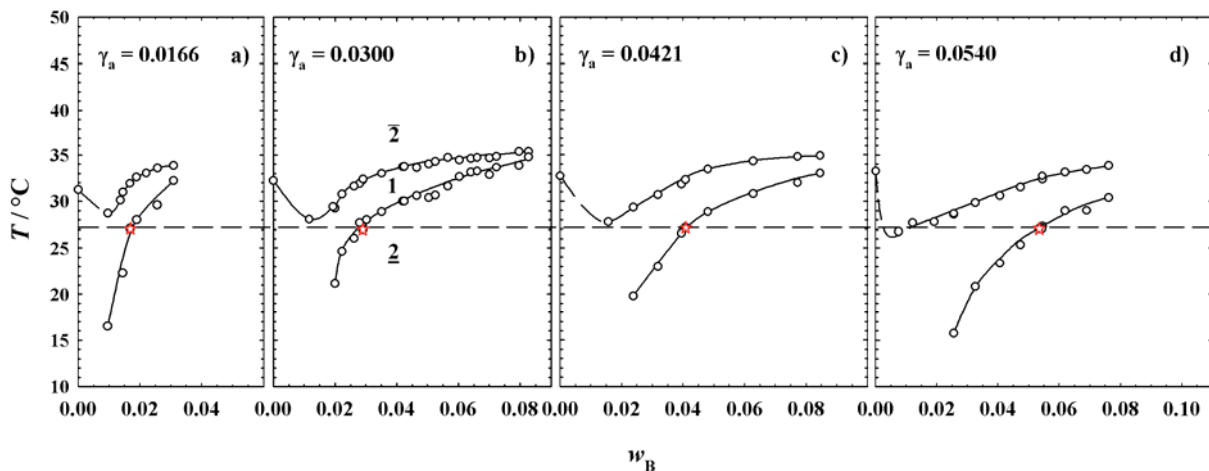
Figure 6.3-11: $T(w_B)$ – sections of the microemulsion system $H_2O - C_{12}E_5 - n$-decane under variation of γ_a. The red stars denote the intersection of the *efb* with the isotherme $T = 27.06 \pm 0.10\,°C$ (dashed line) as measurement points for the DLS measurements.

Figure 6.3-12 shows the isothermal emulsification failure boundary (*efb*) at the water-rich side of the isothermal *Gibbs* triangle of the system $H_2O – C_{12}E_5 – n$-decane at $T = 27.06$ °C. Thereby the *efb* is constructed from the intersection of the *efb* in the $T(w_B)$-sections with this isotherme. From Figure 6.3-12 it is visible, that the isothermal *efb* occurs indeed as a straight line in this region, as it is expected from the theory [55].
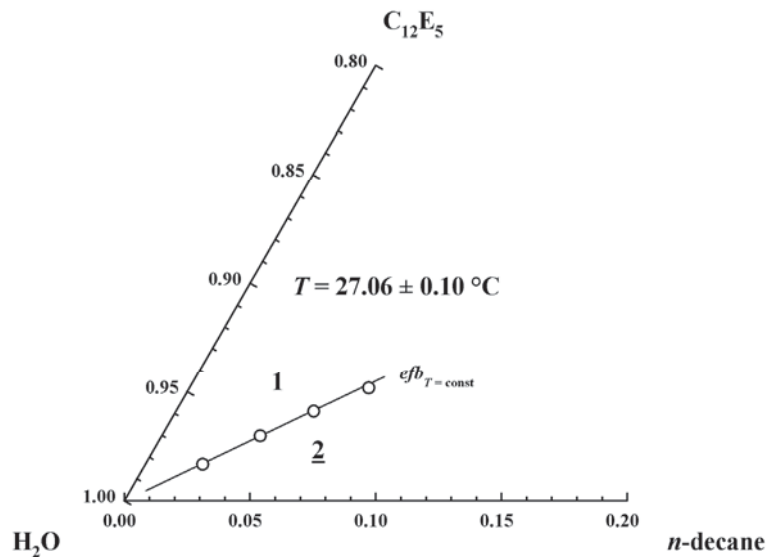
Figure 6.3-12: Isothermal *Gibbs* triangle of the system $H_2O – C_{12}E_5 – n$-decane. The isothermal emulsification failure boundary *efb* (straight black line) occurs as an almost straight line within the observed data range. Note that the origin of the *efb* at the water rich side is not exactly the corner of the triangle but the critical micelle concentration [55], which is not shown in the figure for reasons of clarity.

The radius of the oil-in-water (o/w) droplets can be estimated using equation (2.37). Since we do not determine the polydispersity by DLS in this study we assume monodisperse droplets for convenience, i.e. setting the relative polydispersity p to $p = 0$ in (2.37). $\phi_{c,i}$ is determined from γ_a and w_B, by using the corresponding densities and taking into account the mass fraction of monomerically dissolved $C_{12}E_5$ in n-decane $\gamma_{mon,b}$, taken from reference [206]. With those assumptions, and the values of the volume of a surfactant molecule v_s and the surfactant head group area a_s of $v_s = 698$ Å^3 of $a_s = 58.85$ Å^2 [50, 130], respectively, the radius is calculated to $R_{th} = 6.66 \pm 0.12$ nm.

Table 6-4: Mass fraction γ_a of surfactant in the mixture of water and surfactant and oil mass fraction w_B of the samples of the system $H_2O - C_{12}E_5 - n$-decane at the *efb*. The corresponding volume fractions of the internal interface $\phi_{c,i}$ were calculated by using the monomeric solubility of $C_{12}E_5$ in *n*-decane together with the densities given in Table 8-1. The $1 - \underline{2}$ phase transition temperatures $T_{1-\underline{2}}$ (T_{efb}) corresponds to red stars in Figure 6.3-11. The number particle densities n_p was calculated according to relation (6.4) with the theoretical radius R_{th} according to equation (2.37). The diffusion coefficient and the hydrodynamic radius was obtained from DLS measurements at $T = T_{efb}$.

γ_a	w_B	$\phi_{c,i}$	ϕ_{disp}	$T_{1-\underline{2}}$ (*efb*) [°C]	R_{th} [nm]	n_p [$10^{16}cm^{-3}$]	$D_{efb,DLS}$ [$10^{-12}m^2s^{-1}$]	$R_{H, efb, DLS}$ [nm]
0.0166	0.0168	0.0165	0.0395	27.05	6.71	2.46	24.5±1.0	10.6±0.4
0.0300	0.0290	0.0293	0.0689	26.97	6.54	4.59	24.7±1.2	10.5±0.5
0.0420	0.0408	0.0403	0.0958	27.15	6.63	6.15	26.1±1.4	10.0±0.5
0.0540	0.0534	0.0508	0.123	27.06	6.78	7.42	26.8±1.3	9.7±0.44

The compositions of the samples (γ_a and w_B) and the corresponding $1 - \underline{2}$ phase transition temperatures (T_{efb}) are given in Table 6-4 together with the calculated number particle densities according to relation (6.4). In Figure 6.3-13 the number particle density n_p is shown as function of the volume fraction of the dispersed phase ϕ_{disp}.
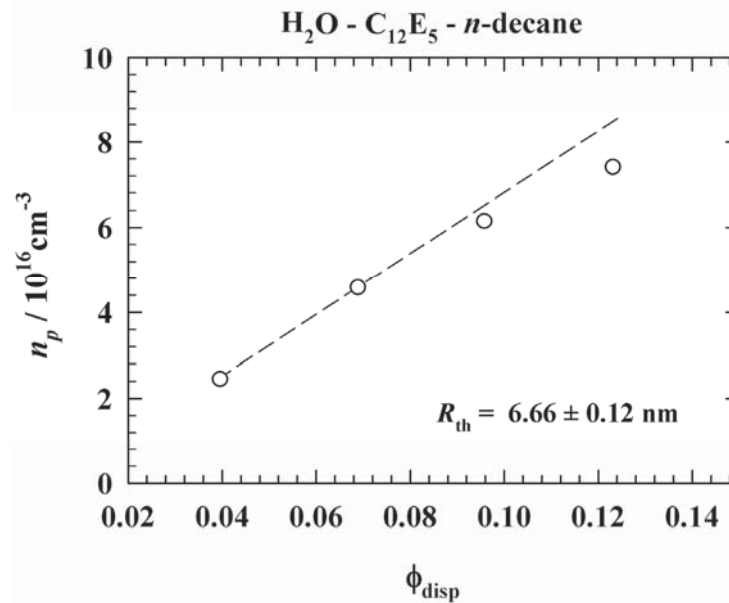
Figure 6.3-13: Number particle density n_p as function of the volume fraction ϕ_{disp} of the dispersed phase for the system $H_2O - C_{12}E_5 - n$-decane. The values of ϕ_{disp}, and n_p can be found in Table 6-4. The mean value of R_{th} was calculated from the values of R_{th} given in Table 6-4. The measurement temperature is $T = 27.06 \pm 0.10$ °C. See text for details.

Thereby with increasing ϕ_{dsip}, the number particle density deviates from a linear trend (indicated by a dashed line) towards lower values of n_p. In the approach leading to the calculation of the

theoretical radius (2.34) [55], it is assumed that $\phi_{c,i}$ scales almost linearly with γ_a. However a slight deviation might occur for this assumption, due to the fact that with increasing amount of oil in the system, some of the surfactant is partly dissolved "out" of the internal interface due to the monomeric solubility of $C_{12}E_5$ in n-decane [206]. Since we included this into the calculation and furthermore took into account the monomerically dissolved surfactant in n-decane also in the calculation of the radius, this might explain the nonlinear behavior of n_p with increasing values of ϕ_{disp}.

In the next step, DLS measurements were performed for the four samples of system H_2O – $C_{12}E_5$ – n-decane and the diffusion coefficients D were determined at the *efb* in the same way as was described above (refer to Figure 6.3-6). In the upper part of Figure 6.3-14 the (apparent) diffusion coefficients D are displayed, while the corresponding hydrodynamic radii R_H are shown in lower part, both as function of the droplet volume fraction ϕ_{disp}.
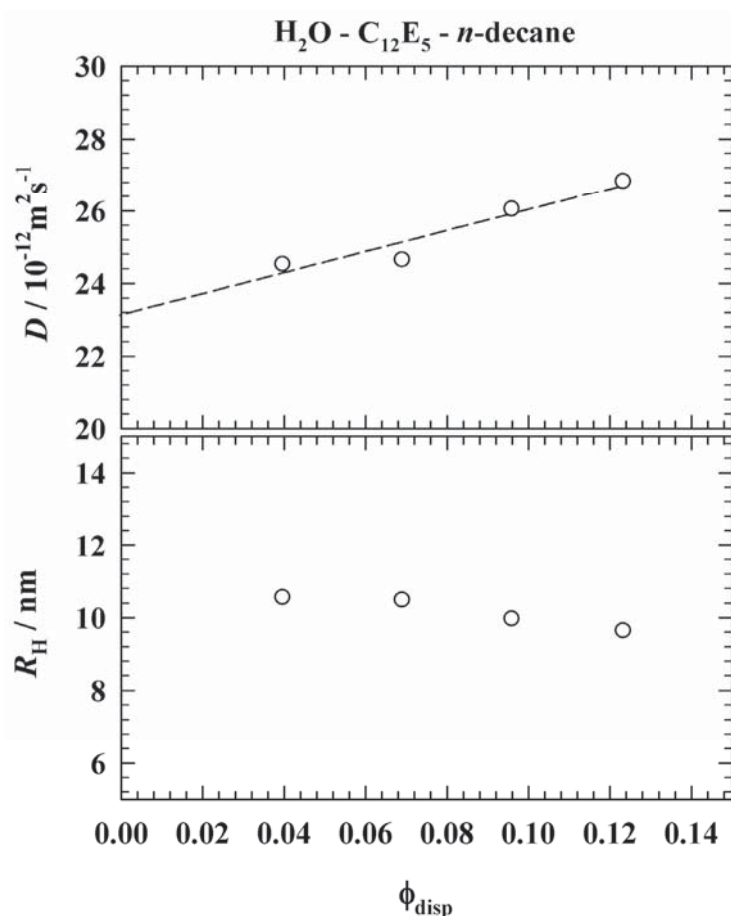
Figure 6.3-14: Top: Diffusion coefficient D of the microemulsion droplets of the system H_2O – $C_{12}E_5$ – n-decane, as a function of the droplet volume fraction ϕ_{disp} at constant temperature $T = 27.06 \pm 0.10\,°C$ and constant theoretical radius $R_{th} = 6.66 \pm 0.12$ nm according to equation (2.37). The dashed line represents a fit of equation (6.5) to the data points. Bottom: Effective hydrodynamic radius R_H corresponding to the diffusion coefficients D according to the *Stokes Einstein* relation as a function of ϕ_{disp}. See text for details.

It can be observed, that the diffusion coefficient D increases with increasing ϕ_{disp}. From the literature [203, 208, 209] it is known, that inter-particle interactions result in a faster diffusion of the particles. Quantitatively a linear dependence is expected according to the relation [203, 209]:

$$D = D_0 (1 + a\phi_{disp}), \qquad\qquad (6.5)$$

where D is the measured (apparent) diffusion coefficient, at given volume fraction of the interacting aggregates ϕ_{disp}. D_0 is the self diffusion coefficient and a is the dynamic virial coefficient. As can be seen from this relation, the value of D_0 can be determined by extrapolation of D to zero volume fraction ϕ_{disp}. The dashed line in the upper part of Figure 6.3-14 represents a fit of D as function of ϕ_{disp} to (6.5), yielding values of $D_0 = 23.09 \times 10^{-12} m^2 s^{-1}$ and $a = 1.29$. It can however be seen, that for the first two samples at $\phi_{disp} = 0.0395$ and $\phi_{disp} = 0.0689$, respectively, just a small difference is visible. At further increased volume fractions of ϕ_{disp}, i.e. from $\phi_{disp} = 0.0958$ to $\phi_{disp} = 0.123$, D shows a more significant increase. It might therefore be possible that a significant influence of the inter-particle interactions becomes evident only at increased droplet volume fractions. Nevertheless, the qualitatively expected trend of a faster diffusion due to interparticle interactions is confirmed. As can be seen from the lower part of Figure 6.3-14, the opposite trend is reflected in the apparent hydrodynamic radius R_H, being calculated by using the *Stokes Einstein* relation (3.7).

However, the resulting decline of R_H with increasing ϕ_{disp} is in contradiction with the result, obtained from the variation of the *n*-alkane in the microemulsion system $H_2O – C_{12}E_5 – n$-alkane at constant temperature Figure 6.3-10. For the latter variation a strong trend towards a significantly slower diffusion, and thus a significantly higher apparent hydrodynamic radius R_H, was found at increasing volume fraction ϕ_{disp}.

From the results presented in this section (6.3.2) it becomes obvious, that the determination of the radius by DLS measurements bears uncertainties. The main reason for this is that the diffusion of the droplets depends not only on their size, but also on the interparticle interaction as well as the viscosity within the system, which is also not exactly known. This emphasizes the necessity to determine the radius of the aggregates by means SANS, which allows separating the interparticle interaction contribution from the structural contribution of the particle itself.

6.3.3 Small Angle Neutron Scattering (SANS) Measurements

SANS measurements yield a scattering intensity distribution in reciprocal space, which is related to the scattering length density distribution in real space (see e.g. [131]). Accordingly, by adjusting the scattering contrast in the system, the dimension of the aggregates can be extracted. Furthermore, in many cases the type and length scale of the interparticle interaction can separately be obtained from the scattering intensity [137]. In this work, the microemulsion droplets were prepared in *film contrast*, whereby the scattering length density of the oil-phase inside the droplets is exactly matched to the scattering length density of the surrounding water. Thus, the coherent scattering intensity of the surfactant film is obtained, which should resemble the scattering pattern of a spherical shell. Accordingly, for the analysis of the experimental scattering intensity distribution a model of polydisperse spherical shells [143, 144] should be applied.

In the following the results of the neutron scattering experiments on the system $D_2O – C_{12}E_5 – $ *n*-alkane at constant surfactant to water-plus-surfactant ratio ($\gamma_{a,h} = 0.030$) and temperature under variation of the alkane chain length are presented. Before the structural parameters of the microemulsion droplets are extracted according to the model approach, mentioned above, a qualitative analysis of the scattering curves will be performed.

6.3.3.1 *Qualitative Interpretation of the Scattering Curves*

It is known, that in the absence of significant interparticle interaction, that lead to a modulation of the scattering intensity at low *q*-values, the scattering intensity of a spherical object becomes independent of the scattering vector *q* in the low *q* region. Thus, in this region the scatting intensity of spherical microemulsion droplets as function of *q* should exhibit an almost horizontal pattern in a double logarithmic plot. Accordingly, in Figure 6.3-15 the experimentally obtained scattering intensity $I(q)$ is shown as function of the scattering vector *q* in a double logarithmic scale for the system $D_2O – C_{12}E_5 – $ *n*-alkane, with *n*-octane (a), *n*-octane/*n*-decane, $\beta \approx 0.50$ (b), *n*-decane (c) and *n*-dodecane (d) as the alkane component.
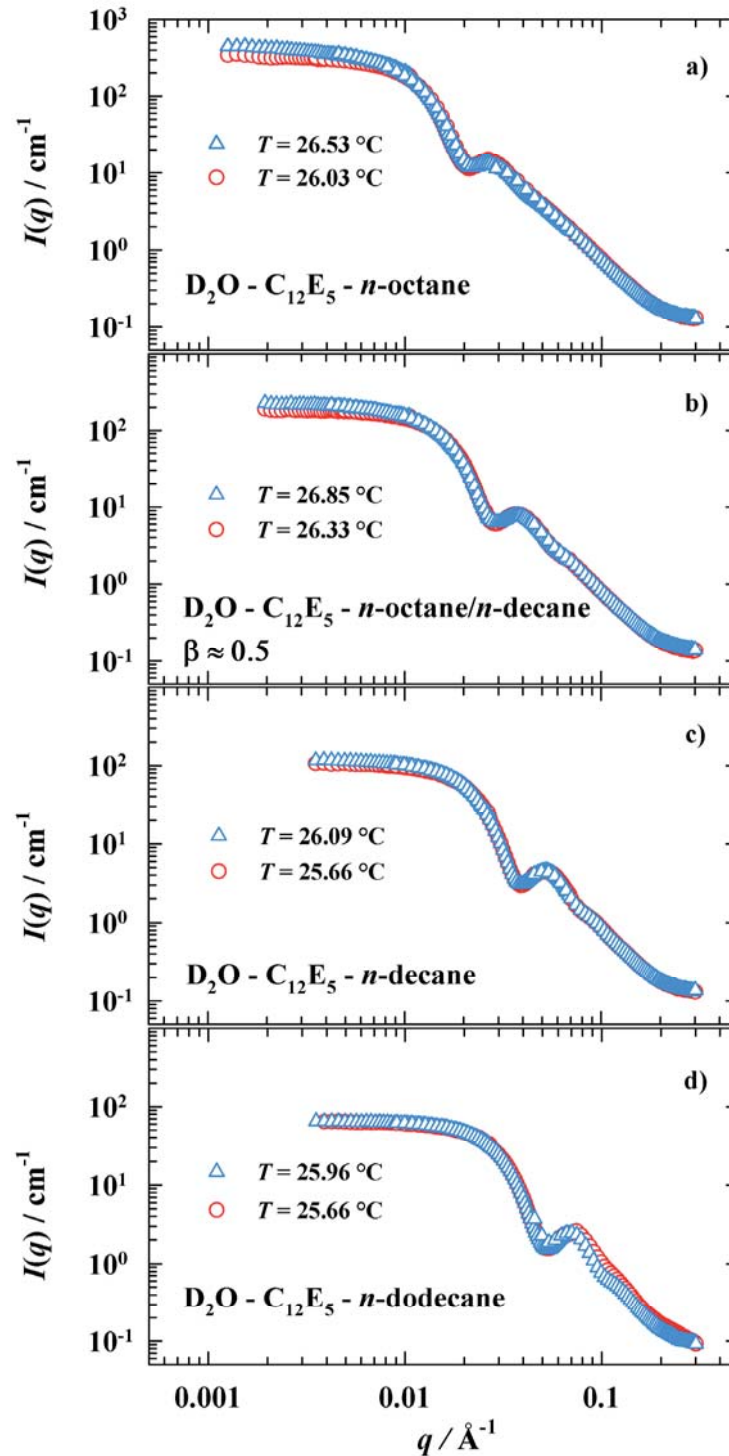
Figure 6.3-15: Experimental scattering intensity $I(q)$ as function of q for the system $H_2O - C_{12}E_5 - n$-alkane ($\gamma_{a,h} = 0.030$), with n-octane (a), n-octane/n-decane, $\beta \approx 0.5$ (b), n-decane (c) and n-dodecane (d) as n-alkane components. The measurements were performed at temperatures in the vicinity of $T_{\underline{2}\text{-}1}$ (T_{efb}) for each sample. See Table 6-5 for the composition and T_{efb} of the samples.

The composition and $\underline{2}$-1 phase transition temperature, $T_{\underline{2}\text{-}1}$ (T_{efb}) of the samples are given in Table 6-5. From Figure 6.3-15 it can be observed, that for the system containing n-octane the scattering intensities at small q-values get slightly increased when the temperature is increased

by $\Delta T = 0.5$ K. Thereby, the scattering curve (blue triangles), being measured almost exactly at the *emulsification failure boundary* of the sample ($T_{efb} = 26.47$ °C, c.f. Table 6-5) shows a slight increase with decreasing q-values in this region. It is known from the literature, e.g. [90, 170, 210], that this slight increase of $I(q)$ is an evidence for slightly elongated aggregates. In contrast, as the measurement temperature was lowered by approximately $\Delta T \sim$ -0.4 K (red circles in Figure 6.3-15 a) no increase of the forward scattering intensity was observed. This observation is a hint that the *efb* was indeed slightly overrated by optical inspection of the phase transition (refer to section 6.2). For the system containing *n*-octane/*n*-decane, $\beta \approx 0.50$ as alkane component (Figure 6.3-15 b) also a small difference between the forward scattering intensities of the scattering curves measured at $T = 26.85$ °C (blue triangles) and 26.33 °C (red circles) can be seen. For this sample the phase transition temperature T_{efb} at the *efb*, was determined to $T_{efb} = 26.79$ °C (c.f. Table 6-5). For the system containing *n*-decane (Figure 6.3-15 c) a small variation of the measurement temperature of $\Delta T = 0.4$ K leads still to a very slight deviation of the scattering intensity in the low q-range. In the scattering pattern of the system containing *n*-dodecane as alkane (Figure 6.3-15 d) a small variation of the measurement temperature of $\Delta T = 0.3$ K, leads to no considerable effect. For *n*-tetradecane (curves not shown in Figure 6.3-15) even no observable effect in the scattering pattern was found, even when the temperature was changed by $\Delta T \approx 1.0$ K.

Table 6-5: Composition of the SANS samples of the water-rich microemulsions D_2O – $C_{12}E_5$ – *n*-alkane at $\gamma_{a,h} = 0.030$ and given mass fraction of oil $w_{B,h}$ in the respective protonated systems, mass fraction of oil in the SANS samples $w_{B,d}$, volume fraction of oil ϕ_B, volume fraction of the dispersed phase ϕ_{disp} and phase transition temperature $T_{2\text{-}1}$ (T_{efb}). The *n*-alkanes are mixtures of protonated and deuterated compounds (see Table 6-1, subsection 6.2).

n-alkane (d/h) / k	$w_{B,h}$	$w_{B,d}$	ϕ_B	ϕ_{disp}	$T_{2\text{-}1}$ (T_{efb}) [°C]
n-octane / 8	0.0600	0.0626	0.0831	0.1115	26.47
n-octane/*n*-decane ($\beta_{octane} \approx 0.5$) / 9	0.0430	0.0447	0.0591	0.0880	26.79
n-decane / 10	0.0290	0.0301	0.0392	0.0690	25.68
n-dodecane / 12	0.0191	0.0197	0.0252	0.0554	25.97
n-tetradecane / 14	0.0131	0.0136	0.0171	0.0475	26.45

These results show that the effect of a small temperature variation on the microstructure, i.e. leading to elongation of the microemulsion droplets, gets stronger with increasing volume fraction of the dispersed phase ϕ_B. This is in agreement with the results, previously observed from the DLS measurements (Figure 6.3-6) and might be related to the location of the

measurement point at the *efb* within the $T(w_B)$-section, i.e. (i) to the vicinity of the lower critical end point temperature T_o and (ii) to the narrow one-phase region of those samples.

Due to the slight anisotropy of the droplets at T_{efb}, in the two samples with the highest droplet volume fraction ϕ_{disp}, [*n*-octane and *n*-octane/*n*-decane ($\beta \approx 0.5$), respectively] (Figure 6.3-15 a and b) for their further evaluation the scattering curves, measured at slightly lower temperatures (red circles) were used. For the other systems we used the scattering curves, which were measured in close vicinity of the *efb*. Figure 6.3-16 summarizes the scattering curves that were chosen for further evaluation.
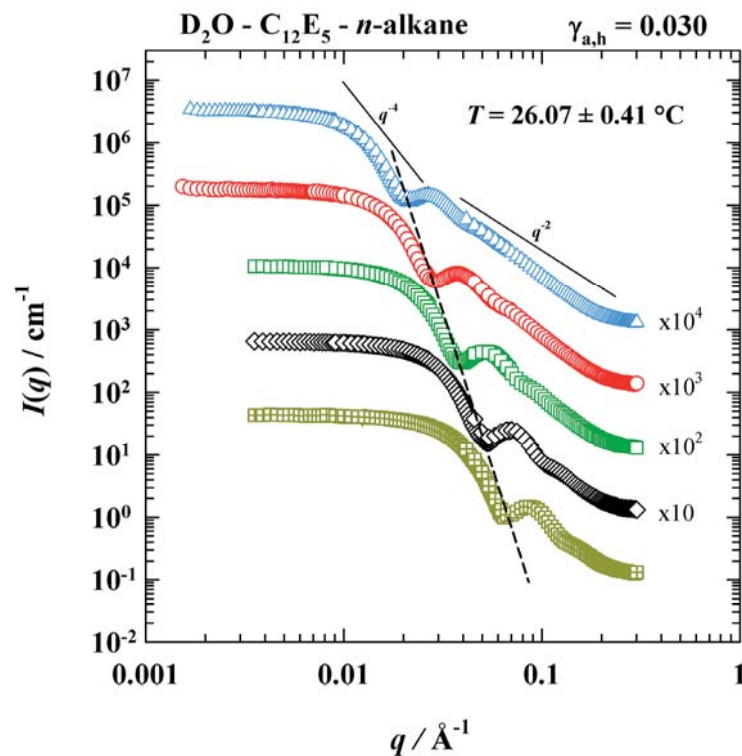
Figure 6.3-16: Scattering curves microemulsions of the system $D_2O – C_{12}E_5 – n$-alkane, $\gamma_{a,h} = 0.030$ under variation of the *n*-alkane at $T = 26.07 \pm 0.41$ °C. Blue triangles: *n*-octane, k = 8, $T = 26.03$ °C. Red circles: *n*-octane/*n*-decane, $\beta \approx 0.5$, k = 9, $T = 26.33$ °C. Green squares: *n*-decane, k = 10, $T = 25.66$ °C. Black diamonds: *n*-dodecane, k = 12, $T = 25.95$ °C. Dark yellow crossed squares: *n*-tetradecane, k = 14, $T = 26.48$ °C. The corresponding droplet volume fraction ϕ_{disp} and phase transition temperature at the *efb* T_{efb} can be found in Table 6-5.

All scattering curves Figure 6.3-16 resemble the typical features of the scattering from polydisperse shells [144]: After the almost constant scattering intensity in the low *q*-regime, with increasing *q*-value the scattering intensity decreases steeply with q^{-4} until the first minimum at intermediate *q*-values. The position of this minimum, which is followed by a small maximum, is related to the radius of the shells according to $q \propto 2\pi / R_0$. Thereby, it can already qualitatively be seen (dashed line as guide to the eyes), that the minimum in shifts systematically to higher values

of the scattering vector q with decreasing volume ϕ_{disp} of the dispersed phase (c.f. Table 6-5), i.e. from k = 8 (blue triangles) over k = 9 (red circles), k = 10 (green squares) and k = 12 (black diamonds) to k = 14 (dark yellow crossed squares). The smearing of the minimum and the following maximum depends, next to the wave-length distribution of the incident neutrons, on the polydispersity of the radius that leads to a smoothing of the oscillations in this part of the scattering curve. Subsequent minima and maxima at higher q-values from these oscillations can also be seen for the systems with smaller droplet radius [n-tetradecane (dark yellow crossed spheres) and n-dodecane (black diamonds)], but disappear in the scattering curves at increasing droplet radius [from n-decane (green spheres) over n-octane/n-decane, $\beta \approx 0.5$ (red circles) to n-octane (blue triangles)]. At further increased q-values the scattering intensity decays with an almost q^{-2}-like dependence until the scattering intensity equals the incoherent background scattering at high q-values. It will later be seen, that this decay deviates from a q^{-2}-like pattern as a result of the diffuse nature of the amphiphilic film, as has been shown in reference [144].

6.3.3.2 *Quantitative Analysis*

In the next step, the scattering curves should be fitted to model scattering intensities in order to obtain the structural parameters of the microemulsions. In a first approach we tried to describe the experimental scattering intensities of the microemulsion droplets with a form factor model for polydisperse spherical shells with diffuse interface [144]. Since this model accounts for the coherent scattering of the surfactant film only, perfect matching of the scattering length densities of the oil inside the microemulsion droplet and the surrounding bulk water is required ($\rho_{bulk} = \rho_{core}$). However, applying this model in the first analysis of the scattering data (not shown), we were not able to describe the experimental scattering intensity of the microemulsion droplets quantitatively. As the reason for this discrepancy it became obvious, that we did not include the undeuterated impurities of the n-alkanes in the calculation of their scattering length densities ρ [refer to equation (6.2)] as well as the monomerically dissolved surfactant [206]. Hence, the above-mentioned condition for shell contrast ($\rho_{bulk} = \rho_{core}$) is not fulfilled and coherent scattering from the droplet core must be taken into account. Therefore we applied the model for polydisperse shells with diffuse interface and additional coherent scattering from the droplet core (2.51), derived by *Foster et al.* [143]. We calculated the scattering contrast of the core scattering ($\Delta\rho_{core} = \rho_{bulk} - \rho_{core}$), by including the monomeric solubility of $C_{12}E_5$ [206] in the respective n-alkanes as well as the fraction of undeuterated impurities as stated by the supplier of the material (refer to Table 8-1) in the calculation of ρ_{bulk} according to equation (6.2).

Figure 6.3-17 shows the experimental scattering intensities $I(q)$ after subtraction of the incoherent background scattering (red circles) as function of the scattering vector q in a double logarithmic plot for the $D_2O - C_{12}E_5 - n$-alkane microemulsion ($\gamma_{a,d} = 0.0272$) with different alkanes. The dashed lines, respectively, represent the scattering intensities of the form factor for polydisperse spherical shells with diffuse interface and core scattering (2.51), i.e. without any coherent scattering contribution due to interparticle interactions [$S(q) = 1$ in equation (2.44)]. It can be seen in Figure 6.3-17a-e that this model describes the declining part including the smeared oscillations of the experimental scattering intensity as function of q quantitatively for all microemulsions under study. Thereby, the mean radius R_0, its polydispersity σ, and the thickness of the diffuse amphiphilic film according to equation (2.52) are obtained as model parameters. The parameter values which are given in Table 6-6 will be discussed below. However, before that, the interparticle interactions should be discussed.

As can be seen, the forward scattering intensity calculated by the form factor model (dashed lines in Figure 6.3-17) is systematically higher than the experimental values. This indicates the existence of excluded volume interactions in the microemulsion system, leading to systematically smaller experimental scattering intensities at low q-values. To account for those interactions, we applied the structure factor for hard spheres [149] (2.62) as well as the structure factor for hard spheres with surface adhesion [150, 151], (*sticky hard spheres*) (2.66). In the model of hard spheres, the model parameters are the effective hard core diameter d_{HS} [149], which was set to $2(R_0+t)$ and the droplet volume fraction $\phi_{disp} = \phi_B + \phi_C$. In analogy, the parameter in the sticky hard sphere model (refer to 2.5.4.6) is the effective hard core diameter d_{eff}, which was equally set to $d_{eff} = 2(R_0+t)$. Furthermore, the relative thickness ε of the attractive well of the potential is given by $\varepsilon = t/d_{eff}$. Since the effective volume fraction η, in this model [151] is also defined by ϕ_{disp}, R_0 and t, via equation (2.70), the remaining free parameter, in order to describe the attractive nature of the microemulsion droplets is the depth u_0 of the attractive well [equation (2.67)].
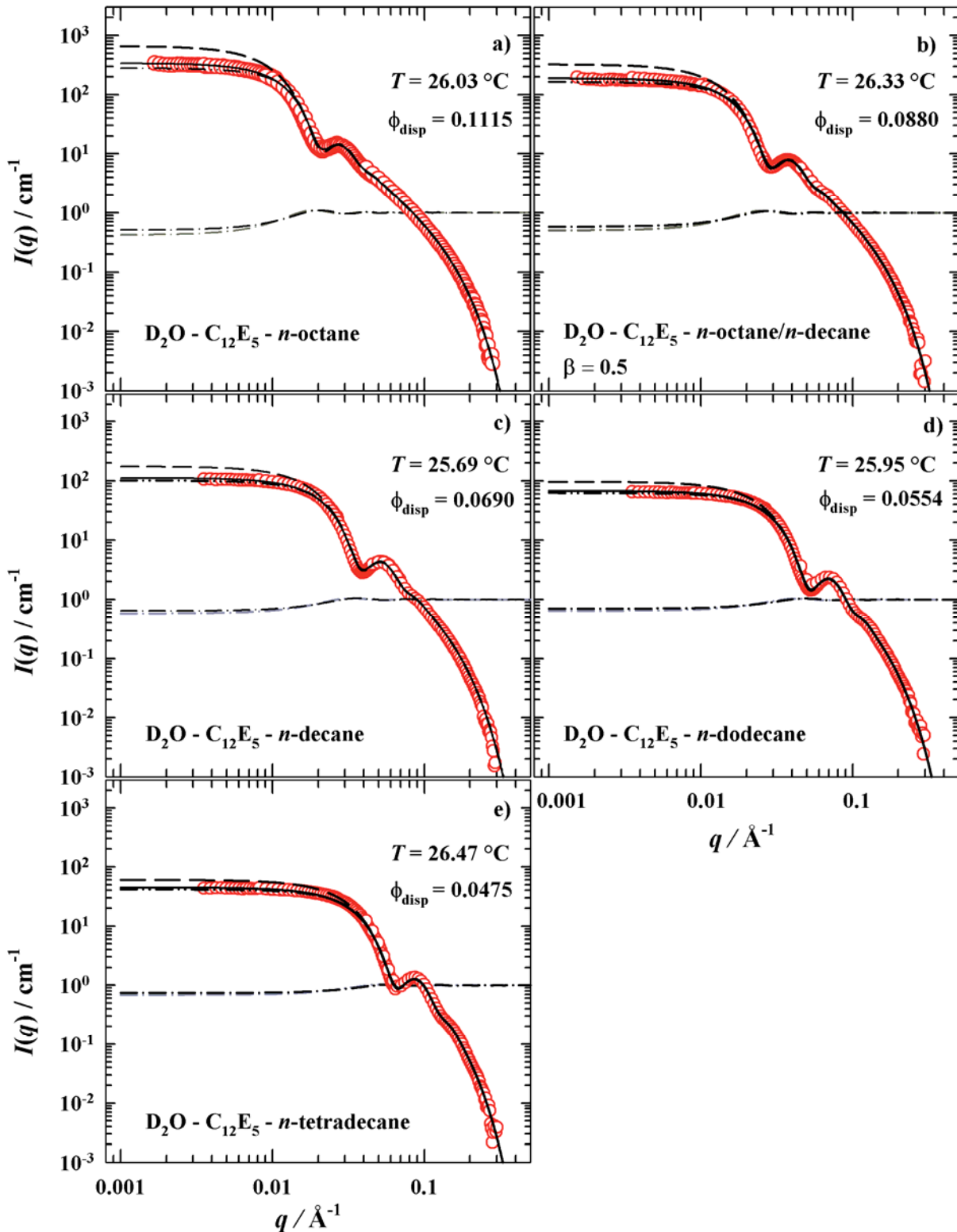
Figure 6.3-17: Scattering curves of the microemulsions of the system $D_2O – C_{12}E_5 – n$-alkane at $\gamma_{a,d} = 0.0272$. The experimental scattering intensity is (red circles) is shown after subtraction of the incoherent background scattering. The full lines are the modeled scattering intensities being the product of a form factor $P(q)$ for spherical shells with diffuse film and core scattering (dashed line) and the structure factor $S(q)$ for sticky hard spheres (black dash-dotted line). Applying a structure factor for hard spheres (grey dash-dotted line) results in a slightly lower scattering intensity (dash-dash-dotted line). This difference gets smaller with decreasing droplet volume fraction, ϕ_{disp} (i.e. in the order a, b, c, d, e). See text for details.

From Figure 6.3-17a, which is the system with the highest droplet volume fraction (D_2O – $C_{12}E_5$ – *n*-octane) it is visible that the scattering intensity (full black line) that is calculated by including the sticky hard sphere structure factor describes the experimental scattering intensity almost perfectly. Thereby it can be seen, that the structure factor (black dash-dotted line) coincides with the calculated intensity of the form factor (dashed line) at *q*-values higher than approximately $q \geq 0.015 \,\text{Å}^{-1}$. The scattering intensity, which is calculated by including the hard sphere structure factor, is represented by the dash-dot-dotted line in Figure 6.3-17a-e, respectively. It can be observed, that the hard sphere model results in systematically smaller scattering intensities at low *q*-values (grey dash-dotted line) compared to the sticky hard sphere model (black dash-dotted lines). Accordingly, a perfect description of the experimental scattering intensity could not be achieved by using the model of pure repulsive hard sphere interaction. It is furthermore visible from Figure 6.3-17a-e, that the difference between both structure factor models decreases with increasing droplet volume fraction ϕ_{disp}, i.e. in the order a, b, c, d, e: For the system containing *n*-decane as alkane component with $\phi_{disp} = 0.0690$ (Figure 6.3-17c) the structure factors are almost indistinguishable (black and grey dash dotted lines) and even coincide for the systems with the highest droplet volume fraction ϕ_{disp} (Figure 6.3-17d and e). Thus, it can be deduced, that the nature of the interaction between the microemulsion droplets is not sufficiently described by pure repulsive hard sphere interaction. This was also found for nonionic micelles in water [176], and water-swollen microemulsion droplets [143]. The attractive interactions might be related to *Van der Waals* interaction. Since the strength of the attractive interaction varies with ϕ_{disp} (see u_0 in Table 6-6) entropic effects might also be assumed.

Table 6-6: Model parameters of the SANS measurements of the water-rich microemulsions $D_2O – C_{12}E_5 – n$-alkane at $\gamma_{a,h} = 0.030$ ($\gamma_{a,d} = 0.0272$) (for the sample composition refer to Table 8-4). Parameter: Surfactant volume fraction ϕ_c, Surfactant volume fraction in the internal interface $\phi_{c,i}$, alkane volume fraction ϕ_B, droplet volume fraction ϕ_{disp}, Temperature SANS measurement T_{SANS}, factor f, Mean droplet radius R_0, droplet polydispersity σ, thickness of the diffuse interface t, rel. thickness of the attractive potential well ε, effective droplet volume fraction η, potential depth u_0, effective diameter d_{eff}, and hard sphere diameter d_{HS}.

alkane(d/h)	ϕ_C	$\phi_{C,i}$	ϕ_{disp}	T_{SANS} [°C]	f	R_0 [Å]	σ [Å]	t [Å]	p	ε	η	$-u_0$ [kT]	d_{eff} (d_{HS}) [nm]
n-octane	0.0284	0.0270	0.1115	26.03	1.35	152.0±3.5	28.0	6.8	0.18	0.021	0.117	1.52	317.6
n-octane/ n-decane ($\beta_{Octane} \approx 0.5$)	0.0292	0.0281	0.0880	26.33	1.38	110.0±3	19.0	6.7	0.17	0.029	0.095	1.23	233.4
n-decane	0.0298	0.0291	0.0690	26.09	1.40	81.0±2.5	13.7	6.5	0.17	0.037	0.077	0.91	175.0
n-dodecane	0.0302	0.0298	0.0554	25.95	1.40	60.0±1.5	9.5	6.5	0.16	0.049	0.064	0.76	133.0
n-tetradecane	0.0305	0.0301	0.0475	26.48	1.42	47.2±1.5	7.6	6.6	0.16	0.061	0.057	0.67	107.6

6.3.3.3 Comparison between SANS, DLS and TDFRS

The main objective of the SANS measurements, was to determine the radius of the microemulsion droplets. Thus, in Figure 6.3-18 we compare the values of the radius obtained from SANS, DLS and TDFRS [205], respectively, being shown as function of the droplet volume fraction ϕ_{disp}. In addition, the theoretical radius R_{th} was calculated with equation (2.37), using the values of the polydispersity index $p = \sigma/R_0$ that has been obtained from the fits of the model for polydisperse shells to the experimental scattering intensities (Table 6-6) .

A value of 6 Å was added to the originally obtained values (Table 6-6) of the mean radius R_0, obtained by the SANS measurements. This equals approximately half of the length of a surfactant molecule and was done in order to account for the thickness of the hydration layer.

In Figure 6.3-18 it can be seen, that the mean radius R_0 (triangles) shows an almost perfect linear dependence of the droplet volume fraction ϕ_{disp}. For comparison, the value of the cross section, that was found by *Menge et al.* [211] for cylindrical aggregates of pure $C_{12}E_5$ in water at $T = 20\,°C$ is also shown after addition of 6 Å (crossed triangle). This would correspond to a droplet volume fraction of $\phi_{disp} = 0.031$ ($w_B = 0$, $\gamma_a = 0.030$) in our study. Extrapolating the values of R_0 (triangles) to this droplet volume fraction, one finds a slightly higher radius. This can be understood since in the work by *Menge et al.* the aggregates exhibited a strongly

elongated structure, which is in agreement with a smaller cross section radius. A similar decrease of the cross section along with the transition from spherical to cylindrical aggregates was e.g. also found for micelles of $C_{12}E_6$ in water in this work (refer to section 4). Comparing the values of R_0 (triangles) with the theoretical values of R_{th} (squares), it is found that the values obtained by SANS are slightly higher, than R_{th} at increasing droplet volume fraction ϕ_{disp}. The reason for this systematic deviation might most probably be the relative polydispersity p of the droplets, being included in the calculation of R_{th}, which increases with increasing ϕ_{disp} (refer to Table 6-6) leading in turn to a smaller value of R_{th} [refer to equation (2.37)].

Between the mean radius obtained by SANS, including the hydration layer, $R_0 + 6$ Å, and the values of the hydrodynamic radii R_H obtained by TDFRS and DLS up to $\phi_{disp} = 0.088$ [n-octane/n-decane ($\beta_{Octane} \approx 0.5$, k = 9)] an offset of approximately $10 - 18$ % is found. This observation might indicate, that the influence of the hydration layer is slightly underestimated by adding a value of 6 Å to the mean radius of the SANS data. It can furthermore be observed, that the hydrodynamic radii obtained from TDFRS and DLS measurements (black circles and triangles in Figure 6.3-18) follow a linear trend as function of ϕ_{dis} up to $\phi_{disp} = 0.088$. However, at higher values of ϕ_{disp} a significant deviation from the linear trend towards larger values of R_H is found, which was already discussed before in section 6.3.2.4 (Figure 6.3-10). It was pointed out, that a small anisotropy of the microemulsion droplets might be the reason for those larger values of R_H. This assumption is supported by the observations from Figure 6.3-15a and b, respectively. There it became obvious, that at the measurement temperature $T = T_{efb}$, that was assigned to the *efb*, the scattering pattern of the microemulsions with higher droplet volume fractions ϕ_{disp} resemble already slight anisotropies. If the measurement temperature is lowered by approximately 0.4 K below T_{efb}, the scattering pattern of almost perfect spherical droplets was found. This suggests, that the phase transition temperature at the *efb*, $T_{1\text{-}2}$ (T_{efb}), has probably slightly been overestimated by the optical inspection method, described in section 6.2. It was shown in Figure 6.3-6, that the hydrodynamic radius R_H follows a quadratic dependency as function of temperature around the *efb*, and furthermore still decreases with decreasing temperature below T_{efb}. Therefore, if we assume the *true efb* being $\Delta T = 0.4$ K below the value, being determined by optical inspection, we obtain a significantly lower hydrodynamic radius. Referring back to Figure 6.3-6a and b, with this correction a value of $R_H = 19$ nm for $\phi_{disp} = 0.1115$ (k = 8), and $R_H = 16$ nm for $\phi_{disp} = 0.0983$ (k = 8.5), respectively is obtained. In Figure 6.3-18 those are represented by the grey circles and show only a small deviation of the linear trend of R_H, that is found up to $\phi_{disp} = 0.088$ (black circles and triangles).
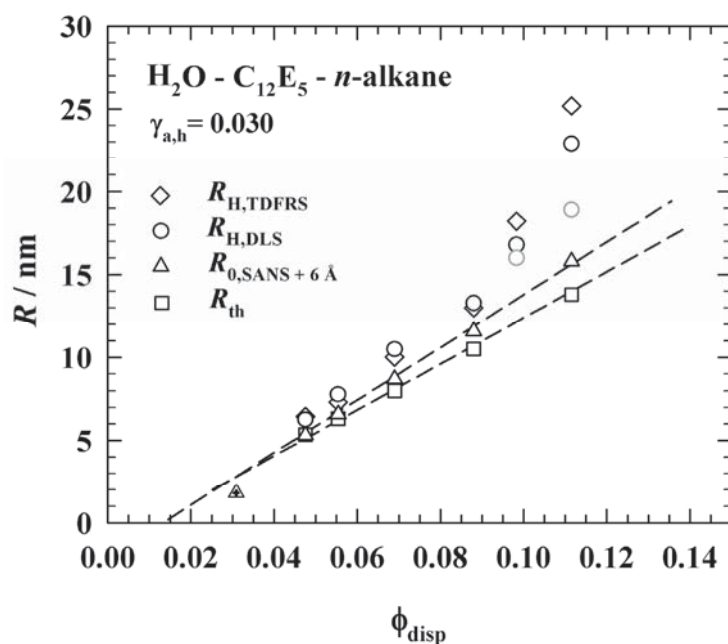
Figure 6.3-18: Values of the hydrodynamic radius R_H obtained by TDFRS [205] and DLS (refer to Table 6-3), respectively, and mean radius $R_0 + 6$ Å obtained from SANS measurements. The value of 6 Å was added to the original values of R_0 (Table 6-6) in order to account for approximately half of the thickness of the surfactant film. The theoretical values of the radius are calculated from the volume fractions given in Table 6-3 using equation (2.37), ($p = 0$). The crossed triangle denotes the value of the cross section of cylindrical micelles of $C_{12}E_5$ in water at 20 °C (1.91 nm + 6 Å) given in ref. [211]. See text for details.

Since the *Soret* coefficient S_T, that is defined by the ratio the thermal diffusion coefficient and the mutual diffusion coefficient, $S_T \equiv {D_T}/{D}$, it can be deduced, that the deviation from a spherical droplet structure, which might be the reason for unexpected high values of the hydrodynamic radius, affects also significantly the values of S_T. This is an important result, which must be kept in mind for the subsequent analysis of S_T.

However, before the results will be related to the measurements of the *Soret* coefficient, that are performed in *Jülich*, it was another objective of this work to determine the derivative of the interfacial tension with respect to the temperature of the microemulsions under study.

6.3.4 Interfacial Tension

The determination of the derivative of the interfacial tension between the water-rich microemulsion and the oil excess phase with respect to the temperature was motivated by the objective to validate the theoretical approach of *Parola* and *Piazza* [41], that relates the interfacial tension σ_{ab} between a solute particle and the solvent to the *Soret* coefficient of the system. The corresponding equation reads [41]:

$$S_{\mathrm{T}} = \frac{4\pi a}{k_{\mathrm{B}}T} \frac{\partial(l\sigma_{ab})}{\partial T}. \tag{6.6}$$

By imposing no-slip boundary conditions at the surface of the sphere [41] the quantity a is equal to the radius of the microemulsion droplets. The parameter l is a measure of the range of the colloid-solvent interaction. According to equation (6.6) the *Soret* coefficient S_{T} is (i) linear dependent on the radius and (ii) linear dependent on the derivative of the product of the interfacial tension σ_{ab} and the parameter l with respect to the temperature T. Our aim was to validate this relation using microemulsion droplets as a model system. Thereby we approximated the interfacial tension between the droplet and the continuous aqueous phase by the experimentally accessible interfacial tension between the aqueous microemulsion and the oil excess phase σ_{ab}. Furthermore, in a first approximation we assume the parameter l to be independent of the temperature in our model system, i.e.

$$S_T = \frac{4\pi a l}{k_B T} \frac{\partial \sigma_{ab}}{\partial T}, \tag{6.7}$$

Taking into account only the bending energy difference of the internal interface of the microemulsion droplet and the macroscopic interface, *Strey* [84] could describe the temperature dependence of the interfacial tension σ_{ab} in microemulsions [56, 212]. In the resulting relation, the interfacial tension σ_{ab} between the aqueous microemulsion phase and the oil excess phase b is given by

$$\sigma_{ab} = \overline{\sigma}_{ab}\left(-\frac{2\kappa + \overline{\kappa}}{\overline{\kappa}}\tau^2 + 1\right), \tag{6.8}$$

with

$$\tau = \frac{2(T - T_m)}{T_u - T_l}, \tag{6.9}$$

where T_l and T_u are the lower and upper critical end-point temperature, respectively, of the three-phase body and T_m is the mean temperature. κ and $\overline{\kappa}$ are the bending rigidity and the saddle splay modulus, respectively. $\overline{\kappa}$ can be determined from the maximum characteristic length scale

of the microstructure $\bar{\xi}$ and the minimum of the interfacial tension $\bar{\sigma}_{ab}$ by using the following relation [50, 56]:

$$\bar{\sigma}_{ab} = -\frac{\bar{\kappa}}{\bar{\xi}^2} . \qquad (6.10)$$

If T_l, T_u and T_m are known from phase behavior measurements, κ remains as the only free parameter in equation (6.8).

In this work, the objective was to validate the dependence of the *Soret* coefficient on the radius and on the derivation of the interfacial tension, according to equation (6.6). Therefore we need to determine the values of the derivative of the interfacial tension with respect to the temperature at $T = 27.6$ °C (refer to Figure 6.3-1) for the system under study $H_2O - C_{12}E_5 - n$-alkane. As n-alkane components we used octane (k = 8), decane (k = 10), dodecane (k = 12) and tetradecane (k = 14). Additionally two mixtures of n-octane and n-decane with n-octane mass fractions of $\beta = 0.50$ (k = 9) and 0.75 (k = 8.5), respectively, were studied.

On the basis of systematic phase behavior, neutron scattering and interfacial tension measurements *Sottmann et al.* [56] determined the parameters T_l, T_u, T_m, κ, $\bar{\kappa}$, $\bar{\xi}$ and $\bar{\sigma}_{ab}$ for a wide range of microemulsion systems of the type water $- n$-alkane $- C_iE_j$. The values of these parameters for $C_{12}E_5$ and the n-alkanes octane (k = 8), decane (k = 10), dodecane (k = 12) and tetradecane (k = 14), obtained from their work, are summarized in Table 6-7.

Table 6-7: Values of the parameters $\bar{\sigma}_{ab}$, $\bar{\xi}$, $\bar{\kappa}$, κ, T_l, T_u, $\Delta T = T_u - T_l$, and T_m for the system water $- C_{12}E_5 - n$-alkane. k is the number of carbon atoms of the n-alkane (k = 8: octane, k = 10: decane, k = 12: dodecane, k = 14: tetradecane). Values taken from Table II in reference [56].

k	$\bar{\sigma}_{ab}$ / mNm^{-1}	$\bar{\xi}$ / Å	$\bar{\kappa}$ / kT	κ / kT	T_l / °C	T_u / °C	ΔT / K	T_m / °C
8	0.0005	550.5	-0.361	1.00	31.25	34.45	3.20	32.85
10	0.0009	386.5	-0.315	0.94	36.67	41.00	4.33	38.84
12	0.0023	267.5	-0.379	1.00	40.95	47.40	6.45	44.18
14	0.0047	193.0	-0.400	1.13	44.60	54.10	9.50	49.35

In the first step we measured the interfacial tension σ_{ab} of the system $H_2O - C_{12}E_5 - n$-alkane in the relevant temperature range around $T = 27.6\,°C$ for the n-alkanes octane (k = 8), decane (k = 10), dodecane (k = 12) and tetradecane (k = 14) [130].

In Figure 6.3-19 the values of σ_{ab} are shown as a function of the temperature for the system $H_2O - C_{12}E_5 - n$-alkane under variation of the alkane chain length k. The open symbols represent the values taken from reference [56].
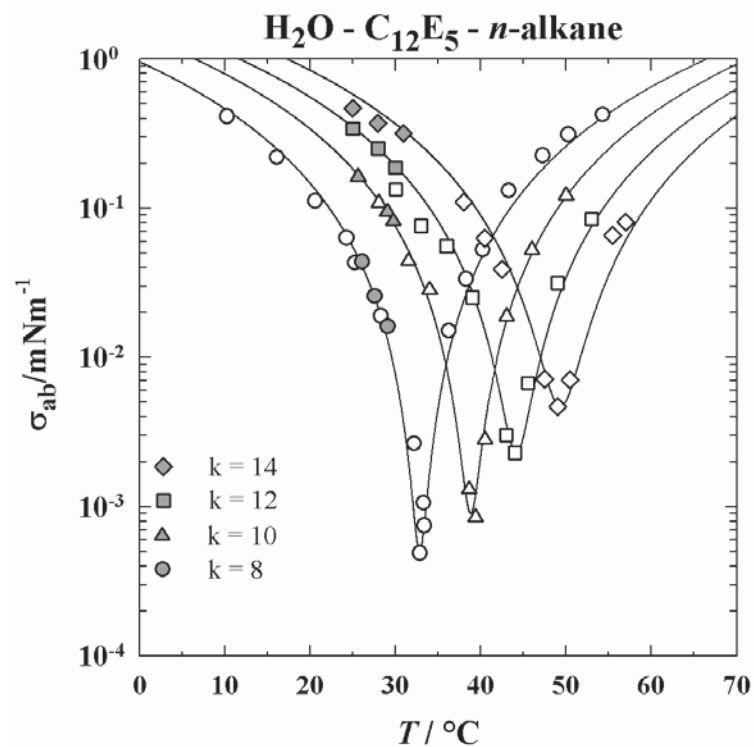
Figure 6.3-19: σ_{ab} as function of T for the microemulsion system under study $H_2O - C_{12}E_5 - n$-alkane for different alkanes with chain length k. The open symbols were taken from reference [56]. The shaded symbols are our measurements.

The full lines represent the theoretical description according to equation (6.8) using the parameters given in Table 6-7. It can be seen that the data obtained in this work (full symbols) are in quantitative agreement with the theoretical description as well as with the measurements of *Sottmann et al*. [56].

It must however be noted, that for the system $H_2O - C_{12}E_5 - n$-tetradecane (grey diamonds in Figure 6.3-19) the theoretical description (full line) yields slightly higher values of σ_{ab} than our experiment. We repeated this measurement two times, but reproduced the values within the

range of the experimental error. This deviation, however might also indicate, that the entropy of dispersion, that leads to smaller values of σ_{ab} can not be neglected in equation (6.8), as was already suggested *Strey* [84]. Nevertheless, since those deviations were small and the only ones that we found, we deduce, that it is feasible to use the parameters given in reference [56] for the calculation of the derivative of σ_{ab} with respect to T for the microemulsions in this study.

In Figure 6.3-20 the values of σ_{ab} for the alkanes *n*-octane (k = 8) and *n*-decane (k = 10) taken from reference [56] (open symbols) are plotted as function of T together with the values of the mixtures *n*-octane/*n*-decane with β = 0.50 (k = 9) and 0.75 (k = 8.5), respectively (grey symbols), that were measured in this work. The data points show the expected trend, i.e. they can be found in between the values of the pure alkanes k = 8 (circles) and 10 (triangles). Thereby the values of σ_{ab} for the mixture β = 0.75 (k = 8.5, crossed diamonds) are (i) slightly lower and (ii) show a slightly steeper decrease as function of T than σ_{ab} for β = 0.50 (k = 9, shaded triangles).
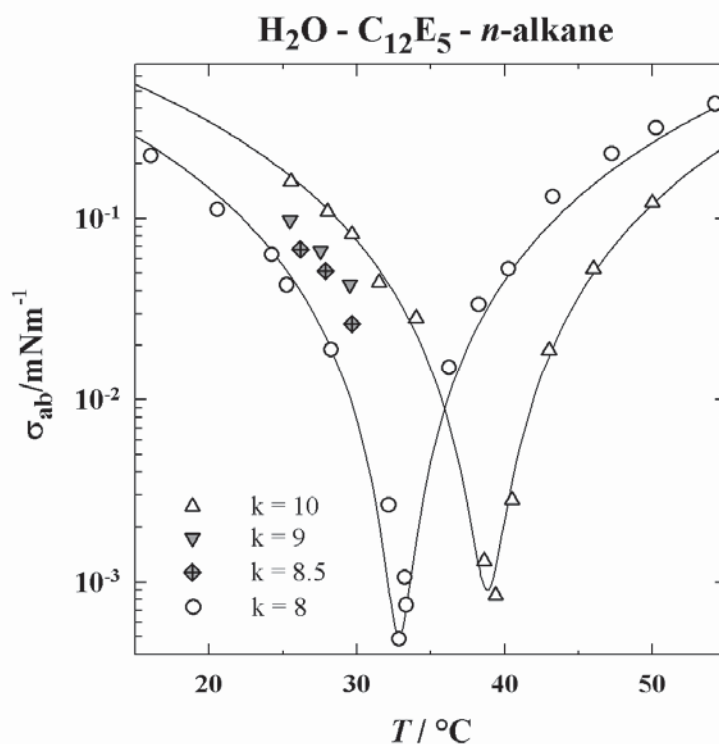
Figure 6.3-20: σ_{ab} as function of T: Data of *n*-octane and *n*-decane microemulsions (open symbols) [56] together with the theoretical description [equation (6.8) full lines]. The grey symbols represent the interfacial tension values for the systems containing mixtures of *n*-octane and *n*-decane, with β = 0.5 (k = 9, grey triangles) and β = 0.75, (k = 8.5, crossed diamonds) measured in this work.

In the next step the parameters, that are used in the theoretical description of the interfacial tension (i.e. $\bar{\sigma}_{ab}$, $\bar{\xi}$, κ, $\bar{\kappa}$ ΔT, and T_m,) should be estimated for the two systems

n-octane/*n*-decane $\beta = 0.50$ (k = 9) and 0.75 (k = 8.5), respectively, since they were not studied in the literature before. Therefore we plot the parameters ($\bar{\sigma}_{ab}$, $\bar{\bar{\xi}}$, κ, ΔT, and T_m, for the systems that were studied in the literature [56], each as function of the *n*-alkane chain length k in order to determine the parameter values for k = 9 and 8.5 by graphical interpolation.

Accordingly, in Figure-6.3-21 the parameters $\bar{\sigma}_{ab}$ (a), $\bar{\bar{\xi}}$ (b), T_m (c) and ΔT (d) are plotted as function of k. The open circles represent the values from reference [56]. The full lines are fits to these data points according to appropriate functions as explained in the following: For the minimum interfacial tension $\bar{\sigma}_{ab}$ (Figure-6.3-21a) we found a quadratic dependence on k, whereas the decrease of the maximum characteristic length scale $\bar{\bar{\xi}}$ (Figure-6.3-21b) could be described by an exponential decay. The mean temperature T_m exhibits a linear trend as function of k and the difference between the upper and lower end point temperature $\Delta T = T_u - T_l$ shows again a quadratic dependency. It can be seen in (Figure-6.3-21a-d) that for the parameters $\bar{\sigma}_{ab}$, $\bar{\bar{\xi}}$, T_m and ΔT the data points from reference [56] can almost quantitatively be described by the above mentioned dependencies. Therefore we determined the values of the parameters $\bar{\sigma}_{ab}$, $\bar{\bar{\xi}}$, T_m and ΔT for the *n*-alkane mixtures with $\beta = 0.50$ (k = 9) and 0.75 (k = 8.5) by interpolation from the full lines in Figure-6.3-21a-d, respectively. Accordingly, the shaded circles in Figure-6.3-21a-d represent the values of the parameters $\bar{\sigma}_{ab}$, $\bar{\bar{\xi}}$, T_m and ΔT, respectively, for those systems.
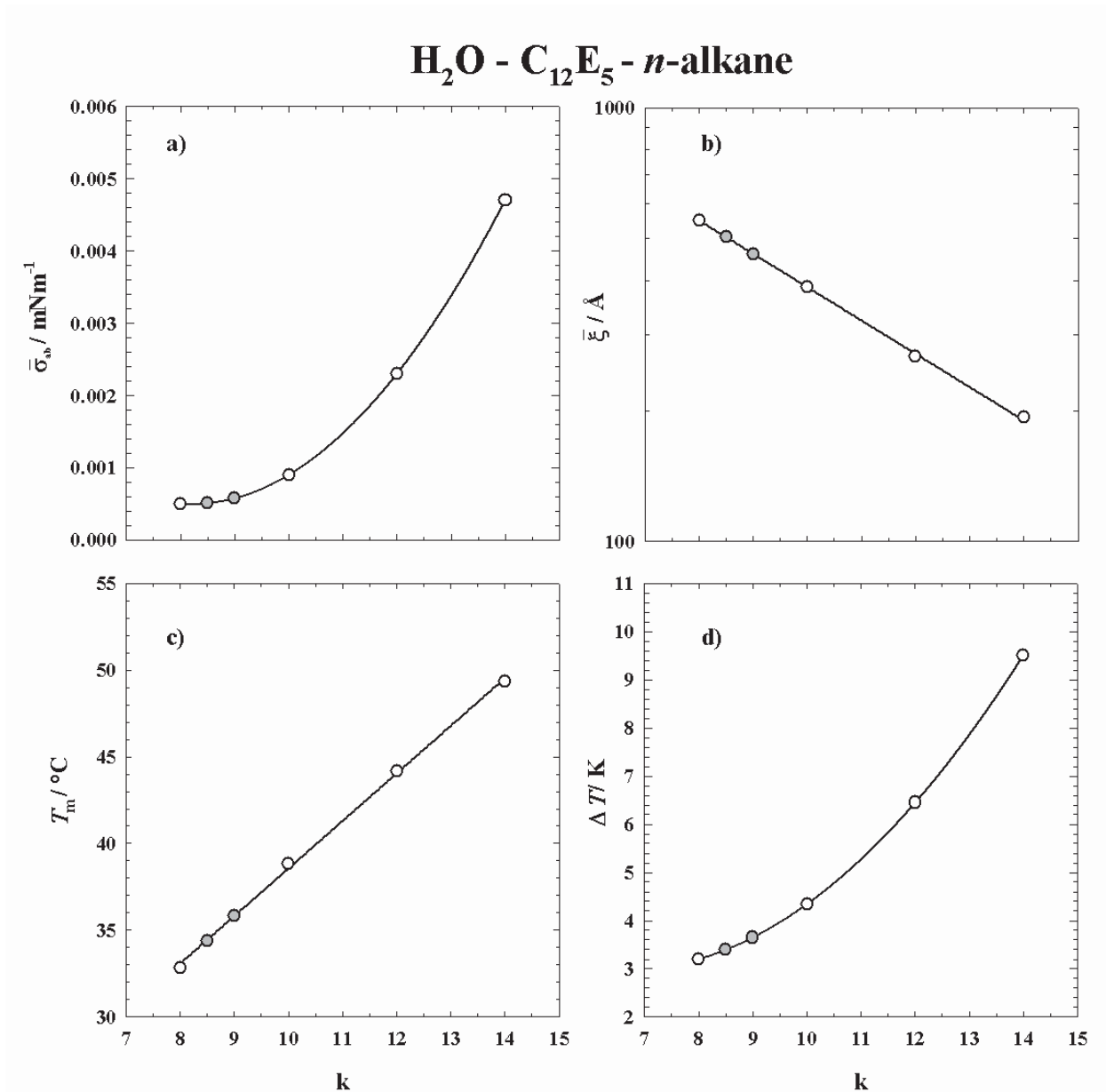
Figure-6.3-21: Values of the minimum interfacial tension $\overline{\sigma}_{ab}$ (a), maximum length scale of the microstructure $\overline{\overline{\xi}}$ (b), mean temperature T_m (c) and temperature difference between the upper and lower end-point temperature $\Delta T = T_u - T_l$ (d) as function of the number of the carbon atoms of the n-alkane. The open circles represent the values taken from reference [56]. The grey circles are the values obtained in this work. See text for details.

The values of the bending rigidity κ from reference [56] as function of k (open circles) are shown in Figure 6.3-22. From this plot a small overall increase of κ with k can be seen. Hence, for convenience we applied a linear fit through the data points of κ from reference [56] as function of k. The shaded circles represent the data points for k = 8.5 and 9, that were estimated from this assumption.
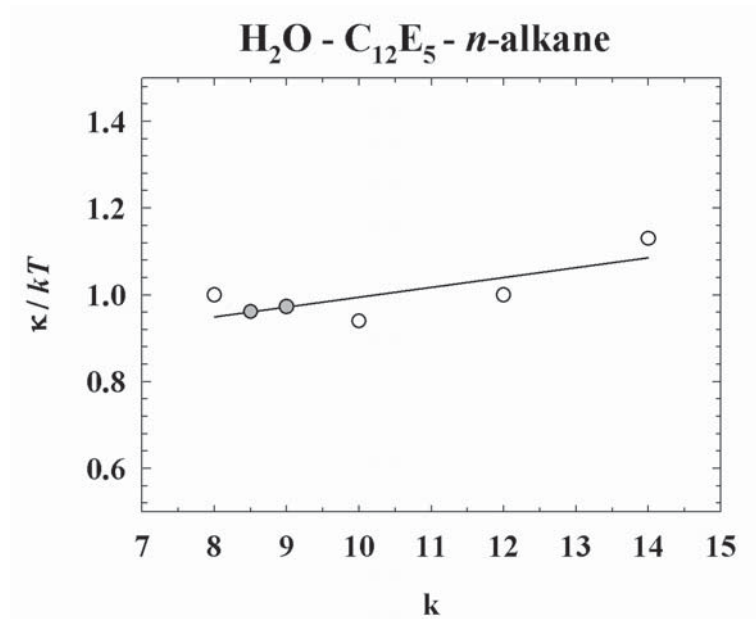
Figure 6.3-22: Bending rigidity κ as function of k. The open circles represent the values taken from reference [56]. The straight line represents a linear fit to the open circles. The shaded circles are the values of κ for k = 8.5 and 9, respectively, according to the linear fit. See text for details.

$\overline{\kappa}$ was then estimated from the values of $\overline{\sigma}_{ab}$ and $\overline{\xi}$ according to equation (6.10). The values of $\overline{\sigma}_{ab}$, $\overline{\xi}$, κ, $\overline{\kappa}$, ΔT, and T_m for the alkane mixtures k = 8.5 and 9, which were determined from the interpolation of the literature data, are given in Table 6.8.

Table 6-8: Values of the parameters $\overline{\sigma}_{ab}$, $\overline{\xi}$, $\overline{\kappa}$, κ, $\Delta T = T_u - T_l$, and T_m for the system water – $C_{12}E_5$ – n-alkane for the n-alkane mixtures n-octane/n-decane, $\beta = 0.5$ (k = 9) and $\beta = 0.75$ (k = 8.5), respectively. The values are obtained from interpolation of the values taken from reference [56]. See text for details.

k	$\overline{\sigma}_{ab}$ / mNm^{-1}	$\overline{\xi}$ / Å	$\overline{\kappa}$ / kT	κ / kT	ΔT / K	T_m / °C
8.5	0.00051	503	-0.308	0.961	3.39	34.40
9	0.00058	460	-0.293	0.973	3.65	35.80

In Figure 6.3-23 the values of the interfacial tension σ_{ab} are shown as function of the temperature T for the system H_2O – $C_{12}E_5$ – n-alkane for the alkane mixtures k = 8.5 (crossed diamonds) and 9 (grey triangles), respectively, together with interfacial tensions found for the n-octane (open circles) and n-decane (open triangles) microemulsions taken from reference [56]. The theoretical description (lines) according to equation (6.8) for the systems that were not studied in the literature before, i.e. k = 8.5 and 9, respectively, were calculated using the parameters given in

Table 6-8, that were derived from interpolation of the literature values. While for the system k = 9 the data points are almost quantitatively described by the theoretical description, slight deviations between the measurement and the theoretical description are found for the system with k = 8.5.
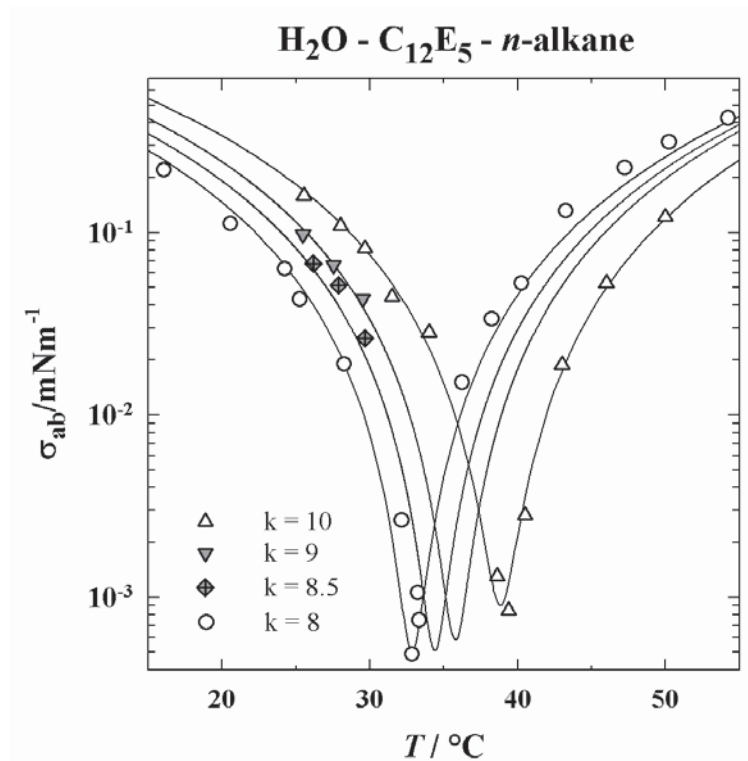
Figure 6.3-23: σ_{ab} as function of T for the microemulsion system under study H$_2$O – C$_{12}$E$_5$ – n-alkane for different alkanes with chain length k together with the theoretical description (lines) according to (6.8). The open symbols were taken from reference [56]. The shaded symbols are our measurements. See text for details.

In the next step we determine the partial derivative of the interfacial tension with respect to the temperature. Rewriting equation (6.8) as

$$\sigma_{ab} = -\overline{\sigma}_{ab} \frac{2\kappa + \overline{\kappa}}{\overline{\kappa}} \tau^2 + \overline{\sigma}_{ab},$$ (6.11)

and replacing

$$-\frac{2\kappa + \overline{\kappa}}{\overline{\kappa}} = b \text{ and } T_u - T_l = a,$$ (6.12)

yields

$$\sigma^{ab} = \overline{\sigma}_{ab} \frac{b4(T - T_m)^2}{a^2} + \overline{\sigma}_{ab} \; . \tag{6.13}$$

This can be expanded to

$$\sigma_{ab} = \frac{4b\overline{\sigma}_{ab}}{a^2}(T^2 - 2TT_m + T_m^{\;2}) + \overline{\sigma}_{ab} \tag{6.14}$$

and

$$\sigma_{ab} = \frac{4b\overline{\sigma}_{ab}}{a^2}T^2 - \frac{8b\overline{\sigma}_{ab}}{a^2}TT_m + \frac{4b}{a^2}\overline{\sigma}_{ab}T_m^{\;2} + \overline{\sigma}_{ab} \; . \tag{6.15}$$

Then the partial derivative with respect to T is given by

$$\left(\frac{\partial \sigma_{ab}}{\partial T}\right) = \frac{8b\overline{\sigma}_{ab}}{a^2}T - \frac{8b\overline{\sigma}_{ab}}{a^2}T_m \; , \tag{6.16}$$

which can be simplified to

$$\left(\frac{\partial \sigma_{ab}}{\partial T}\right) = \frac{8b\overline{\sigma}_{ab}}{a^2}(T - T_m) \; . \tag{6.17}$$

Replacing a and b (6.12) in (6.17) yields

$$\left(\frac{\partial \sigma_{ab}}{\partial T}\right) = -8\overline{\sigma}_{ab}\left(\frac{2\kappa + \overline{\kappa}}{\overline{\kappa}}\right)\frac{(T - T_m)}{(T_u - T_l)^2} \; . \tag{6.18}$$

Using equation (6.18) with the parameters given in Table 6-7 and Table 6-8 yields the following values of the derivative of the interfacial tension with respect to T at our working isotherme $T = 27.6\,°C$.

Table 6-9: Values of the partial derivative of the interfacial tension with respect to the temperature ($\partial\sigma_{ab}/\partial T$) at $T = 27.6\,°C$ for the system $H_2O – C_{12}E_5 – n$-alkane as function of the n-alkane chain length k.

k	$\left(\dfrac{\partial\sigma_{ab}}{\partial T}\right)$
	$[mN(mK)^{-1}]$
8	-0.0093
8.5	-0.0125
9	-0.0160
10	-0.0214
12	-0.0313
14	-0.0421

Figure 6.3-24 shows the values of the derivative $\left(\dfrac{\partial\sigma_{ab}}{\partial T}\right)$ at $T = 27.6\,°C$ as function of the

n-alkane chain length k. It can be seen that, $\left(\dfrac{\partial\sigma_{ab}}{\partial T}\right)$ depends almost perfectly linear on k.
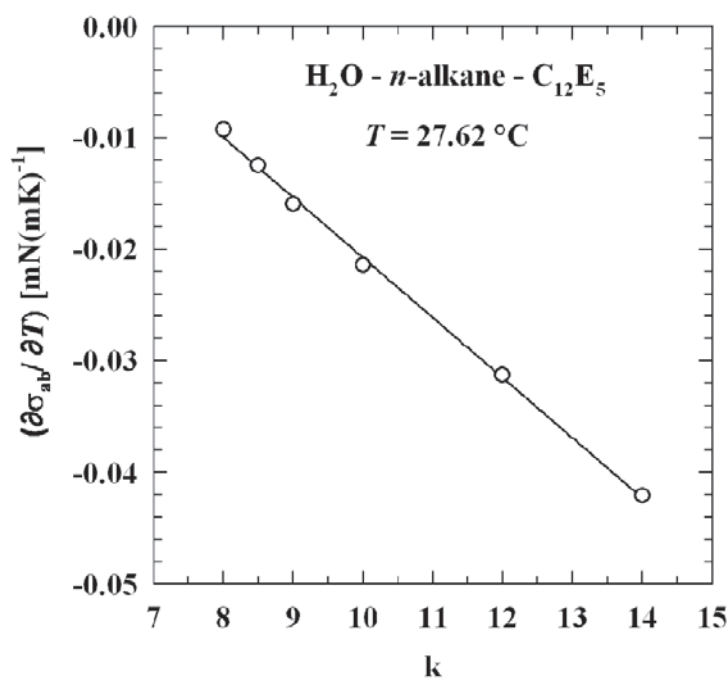
Figure 6.3-24: Values (open circles) of the partial derivative of the interfacial tension with respect to the temperature ($\partial\sigma_{ab}/\partial T$) at $T = 27.6\,°C$ for the system $H_2O – C_{12}E_5 – n$-alkane as function of the n-alkane chain length k. The straight line is shown as guide to the eye.

In this section we determined the derivative of the interfacial tension between the water-rich microemulsion and the oil excess phase for the system $H_2O – C_{12}E_5 – n$-alkane under variation of the n-alkane chain length k at constant temperature. In the previous section (6.3.3) we

determined the radius of the microemulsion droplets at constant temperature by means of small angle neutron scattering (SANS). On the basis of data, the next step is to relate those quantities to the *Soret* coefficient, which is the main purpose of this study.

6.4 Discussion and Conclusion

It was the objective of this part of the work, to study the dependence of the *Soret* coefficient S_T on (i) the radius R_0 of microemulsion droplets and (ii) the slope ($\partial \sigma_{ab}/\partial T$) of the interfacial tension σ_{ab} between the water-rich microemulsion and the oil excess phase with respect to the temperature. Therefore in section 6.3.4 and 6.3.3, both, the radius R_0 and the interfacial tension σ_{ab} were determined for the systems $H_2O – C_{12}E_5 – n$-alkane, around $T = 27.6\,°C$. In the following, those results should be related to the measurements of the *Soret* coefficient, that were performed in *Jülich* [205].

Figure 6.4-1a shows the *Soret* coefficient S_T as a function of the mean droplet radius R_0 that was determined by SANS measurements. The temperature of the S_T measurements is $T = 27.6 \pm 0.3$ °C (refer to Table 6-3), while the temperature of the SANS measurements is $T = 26.1 \pm 0.2$ °C (refer to Table 6-6) due to the lowering of the phase transition temperatures by $\Delta T \approx 1.5\,K$ that occurs upon the replacement of H_2O by D_2O and replacing hydrogenated oils by deuterated ones. This shift is in agreement with the literature [171] and we assume, that it does not affect the correlation between S_T and R_0. The value of S_T, that was found for the largest droplets, i.e. for the microemulsion $H_2O – C_{12}E_5 – n$-octane ($\gamma_a = 0.030$, $\phi_{disp} = 0.1115$), seems to be far from the linear trend, observed for the other droplets. This significant deviation might be related to the observations from the DLS and SANS measurements. From those results it was obvious, that for the systems with large droplet volume fraction ϕ_{disp} already at the phase transition temperature (T_{efb}) prolate- and oblate- like structures exist instead of spherical droplets (refer to Figure 6.3-15a), leading to larger values of both, R_0 and R_H, i.e. smaller values of the diffusion coefficient D (Figure 6.3-18).
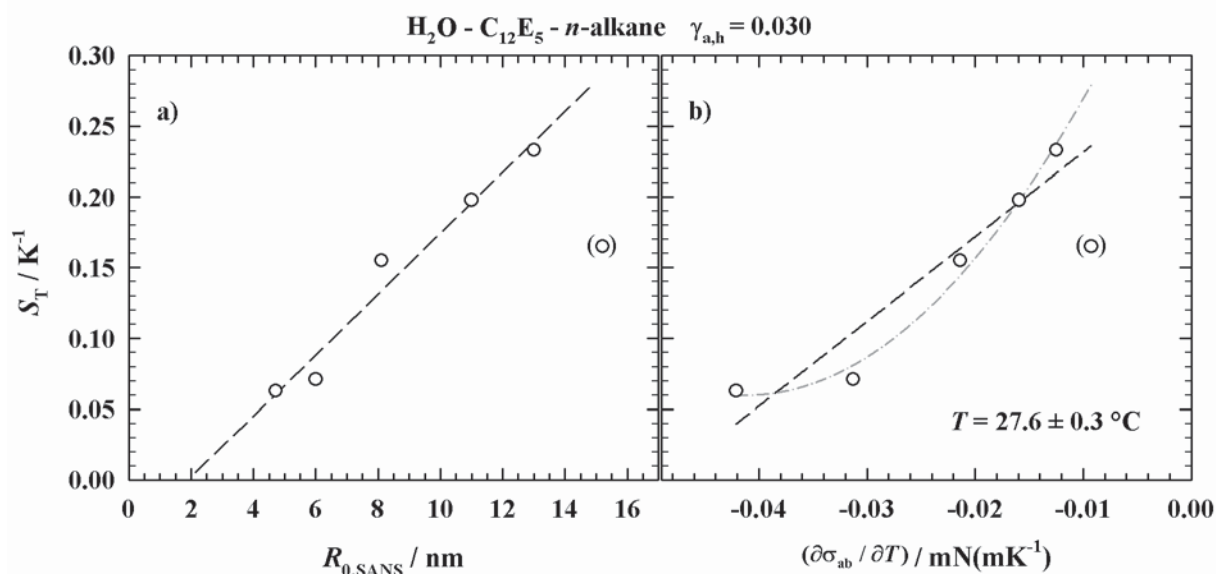
Figure 6.4-1: *Soret* coefficient S_T as function of the mean radius $R_{0,SANS}$ (a), that was determined by SANS measurements and as function of the derivative of the interfacial tension with respect to the temperature $(\partial\sigma_{ab}/\partial T)$ (b). The variation of the radius was achieved by the variation of the *n*-alkane at constant temperature. The measurement temperature of the S_T measurements is $T = 27.6 \pm 0.3$ °C (refer to Table 6-3). The temperature of the SANS measurements is $T = 26.1 \pm 0.2$ °C (refer to Table 6-6). This deviation is due to the decrease of the phase boundaries upon replacing H_2O by D_2O and applying deuterated oils for the SANS measurements. Note that for the pair of values ($R_0 = 13.5$ nm ; $S_T = 0.233$ K^{-1}) the mean radius was determined by interpolation from Figure 6.3-18, since no SANS measurements were performed on the corresponding microemulsion, H_2O – $C_{12}E_5$ - *n*-octane/*n*-decane, $\beta = 0.75$. The values of S_T are given in Table 6-10 [194]. See text for details.

If this value is neglected, a linear trend of S_T as a function of R_0 (dashed line in Figure 6.4-1a) is found. Thus, a quadratic increase of S_T as a function of R, that was found by *Duhr* and *Braun* [35] is clearly not supported by our data.

In Figure 6.4-1b S_T is shown as function of the slope of the interfacial tension with respect to the temperature, i.e. $(\partial\sigma_{ab} / \partial T)$ at $T = 27.6 \pm 0.3$ °C. Again, the value of S_T for the *n*-octane system seems to deviate strongly from the linear trend of the other values. Nevertheless, an overall increase of S_T is found as function of $(\partial\sigma_{ab} / \partial T)$. However, this trend can not clearly be assigned to a linear (black dashed line) or a quadratic (grey dash-dotted line) dependence of S_T on $(\partial\sigma_{ab} / \partial T)$.

Table 6-10: The quantity $R_0(\partial\sigma_{ab}/\partial T)$ for the system $H_2O – C_{12}E_5 – n$-alkane under variation of the alkane chain length k. The values of R_0 are the same as in Table 6-6, (the value $R_o = 13.0 \pm 0.32$ nm was determined by extrapolation of R_0 as function of ϕ_{disp} from Figure 6.3-18). The values of S_T are measured by B. Arlt, *Jülich* [194]. The errors of $R_0(\partial\sigma_{ab}/\partial T)$ were calculated from the uncertainty of R_0, derived from the model approximation of the SANS measurements.

k	R_0 [nm]	S_T [K^{-1}]	$(\partial\sigma_{ab}/\partial T)$ [mN(mK)$^{-1}$]	$R_0(\partial\sigma_{ab}/\partial T)$ [10^{-12} N K^{-1}]
14	4.7±0.15	0.063±0.001	-0.0421	-0.200±0.006
12	6.0±0.15	0.071±0.003	-0.0313	-0.188±0.005
10	8.1±0.25	0.155±0.007	-0.0214	-0.173±0.005
9	11.0±0.3	0.198±0.010	-0.0160	-0.175±0.005
8.5	13.0±0.32	0.233±0.031	-0.0125	-0.162±0.004
8	15.2±0.35	0.165±0.011	-0.0093	-0.140±0.003

In order to study the correlation of the *Soret* coefficient S_T with the product of R_0 and $(\partial\sigma_{ab}/\partial T)$, in Figure 6.4-2 S_T is plotted as a function of $R_0(\partial\sigma_{ab}/\partial T)$ for the microemulsion system under study, $H_2O – C_{12}E_5 – n$-alkane at constant temperature $T = 27.6\ °C$.
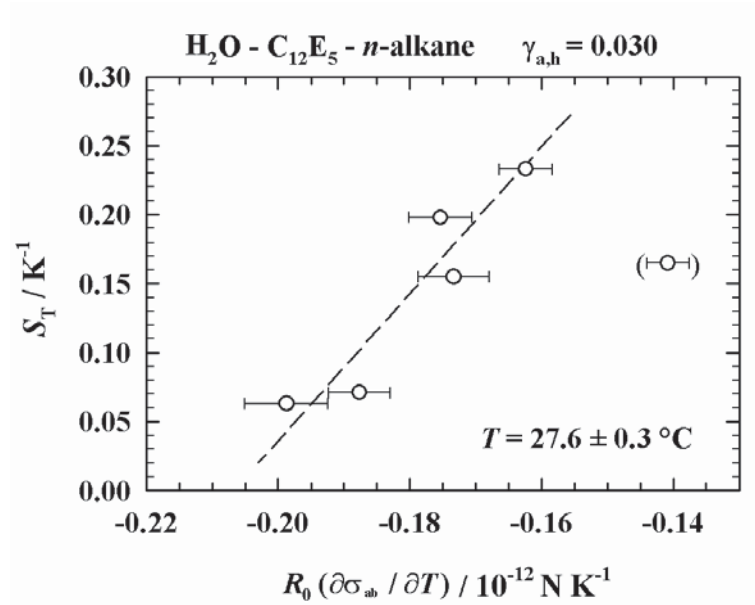
Figure 6.4-2: S_T as function of the product of R_0 and $(\partial\sigma_{ab}/\partial T)$ at $T = 27.6 \pm 0.3\ °C$. The values of the latter quantities are given in table Table 6-10. See text for details.

The corresponding values are given in Table 6-10 for the different alkanes with chain length k. According to *Parola* and *Piazza* [41] a linear relation is expected for this dependence under the assumption that the parameter l in their theory [refer to equation (6.6)] as a measure of the range

of the particle-solvent interaction is not dependent on T. It can be seen in Figure 6.4-2, that S_T shows indeed a linear trend as a function of $R_0(\partial\sigma_{ab}/\partial T)$, which would confirm the theory. However, it must be kept in mind that our assumption represents a simplification, since it neglects the role of the interaction length l.

Since we performed our study at isothermal conditions, the temperature dependent variation of l is not accessible from our data. It might be a starting point for further investigations of the nature of l, to study in more detail the variation of the depth u_0 of the attractive well of the interaction potential between the aggregates (refer to 2.5.4.6) in the microemulsion system. This quantity is deduced from the analysis of the SANS curves of the microemulsion droplets (refer to Table 6-6) and decreases linearly with increasing droplet radius R_0 as can be observed in Figure 6.4-3.
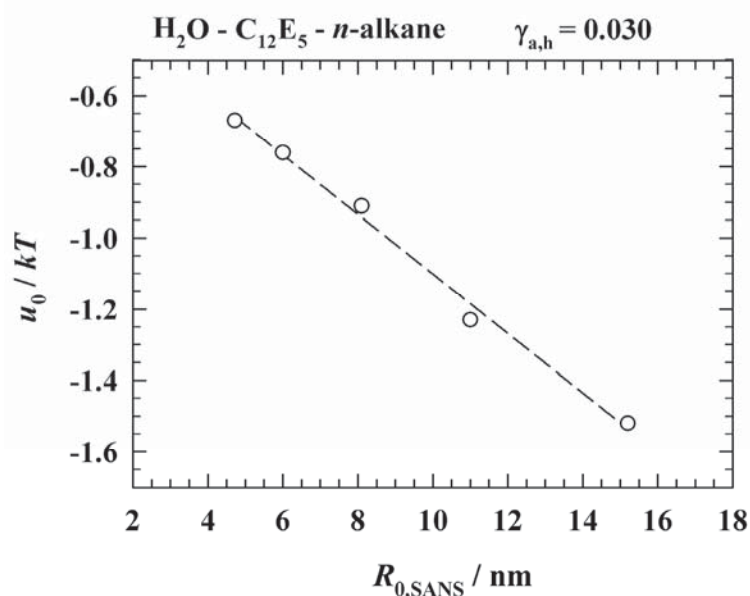
Figure 6.4-3: Depth of the attractive well u_0 of the sticky hard sphere potential that is obtained from the fits of the scattering curves to this model as function of the mean radius of the droplets $R_{0,SANS}$, that is obtained from the form factor of polydisperse shells. See text for details.

Thus the microemulsion system studied in this work might also provide a suitable model system for further theoretical considerations, that focus also the interaction between the microemulsion droplets, being extracted from the SANS measurements.

7 Summary and Conclusion

Both, non-ionic surfactant micelles and microemulsion droplets represent very promising model systems to investigate the thermal diffusion behavior of high molecular weight particles in a thermodynamically stable solution. However, due to their complex phase behavior and microstructure, along with difficulties in the experimental determination of the *Soret* coefficient S_T the thermal diffusion behavior of these self-assembled nanostructured systems was not systematically studied so far. In this context, the objective of this work was the formulation and characterization of aqueous surfactant systems and microemulsions allowing for a systematic investigation of the influence of thermodynamic and structural parameters on the thermal diffusion behavior. Within the scope of a joint project between the groups of *T. Sottmann* and *R. Strey* in *Cologne* and *S. Wiegand* in *Jülich* the thermal diffusion behavior of these self-assembled nanostructured systems could subsequently be studied by means of the thermal diffusion forced *Rayleigh* scattering (TDFRS) method.

The first goal of this work was to investigate the influence of the ionic dye Basantol® Yellow 215 on the binary system water – hexaethylene glycol monododecyl ether ($C_{12}E_6$). These studies were motivated by the observation of an unexpected two-mode signal which occurs in the classical TDFRS experiment only in the presence of the dye under certain experimental conditions [28, 160]. The results of this work clearly show that this unexpected signal is related to the influence of the dye on both, the phase behavior and the microstructure of the binary water - $C_{12}E_6$ system. Studying the phase behavior, it was found that the dye induces a shift of the

lower phase boundary of the upper miscibility gap towards higher temperatures. In analogy to the occurrence of the second mode in the classical TDFRS experiment, where a constant concentration of the dye in water is used, this effect becomes increasingly pronounced at low $C_{12}E_6$ weight fractions (Figure 4.3-3). The small angle neutron scattering (SANS) experiments revealed long range interactions between the aggregates, which were assigned to electrostatic repulsions induced by the dye molecules (Figure 4.3-4, Figure 4.3-6). From those results and additional experiments, studying the influence of the well known ionic surfactant SDS (Figure 4.3-6), it could be shown that the ionic dye is incorporated into the aggregates acting as an ionic cosurfactant. Analyzing the scattering curves by the combination of appropriate form- and structure factors it was found that the dye, although inducing significant interactions between the aggregates, has only a small influence on their shape and size. In addition, the influence of the dye on both the microstructure and the occurrence of the second mode in the TDFRS experiments could semi-quantitatively be related to the number $N_{BY,agg}$ of dye molecules per aggregate. It was found that $N_{BY,agg}$ increases either by decreasing the volume fraction ϕ_C of $C_{12}E_6$, or due to the elongation of the aggregates by increasing the temperature (Figure 4.4-1). These results strongly suggest to ban the use of surface-active dyes for TDFRS experiments on self-assembled systems, as they significantly influence not only the thermal diffusion behavior but also the phase behavior and microstructure of these systems.

The second and main objective of this work was the formulation and characterization of non-ionic droplet-microemulsions for the systematic investigation of the *Soret* coefficient S_T as function of (i) the droplet radius and (ii) the derivative of the interfacial tension with respect to the temperature. Thereby the influence of both quantities on the *Soret* coefficient S_T should be studied at isothermal conditions. This condition was achieved by formulating microemulsions which contain different *n*-alkanes, i.e. *n*-octane, *n*-decane, *n*-dodecane, *n*-tetradecane and several mixtures of them (Figure 6.3-1). Studying the $T(w_B)$-sections, of systems of the type $H_2O - C_{12}E_5 - n$-alkane at a fixed mass fraction $\gamma_a=0.03$ of $C_{12}E_5$ in the water/$C_{12}E_5$-mixture, revealed the typical phase behavior of non-ionic, water-rich microemulsions (Figure 6.3-1). Increasing the chain length k of the alkane, a shift of the $1-\overline{2}$ and $\underline{2}-1$ phase boundaries [*emulsification failure* - (efb) and *near critical boundary* (ncb), respectively] towards higher temperatures was observed. Furthermore, the mass fraction w_B of oil at the lower critical end-point temperature T_l, i.e. the intersection between the *efb* and the *ncb* shifts to smaller values of w_B. Accordingly, the maximum mass fraction w_B of oil, that could be solubilized in a droplet microemulsion

(*emulsification failure*) at a given temperature (here $T = 27.6\ °C$) also decreases with increasing k from $w_B = 0.060$ (*n*-octane) to $w_B = 0.013$ (*n*-tetradecane).

The microstructure of the formulated oil-in-water (o/w) microemulsion droplets was examined by means of small angle neutron scattering (SANS) and dynamic light scattering (DLS). The SANS data were analyzed using a combination of a core-shell form factor [143] and the structure factor of *sticky hard spheres* [151]. Thereby the spherical structure of the droplets was confirmed at – or somewhat below (*n*-octane) – the efb, revealing that the mean radius decreases with increasing chain length k of the *n*-alkane from $R_0 = 152.0$ (for k = 8) to $R_0 = 47.2\ Å$ (for k = 14) [Figure 6.3-17 and Table 6-6]. Plotting the obtained mean droplet radius R_0 as a function of the droplet volume fraction ϕ_{disp} a linear trend was observed (Figure 6.3-18). The attractive interaction between the aggregates, expressed by the depth $-u_0$ of the attractive well of the potential used in the *sticky hard sphere* structure factor, increases with increasing droplet volume fraction ϕ_{disp} (Figure 6.4-3). Accordingly, applying the simpler *hard sphere* interaction model could not quantitatively describe the scattering curves.

The hydrodynamic radii of the droplets, determined with DLS by using the *Stokes-Einstein* relation, also decrease with increasing chain length k of the *n*-alkane from $R_H = 197.0\ Å$ (k = 8) to $R_H = 62.6\ Å$ (k = 14). These values are significantly larger than the radii obtained from the analysis of the SANS data which can be attributed to the fact that the diffusion of the droplets is slowed down by the surrounding hydration shell. In addition, a deviation of the linear trend of R_H as function of ϕ_{disp} was found with increasing ϕ_{disp}, i.e. decreasing k (Figure 6.3-18). This deviation, but also the SANS-curve of the *n*-octane-microemulsion recorded at $T_{efb} = 27.6\ °C$ point to the existence of prolate and oblate structures due to the vicinity to the lower critical endpoint temperature T_l. Comparing the mutual diffusion coefficients D obtained from DLS with the ones extracted from TDFRS measurements systematic deviations were found which could be explained by a temperature shift in the sample cell of the TDFRS setup of $\Delta T \approx +0.3\ K$, that occurs locally from the heating of the laser and is thus not detected by the temperature sensor in the sample holder.

In order to obtain the partial derivative $(\partial\sigma_{ab}/\partial T)$ of the interfacial tension σ_{ab} with respect to the temperature [equation (6.18)], at constant pressure and composition, between the respective microemulsion and *n*-alkane excess phases, σ_{ab} was measured at three temperatures around $T = 27.6\ °C$ using the spinning drop technique. Comparing the obtained values of σ_{ab} with the

ones determined by *Sottmann et al.* [56] some years ago a nearly quantitative agreement was found (Figure 6.3-19). Subsequently, the partial derivative $(\partial\sigma_{ab}/\partial T)$ was determined using the theoretical description of the interfacial tension in terms of bending energy [84, 212]. It was found that at $T = 27.6\,°C$ the slope of the $\sigma_{ab}(T)$-curves, i.e. $(\partial\sigma_{ab}/\partial T)$, decreases linearly with decreasing chain length of the *n*-alkane (Figure 6.3-24).

The quantitative determination of both, the droplet radius and the slope of the $\sigma_{ab}(T)$-curves allows to relate R and $(\partial\sigma_{ab}/\partial T)$ to the *Soret* coefficient S_T measured by the group of *S. Wiegand* [213]. *Vigolo et al.* [33] and *Putnam* [34] proposed that the *Soret* coefficient S_T varies linear with the droplet radius (Figure 6.4-1). Our results support the linear size dependence of S_T. However, they are in contradiction with the results of *Duhr* and *Braun* [35] which revealed a quadratic size dependence of S_T. Furthermore we found a linear trend of S_T as a function of both $(\partial\sigma_{ab}/\partial T)$ (Figure 6.4-1) and the product $R_0(\partial\sigma_{ab}/\partial T)_{p,}$ (Figure 6.4-2), which supports the theory of *Iacopini et al.* [53], predicting a linear dependence of S_T on these paramemeters. However, it should be mentioned that the additional $(\partial l/\partial T)$ term existing in the theory [equation (6.6)] of *Iacopini et al.* [53] was neglected assuming that the microscopic interaction length l is independent of T. The depth $-u_0$ of the attractive well in the interaction potential between the microemulsion droplets, that was extracted from the analysis the SANS data (Figure 6.4-3) might be used as a starting point for a further clarification of this feature in subsequent works.

The third part of this work, was motivated by recently published results of *Santos et al.* [180] which provide a strong indication for the existence of a drastic change of the *Soret* coefficient S_T at the critical micelle concentration (cmc) in binary surfactant systems [180]. However, due to experimental difficulties, *Santos et al.* were not able to determine S_T quantitatively. In order to obtain a more generic picture about the thermal diffusion behavior of aqueous surfactant systems near the cmc, the *Soret* coefficient of aqueous solutions of *n*-alkyl glucoside surfactants (C_iG_j), which exhibit a fairly high cmc, was determined by the group of *S. Wiegand*. Parallel to this thermal diffusion studies the critical micelle concentration of *n*-octyl-β-D-glucopyranoside (C_8G_1), *n*-heptyl-β-D-glucopyranoside (C_7G_1) and *n*-octyl-β-glucomaltoside (C_8G_2) in water was systematically determined in *Cologne* from measurements of the surface tension γ^s using the well known ring method of *Du Noüy*. The cmc of C_8G_1 decreases with increasing temperature from $c = 0.024$ mol/L at $T = 15\,°C$ to 0.0185 mol/L at 40 °C. The same trend was found for C_7G_1 (Figure 5.3-3). As expected due to the shorter alkyl-chain, the cmc of C_7G_1 ($c = 0.0792$ mol/l at $T = 15.0\,°C$) is considerably larger than the one of C_8G_1. The cmc of C_8G_2 at $T = 15.0\,°C$ was

found to be located at $c = 0.00460$ mol/l and thus was considerably lower than that of C_7G_1 and C_8G_1. Having determined the cmc-values for the three different systems, the data could be compared to the measurements of the *Soret* coefficient S_T performed by the group in *Jülich* [214]. It turned out that S_T determined for the system water – C_8G_1 shows indeed a considerable change at the cmc (Figure 5.4-1). However, only a less pronounced effect is found for the system water – C_7G_1 (Figure 5.4-2). Further thermal diffusion measurements and their interpretation are object of presently ongoing work and will be discussed in detail in the thesis of *B. Arlt*.

The results of this work show that aqueous surfactant systems and microemulsions are eminently suited to study the thermal diffusion behavior of nano-structured aggregates. Having studied the thermal diffusion behavior of oil-in-water droplet microemulsions it might be of interest to investigate the influence of the droplet radius and $(\partial\sigma_{ab}/\partial T)$ on the *Soret* coefficient S_T also for water-in-oil microemulsions. Thereby, first measurements point towards a sign change of the *Soret* coefficient S_T, if one switches from oil-in-water to water-in-oil microemulsions. Using block-copolymeric additives, larger structured microemulsions could be formulated that allow studying the size dependence of S_T over a wider radius-range. These are only a few but highly interesting objectives of the *DFG*-project which will be supported for almost another three years.

8 Appendix

The surfactant $C_{12}E_6$ (*n*-dodecyl-hexaoxylethylene, quoted >98 % was obtained from *Nikkol* (*Tokyo*, Japan), $C_{12}E_5$ (*n*-dodecyl-pentaoxyethylene, quoted 98.1 % was obtained from *Sigma-Aldrich* (*Steinheim*, Germany). The cloud point temperatures T_c at the critical composition of the binary system H_2O -surfactant were checked to verify the purity and to monitor possible degradation of surfactants. The surfactants C_8G_1 (n-octyl β-Dglucopyranoside, quoted 99.5%), C_7G_1 (n-heptyl β-D-glucopyranoside, quoted 99.5%) and C_8G_2 (n-octyl β-D-glucomaltoside, quoted 99.7%) were obtained from Glycon (Luckenwalde, Germany). Protonated *n*-octane(h18) (quoted 99.5 %), *n*-decane(h22) (quoted 99 %), *n*-dodecane(h26) (quoted 99.2 %), *n*-tetradecane(h30) (quoted 99.4%) was purchased from *Sigma-Aldrich* (*Steinheim,* Germany). Deuterated *n*-octane(d18), *n*-decane(d22), *n*-dodecane(d26), *n*-tetradecane(d30) was provided by *Euriso-top Groupe Saclay* (*Gif-sur-Yvette*, France), their purity is given in table 8-4. Bi-distilled water was used in all experiments with H_2O. D_2O was purchased from *Euriso-top Groupe Saclay* (*Gif-sur-Yvette*, France) and was stated to contain 0.0053 %-Vol. of water (H_2O). The dye *Basantol Yellow* 215 was allocated as a free sample from *BASF Group* (*Frankfurt* am Main, Germany).

8.1 Materials

Table 8-1: Molar masses M, macroscopic densities ρ^0 and scattering length densities ρ of the components used to prepare the samples in this work.

component	M	ρ^0	ρ
	$[g \cdot mol^{-1}]$	$[g \cdot cm^{-3}]$	$[10^{10} \cdot cm^{-2}]$
H_2O	18.01	0.998	-0.560
D_2O	20.00	1.105	6.389
$C_{12}E_5$	406.60	0.967	0.128
$C_{12}E_6$	450.65	0.980	0.171
Basantol® Yellow 215	929.9	n.n.	n.n.
C_7G_1	277.10	n.n.	n.n.
C_8G_1	292.38	n.n.	n.n.
C_8G_2	454.40	n.n.	n.n.
n-octane (h18)	114.23	0.702	-0.524
n-octane (d18) 98%d	132.09	0.814	6.449
n-decane (h22)	142.28	0.730	-0.489
n-decane (d22) 99%d	164.11	0.833	6.608
n-dodecane (h26)	170.34	0.751	-0.465
n-dodecane (d26) 98%d	196.13	0.864	6.737
n-tetradecane (h30)	198.39	0.762	-0.444
n-tetradecane (d30) 98%d	228.15	0.967	6.845

8.2 Binary System: Water – $C_{12}E_6$

Table 8-2: Sample compositions and model parameter for the description of the scattering curves of the systems $D_2O - C_{12}E_6$ (BIN), $D_2OBY215 - C_{12}E_6$ (BY215) and $D_2O/SDS - C_{12}E_6$ (SDS) at different volume fractions of $C_{12}E_6$, ϕ_C. Parameter: ($T_{meas.}$) Measurement temperature, (f) Scaling factor; Form factor models: (Sph.) Spherical micelles (Cyl.) cylindrical aggregates; Structure factor models: (OZ) *Ornstein Zernike* critical scattering (RMSA) Charged particle interaction, (HS) Hard sphere interaction, (HS+OZ) Hard spheres plus attractive interaction.

| Sample information | | | | Form factor $P(q)$ | | | | | Structure factor $S(q)$ | | | | | | |
System	ϕ_C	$T_{meas.}$ [°C]	f	Model	L [Å]	R_0 [Å]	σ [Å]	t [Å]	Model	ξ_{OZ} [Å]	I_0	R_{eff} [Å]	z	c_{salt} [mol/L]	d_{HS} [Å]
BIN	0.0025	21.3	0.90	Sph.	-	24.0	5.0	2.0	-	-	-	-	-	-	-
BIN	0.0025	21.3	0.95	Cyl.	70.0	20.0	4.6	-	-	-	-	-	-	-	-
BIN	0.0025	32.5	0.90	Cyl.	295.0	19.4	4.2	-	-	-	-	-	-	-	-
BIN	0.0025	32.5	0.90	Cyl.	360.0	19.4	4.6	-	-	-	-	-	-	-	-
BY215	0.0025	21.3	1.0	Sph.	-	23.5	5.0	2.2	RMSA	-	-	23.5	11	10^{-9}	-
BY215	0.0025	48.0	1.0	Cyl.	350.0	19.5	5.3	-	RMSA	-	-	76.0	62	10^{-9}	-
SDS	0.0025	48.0	1.0	Cyl.	340.0	19.3	5.0	-	RMSA	-	-	72.0	62	10^{-9}	-
BIN	0.0051	20.2	0.82	Sph.	-	22.9	4.5	4.3	-	-	-	-	-	-	-
BIN	0.0051	25.0	0.80	Cyl.	130.0	19.0	4.0	-	-	-	-	-	-	-	-
BIN	0.0051	35.5	0.80	Cyl.	364.0	19.6	4.5	-	-	-	-	-	-	-	-
BIN	0.0051	48.0	0.80	Cyl.	365.0	19.2	4.4	-	OZ	265	7.4	-	-	-	-
BIN	0.0076	17.5	0.72	Sph.[a]	-	23.2	4.8	2.8	-	-	-	-	-	-	-
BIN	0.0076	23.0	0.80	Cyl.	98.0	19.3	4.6	-	-	-	-	-	-	-	-
BIN	0.0076	32.5	0.80	Cyl.	335.0	19.3	4.5	-	-	-	-	-	-	-	-
BIN	0.0076	48.0	0.80	Cyl.	365.0	18.9	4.4	-	OZ	280	7.8	-	-	-	-
BIN	0.102	10.5	0.90	Sph.	-	22.0	4.4	4.3	HS	-	-	-	-	-	78.0
BIN	0.102	25.1	0.80	Sph.	-	22.0	4.3	4.6	HS+OZ	$R_0 + t$	1.2	-	-	-	84.0
BIN	0.102	30.0	0.80	Sph.	-	22.5	4.3	4.8	HS+OZ	$R_0 + t$	1.4	-	-	-	84.0
BIN	0.102	40.0	0.80	Sph.	-	21.5	4.0	4.6	HS+OZ	$R_0 + t$	2.1	-	-	-	84.0

[a]This curve can more exactly be described using a form factor for polydisperse prolate ellipsoids. See reference [138] for details of the model. Parameters: Minor radius $R_0 = 24.5$ Å, axis ratio $\nu = 1.7$, polydispersity $\sigma = 2.9$ Å and $f = 0.73$.

8.3 Binary System H$_2$O – C$_i$G$_j$: *Soret* Effect at the Critical Micelle Concentration
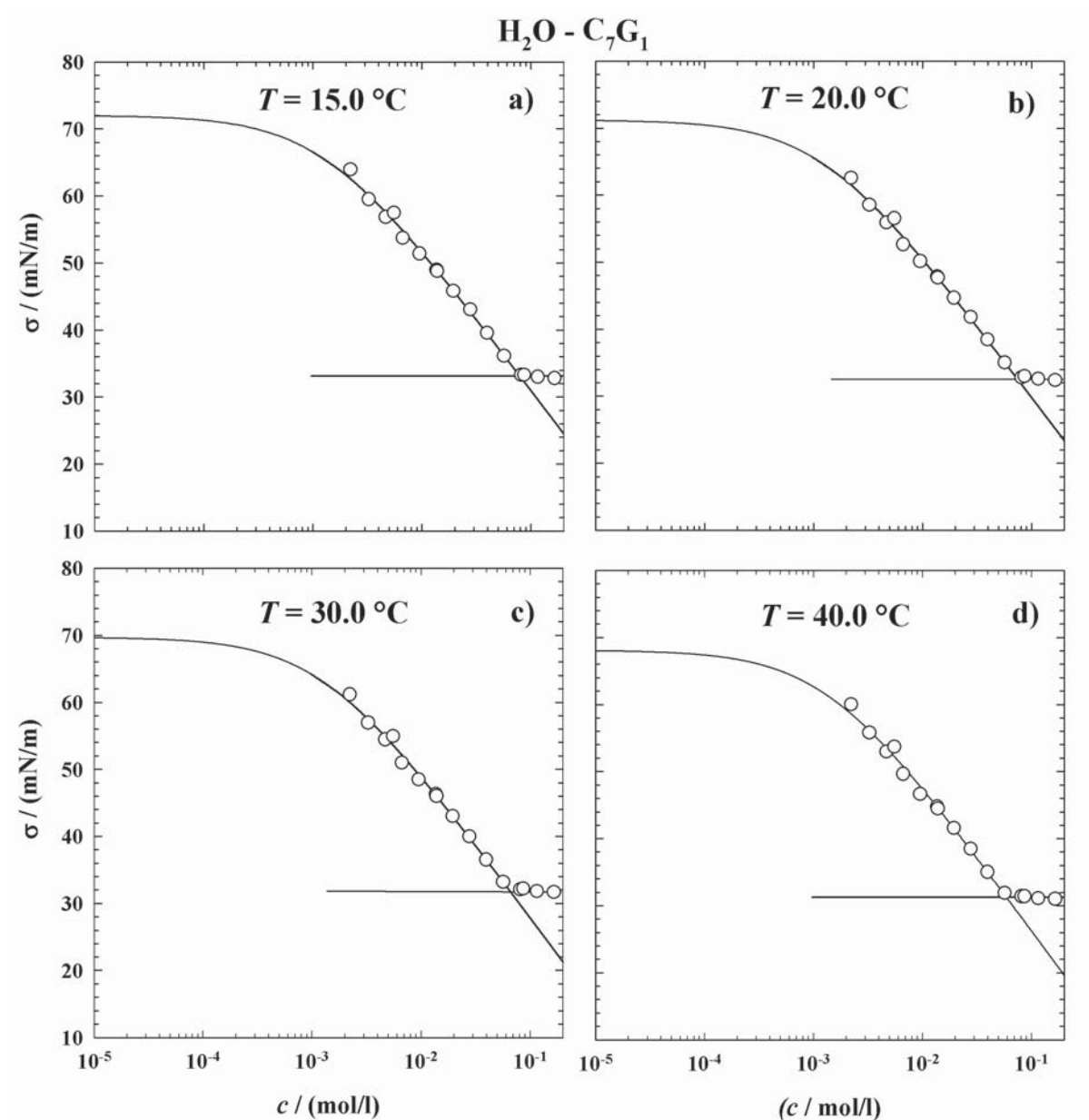
Figure 8.3-1: Surface tension measurements: γ^s as function of c of C$_7$G$_1$ in water at different temperatures, $T = 15\,°C$ (a), $T = 20\,°C$ (b), $T = 30\,°C$ (c), $T = 40\,°C$ (d).
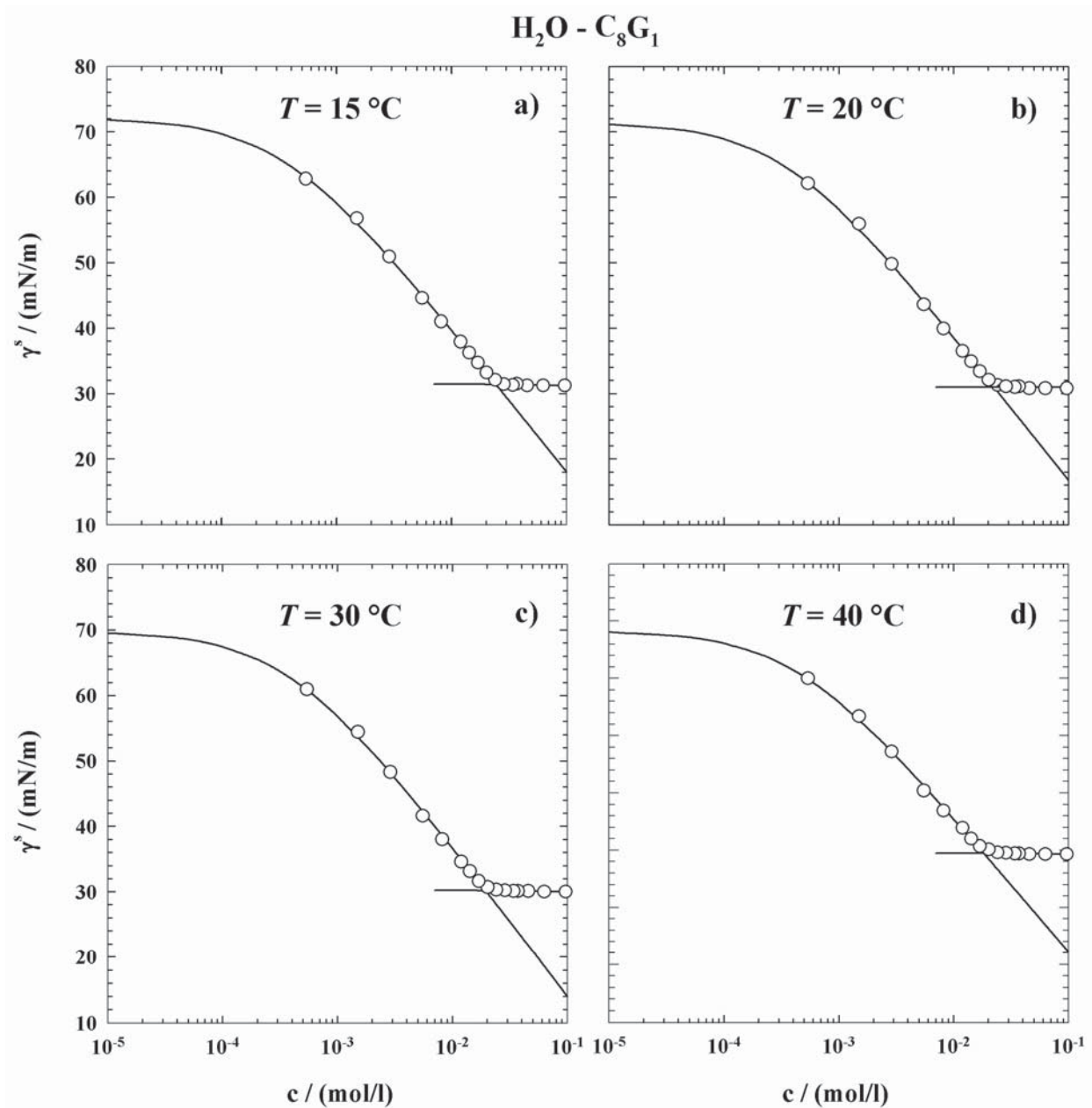
Figure 8.3-2: Surface tension measurements: γ^s as function of c, of C_8G_1 in water at different temperatures, $T = 15\ °C$ (a), $T = 20\ °C$ (b), $T = 30\ °C$ (c), $T = 40\ °C$ (d).
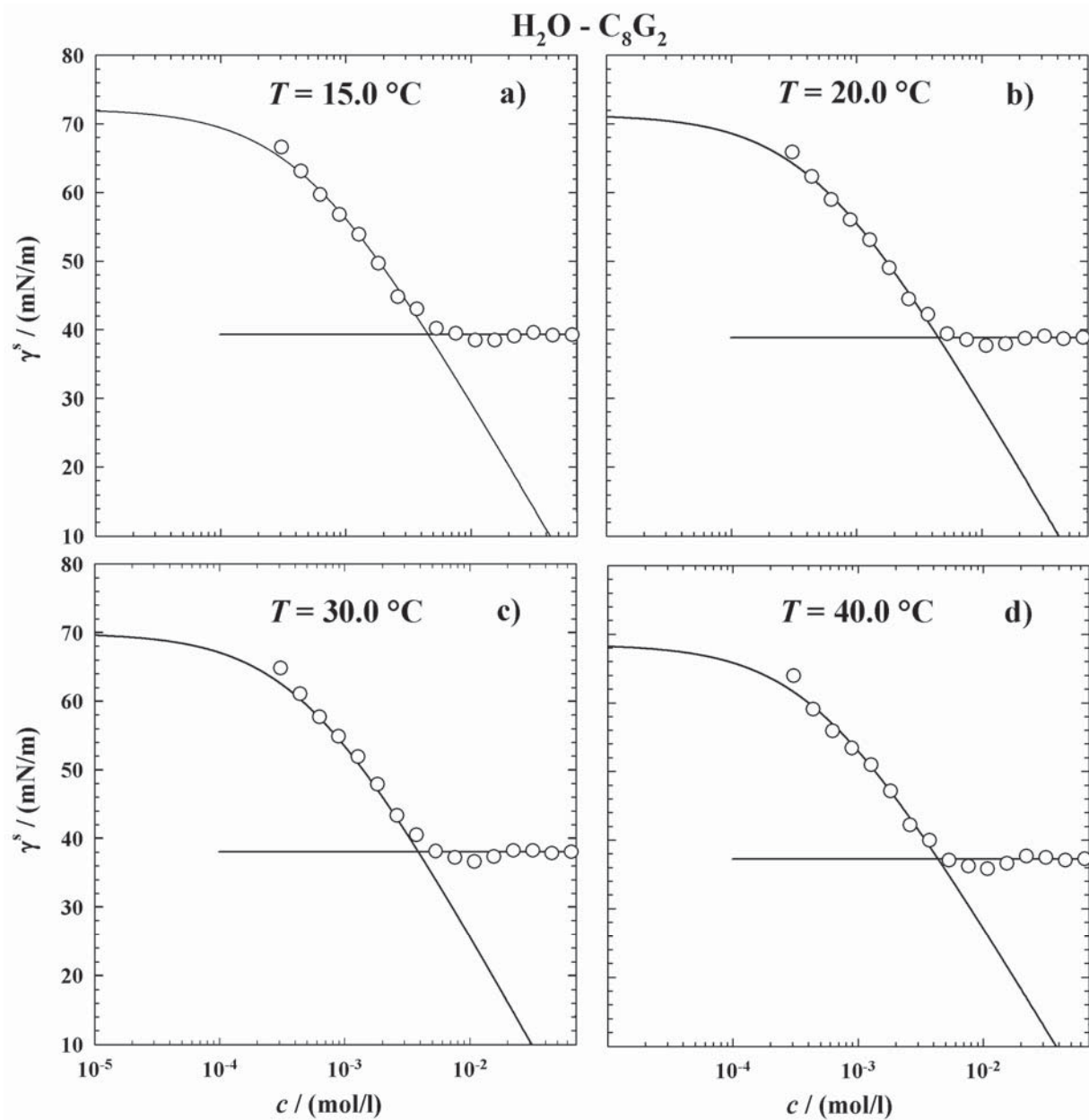
Figure 8.3-3: Surface tension measurements: γ^s as function of c, of C_8G_2 in water at different temperatures, $T = 15\,°C$ (a), $T = 20\,°C$ (b), $T = 30\,°C$ (c), $T = 40\,°C$ (d).

Table 8-3: Parameter of the surface tension measurements, σ as function of c, for C_8G_1, C_7G_1 and C_8G_2 in water at different temperatures, $T = 15, 20, 30$ and $40\,°C$. a_s: head group area of surfactant. cmc: Critical micelle concentration. σ^{cmc}: Surface tension at $c \geq$ cmc. σ_0: Surface tension at $c = 0$ (pure water). a and b: Fit parameter for the *Langmuir-Szyszkowski* equation (5.3).

H_2O - C_7G_1

$T\,/\,°C$	$a_s\,/\,Å^2$	cmc / (mol/l)	$\sigma^{cmc}\,/\,(mN/m)$	$\sigma_0\,/\,(mN/m)$	a / (mN/m)	b
15	44.6	0.0792	33.1	72	9.4	787
20	45.5	0.073	32.7	71.2	9.365	820.4
30	46.6	0.0644	32	69.7	9.54	793.8
40	48.0	0.0591	31.2	68.1	9.648	756

H_2O - C_8G_1

$T\,/\,°C$	$a_s\,/\,Å^2$	cmc / (mol/l)	$\sigma^{cmc}\,/\,(mN/m)$	$\sigma_0\,/\,(mN/m)$	a / (mN/m)	b
15	43.7	0.024	31.28	72.1	9.5	2941.6
20	43.9	0.022	30.97	71.4	9.6	2991.4
30	47.6	0.0195	30.08	69.8	9.96	2690.3
40	49.1	0.0185	29.37	68.3	10.26	2358.3

H_2O - C_8G_2

$T\,/\,°C$	$a_s\,/\,Å^2$	cmc / (mol/l)	$\sigma^{cmc}\,/\,(mN/m)$	$\sigma_0\,/\,(mN/m)$	a / (mN/m)	b
15	35.4	0.00460	39.15±0.15	72.2	13.55	2271
20	36.3	0.00456	38.7±0.2	71.3	13.52	2230
30	36.4	0.00429	37.85±0.15	69.9	14.08	2232
40	40.2	0.00440	37.1±0.1	68.5	13.07	2283

8.4 Ternary System: Microemulsions

Table 8-4: Composition of the SANS samples of the water-rich microemulsions $D_2O - C_{12}E_5 - n$-alkane, $\gamma_a = 0.030$. (D_2O contaminated with H_2O, mass fraction of oil in the respective protonated systems $w_{B,h}$, mass fraction of oil in the SANS samples $w_{B,d}$, volume fraction of oil ϕ_B, phase transition temperatures $T_{\bar{2}\to1}$ and $T_{\underline{2}\to1}$, monomeric solubility of $C_{12}E_5$ in the oil $\gamma_{mon,b}$, taken from ref. [206], and the respective volume fraction $\phi_{mon,b}$ calculated using the densities given in Table 6-1). The n-alkanes are mixtures of protonated and deuterated compounds, as given in Table 6-1 (see subsection 6.2).

n-alkane(d/h)	$w_{B,h}$	$w_{B,d}$	ϕ_B	$T_{\bar{2}-1}$ / °C	$T_{\underline{2}-1}$ / °C	$\gamma_{mon,b}$	$\phi_{mon,b}$
n-octane	0.0600	0.0626	0.0831	28.38	26.47	0.016	0.014
n-octane/n-decane ($\beta_{Octane} \approx 0.5$)	0.0430	0.0447	0.0591	29.84	26.79	0.015	0.013
n-decane	0.0290	0.0301	0.0392	30.96	25.68	0.015	0.013
n-dodecane	0.0191	0.0197	0.0252	33.75	25.97	0.019	0.017
n-tetradecane	0.0131	0.0136	0.0171	35.74	26.45	0.019	0.017

Table 8-5: Measurement temperatures T, diffusion coefficients D and the corresponding (effective) hydrodynamic radii R_H, obtained from dynamic light scattering measurements on the microemulsions of the basic system H_2O – $C_{12}E_5$ – n-alkane, $\gamma_a = 0.030$, under variation of the n-alkane. The mass fraction of oil w_B as well as the phase transition temperature for the emulsification failure T_{efb} is specified at the outer left column for each sample.

Sample	T / °C	D / m²s⁻¹10⁻¹²	R_H / nm
n-octane	29.50	2.01	158.60
$w_B = 0.0598$	28.70	6.32	42.89
$T_{efb} = 27.69$ °C	27.90	10.36	25.58
	27.80	11.83	25.41
	27.60	12.47	21.10
	27.40	13.31	19.70
n-octane/n-decane	30.20	1.74	217.9
($\beta_{Octane} = 0.75$)	29.10	9.12	29.92
$w_B = 0.0505$	28.00	14.88	17.86
$T_{efb} = 27.78$ °C	27.40	16.29	16.04
n-octane/n-decane	27.40	19.68	13.31
($\beta_{Octane} = 0.50$)	27.80	18.98	13.90
$w_B = 0.043$	28.00	18.56	14.30
$T_{efb} = 27.36$ °C	28.20	17.52	15.23
	28.40	16.90	15.87
	28.58	16.01	16.83
	28.78	15.10	17.92
	28.98	13.88	19.63
	29.25	12.55	21.86
	29.58	10.52	26.26
	29.90	8.68	32.05
n-decane	32.00	1.30	233.90
$w_B = 0.029$	29.67	14.69	18.93
$T_{efb} = 26.97$ °C	28.00	24.48	11.80
	27.40	24.27	10.80
	27.00	24.66	10.50
n-dodecane	35.60	13.44	24.67
$w_B = 0.0193$	31.70	22.04	13.21
$T_{efb} = 27.58$ °C	29.50	34.33	8.08
	28.50	34.87	7.73
	27.80	33.42	7.90
n-tetradecane	37.10	3.04	112.30
$w_B = 0.0131$	32.50	25.14	11.79
$T_{efb} = 27.63$ °C	28.00	42.42	6.26

Table 8-6: Values of the interfacial tension σ_{ab} between the water-rich microemulsion and the oil excess phase obtained by spinning drop measurements at different temperatures. All samples were prepared with a mass fraction γ_a of $C_{12}E_5$ in the water/$C_{12}E_5$ mixture of $\gamma_a = 0.030$ and equilibrated at the respective temperature with a mass fraction of oil $w_B = 0.3$.

System	T / °C	σ_{ab} / mNm^{-1}
H_2O - $C_{12}E_5$ - *n*-octane	26.09	0.0440
	27.55	0.0260
	29.07	0.0162
	29.07	0.0174
H_2O -$C_{12}E_5$ - *n*-decane	25.60	0.1591
	25.60	0.1630
	29.00	0.0950
	29.73	0.0820
H_2O -$C_{12}E_5$ - *n*-octane/*n*-decane	25.49	0.0924
	25.49	0.0977
($\beta_{octane} = 0.50$)	29.55	0.0434
	29.55	0.0457
	27.60	0.0665
	27.60	0.0630
H_2O -$C_{12}E_5$ - *n*- octane/*n*-decane	26.18	0.0677
	27.90	0.0520
($\beta_{octane} = 0.75$)	29.68	0.0263
H_2O -$C_{12}E_5$ -*n*-dodecane	25.00	0.3430
	27.95	0.2517
	27.95	0.2590
	30.14	0.1880
H_2O - $C_{12}E_5$ - *n*-tetradecane	24.95	0.468
	24.95	0.449
	27.95	0.360
	27.95	0.373
	27.95	0.349
	30.95	0.319
	30.95	0.317
	30.95	0.309
	30.95	0.297

8.5 Symbols and Abbreviations

1	index of the one phase state
2	index of a two phase state
$\underline{2}$	index of an oil-in-water microemulsion
$\overline{\underline{2}}$	index of a water-in-oil microemulsion
3	index of the three phase state
α	weight fraction of oil in the binary mixture of water and oil
a_s	head group area of a single surfactant molecule
A	index of the hydrophilic microemulsion sub-phase
A	interfacial area
A	*Avogardo* Number
$A(\Gamma)$	distribution function of the relaxation rate Γ
$A(q)$	scattering amplitude of a particle
$A_{core}(q)$	scattering amplitude of the droplet core
$A_{cs}(q)$	scattering amplitude of a droplet with core-shell architecture
$A_{film}(q)$	scattering amplitude of the droplet film
A_v	surface area of a microemulsion droplet
β	mass fraction of co-oil in a binary oil-mixture
b_{incoh}	incoherent scattering background
B	index of the hydrophobic microemulsion sub-phase
χ_T	isothermal compressibility
c_1, c_2	principle curvatures
cep_α	upper critical end point
cep_β	lower critical end point
cl_α	critical line on the oil rich side
cl_b	critical line on the water rich side
cmc	critical micelle concentration
cp_α	critical point of the binary oil-surfactant mixture
cp_β	critical point of the binary water-surfactant mixture
c_{salt}	concentration of salt
C	index of the amphiphilic microemulsion sub-phase

δ	weight fraction of the co-surfactant in the surfactant/co-surfactant mixture
δ	inner *hard core* diameter
Δ	is the thickness of the attractive well
d	cross section of a cylinder
d_{HS}	interaction diameter of a hard sphere
d_{eff}	effective diameter for charged interactions
$d\Sigma/d\Omega$	differential scattering cross-section
D	diameter of macroions
D	diffusion coefficient
D_T	thermal diffusion coefficient
DLS	dynamic light scattering
ε	relative thickness of the attractive well
ε	permittivity
ε_0	electric constant
efb	*emulsification failure boundary*
E_b	curvature energy
$E(q,\tau)$	electric field
ϕ	volume fraction of oil in the binary mixture of water and oil
ϕ_a	overall water volume fraction in a microemulsion
ϕ_b	overall oil volume fraction in a microemulsion
ϕ_c	overall surfactant volume fraction in a microemulsion
$\phi_{c,i}$	volume fraction of the surfactant in the internal interface
ϕ_{disp}	volume fraction of the dispersed phase
ϕ_k	volume fraction of the component k
γ	overall surfactant weight fraction in a microemulsion
$\tilde{\gamma}$	surfactant weight fraction at the $\tilde{X}$-point
γ_0	weight fraction of surfactant monomers in a water-oil mixture
γ_a	surfactant weight fraction in a binary water-surfactant mixture
γ_b	surfactant weight fraction in a binary oil-surfactant mixture
γ^s	surface tension
$g^{(1)}(q,\tau)$	normalised time-field correlation function
$g^{(2)}(q,\tau)$	normalised time – intensity correlation function

Γ	relaxation rate of the particle diffusion
Γ	surface excess concentration
GIFT	*generalized indirect Fourier transformation*
η	viscosity
h	*Planck*'s constant = $6.626 \cdot 10^{-34}$ Js
η	reduced *Planck* constant = $h/2\pi$
H	mean curvature of the amphiphilic film
c_0	spontaneous curvature of the amphiphilic film
c	surfactant concentration
$c_{BÝ}$	*concentration of Basantol® Yellow 215 in water*
HLB	hydrophilic lipophilic balance
$I(q)$	*q*-dependent scattering intensity
$I_{Bg}(q)$	environmental background intensity
$I_{core}(q)$	scattering intensity of the droplet core
$I_{cross}(q)$	scattering intensity of the cross term
$I_{Ec}(q)$	scattering intensity from the empty sample-cell
$I_{Ec,St}(q)$	scattering intensity from the empty cell of the calibration standard
$I_{film}(q)$	scattering intensity of the droplet film
$I_{St}(q)$	scattering intensity from calibration standard H_2O
$I_{Sa}(q)$	scattering intensity from the sample
J_i	flux of component i
$J_1(qr)$	first order *Bessel* function of first kind
κ	bending rigidity of the amphiphilic film
κ	inverse screening length
$\bar{\kappa}$	saddle splay modulus
k	number of carbon atoms in *n*-alkanes
k_B	*Boltzmann* constant
$\vec{k}_e$	wave vector of the scattered neutron wave
$\vec{k}_i$	wave vector of the incident neutron wave
K	*Gaussian curvature*
λ	wave length
l_s	length of a single surfactant molecule
L	cylinder length

L_1	micellar phase
L_2	inverse micellar phase
L_3	L_3-Phase
L_α	lamellar phase
m_i	mass of the component i
m_n	neutron mass = $1.675 \cdot 10^{-27}$ kg
M	molar mass
∇c	concentration gradient
∇T	temperature gradient
n	particle number density
ncb	near critical boundary
N	total number of particles
N_a	*Avogadro*'s constant = $6.022 \cdot 10^{23}$ mol^{-1}
OD	optical density
Π	packing parameter
p	polydispersity index
p	pressure
$P(q)$	particle form factor
$P_{cross}(q)$	scattering function for a cylinder cross-section
$P_{rod}(q)$	monodisperse form factor of an infinitely thin rod
θ	scattering angle
q	absolute value of the scattering vector
$\vec{q}$	scattering vector; also called momentum transfer vector
ρ	scattering length density
ρ^0	macroscopic or mass density
ρ_{bulk}	scattering length density of the continuous bulk-phase of a droplet microemulsion
ρ_{core}	scattering length density of the droplet core
ρ_{film}	scattering length density of the amphiphilic film
ρ_k	scattering length density of the component k
ρ_{phase}	scattering length density of a phase
$\Delta\rho$	scattering length density difference

$\Delta\rho_{core}$	difference in the scattering length densities of the droplet core and the surrounding bulk-medium
$\Delta\rho_{film}$	difference in the scattering length densities of the amphiphilic film and the surrounding bulk-medium
R	droplet radius
R	universal gas constant = 8.314 $J\cdot mol^{-1}\cdot K^{-1}$
R_0	mean droplet radius
R_H	hydrodynamic radius
r_1, r_2	principle curvature radii
σ	standard variation of the size distribution of the radius
σ_{ab}	interfacial tension
S/V	specific internal interface
$S(q)$	structure factor
S_T	*Soret* coefficient
SANS	small angle neutron scattering
τ	stickiness parameter
τ	relaxation time
t	standard variation of the *Gaussian* function for the density profile of the amphiphilic film (~ thickness of the amphiphilic film)
t	time
T	temperature
$\tilde{T}$	temperature at the $\tilde{X}$-point
T_α	critical temperature of the binary oil-surfactant mixture
T_β	critical temperature of the binary water-surfactant mixture
T_c	critical temperature
T_l	lower critical end point temperature
T_m	mean temperature, *i.e.* temperature at the *optimum point*
T_u	upper critical end point temperature
TDFRS	thermal diffusion forced *Rayleigh* scattering
u_0	depth of the interaction potential of sticky hard spheres
v	velocity of a neutron
v_s	volume of a single surfactant molecule
V	volume of a particle

V_{core}	volume of the droplet core
V_{film}	volume of the droplet film
V_i	volume of component i
w_B	overall oil weight fraction
$W(R,R,\sigma)$	distribution function of the radius R around the mean value R_0 (polydispersity σ)
ξ	correlation length of critical fluctuations
$\bar{\xi}$	maximal characteristic length scale of microemulsions
X	number BY215 molecules per aggregate
$\tilde{X}$	fish tail point of a microemulsion with arbitrary α
ψ	weight fraction of additives in the hydrophilic sub-phase
$\psi_0(z)$	surface potential
z	effective number of charges

9 Literature and Notes

1   C. Ludwig, Sitz. ber. Akad. Wiss. Wien Math.-naturw. Kl. **20**, 539 (1856).
2   S. Wiegand, in *Bunsen - Magazin* (Deutsche Bunsen Gesellschaft für Physikalische Chemie, 2006), Vol. 8, p. 130.
3   K. Clusius and G. Dickel, Naturwissenschaften **26** (1938).
4   K. Clusius and G. Dickel, Naturwissenschaften **27**, 148 (1939).
5   More information can be found at the homepage of the U.S. Department of Energy, Office of History and Heritage Resources, http://www.cfo.doe.gov/me70/manhattan/index.htm
6   H. Colfen and M. Antonietti, New Developments in Polymer Analytics I **150**, 67 (2000).
7   J. C. Giddings, Science **260**, 1456 (1993).
8   N. B. Nia and K. Movagharnejad, Fluid Phase Equilib. **262**, 174 (2007).
9   G. Galliero and F. Montel, Physical Review E **78**, 10 (2008).
10   P. W. Atkins, *Physikalische Chemie* (Wiley-VCH, 2001).
11   S. Chapman and T. G. Cowling, *The Mathematical Theory of Non Uniform Gases* (University Press, Cambridge, 1970).
12   K. I. Morozov, Physical Review E **79**, 031204 (2009).
13   P. Blanco, M. M. Bou-Ali, J. K. Platten, P. Urteaga, J. A. Madariaga, and C. Santamaria, J Chem Phys **129** (2008).
14   J. F. Dutrieux, J. K. Platten, G. Chavepeyer, and M. M. Bou-Ali, Journal of Physical Chemistry B **106**, 6104 (2002).
15   C. Debuschewitz and W. Kohler, Phys Rev Lett **8705** (2001).
16   P. Polyakov, J. Luettmer-Strathmann, and S. Wiegand, Journal of Physical Chemistry B **110**, 26215 (2006).
17   P. Polyakov and S. Wiegand, Physical Chemistry Chemical Physics **11**, 864 (2009).
18   G. Wittko and W. Kohler, European Physical Journal E **21**, 283 (2006).
19   S. Wiegand, Journal of Physics-Condensed Matter **16**, R357 (2004).
20   J. K. Platten, Journal of Applied Mechanics-Transactions of the Asme **73**, 5 (2006).
21   W. Kohler and R. Schafer, New Developments in Polymer Analytics Ii **151**, 1 (2000).
22   W. Kohler, A. Krekhov, and W. Zimmermann, in *Complex Macromolecular Systems I*, 2010), Vol. 227, p. 145.

23   J. Luettmer-Strathmann, International Journal of Thermophysics **26**, 1693 (2005).

24   K. I. Morozov, Journal of Magnetism and Magnetic Materials **201**, 248 (1999).

25   R. Piazza and A. Parola, Journal of Physics-Condensed Matter **20** (2008).

26   H. Ning, J. K. G. Dhont, and S. Wiegand, Langmuir **24**, 2426 (2008).

27   H. Ning, J. Buitenhuis, J. K. G. Dhont, and S. Wiegand, J Chem Phys **125** (2006).

28   H. Ning, R. Kita, H. Kriegs, J. Luettmer-Strathmann, and S. Wiegand, Journal of Physical Chemistry B **110**, 10746 (2006).

29   H. Ning, R. Kita, and S. Wiegand, Progress in Colloid and Polymer Science **133**, 111 (2006).

30   R. Piazza, Philos. Mag. **83**, 2067 (2003).

31   R. Piazza and A. Guarino, Phys Rev Lett **88** (2002).

32   S. Duhr, S. Arduini, and D. Braun, European Physical Journal E **15**, 277 (2004).

33   D. Vigolo, G. Brambilla, and R. Piazza, Physical Review E **75** (2007).

34   S. A. Putnam, D. G. Cahill, and G. C. L. Wong, Langmuir **23**, 9221 (2007).

35   S. Duhr and D. Braun, Phys Rev Lett **96** (2006).

36   J. Rauch and W. Kohler, Phys Rev Lett **88** (2002).

37   J. Rauch and W. Kohler, J Chem Phys **119**, 11977 (2003).

38   K. J. Zhang, M. E. Briggs, R. W. Gammon, J. V. Sengers, and J. F. Douglas, J Chem Phys **111**, 2270 (1999).

39   J. Rauch and W. Kohler, Macromolecules **38**, 3571 (2005).

40   H. Ning and S. Wiegand, J Chem Phys **125** (2006).

41   A. Parola and R. Piazza, European Physical Journal E **15**, 255 (2004).

42   W. Poon, Science **304**, 830 (2004).

43   R. Rusconi, L. Isa, and R. Piazza, Journal of the Optical Society of America B-Optical Physics **21**, 605 (2004).

44   A. Vanblaaderen and A. P. M. Kentgens, Journal of Non-Crystalline Solids **149**, 161 (1992).

45   A. Vanblaaderen, J. Vangeest, and A. Vrij, J Colloid Interf Sci **154**, 481 (1992).

46   X. D. Wang, Z. X. Shen, T. Sang, X. B. Cheng, M. F. Li, L. Y. Chen, and Z. S. Wang, J Colloid Interf Sci **341**, 23 (2010).

47   M. Kahlweit and R. Strey, Angewandte Chemie-International Edition in English **24**, 654 (1985).

48   J. Israelachvili, *Intermolecular and Surface Forces* (Academic Press, London, 1992).

49   R. G. Laughlin, *The Aqueous Phase Behaviour of Surfactants* (Academic Press, New York, 1994).

50   T. Sottmann and R. Strey, in *Fundamentals of interface and colloid science*, edited by J. Lyklema (Elsevier Academic Press, Amsterdam, 2005), Vol. V Soft Colloids.

51   D. G. Leaist and L. Hui, J Phys Chem-Us **93**, 7547 (1989).

52   N. Takeyama and K. Nakashima, J Phys Chem-Us **97**, 9073 (1993).

53   S. Iacopini, R. Rusconi, and R. Piazza, European Physical Journal E **19**, 59 (2006).

54   S. Wiegand (private communication).

55   M. Kahlweit, R. Strey, and G. Busse, Physical Review E **47**, 4197 (1993).

56   T. Sottmann and R. Strey, J Chem Phys **106**, 8606 (1997).

57   M. P. Santos, S. L. Gomez, E. Bringuier, and A. M. F. Neto, Physical Review E **77** (2008).

58   P. W. Atkins, *Physical Chemistry* (VCH, Weinheim, 1988).

59   A. Perronace, C. Leppla, F. Leroy, B. Rousseau, and S. Wiegand, J Chem Phys **116**, 3718 (2002).

60   G. J. T. Tiddy, Physics Reports-Review Section of Physics Letters **57**, 2 (1980).

61   H. Wennerstrom and B. Lindman, Physics Reports-Review Section of Physics Letters **52**, 1 (1979).

62   D. F. Evans and H. Wennerstrom, *The Colloidal Domain* (VCH, 1994).

63   R. Strey, W. Jahn, G. Porte, and P. Bassereau, Langmuir **6**, 1635 (1990).

64   T. Foster, PhD - thesis, Universität zu Köln, 2006.

65   M. E. Cates, D. Roux, D. Andelman, S. T. Milner, and S. A. Safran, Europhysics Letters **5**, 733 (1988).

66   G. Gompper and D. M. Kroll, Phys Rev Lett **81**, 2284 (1998).

67   S. A. Safran and L. A. Turkevich, Phys Rev Lett **50**, 1930 (1983).

68   W. Helfrich, Z. Naturforsch. **28c**, 693 (1973).

69   P. G. Nilsson and B. Lindman, J Phys Chem-Us **87**, 4756 (1983).

70   S. Puvvada and D. Blankschtein, J Chem Phys **92**, 3710 (1990).

71   R. Nagarajan, Langmuir **18**, 31 (2002).

72   J. N. Israelachvili and D. J. Mitchell, Biochimica Et Biophysica Acta **389**, 13 (1975).

73   J. N. Israelachvili, D. J. Mitchell, and B. W. Ninham, Journal of the Chemical Society-Faraday Transactions Ii **72**, 1525 (1976).

74   V. Posselt, PhD-Thesis, Universität zu Köln, 2010.

75   M. Kahlweit, et al., J Colloid Interf Sci **118**, 436 (1987).

76   J. F. Bodet, J. R. Bellare, H. T. Davis, L. E. Scriven, and W. G. Miller, J Phys Chem-Us **92**, 1898 (1988).

77   W. Jahn and R. Strey, J Phys Chem-Us **92**, 2294 (1988).

78   P. K. Vinson, J. G. Sheehan, W. G. Miller, L. E. Scriven, and H. T. Davis, J Phys Chem-Us **95**, 2546 (1991).

79   F. Lichterfeld, T. Schmeling, and R. Strey, J Phys Chem-Us **90**, 5762 (1986).

80   R. Strey, O. Glatter, K. V. Schubert, and E. W. Kaler, J Chem Phys **105**, 1175 (1996).

81   R. Strey, J. Winkler, and L. Magid, J Phys Chem-Us **95**, 7502 (1991).

82   M. Teubner and R. Strey, J Chem Phys **87**, 3195 (1987).

83   U. Olsson, K. Nagai, and H. Wennerstrom, J Phys Chem-Us **92**, 6675 (1988).

84   R. Strey, Colloid Polym. Sci. **272**, 1005 (1994).

85   J. M. Corkill, J. F. Goodman, and R. H. Ottewill, Transactions of the Faraday Society **57**, 1627 (1961).

86   J. S. Clunie, J. M. Corkill, J. F. Goodman, P. C. Symons, and J. R. Tate, Transactions of the Faraday Society **63**, 2839 (1967).

87   D. J. Mitchell, G. J. T. Tiddy, L. Waring, T. Bostock, and M. P. Mcdonald, J Chem Soc Farad T 1 **79**, 975 (1983).

88   R. Strey, Ber Bunsen Phys Chem **100**, 182 (1996).

89   A. Bernheim-Groswasser, E. Wachtel, and Y. Talmon, Langmuir **16**, 4131 (2000).

90   O. Glatter, G. Fritz, H. Lindner, J. Brunner-Popela, R. Mittelbach, R. Strey, and S. U. Egelhaaf, Langmuir **16**, 8692 (2000).

91   R. Strey and A. Pakusch, in *Surfactants in Solution*, edited by K. L. Mittal and P. Bothorel (Plenum Publishing Corporation, 1987), Vol. 4, p. 465.

92   A. G. Zilman and S. A. Safran, Physical Review E **66** (2002).

93   A. Zilman, S. A. Safran, T. Sottmann, and R. Strey, Langmuir **20**, 2199 (2004).

94   J. C. Lang and R. D. Morgan, J. Chem. Phys. **73**, 5849 (1980).

95   K. V. Schubert, R. Strey, and M. Kahlweit, J Colloid Interf Sci **141**, 21 (1991).

96   F. Harusawa, S. Nakamura, and T. Mitsui, Colloid Polym. Sci. **252**, 613 (1974).

97   R. Strey, R. Schomacker, D. Roux, F. Nallet, and U. Olsson, J Chem Soc Faraday T **86**, 2253 (1990).

98   D. Varade, H. Kunieda, R. Strey, and C. Stubenrauch, J Colloid Interf Sci **300**, 338 (2006).

99   C. B. Douglas and E. W. Kaler, Langmuir **10**, 1075 (1994).

100   V. M. Garamus, Langmuir **19**, 7214 (2003).

101   J. Penfold, I. Tucker, R. K. Thomas, E. Staples, and R. Schuermann, Journal of Physical Chemistry B **109**, 10760 (2005).

102   S. Puvvada and D. Blankschtein, J Phys Chem-Us **96**, 5579 (1992).

103   A. Shiloach and D. Blankschtein, Langmuir **14**, 7166 (1998).

104   H. G. Thomas, A. Lomakin, D. Blankschtein, and G. B. Benedek, Langmuir **13**, 209 (1997).

105   P. Firman, D. Haase, J. Jen, M. Kahlweit, and R. Strey, Langmuir **1**, 718 (1985).

106   M. Jonstromer and R. Strey, J Phys Chem-Us **96**, 5993 (1992).

107   L. De Salvo Souza, M. Corti, L. Cantu, and V. Degiorgio, Chem Phys Lett **131**, 160 (1986).

108   M. Carvell, C. A. Leng, F. J. Leng, and G. J. T. Tiddy, Chem Phys Lett **137**, 188 (1987).

109   A. Shiloach and D. Blankschtein, Langmuir **14**, 1618 (1998).

110   H. Saito and K. Shinoda, J Colloid Interf Sci **24**, 10 (1967).

111   T. Sottmann and R. Strey, Journal of Physics-Condensed Matter **8**, A39 (1996).

112   C. L. Sassen, A. G. Casielles, T. W. Deloos, and J. D. Arons, Fluid Phase Equilib. **72**, 173 (1992).

113   M. Kahlweit, R. Strey, and G. Busse, J Phys Chem-Us **94**, 3881 (1990).

114   M. Gradzielski, D. Langevin, T. Sottmann, and R. Strey, J Chem Phys **106**, 8232 (1997).

115   U. Olsson and P. Schurtenberger, Optical Methods and Physics of Colloidal Dispersions **104**, 157 (1997).

116   K. Shinoda and H. Kunieda, J Colloid Interf Sci **42**, 381 (1973).

117   K. Shinoda, H. Kunieda, T. Arai, and H. Saijo, J Phys Chem-Us **88**, 5126 (1984).

118   U. Olsson, U. Wurz, and R. Strey, J Phys Chem-Us **97**, 4535 (1993).

119   B. W. Ninham, I. S. Barnes, S. T. Hyde, P. J. Derian, and T. N. Zemb, Europhysics Letters **4**, 561 (1987).

120   T. N. Zemb, S. T. Hyde, P. J. Derian, I. S. Barnes, and B. W. Ninham, J Phys Chem-Us **91**, 3814 (1987).

121   M. Nyden, O. Soderman, and P. Hansson, Langmuir **17**, 6794 (2001).

122   D. Anderson, H. Wennerstrom, and U. Olsson, J Phys Chem-Us **93**, 4243 (1989).

123   M. S. Leaver, U. Olsson, H. Wennerstrom, and R. Strey, Journal De Physique Ii **4**, 515 (1994).

124   A. Bernheim-Groswasser, T. Tlusty, S. A. Safran, and Y. Talmon, Langmuir **15**, 5448 (1999).

125   P. K. Kilpatrick, C. A. Gorman, H. T. Davis, L. E. Scriven, and W. G. Miller, J Phys Chem-Us **90**, 5292 (1986).

126   T. Tlusty, S. A. Safran, R. Menes, and R. Strey, Phys Rev Lett **78**, 2616 (1997).

127   T. Tlusty, S. A. Safran, and R. Strey, Phys Rev Lett **84**, 1244 (2000).

128   G. Porte, Journal of Physics-Condensed Matter **4**, 8649 (1992).

129   M. Gradzielski, D. Langevin, and B. Farago, Physical Review E **53**, 3900 (1996).

130   T. Sottmann, PhD Thesis, Georg-August-Universität zu Göttingen, 1997.

131   P. Lindner and T. Zemb eds., *Neutrons, X-Rays and Light Scattering Methods Applied to Soft Condensed Matter* (North-Holland, Amsterdam, 2002).

132   O. Glatter and O. Kratky eds., *Small Angle X-Ray Scattering* (Academic Press, London, 1982).

133   G. Wedler, *Lehrbuch der Physikalischen Chemie* (Wiley-VCH, Weilheim, 2004).

134   *webpage-FRM II - the neutron source.* [cited; Available from: http://www.frm2.tum.de/en/technik/index.html.

135   *JCNS-webpages / instruments / KWS 1 and KWS 2.* [cited; Available from: www.jcns.info/jcns_kws1 www.jcns.info/jcns_kws2.

136   V. Pipich and I. Vasilief, 03/04/2008).

137   M. Kotlarchyk and S. H. Chen, J Chem Phys **79**, 2461 (1983).

138   J. S. Pedersen, Adv Colloid Interfac **70**, 171 (1997).

139   G. Porod, in *Small Angle X-Ray Scattering*, edited by O. Kratky and O. Glatter (Academic Press, London, 1982).

140   L. Rayleigh, Proceedings of the Royal society of London **84**, 25 (1910).

141   R. Strey, Habilitationschrift, Georg-August-Universität 1992.

142   M. Stieger, J. S. Pedersen, P. Lindner, and W. Richtering, Langmuir **20**, 7283 (2004).

143   T. Foster, T. Sottmann, R. Schweins, and R. Strey, J Chem Phys **128** (2008).

144   M. Gradzielski, D. Langevin, L. Magid, and R. Strey, J Phys Chem-Us **99**, 13232 (1995).

145   T. Neugebauer, Annalen der Physik **5**, 510 (1943).

146   M. Corti and V. Degiorgio, Phys Rev Lett **45**, 1045 (1980).

147   M. Kotlarchyk, S. H. Chen, and J. S. Huang, Phys Rev A **28**, 508 (1983).

148   L. S. Ornstein, Zernike, F., in *Proc.Ned.Akad.Sci.*, 1914), p. 793.

149   D. J. Kinning and E. L. Thomas, Macromolecules **17**, 1712 (1984).

150   R. J. Baxter, J Chem Phys **49**, 2770 (1968).

151   S. V. G. Menon, C. Manohar, and K. S. Rao, J Chem Phys **95**, 9186 (1991).

152   J. P. Hansen and J. B. Hayter, Mol Phys **46**, 651 (1982).

153   J. B. Hayter and J. Penfold, Mol Phys **42**, 109 (1981).

154   O. Glatter, Brunner-Popela,J.,Fritz, G., Bergmann, A.,Frühwirth, Th.,Innerlohinger, *GIFT neogenes*, 2008.

155   P. Pusey, in *Neutrons, X-Rays and Light: Scattering Methods Applied to Soft Matter*, edited by P. Lindner and T. Zemb (Elsevier North-Holland 2002).

156   A. Top, *BATCON 3*. 3/95.

157   *CONTIN (PCS-1 PACK) VERSION 2DP* MAR 1984

158   S. W. Provencher and P. Stepanek, Part. Part. Syst. Charact. **13**, 291 (1996).

159   S. Wiegand, H. Ning, and H. Kriegs, Journal of Physical Chemistry B **111**, 14169 (2007).

160   H. Ning, S. Datta, T. Sottmann, and S. Wiegand, Journal of Physical Chemistry B **112**, 10927 (2008).

161   Basantol® Yellow 215 is a registered trademark of BASF. It is an Azo/1:2 cobalt-complex which is soluble in water and has a strong absorption around = 480 nm. (http://worldaccount.basf.com/wa/NAFTA~en_US/Catalog/Pigments/pi/BASF/range/co_woo_dyes_basantol)

162   A. Khatory, F. Lequeux, F. Kern, and S. J. Candau, Langmuir **9**, 1456 (1993).

163   D. J. Cebula and R. H. Ottewill, Colloid Polym. Sci. **260**, 1118 (1982).

164   B. Lindman and H. Wennerstrom, J Phys Chem-Us **95**, 6053 (1991).

165   T. Foster, S. A. Safran, T. Sottmann, and R. Strey, J Chem Phys **127**, 204711 (2007).

166   J. Penfold, E. Staples, L. Thompson, I. Tucker, J. Hines, R. K. Thomas, J. R. Lu, and N. Warren, Journal of Physical Chemistry B **103**, 5204 (1999).

167   E. W. Kaler, J.Appl.Cryst **21**, 729 (1988).

168   W. Brown, R. Johnsen, P. Stilbs, and B. Lindman, J Phys Chem-Us **87**, 4548 (1983).

169   T. Kato, M. Kanada, and T. Seimiya, Langmuir **11**, 1867 (1995).

170   O. Glatter, R. Strey, K. V. Schubert, and E. W. Kaler, Ber Bunsen Phys Chem **100**, 323 (1996).

171   J. P. Wilcoxon, D. W. Schaefer, and E. W. Kaler, J Chem Phys **90**, 1909 (1989).

172   G. Fritz, A. Bergmann, and O. Glatter, J Chem Phys **113**, 9733 (2000).

173   W. Caetano, E. L. Gelamo, M. Tabak, and R. Itri, J Colloid Interf Sci **248**, 149 (2002).

174   L. Galantini, E. Giglio, A. Leonelli, and N. V. Pavel, Journal of Physical Chemistry B **108**, 3078 (2004).

175   A. Isihara, J Chem Phys **18**, 1446 (1950).

176   S. V. G. Menon, V. K. Kelkar, and C. Manohar, Phys Rev A **43**, 1130 (1991).

177   K. S. Rao, P. S. Goyal, B. A. Dasannacharya, S. V. G. Menon, V. K. Kelkar, C. Manohar, and B. K. Mishra, Physica B **174**, 170 (1991).

178   S. H. Chen, J. Rouch, F. Sciortino, and P. Tartaglia, J. Phys.: Condens. Matter **6**, 10855 (1994).

179   P. G. Cummins, E. Staples, and J. Penfold, J Phys Chem-Us **95**, 5902 (1991).

180   M. P. Santos, S. L. Gomez, E. Bringuier, and A. M. F. Neto, Physical Review E **77**, 011403 (2008).

181   P. L. Du Nouey, The Journal of General Physiology **7**, 625 (1925).

182   Manual, *Krüss digital Tensiometer K10T*.

183   B. von Szyszkowski, Z. Phys. Chem. **64**, 385 (1908).

184   P. C. Hiemenz, *Principles of colloid and surface chemistry* (Dekker, Inc, New York, 1986).

185   S. Matsumura, K. Imai, S. Yoshikawa, K. Kawada, and T. Uchibori, J. Am. Oil Chem. Soc. **67**, 996 (1990).

186   F. Nilsson, O. Soderman, and I. Johansson, J Colloid Interf Sci **203**, 131 (1998).

187   R. T. Zhang, P. A. Marone, P. Thiyagarajan, and D. M. Tiede, Langmuir **15**, 7510 (1999).

188   B. J. Boyd, C. J. Drummond, I. Krodkiewska, and F. Grieser, Langmuir **16**, 7359 (2000).

189   J. Thiem and T. Bocker, in *Industrial Applications of Surfactants Iii*, edited by D. R. Karsa (Royal Soc Chemistry, Cambridge, 1992), p. 123.

190   M. Aoudia and R. Zana, J Colloid Interf Sci **206**, 158 (1998).

191   L. J. Chen, S. Y. Lin, C. C. Huang, and E. M. Chen, Colloids and Surfaces a-Physicochemical and Engineering Aspects **135**, 175 (1998).

192   B. Arlt, S. Datta, T. Sottmann, and S. Wiegand, Journal of Physical Chemistry B **114**, 2118 (2010).

193   H. U. Kim and K. H. Lim, Bulletin of the Korean Chemical Society **24**, 1449 (2003).

194   B. Arlt. Unpublished results

195   G. Galliero and S. Volz, J Chem Phys **128** (2008).

196   S. Christ and P. Schurtenberger, J Phys Chem-Us **98**, 12708 (1994).

197   M. Zulauf and H. F. Eicke, J Phys Chem-Us **83**, 480 (1979).

198   R. Keil, Z. Anal. Chem. **249**, 289 (1970).

199   B. Vonnegut, Rev. Sci. Instr. **13**, 6 (1942).

200   B. Arlt (private communication).

201   C. Leppla and S. Wiegand, Philos. Mag. **83**, 1989 (2003).

202   J. K. Platten, M. M. Bou-Ali, P. Costeseque, J. F. Dutrieux, W. Kohler, C. Leppla, S. Wiegand, and G. Wittko, Philos. Mag. **83**, 1965 (2003).

203   T. Hellweg and W. Eimer, Colloids and Surfaces a-Physicochemical and Engineering Aspects **136**, 97 (1998).

204   T. Hellweg and R. von Klitzing, Physica A **283**, 349 (2000).

205   (private communication).

206   S. Burauer, T. Sachert, T. Sottmann, and R. Strey, Physical Chemistry Chemical Physics **1**, 4299 (1999).

207   M. Kahlweit, R. Strey, and P. Firman, J Phys Chem-Us **90**, 671 (1986).

208   T. Hellweg and D. Langevin, Physica a-Statistical Mechanics and Its Applications **264**, 370 (1999).

209   D. Guest and D. Langevin, J Colloid Interf Sci **112**, 208 (1986).

210   J. Penfold, E. Staples, and I. Tucker, Journal of Physical Chemistry B **106**, 8891 (2002).

211   U. Menge, P. Lang, G. H. Findenegg, and P. Strunz, Journal of Physical Chemistry B **107**, 1316 (2003).

212   H. Leitao, A. M. Somoza, M. M. T. daGama, T. Sottmann, and R. Strey, J Chem Phys **105**, 2875 (1996).

213   B. Arlt. unpublished results

214   B. Arlt, S. Datta, T. Sottmann, and S. Wiegand, Journal of Physical Chemistry B **114**, 2118.

Erklärung

Ich versichere, dass ich die von mir vorgelegte Dissertation selbständig angefertigt, die benutzten Quellen und Hilfsmittel vollständig angegeben und die Stellen der Arbeit - einschließlich Tabellen, Karten und Abbildungen -, die anderen Werken im Wortlaut oder dem Sinn nach entnommen sind, in jedem Einzelfall als Entlehnung kenntlich gemacht habe; dass diese Dissertation noch keiner anderen Fakultät oder Universität zur Prüfung vorgelegen hat; dass sie - abgesehen von unten angegebenen Teilpublikationen - noch nicht veröffentlich worden ist sowie, dass ich eine solche Veröffentlichung vor Abschluss des Promotionsverfahrens nicht vornehmen werde. Die Bestimmungen der Promotionsordnung sind mir bekannt. Die von mir vorgelegte Dissertation ist von Prof. Dr. R. Strey betreut worden.

Köln, den 19. November 2010

Curriculum Vitae

Personal Datails

Name: Sascha Datta
Date of birth: 4th August 1977
Place of birth: Leverkusen

Academic Background

10/2007 - 01/2011	Research Assistant and PhD-thesis University of Cologne, Institute for Physical Chemistry Dissertation advisor: Prof. Dr. R. Strey
12/2003 – 07/2007	Diploma, Chemistry University of Cologne (from 10/2004) and RWTH Aachen (12/2003 – 08/2004) Diploma thesis (University of Cologne, Supervisor Prof. Dr. R. Strey): „*Untersuchung der Homogenisierungskinetik von Wasser-Diesel-Mikroemulsionen mit einer Stopped-Flow Apparatur*"
10/1999 – 12/2003	Diploma (FH), Chemical Engineering Aachen University of Applied Sciences Diploma Thesis (Supervisor Prof. Dr. Th. Mang): „*Kontrollierte Freisetzung von Wirkstoffen aus Thermosensitiven Hydrogelen*"
04/1998 – 03/1999	Philipps-Universität Marburg Human Medicine

School

08/1987 – 06/1996	Integrierte Gesamtschule Paffrath, Bergisch Gladbach General qualification for university entrance (*Abitur*)
08/1983 – 08/1987	Katholische Grundschule Voiswinkel, Odenthal Elementary school

International Experience

08/2002 – 01/2003	Mid-Sweden University, Sundsvall, Sweden Study Abroad, Chemistry
10/1997 – 11/1997	Belfast City Hospital, Belfast, Northern Ireland Work Experience in Nursing

Alternative National Service

09/1996 – 10/1997	Die Kette e.V., Bergisch Gladbach Assistance for mentally ill people